

UNIVERSITY OF RIJEKA  
FACULTY OF ENGINEERING

David Liović

**THE EFFECTS OF MECHANICAL  
AND SURFACE PROPERTIES ON  
THE DESIGN OF ADDITIVELY  
MANUFACTURED Ti6Al4V ALLOY  
COMPONENTS**

DOCTORAL THESIS

Rijeka, 2024.







UNIVERSITY OF RIJEKA  
FACULTY OF ENGINEERING

David Liović

**THE EFFECTS OF MECHANICAL  
AND SURFACE PROPERTIES ON  
THE DESIGN OF ADDITIVELY  
MANUFACTURED Ti6Al4V ALLOY  
COMPONENTS**

DOCTORAL THESIS

Supervisor: Prof. D. Sc. Marina Franulović

Co-supervisor: Prof. D. Sc. Dražan Kozak

Rijeka, 2024.



SVEUČILIŠTE U RIJECI  
TEHNIČKI FAKULTET

David Liović

MEĐUDJELOVANJE MEHANIČKIH  
SVOJSTAVA I HRAPAVOSTI PRI  
OBLIKOVANJU ADITIVNO  
PROIZVEDENIH Ti6Al4V  
ELEMENATA

DOKTORSKI RAD

Mentor: prof. dr. sc. Marina Franulović

Komentor: prof. dr. sc. Dražan Kozak

Rijeka, 2024.





Doctoral thesis supervisor: Prof. D. Sc. Marina Franulović, University of Rijeka,  
Faculty of Engineering, Croatia

Doctoral thesis co-supervisor: Prof. D. Sc. Dražan Kozak, University of Slavonski  
Brod, Mechanical Engineering Faculty in Slavonski Brod, Croatia

The doctoral thesis was defended on \_\_\_\_\_ at the University of Rijeka,  
Faculty of Engineering, Croatia, in front of the following Evaluation Committee:

1. \_\_\_\_\_

2. \_\_\_\_\_

3. \_\_\_\_\_



*To her, who brightens my days.*



# ACKNOWLEDGMENTS

Firstly, I would like to express my deepest gratitude to my supervisor, Prof. D. Sc. Marina Franulović, for providing all the advice and support I could ask for in this challenging and costly research. Many thanks to my co-supervisor, Prof. D. Sc. Dražan Kozak for his guidance and advice during my studies. Thank you both for the encouragement!

Grateful acknowledgment goes to the Croatian Science Foundation for the support under project numbers IP-2019-04-3607, as well as the University of Rijeka for their support through projects uniri-tehnic-18-34 and uniri-iskusni-tehnic-23-224. This research would not be possible without this support.

Many thanks to Dr. Ing. Emanuele Vaglio for all his advice and technical assistance related to the additive manufacturing of specimens. Sincere thanks to Prof. D. Sc. Nenad Gubelj, Luka Ferlič, and Prof. D. Sc. Ervin Kamenar for their help and expertise throughout the extensive experimental procedures. Special thanks go to Prof. D. Sc. Mirta Benšić, for all her valuable advice on statistical analysis and mathematical modeling done as part of this thesis.

Many thanks to my friends and colleagues Tomislav, Jelena, and Ervin for making this whole journey more fun and entertaining. Thanks as well to all my colleagues from the Department of Engineering Design for their assistance and support during these years.

I am deeply grateful to my parents for the unconditional support and encouragement they have always shown.

Lastly, my deepest gratitude goes to my beloved wife, Anja, who has taken this long journey by my side. Thank you for all the sacrifices you made, for your understanding and strong belief in me. I feel truly privileged to have you by my side and look forward to sharing many more moments with you.

*Author*

# ABSTRACT

Additive manufacturing (AM) technologies facilitate the customization of components by adjusting mechanical and surface properties, thereby meeting specific design requirements. Laser beam - powder bed fusion (PBF-LB), a rapidly advancing AM technology, allows for the customization of process parameters to achieve desired product quality. This technology is particularly effective for processing challenging-to-machine materials, such as titanium and its alloys, enabling the production of complex-shaped components. To achieve the desired product quality, knowing how exactly different combinations of process parameters influence those properties is mandatory.

Therefore, this study aimed to investigate whether adjusting laser power and scanning speed in the PBF-LB process for manufacturing Ti6Al4V components could enable the customization of mechanical performance and surface roughness to meet specific design requirements. Additionally, the study explored whether altering the unit cells in lattice structures could further expand the range of achievable mechanical properties, given that lattices can be integrated into components produced using PBF-LB technology. To achieve this, state-of-the-art in the field of AM of metallic materials was conducted with an emphasis on processing Ti6Al4V alloy using PBF-LB technology. Different specimen types and configurations were manufactured to investigate this material from multiple aspects at different scales. The variations in mechanical properties identified were insufficient to customize the properties of manufactured components substantially. Consequently, laser power and scanning speed combinations can be chosen from the defined ranges (200 to 250 W and 1000 to 1500 mm/s) without compromising mechanical performance. This flexibility enables the customization of other properties, such as surface roughness, without influencing component mechanical properties. Nonlinear regression models incorporating laser power and scanning speed accurately describe the influence on average surface roughness of PBF-LB Ti6Al4V alloy components. Higher laser powers effectively reduce the surface roughness and mitigate the influence of scanning speed. In addition to investigating mechanical properties at the

macro-scale, the influence of laser power, scanning speed, and annealing heat treatment was analyzed at the micro- and nano-scale. The annealing heat treatment led to a decrease in hardness and creep resistance at the nano-scale. Furthermore, the laser power and scanning speed influence Young's modulus at the nano-scale. The analysis of Young's modulus and hardness results from annealed specimens at the nano-scale revealed a strong correlation. Lastly, since it was found that the proposed laser power and scanning speed ranges do not enable the customization of mechanical properties at the macro-scale to an extent relevant for making a substantial difference in engineering applications, the potential to customize mechanical properties was investigated by tapering strut diameters of body-cubic centered (BCC) unit cells. It was found that tapering the diameters at the midpoint and endpoints of the struts in the BCC unit cell can significantly influence tensile mechanical properties. Lastly, the proposed finite element approach enabled efficient estimation of the mechanical properties of the BCC lattice structures subjected to tensile load.

The performed research in this thesis provides a significant scientific contribution in the field of additive manufacturing of Ti6Al4V alloy by investigating the influence of PBF-LB process parameters on surface roughness and mechanical response at different scales. It also provides a procedure that can be used to estimate tensile mechanical properties of lattice structures consisting of BCC unit cells with tapered struts.

**Keywords:** additive manufacturing, Ti6Al4V alloy, mechanical properties, surface roughness, lattice structures

## PROŠIRENI SAŽETAK

Postupci aditivne proizvodnje (AM) omogućuju izradu topološki složenih komponenti specifičnih mehaničkih i površinskih svojstava, što je od izrazitog značaja tijekom različitih faza razvoja proizvoda. Lasersko srašćivanje metalnog praha (PBF-LB), tehnologija AM koja se rapidno razvija, omogućuje prilagodbu procesnih parametara u svrhu postizanja željene kvalitete proizvoda. Ova tehnologija posebno je učinkovita za obradu materijala koji su zahtjevni za strojnu obradu, kao što su titan i njegove legure, omogućujući proizvodnju komponenti složenih oblika. Da bi se postigla željena kvaliteta proizvoda, potrebno je utvrditi utjecaj različitih kombinacija procesnih parametara na svojstva i kvalitetu proizvoda.

Prema tome, u okviru ove disertacije istraženo je može li se promjenom snage lasera i brzine skeniranja u PBF-LB procesu za proizvodnju komponenti od legure Ti6Al4V omogućiti postizanje različitih mehaničkih svojstava i hrapavosti površine. Osim toga, istražena je mogućnost postizanja različitih mehaničkih svojstava promjenom jediničnih ćelija rešetkastih struktura, obzirom da se ove strukture mogu integrirati u komponente za čiju proizvodnju je namijenjena PBF-LB tehnologija. Za postizanje ovih ciljeva, korištene su recentne spoznaje u području aditivne proizvodnje metalnih materijala, s posebnim naglaskom na obradu metalnog praha legure Ti6Al4V pomoću PBF-LB tehnologije. Ova tehnologija se pokazala učinkovitom za proizvodnju složenih komponenti iz praha Ti6Al4V legure. Proizvedene su različite vrste i konfiguracije uzoraka kako bi se materijal istražio sa različitih stajališta na različitim razinama. Utvrđeno je da varijacije u mehaničkim svojstvima, nakon toplinske obrade žarenjem, nisu dovoljno izražene da bi značajno promijenile svojstva proizvedenih komponenti. U toplinski neobrađenom stanju, mikrostruktura se sastoji dominantno od igličastog martenzita ( $\alpha'$ ), dok se nakon žarenja mikrostruktura sastoji od  $\alpha + \beta$  faza. Sve kombinacije procesnih parametara rezultirale su mješovitim lomom (duktilno-krhkim) s izraženim ravnim dijelom prijelomne površine u sredini ispitnog uzorka i nagnutim dijelom na rubovima. Analizom poroznosti i prijelomnih površina utvrđena je prisutnost raznih grešaka u strukturi materijala, poglavito blizu rubova ispitnog uzorka gdje su uočene veće



koncentracije, koje uz površinske nepravilnosti predstavljaju potencijalna mjesta za inicijaciju pukotine. Nadalje, kombinacije snage lasera i brzine skeniranja mogu se odabrati unutar definiranih raspona (200 do 250 W i 1000 do 1500 mm/s) bez značajnog narušavanja mehaničkih svojstava komponente, čime se otvara mogućnost utjecaja na druga svojstva, kao što je hrapavost površine. Nelinearni regresijski modeli koji uključuju snagu lasera i brzinu skeniranja s visokom točnošću opisuju utjecaj na prosječnu površinsku hrapavost komponenti legure Ti6Al4V proizvedenih PBF-LB tehnologijom. Veće snage lasera učinkovito smanjuju hrapavost površine i umanjuju utjecaj brzine skeniranja. Uz istraživanje mehaničkih svojstava na makro razini, analiziran je utjecaj snage lasera, brzine skeniranja i toplinske obrade žarenjem na mikro- i nano razini. Toplinska obrada žarenjem smanjila je tvrdoću i otpornost na puzanje na nano razini. Nadalje, snaga lasera i brzina skeniranja utječu na modul elastičnosti na nano razini koji je pak ovisan o dubini indentacije. Za slučaj toplinski neobrađenih uzoraka, modul elastičnosti i tvrdoća se stabiliziraju na dubinama indentacije većim od 300 nm, dok u slučaju žarenih uzoraka stabilizacija nastupa na dubinama većim od 1000 nm. Analiza rezultata modula elastičnosti i tvrdoće za žarene uzorke na nano razini otkrila je jaku korelaciju. Obzirom da je utvrđeno da predloženi rasponi snage lasera i brzine skeniranja ne omogućuju značajnu promjenu mehaničkih svojstava na makro razini, istražena je mogućnost promjene mehaničkih svojstava kontinuiranim sužavanjem ili povećavanjem promjera štapova koji tvore kubnu prostorno centriranu (BCC) rešetku. Utvrđeno je da se promjenom promjera na središnjoj i krajnjoj točki štapova u BCC jediničnoj ćeliji može značajno utjecati na vlačna mehanička svojstva. Konačno, predloženi pristup numeričkog modeliranja metodom konačnih elemenata omogućio je učinkovitu procjenu mehaničkih svojstava BCC rešetkastih struktura izloženih vlačnom opterećenju što je u literaturi slabo zastupljeno unatoč tome što ovakve strukture pronalaze široku primjenu u proizvodima za koje se zahtjeva visoka nosivost i niska masa.

Provedeno istraživanje u okviru ove disertacije predstavlja značajan znanstveni doprinos u području aditivne proizvodnje legure Ti6Al4V ispitivanjem utjecaja PBF-LB procesnih parametara na hrapavost površine i mehanički odziv na različitim razinama. Također pruža postupak koji se može koristiti za procjenu vlačnih mehaničkih svojstava rešetkastih struktura koje se sastoje od BCC jediničnih ćelija sa konusnim štapovima.

**Ključne riječi:** aditivna proizvodnja, Ti6Al4V legura, mehanička svojstva, površinska hrapavost, rešetkasta struktura

# Contents

Acknowledgments . . . . .	i
Abstract . . . . .	ii
Prošireni sažetak . . . . .	iv
<b>1. Introduction . . . . .</b>	<b>1</b>
1.1. Motivation . . . . .	1
1.2. Objectives and Hypotheses . . . . .	2
1.3. Scientific Contributions . . . . .	3
1.4. Structure of the Doctoral Thesis . . . . .	3
<b>2. State-of-the-Art . . . . .</b>	<b>6</b>
2.1. Additive Manufacturing Process Categories . . . . .	6
2.2. Powder Bed Fusion Process . . . . .	7
2.2.1. Powder Bed Fusion - Laser Beam Process. . . . .	8
2.2.2. Process Parameters . . . . .	10
2.2.3. Heat Treatments . . . . .	13
2.2.4. Dimensional Accuracy . . . . .	15
2.3. Solid Ti6Al4V Parts Produced Using PBF-LB. . . . .	15
2.3.1. Mechanical Properties . . . . .	16
2.3.2. Nano-mechanical Properties . . . . .	19
2.3.3. Surface Roughness . . . . .	20
2.4. Lattice Structures . . . . .	23
2.4.1. BCC Unit Cells. . . . .	26
<b>3. Materials and Methods . . . . .</b>	<b>28</b>
3.1. Central Composite Design . . . . .	28
3.2. Mathematical Modeling and Statistical Analysis. . . . .	30
3.2.1. Response Surface Modeling . . . . .	30

3.2.2. Multiple Comparison Tests . . . . .	32
<b>3.3. Specimen Design and Manufacturing . . . . .</b>	<b>33</b>
3.3.1. Cubic Specimens . . . . .	34
3.3.2. Flat Specimens . . . . .	35
3.3.3. Lattice Specimens. . . . .	37
<b>3.4. Heat Treatment . . . . .</b>	<b>39</b>
<b>3.5. Metallographic Preparation . . . . .</b>	<b>39</b>
<b>3.6. Indentation Experiments . . . . .</b>	<b>40</b>
<b>3.7. Tensile Tests . . . . .</b>	<b>44</b>
<b>3.8. Surface Roughness Measurements. . . . .</b>	<b>47</b>
3.8.1. Contact Measurements. . . . .	47
3.8.2. Non-contact Measurements . . . . .	48
<b>3.9. Optical Microscopy . . . . .</b>	<b>49</b>
<b>3.10. Relative Density Measurements . . . . .</b>	<b>49</b>
<b>4. Characterization of PBF-LB Ti6Al4V Alloy . . . . .</b>	<b>51</b>
4.1. Microstructure . . . . .	51
4.2. Porosity Estimation. . . . .	52
4.3. Mechanical Properties of PBF-LB Ti6Al4V Alloy . . . . .	54
4.3.1. Young’s modulus and shear modulus. . . . .	58
4.3.2. Offset Yield Strength and Ultimate Tensile Strength . . . . .	60
4.3.3. Poisson’s ratio . . . . .	62
4.3.4. Fracture surfaces . . . . .	64
4.4. Low-force Vickers Hardness. . . . .	65
4.5. Nano-mechanical Properties . . . . .	67
4.5.1. Dependence of Nano-mechanical Properties on Indentation Location . . . . .	68
4.5.2. Young’s modulus and Nano-hardness. . . . .	70
4.5.3. Creep properties . . . . .	77
4.6. Mechanical Properties of BCC Lattice Specimens . . . . .	81
<b>5. Surface Roughness of PBF-LB Ti6Al4V Alloy Components . . . . .</b>	<b>87</b>
5.1. Line Average Surface Roughness . . . . .	89
5.2. Area Average Surface Roughness . . . . .	90

<b>6. Numerical Modeling . . . . .</b>	<b>94</b>
<b>6.1. Material Modeling . . . . .</b>	<b>95</b>
6.1.1. Identification and Validation of Material Parameters . . . . .	97
<b>6.2. Lattice Specimen Modeling . . . . .</b>	<b>102</b>
6.2.1. Material Parameters . . . . .	103
6.2.2. Boundary Conditions . . . . .	105
6.2.3. Mesh Sensitivity Analysis . . . . .	106
6.2.4. Validation of Results . . . . .	108
6.2.5. Regression Models . . . . .	111
<b>7. Discussion . . . . .</b>	<b>116</b>
<b>8. Conclusion . . . . .</b>	<b>122</b>
<b>BIBLIOGRAPHY. . . . .</b>	<b>124</b>
<b>NOMENCLATURE. . . . .</b>	<b>139</b>
<b>LIST OF FIGURES. . . . .</b>	<b>144</b>
<b>LIST OF TABLES . . . . .</b>	<b>148</b>
<b>Appendices . . . . .</b>	<b>150</b>
<b>Curriculum Vitae . . . . .</b>	<b>154</b>

# 1. INTRODUCTION

Within this chapter, essential information about the doctoral thesis is outlined. It identifies the factors that motivate the study and explains its significance. Subsequently, it outlines the specific objectives and hypotheses guiding the research. In addition, the chapter details the scientific contributions derived from the conducted research, highlighting its findings. Finally, it provides a detailed overview of the organizational structure of the doctoral thesis, outlining a systematic arrangement of chapters and their contents.

## 1.1. Motivation

Additive manufacturing technologies facilitate the efficient fabrication of components with complex geometries utilizing different process parameters. Nevertheless, the mechanical properties [1, 2, 3, 4, 5, 6, 7, 8] and surface roughness [9, 10, 11, 12, 13, 14, 15, 16, 17, 18] of these components differ from those manufactured using conventional methods such as casting, forging or material removing. This prompts the question: Can altering different combinations of process parameters in additive manufacturing technology customize the mechanical performance and surface roughness to align with the specific design requirements of the component? Alternatively, is it necessary to modify unit cells, constituting lattice structures in specific component areas, to meet specific mechanical response requirements? This holds significant importance in tailoring individual components' mechanical properties to meet design prerequisites as precisely as possible [19, 20, 21]. Furthermore, additive manufacturing enables the creation of complex shaped components [22], even utilizing challenging-to-machine materials like titanium and its alloys [23]. Consequently, achieving desired mechanical properties and fabricating topologically complex products from materials possessing corrosion resistance, biocompatibility, and lightweight properties is crucial for further technological advancement. Furthermore, these additive manufacturing technologies are characterized by low material wastage [24, 25, 26], thereby significantly reducing environmental impact and

creating opportunities to enhance sustainability further [27, 28].

Of particular interest in this thesis is the laser beam powder bed fusion (PBF-LB) technology, specifically its application in fabricating components from the Ti6Al4V alloy powder. Adjusting process parameters within this technology can impact the resultant material microstructure and porosity, consequently altering its mechanical properties [9, 29, 30, 31]. Moreover, altering these parameters might also have an effect on the surface roughness of components [32, 33]. Understanding the precise influence of selected process parameters on mechanical properties, surface roughness, and their interaction holds practical significance. This understanding could enable the tailored adjustment of mechanical properties and surface roughness by altering process parameters to meet specific design criteria.

In the PBF-LB process, many parameters can be tuned, making considering all potential combinations impractical. However, among these parameters, laser power and scanning speed stand out as the two important parameters [34, 35, 36], while remaining easily adjustable. In addition, controlling only these two parameters can effectively govern underlying physical processes during melting [31, 35, 37], influencing mechanical properties and surface roughness. Understanding the influence of these specific parameters is crucial in unlocking the full potential of PBF-LB technology, which is tailoring the mechanical properties and surface roughness to meet specific design requirements.

### 1.2. Objectives and Hypotheses

According to the scientific motivation stated above, the main objective of this research is to investigate the possibility of tailoring the mechanical properties and surface roughness of the Ti6Al4V alloy components, produced using laser beam powder bed fusion, to meet design requirements. Therefore, it is expected that the research conducted on different scales will deepen the understanding of the influence of process parameters on the mechanical properties and surface characteristics of Ti6Al4V alloy produced by laser beam powder bed fusion.

The research hypotheses are as follows:

- The surface roughness of Ti6Al4V alloy components produced through laser beam powder bed fusion can be correlated with laser power and scanning speed using regression models.
- By employing different combinations of laser power levels at 200, 225, and 250 W along

with scanning speed levels at 1000, 1250, and 1500 mm/s in the laser beam powder bed fusion process, it is possible to influence the elasticity modulus of the Ti6Al4V alloy.

- Hardness and elasticity modulus at the nanoscale are interdependent.
- Annealing heat treatment reduces the creep resistance at the nanoscale of Ti6Al4V alloy produced through laser beam powder bed fusion.
- The established procedure allows for modeling the elastoplastic behavior of simple and complex components manufactured through the laser beam powder bed fusion process.

### 1.3. Scientific Contributions

The novel scientific contributions are outlined in four points in this thesis:

1. Investigated the influence of laser power and scanning speed on mechanical properties at different scales of the Ti6Al4V alloy produced using laser beam powder bed fusion.
2. Developed models that relate surface roughness with laser power and scanning speed within predefined ranges, ensuring reliable component production.
3. Investigated effects of annealing heat treatment on the creep behavior at the nanoscale of Ti6Al4V alloy produced using laser beam powder bed fusion.
4. The established procedure for modeling the elastoplastic behavior of lattice structures produced via laser beam powder bed fusion.

### 1.4. Structure of the Doctoral Thesis

This thesis is structured into eight chapters and accompanied by appendices, providing a systematic and thorough presentation of the conducted research. Below is a concise overview of the thesis chapters for reader convenience:

- **Chapter 1** outlines the scientific motivation behind the study, details the objectives and hypotheses, and highlights the significant contributions made to the research field.

- **Chapter 2** covers the state-of-the-art additive manufacturing technologies for the processing of metallic materials, with a focus on the powder bed fusion technologies used to process metallic powders. It describes the typical mechanical and nano-mechanical properties of solid Ti6Al4V parts produced using a laser beam powder bed fusion process. Furthermore, it discusses lattice structures composed of unit cells and their various applications. Special attention is given to body-centered cubic cells, examining how geometry and process parameters influence their mechanical response.
- **Chapter 3** begins by outlining the face-centered central composite design used in the study, followed by the mathematical modeling methods and statistical analysis tests employed. It thoroughly describes the specimen design, manufacturing conditions, heat treatment, and metallographic preparation. Detailed experimental test procedures are presented, including tensile testing, indentation techniques, contact and non-contact surface measurements, optical microscopy, and relative density measurements.
- **Chapter 4** focuses on the experimental characterization of Ti6Al4V alloy produced via laser beam powder bed fusion. It begins by examining the Ti6Al4V alloy's microstructure in both as-built and annealed conditions, alongside an analysis of resulting porosity. The chapter details macro-scale mechanical properties across various combinations of laser powers and scanning speeds, presenting models that correlate these properties with the process parameters. Additionally, it includes micro-scale hardness results obtained using the low-force Vickers method and reports nano-mechanical properties such as Young's modulus, nano-hardness, and indentation creep behavior. Finally, the chapter discusses the mechanical response and mechanical properties observed in lattice structures featuring body-centered cubic cells under different configurations.
- **Chapter 5** presents experimental findings on average surface roughness measured through both contact and non-contact methods. It includes regression models that establish relationships between laser power, scanning speed, and average surface roughness. The chapter also provides typical average surface roughness values for components manufactured using laser beam powder bed fusion technology.
- **Chapter 6** describes the application of the finite element method used to model the elastoplastic and damage behavior of lattice structures featuring various configurations.



ons of body-centered cubic unit cells. It includes a comprehensive overview of the material parameters, boundary conditions, and mesh sensitivity analysis employed in the simulations. The chapter presents a comparison between numerically estimated and experimentally determined mechanical properties for different unit cell configurations with varying tapering diameters. Additionally, regression models are developed to correlate tapering diameters with the numerically predicted mechanical properties, offering insights into their relationship with experimental findings.

- **Chapter 7** synthesizes experimental and numerical findings, consolidating the main results from all research phases while offering deeper insights and a comprehensive overview. It critically examines the limitations, strengths, and weaknesses inherent in the thesis research.
- **Chapter 8** summarizes the key findings regarding the influence of laser power and scanning speed on mechanical properties across various scales, the resulting surface roughness, and the effects of different tapering diameters on mechanical responses and properties. Lastly, it outlines the future research needed to be carried out in order to provide further progress in this field of research.

## 2. STATE-OF-THE-ART

This chapter provides recent findings in the field of additive manufacturing, beginning with categories of different processes and relevant terminology. A detailed description of the powder bed fusion-laser beam (PBF-LB) process is also provided, which is of particular interest in this thesis. The discussion then covers the influence of PBF-LB process parameters, commonly used heat treatments and typical dimensional accuracy. Furthermore, the latest findings on the mechanical properties at different scales and surface roughness of PBF-LB Ti6Al4V alloy are provided, highlighting their significance in the research field. Lastly, recent advancements in the field of additively manufactured lattice structures are provided, emphasizing body-centered cubic unit cells.

### 2.1. Additive Manufacturing Process Categories

In general, manufacturing technologies that join materials to produce a physical object based on a predetermined 3D model are termed additive manufacturing technologies [38]. Given the rapid growth in this field, an increasing variety of technologies are emerging, requiring their classification. Especially since a vast number of different commercial names are used to refer to the identical technology. Therefore, to enhance communication clarity, it becomes essential to categorize them and establish standardized terminology.

According to ISO/ASTM 52900:2021 standard, additive manufacturing technologies are classified into the following seven categories [38]:

- Binder Jetting (BJT) - represents selective deposition of a liquid bonding agent used to join powder materials.
- Directed Energy Deposition (DED) - represents a fusion of materials through melting, employing focused thermal energy during the deposition process.

- Material Extrusion (MEX) - represents selective dispensation of the material through a nozzle or orifice.
- Material Jetting (MJT) - represents selective deposition of droplets of feedstock material.
- Powder Bed Fusion (PBF) - represents a selective fusion of powder bed regions using thermal energy.
- Sheet Lamination (SHL) - represents the bonding of sheets of material to form a part.
- Vat Photopolymerization (VPP) - represents selective curing of liquid photopolymer in a vat using light-activated polymerization

This doctoral thesis has delved into the specifics of the PBF technology utilized to fabricate all included specimens. As a result, the subsequent chapter will focus exclusively on this technology, offering a thorough description and comprehensive insights into its functioning.

## 2.2. Powder Bed Fusion Process

The powder bed fusion (PBF) process is based on the fusion (melting or sintering) of the stationary powder bed, using a laser or electron beam as the energy source. After the initial layer is processed, the powder is again spread using a recoater across the build platform with a predetermined height and then melted or sintered layer by layer. Repeating the process of spreading the powder and fusing it in layers creates a 3D object. The first process in PBF production was selective laser sintering (SLS), from which the selective laser melting is further developed [39]. Selective laser sintering is still used to produce composites by mixing metal or ceramic powder with polymer powder, where the polymer acts as a binder that is subsequently removed similarly to the binder jetting process [40].

Various terms and definitions have been used throughout the evolution of powder bed fusion technology, frequently linked to specific applications and trademarks: electron beam sintering (EBS), electron beam melting (EBM), selective laser sintering (SLS), direct metal laser sintering (DMLS), and selective laser melting (SLM). This has led to ambiguity and confusion, hindering effective communication and broader technology adoption. Therefore, it became essential to establish precise definitions for the terms and nomenclature related to additive manufacturing technology. In 2021, ISO/ASTM 52900:2021 was established

to define general principles and vocabulary for global communication among individuals involved in this technology field.

Depending on the energy source, PBF is classified according to ISO/ASTM 52900:2021 into powder bed fusion - laser beam (PBF-LB) and powder bed fusion - electron beam melting (PBF-EB).

The PBF-LB process is among the most extensively utilized techniques in the additive manufacturing sector [41]. This process occurs within a sealed chamber, typically filled with an inert gas such as nitrogen or argon, selected based on the metal powder's reactivity [41]. Moreover, the build chamber operates under over-pressure conditions. These factors, the inert gas atmosphere, and over-pressure, significantly reduce oxygen contamination [41]. The versatility of the PBF-LB process is highlighted by its ability to handle a broad spectrum of materials, including aluminum-based, titanium-based, iron-based, nickel-based, cobalt-based, and copper-based alloys, as well as their composites [41, 42]. This process allows the powder to be reused multiple times, reducing material waste and improving sustainability [42]. Compared to PBF-EB, the parts produced using PBF-LB have lower surface roughness since smaller powder particles, thinner powder layers, smaller beam diameters, and lower scanning speeds are used [43]. However, due to the high cooling rates present during PBF-LB, parts produced using this technology have higher residual stresses than parts produced using PBF-EB, requiring subsequent heat treatments [41].

The PBF-EB process shares similarities with the PBF-LB process, utilizing layer-by-layer technology [41]. However, instead of a laser beam, it uses an electron beam to fuse powder, requiring a vacuum chamber [40]. The powder bed is maintained at high temperatures (above 870 K) and requires overnight cooling to return to room temperature after the build [41].

Commercial PBF-EB machines are limited to a few materials, such as Ti Grade 2, Ti6Al4V, Inconel 718, and CoCrMo [41]. Additionally, there are restrictions on the size of parts since they are printed in a vacuum chamber [41]. The vacuum chamber is used to reduce impurities and protect material from oxidation [40].

### **2.2.1. Powder Bed Fusion - Laser Beam Process**

This research focuses on utilizing PBF-LB technology to produce metallic components, so a detailed explanation of its working principles is provided in this subsection. This technology

is based on melting stationary metal powder layer by layer using a laser beam. To achieve this, the powder tank must be filled with metal powder of appropriate granularity, typically between 15-45 micrometers. A build platform is also needed for the substrate, where layers are being fused. Once a 3D model is prepared and process parameters such as laser power, scanning speed, powder layer thickness, hatch distance, focal diameter, and scanning strategy are defined, the process can start. The typical PBF-LB process equipment and working principle are depicted in Figure 2.1.

At this point, the hermetically sealed chamber is filled with an inert atmosphere, usually argon or nitrogen. Inside the chamber are two movable compartments: the powder tank and the build platform. The metal powder spreads over the build platform in a layer matching the set thickness via a recoater, which can be either rigid or flexible. Any excess powder is pushed into an overflow container. The fusion process can begin once the powder is spread to the appropriate thickness. This requires synchronized action between the laser and optical systems. The laser provides the energy for powder fusion, while the optical system directs and focuses this energy onto specific regions along the programmed path with its lenses and mirrors.

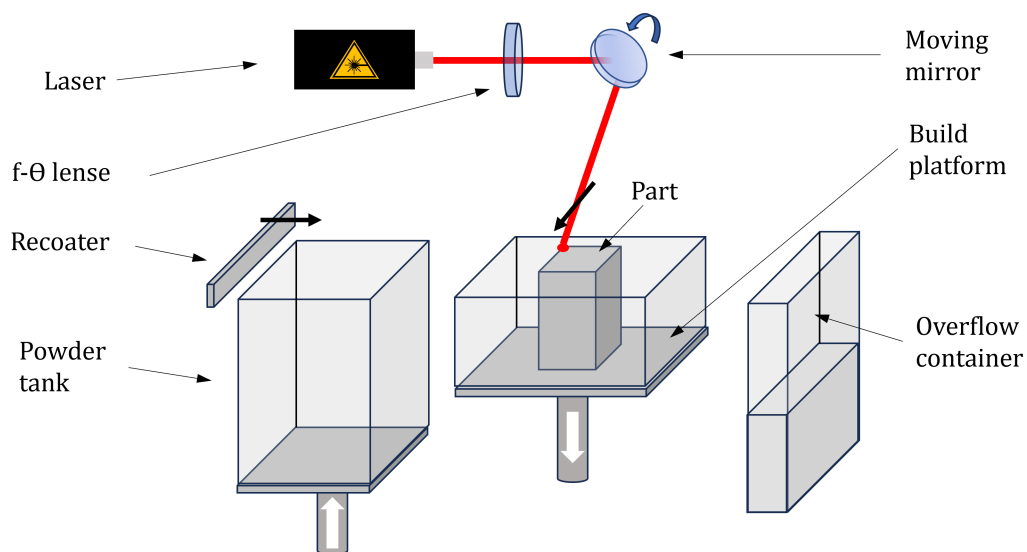


**Figure 2.1:** *Schematic representation of the working principle of PBF-LB process.*

After the powder is fused according to the programmed path, the build platform lowers, and the powder tank platform rises by the corresponding amount. The recoater then spreads another layer of powder from the powder tank platform toward the build platform, continuing its movement to the overflow container to collect the excess powder. The laser beam, via the optical system, then melts this new layer of powder. Repeating this process layer by

layer ultimately forms the 3D object. Depending on the object's size, the procedure can take weeks. Once the process is finished, the inert gas flow is stopped, and the operator collects the excess powder remaining in the chamber, placing it in the overflow container. The powder is then sieved and reused multiple times. Following this, the build platform is detached from the machine, and the manufactured components undergo appropriate heat treatment. After heat treatment, the components are typically removed from the build platform using a band saw. Once the components are removed, the build platform is milled to achieve a flat surface, preparing it for the next PBF-LB process.

The laser power used in PBF-LB machines can vary from low values such as 42 W [44], to even 4000 W on modified machines [45]. The typical wavelength of the laser beam is around 1.07 micrometers [44, 45]. The scanning speed, which is the movement of the focused laser beam per unit time per powder layer, can range from a couple of hundred to several thousand mm/s [9, 46]. Commercially available PBF-LB devices often use a laser beam diameter of 100  $\mu\text{m}$  to balance accuracy and productivity [47, 48]. Newer systems employ multiple high-power lasers with optical systems to reduce production time even further. Increasing the laser power allows for higher scanning speeds while maintaining the same energy density, resulting in higher productivity.

### 2.2.2. Process Parameters

Depending on the PBF-LB machine used, different process parameters for identical material can be used for requests related to higher mechanical performance, dimensional accuracy, surface roughness or productivity. These parameters can be grouped into three categories [11]: exposure, material, and environmental parameters.

In recent years, high attention has been paid to optimizing exposure parameters since they can be controlled in a high range, offering high flexibility for achieving desired manufacturing outcomes. For this purpose, the central composite design of the experiment is effective, as demonstrated in [33, 49]. This approach enables combinations of laser power, scanning speed, layer thickness, hatch distance, or focal diameter to be systematically investigated. Those parameters influence the energy density, which is an important factor in achieving the proper fusion of powder. Energy density is defined as the amount of energy delivered to the powder particles per unit of time by a laser beam. Therefore, linear energy density ( $E_L$ ) is defined as the ratio of laser power and scanning speed [50]:

$$E_L = \frac{P}{v}. \quad (2-1)$$

When optimizing PBF-LB parameters for processing Ti6Al4V powder using a laser spot diameter of 50  $\mu\text{m}$ , Vaglio et al. reported that the best candidates for producing solid parts are in the range between 0.1 to 0.2 J/mm [50]. However, this approach does not consider the influences of hatch distance and layer thickness, which are important parameters as well. Therefore, by expanding the equation (2-1) with hatch distance ( $h$ ) and layer thickness ( $t$ ), the volumetric energy density ( $E_V$ ) can be calculated as [9]:

$$E_V = \frac{P}{vht}. \quad (2-2)$$

The influence of volumetric energy density on mechanical properties of Ti6Al4V alloy, porosity, surface roughness, and microstructure has been extensively studied [9, 29, 51]. Nevertheless, identical volumetric energy can be achieved by using different combinations of process parameters included in equation (2-2). This, in turn, can result in different outcomes for the same energy density. Hence, when interpreting results, it is beneficial to consider individual parameters and their interactions.

Another crucial exposure parameter influencing overall product quality is the scanning strategy, which determines the path the laser beam follows to fuse powder particles. Various scanning strategies can be chosen to meet specific product requirements, with the standard ones used as illustrated in Figure 2.2.

A continuous bidirectional scanning strategy with alternations of scan vector on each layer can be used to distribute heat input evenly on a specimen during manufacturing, reduce pore size, and distribute them more homogeneously [52]. In the Figure 2.2b scan vectors are rotated by an angle of 90° on each layer. However, different angles can also be selected. An island strategy with translations and alternations on each layer (Figure 2.2d) is often used to increase productivity and prevent warping caused by residual stresses present in the material's microstructure during rapid cooling, which is especially beneficial when producing larger components [53]. However, the benefits of the island scanning strategy can not be achieved on smaller components, as it requires larger sizes of islands to be effective, such as 5 × 5 mm<sup>2</sup> [53].

In addition, material parameters take into account the type of material to be processed,

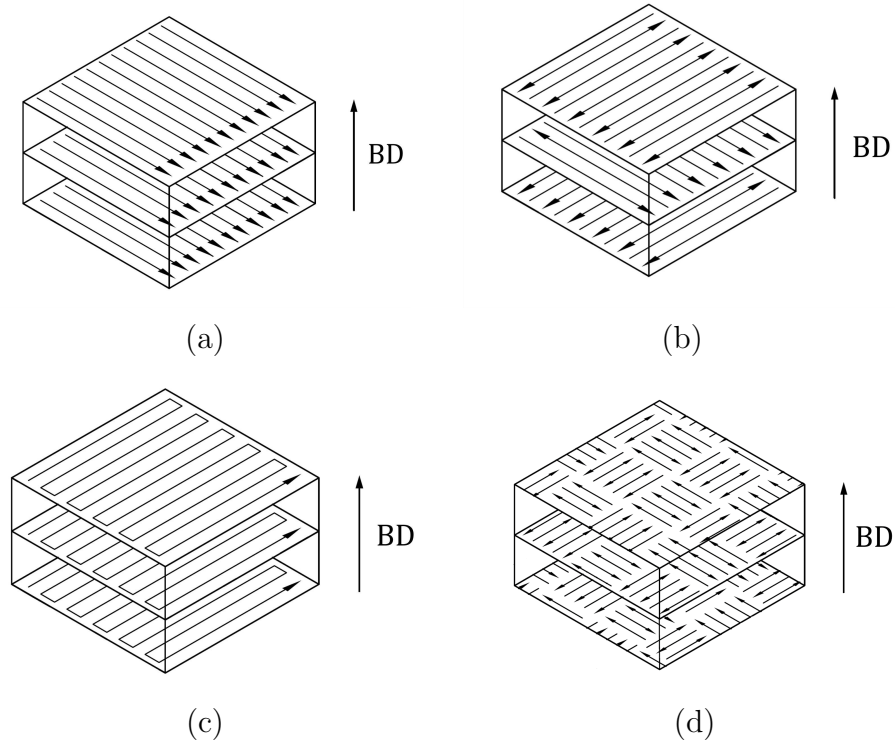


**Figure 2.2:** Scanning strategy applied to each layer stacked along the build direction (*BD*): (a) *Continuous unidirectional*, (b) *Continuous bidirectional with alternations of scan vectors on each layer*, (c) *Continuous bidirectional with meander*, (d) *Island with translation and alternations on each layer*.

its powder characteristics, and chemical composition. Different material types can be processed using PBF-LB, such as aluminum-based, titanium-based, iron-based, nickel-based, cobalt-based, and copper-based alloys, as well as their composites [41, 42]. Material parameters directly influence exposure parameters through the material selected. Furthermore, the size distribution of the powder particles and their shape affects the performance of powder during the recoating process [54], which in turn influences the powder fusion and overall product quality. The chemical composition of the powder influences the chemical composition of the solid parts produced using PBF-LB, potentially compromising their mechanical properties [55]. Specifically, oxidation during powder reuse alters the chemical composition at the surfaces of the powder particles [55]. Therefore, to maintain the product quality it is advisable to monitor the chemical composition more frequently with increased powder reuse.

The environmental parameters include the chemical composition of the inert gas atmosphere, its flow dynamics, and the temperature of the build chamber, which can be controlled by heating the build platform in some machines [11]. Heating the build platform during the PBF-LB process reduces heat conduction and consequently lowers the cooling rate. This



adjustment affects the microstructure and reduces residual stresses [56].

The choice of inert gas atmosphere depends on the material type, and typical argon, nitrogen, or helium are being used [57]. Some materials, such as titanium and its alloys, are sensitive to oxidation. Namely, oxygen is an interstitial element in titanium alloys that promotes strengthening and stabilization of the  $\alpha$  phase [58]. As a result, oxygen increases the hardness and strength while further reducing the already quite low ductility [59]. Therefore, it is necessary to reduce the oxygen content during the PBF-LB process. For this purpose, argon gas is most commonly used while processing titanium and its alloys. However, the argon gas can end up trapped in the molten metal and result in spherical porosities [60].

The inert gas flow is as well a factor in the quality control of the PBF-LB process [17]. In addition to its primary function of reducing oxidation, the gas flow effectively directs process by-products, such as spatter and fumes, toward the gas outlet, minimizing contamination and defects [61]. Furthermore, it assists in cooling the powder bed surface, ensuring a stable and controlled environment for the PBF-LB process [62].

### 2.2.3. Heat Treatments

Due to the extremely high cooling rates present in the PBF-LB process,  $10^4$ - $10^6$  K/s, as-built components have high residual stresses [41]. Heat treatments like annealing, stress relief, hot isostatic pressing, solution heat treatment, and aging are commonly used for titanium and its alloys [63]. These techniques require careful parameter selection, including heating rate, temperature, holding time, cooling rate, inert atmosphere type, and cooling medium [63].

When heat treatments are performed on PBF-LB Ti6Al4V parts at temperatures below 600°C, minor microstructural changes occur due to partial dissolution of the  $\alpha'$  phase. As the temperature increases to 750°C, more  $\alpha'$  phase dissolves into the  $\alpha + \beta$  phase, forming fine  $\alpha$  needles. Temperatures above the  $\beta$ -transus lead to the formation of coarse equiaxed or semiequiaxed grains by partitioning long columnar prior- $\beta$  grains [64]. Additionally, low cooling rates result in a lamellar  $\alpha + \beta$  phase with  $\alpha$  phase at the grain boundary [64]. The  $\beta$ -transus temperature of the Ti6Al4V alloy is around 980°C, depending on its chemical composition [65].

Higher temperatures significantly affect the microstructure through cooling rates, particularly influencing the growth of the  $\alpha$  phase [63]. Starting cooling above the  $\beta$ -transus line

makes the cooling rate's impact on the  $\alpha$  needle size more noticeable [63]. At temperatures below the  $\beta$ -transus (850°C), the sizes of  $\alpha$  needles remain similar despite varying cooling rates [63]. Vilaro et al. reported that furnace cooling (FC) at a rate of 1 K/min from a high temperature of 950°C promotes the growth of  $\alpha$  lamellae to a size of 4.5 to 5  $\mu\text{m}$  [60]. They also indicated that rapid cooling of 1500 K/s which occurs in water quenching from a high temperature of 1050°C, results in a distinctive microstructure known as  $\alpha'$ -needles [60]. Additionally, air cooling (AC) at 500 K/s from high temperatures around 900°C encourages the formation of fine  $\alpha'$  needles. Ter Harr et al. reported that in furnace-cooled specimens, the  $\beta$  grain width was thinner, and the  $\alpha/\beta$  phase fraction was larger compared to air-cooled specimens [66]. Therefore, FC results in lamellar  $\alpha + \beta$ , while AC results in basket weave structure or  $\alpha$ -Widmanstätten microstructure [6].

An important parameter is also the holding time which influences phase transition, grain size and development, stabilization, and disintegration as reported in [63]. Vrancken et al. reported that holding time does not significantly influence the microstructure when heat treatments are performed at temperatures below  $\beta$ -transus temperature [6]. However, when temperatures are closer to the  $\beta$ -transus temperature, the influence of the holding time becomes more prominent [6].

Therefore, by different holding temperatures and cooling rates achieved by selecting FC, AC, or WQ, it is possible to significantly influence the PBF-LB Ti6Al4V alloy's microstructure. Contrary, the heating rate has a negligible effect on the microstructure [6].

For PBF-LB Ti6Al4V alloy, annealing heat treatment performed in temperatures between 750°C and 900°C showed to be effective in martensite decomposition and improving ductility [67]. More specifically, this enables the transformation of the  $\alpha'$  phase into the  $\alpha + \beta$  phase, reducing tensile strength, yield strength, and hardness while increasing ductility. Typically, stress relaxation treatments are carried out at lower temperatures to specifically reduce residual stresses without significant microstructural changes [67]. Hot isostatic pressing (HIP) is also frequently performed at temperatures ranging from 900 to 950°C under hydrostatic pressure of inert gas in the range between 100 and 150 MPa with holding time ranging from 2 to 4 hours [67]. This method closes pores within the material, reducing porosity and residual stresses while transforming the  $\alpha'$  phase into the  $\alpha + \beta$  phase. Through water quenching, it is possible to create a gradient microstructure, resulting in varied surface and internal mechanical properties. Employing high-frequency induction quenching for 5.2 seconds, followed

by aging at 400°C for 6 hours, can lead to the development of excellent strength-ductility synergistic property [68].

#### **2.2.4. Dimensional Accuracy**

In recent years, PBF-LB has proven effective in producing complex-shaped components from hard-to-process materials. Dimensional accuracy and precision are crucial for these components. Factors such as component build angles, machine type, process parameters, material type, and powder characteristics influence the dimensional accuracy of the final product [11, 69, 70, 71]. Hossain et al. studied the impact of the build angle of thin struts on morphological properties, circularity, and roughness [70]. Their findings indicated that lower angles resulted in poorer morphology, higher roughness, and reduced circularity [70]. Scalzo et al. produced lattice structures with different configurations in order to investigate the high-damping properties [71]. They have reported dimensional error for the vertical struts to be within  $\pm 0.15$  mm, and for the inclined struts in the range from 0.1 to 0.2 mm [71]. In addition, they have considered two different alloys, AlSi10Mg and AISI 316L, and reported higher errors for the AISI 316L alloy [71]. These dimensional errors are significant, especially considering that the strut diameters defined by the 3D model ranged from 0.4 to 1.1 mm. Pelegatti et al. reported that the vertical struts of the strut-based and the vertical walls of the gyroid lattice exhibited geometrical errors not exceeding 0.06 mm and 0.13 mm for the unit cell of 2 mm, respectively [72]. However, for the horizontal walls of the gyroid unit cell, they noted that geometrical errors can exceed 0.3 mm [72]. Gruber et al. compared dimensional accuracy and tolerances of powder bed-based and nozzle-based AM processes and reported that PBF-LB provides the highest accuracy for dimensions as well as position and perpendicularity tolerances [69]. They have attributed the difference between PBF-LB and PBF-EB to the optimized set of parameters, smaller powder particle size, laser spot diameter, and layer thickness [69].

### **2.3. Solid Ti6Al4V Parts Produced Using PBF-LB**

Solid parts are constructed layer by layer through the melting of powder particles along predefined paths, with a diverse range of manufacturing parameters and strategies employed. These parameters and strategies often differ from those used for producing single tracks or lattice structures. Therefore, the typical mechanical properties at the macro scale and nano-

mechanical properties of PBF-LB Ti6Al4V alloy are discussed in detail in this section, as well as the porosity fraction for the given combination of process parameters. This section also covers the influence of process parameters and other manufacturing conditions on surface roughness, along with typical surface roughness values.

### 2.3.1. Mechanical Properties

The possibility of achieving targeted mechanical properties of components is of high interest in the scientific community and industry. In general, the mechanical response of materials manufactured using the PBF-LB can be influenced by many factors. Therefore, setting the optimal PBF-LB parameters and investigating their influence on the mechanical properties of PBF-LB Ti6Al4V alloy was the subject of many publications [9, 73, 74]. When using PBF-LB technology to manufacture components, it is crucial to consider and carefully select parameters such as laser power, scanning speed, layer thickness, hatch distance, focus position, laser beam diameter, scanning strategy, component orientation, and position, applied heat treatment, granulation, shape, and distribution of powder stock. Laser power, scanning speed, hatch distance, and scanning strategy directly influence the stability and quality of the PBF-LB process, which, in turn, impacts the void types and fractions, which can deteriorate the mechanical properties of produced components. The orientation of components on the build platform highly affects residual stresses [75], which directly reflects on the product quality. The granulation, shape, and distribution of the used metal powder stock impact the flowability, which affects the PBF-LB recoating process [17, 41, 75]. The chemical composition and the impurities of the powder can also influence the mechanical properties of these materials [76]. These numerous influencing factors limit understanding of how physical processes during the PBF-LB process affect surface roughness and mechanical behavior.

Due to the wide applicability of Ti6Al4V alloy, there is a high interest in evaluating the mechanical behavior of material when subjected to monotonic or cyclic loading [77]. Typical mechanical properties of PBF-LB Ti6Al4V alloy produced using different manufacturing and heat treatment conditions are listed in Table 2.1. It is reported that the PBF-LB Ti6Al4V alloy in an as-built state has a lower degree of anisotropy than the wrought Ti6Al4V alloy [78]. Furthermore, through hot isostatic pressing, annealing, or solution-aging heat treatment, it is possible to significantly reduce the anisotropy of the PBF-LB Ti6Al4V alloy [64, 79]. Ren et al. reported significant differences in the mechanical properties of as-built PBF-

LB Ti6Al4V specimens with varying build directions (BD) due to differences in residual stresses and distribution of pores [64]. By subjecting the material to low-temperature heat treatment, the differences become less noticeable [64]. Additionally, hot isostatic pressing or high-temperature heat treatments eliminate the influence of build orientations on mechanical properties [64]. Even if a certain anisotropy is reported, it is usually manifested in the material's ductility [58], while the values of the ultimate tensile strength ( $R_m$ ) and offset yield strength ( $R_{p0.2}$ ) are in practical sense almost independent on testing direction, and therefore can be considered isotropic [80]. Young's modulus of Ti6Al4V alloy processed using PBF-LB or PBF-EB differs by approximately 10% compared to the wrought one, which is similar, as stated in [81]. Yang et al. reported for vertical, diagonal and horizontal orientation of annealed PBF-LB Ti6Al4V alloy Young's modulus values of  $112.78 \pm 3.32$ ,  $115.87 \pm 0.20$  and  $118.71 \pm 0.85$  GPa, respectively.

When PBF-LB process parameters are considered, it is known that various parameters can influence the process stability and reflect on mechanical properties. The most frequently investigated are laser power, scanning speed, hatch distance, layer thickness, focus position and scanning strategy. However, laser power and scanning speed are the two most important factors that influence defect density [51, 86]. It is reported that the hatch distance in the range from 40 to 180  $\mu\text{m}$  has a low influence on the defect density, while the focus position influences the defect density only when it is located substantially downwards and below the powder bed surface [51]. The effect of powder layer thickness on porosity fraction is significant only when higher powder layer heights are used [87]. Larger powder layer heights lead to higher productivity but negatively affect the dimensional accuracy and density [88]. On the other hand, lower layer heights cause lower porosity and higher product accuracy but lead to lower productivity [88].

Although significant advancements in the customization of mechanical properties of the PBF-LB Ti6Al4V alloy have been made in recent years, the knowledge in this field remains incomplete. Studies that systematically present straightforward models for the impact of laser power and scanning speed on mechanical properties and include information on how these factors affect other properties such as surface roughness, hardness, nano-hardness, and porosity are still rarely available.

**Table 2.1:** Comparison of mechanical properties of PBF-LB Ti6Al4V alloy.

Ref.	$P/v$	Cond.	Orient.	$R_m$ , MPa	$R_{p0.2}$ , MPa	$E$ , GPa	Frac. str., %	Por., %
[82]	200 W / 200 mm/s	As-built	H	1035 ± 29	910 ± 9.9	-	3.3 ± 0.76	-
[83]	75 W / 600 mm/s	As-built	-	1420	1230	-	5.6 ± 1	0.55
[84]	200 W / -	850°C for 1 h, FC	H	1018	982	97.2	1.3	-
	200 W / -	850°C for 1 h, FC	V	873	868	95.1	0.98	-
[73]	200 W / 1250 mm/s	700°C for 1 h, FC	V	1115	1051	117.4	11.3	0.077
[85]	-	890°C for 2 h, FC	H	996 ± 10	973 ± 8	-	3 ± 0.4	<1
	-	890°C for 2 h, FC	V	998 ± 14	946 ± 7	-	6 ± 2	<1
[6]	250 W / 1600 mm/s	850°C for 2 h, FC	H	1004 ± 6	955 ± 6	114.7 ± 3.6	12.84 ± 1.36	≈ 0
[79]	500 W / 1000 mm/s	800°C for 2 h, FC	H	992 ± 0.2	919 ± 3	118.71 ± 0.85	19.5 ± 0.8	-
		800°C for 2 h, FC	V	974 ± 4	884 ± 9	112.78 ± 3.32	19.3 ± 0.8	-
		800°C for 2 h, FC	D	986 ± 2	894 ± 5	115.87 ± 0.20	19.7 ± 0.9	-
		Solution -aging	H	956 ± 2	862 ± 4	121.15 ± 1.68	21.4 ± 0.5	-
		Solution -aging	V	937 ± 1	838 ± 1	117.76 ± 0.73	21.9 ± 0.5	-
		Solution -aging	D	954 ± 3	845 ± 3	118.38 ± 0.02	20.7 ± 0.6	-
[64]	175W / 775 mm/s	As-built	H	1053	919	-	9.2	0.183 ± 0.008
		As-built	V	1004	864	-	7.4	0.109 ± 0.018
		As-built	D	1134	1049	-	3.5	0.326 ± 0.028
		800°C for 2 h, FC	H	986	910	-	10.1	-
		800°C for 2 h, FC	V	1026	986	-	6.9	-
		800°C for 2 h, FC	D	1003	930	-	8.3	-
		HIP	H	920	822	-	12	≈ 0
		HIP	V	930	836	-	12.3	≈ 0
		HIP	D	938	831	-	10.4	≈ 0
		1050°C for 2 h, FC	H	841	757	-	9.9	-
		1050°C for 2 h, FC	V	839	749	-	8.8	-
1050°C for 2 h, FC	D	835	761	-	8.6	-		

Notes: Orient. indicates the specimen orientation on the build platform (H is horizontal, V is vertical, and D is diagonal), Frac. str. represents the fracture strain, Por. denotes the porosity fraction within the material and HIP is hot isostatic pressing performed at 920°C for 2 h at pressure of 100 MPa followed by furnace cooling (FC).

### 2.3.2. Nano-mechanical Properties

Experimental tests using nanoindentation can be conducted on small-volume specimens, reducing manufacturing costs during the initial development stages. Nanoindentation has been successfully employed to characterize material properties in the heat-affected zone of resistance spot welds on dual-phase steels [89], to examine strain-rate sensitivity as a factor in cold-dwell fatigue [90], and to analyze dislocation substructures in titanium  $\alpha$  grains [91], among other applications. This technique is also effective for determining mechanical properties such as nano-hardness and Young's modulus, as well as for investigating material strain-rate sensitivity and creep behavior [90, 92].

Testing PBF-LB and PBF-EB Ti6Al4V alloy is particularly challenging for thin-walled or topologically complex structures [93], necessitating the use of smaller test specimens. Standardized procedures for mechanical testing of AM parts are currently unavailable, and producing and preparing specimens for destructive testing using PBF technologies incurs additional costs. These costs are especially significant in the early development stages of new materials and technologies, where process parameter optimization is required [94]. In this context, nanoindentation has been used to investigate the influence of process parameters, heat treatments, and orientation on the modulus of elasticity and hardness of PBF-LB Ti6Al4V alloy [95, 96, 97].

Cherneva et al. found that the PBF-LB Ti6Al4V alloy has mean values of 144.12 GPa for the modulus of elasticity and 4.53 GPa for the hardness [95]. Compared to milled Ti6Al4 alloy, both the modulus of elasticity and hardness were higher for PBF-LB Ti6Al4V alloy [95]. They also reported a slight decrease in modulus of elasticity and hardness with indentation depth [95]. Liu et al. investigated the influence of different heat treatments on the modulus of elasticity of PBF-LB Ti6Al4 alloy and reported little effect on the elasticity modulus [96]. Chen et al. performed nanoindentation measurements on three different planes (X-plane, Y-plane and Z-plane) of PBF-LB Ti6Al4V alloy cubic specimen and reported basically the same modulus of elasticity ( $127 \pm 2$ ,  $128 \pm 2$  and  $127 \pm 4$  GPa, respectively) [97]. They reported hardness values to be lower in the X-plane ( $4.2 \pm 0.5$ ) than in the Y-plane and Z-plane, which were identical ( $5.1 \pm 0.5$  and  $5.1 \pm 0.5$ ). The lower hardness values measured in the X-plane are attributed to discontinuous laser melting paths, which were pronounced on this plane due to the use of a zigzag back-and-forth path strategy on the Z-plane [97]. In this way, the fusion and powder binding conditions were different on the Y- and Z- planes

when compared to the X-plane, reflecting on hardness [97].

Peng et al. discovered that Ti6Al4V alloy manufactured via EB-PBF exhibited higher creep resistance and nano-hardness when a linear scanning strategy without scan vector rotation was used, compared to a linear strategy with a 90° scan vector rotation [30]. Creep resistance can be evaluated using a creep stress exponent ( $n$ ), with higher nanoindentation creep exponents indicating greater resistance [98]. Xu et al. reported that the creep stress exponent ( $n$ ) for a CoCrFeMnNi high-entropy alloy manufactured using PBF-LB is high and depends on the applied force during the holding stage, suggesting dislocation motion as the dominant creep mechanism [99]. Choi et al. identified two main reasons for high values of  $n$ : the difference between indentation creep and conventional uniaxial creep tests, as well as the complex stress state beneath the indenter tip [100]. Zhang et al. attributed high  $n$  values to the formation of more dislocations during material deformation [101]. Sadeghilaridjani et al. observed that  $n$  decreases with increasing temperature for pure Ni and a CoCrNi alloy, but this effect is not pronounced for the CoCrFeMnNi alloy, likely due to a thermally insensitive dislocation-glide-dictated deformation mechanism [102].

Overall, the creep behavior of AM titanium alloys is not yet fully understood, and studies on the nano-mechanical behavior of these new materials are limited.

Furthermore, the impact of PBF-LB process parameters on the creep behavior and nano-mechanical properties of Ti6Al4V alloy has not been extensively reported in the literature. The relationship between Young's modulus and nano-hardness, as well as the specific indentation depths at which these values stabilize, remains unidentified despite their practical importance. The effects of commonly used annealing heat treatments on nano-mechanical properties and creep resistance, and the relationship between applied strain rates and nano-hardness values, are also unclear. Detailed studies on the nano-mechanical properties of PBF-LB Ti6Al4V alloy are needed to address these gaps.

### 2.3.3. Surface Roughness

Surface roughness and product quality in the PBF-LB process are influenced by several interacting factors, including laser power, scanning speed, component orientation and position, applied heat treatment, and the granulation, shape, and distribution of the powder stock [3, 9, 10, 103]. Vaglio has found that laser power and scanning speed significantly impact the average surface roughness of vertical side surfaces more than the hatch distance [11]. The



staircase effect, related to the layer-wise manufacturing process and surface inclination angle, also significantly affects surface roughness [104, 105]. When manufacturing components with inclined surfaces, the staircase effect becomes prominent due to layer-wise manufacturing, drastically increasing the surface roughness on the down-skin surface. Specifically, the influence zone of the melt pool and heat-affected zone extends beyond the boundaries defined by the 3D model (see Figure 2.3), causing surrounding powder particles to adhere to the surface, thereby increasing surface roughness. More specifically, the loose powder has poor thermal conductivity, which contributes to the formation of an excessively large melt pool and heat-affected zone [106]. Additionally, due to incomplete and irregular fusion and flow of the molten material into the powder, many particles do not fully melt, resulting in the formation of dross and numerous porosities near the down-skin surface (Figure 2.4). In close proximity to partially melted particles, microcracks are often present. They occur due to the shrinkage of the melt pool during solidification around the partially melted particle, which separates from the rest of the material [9]. All those factors, in turn, affect the mechanical performance of the material near the down-skin surface, its dimensional accuracy, and the final surface finish [106].

Furthermore, the granulation, shape, and distribution of the metal powder stock impact flowability, influencing the PBF-LB recoating process [17]. These numerous factors complicate understanding how physical processes during PBF-LB affect surface roughness.

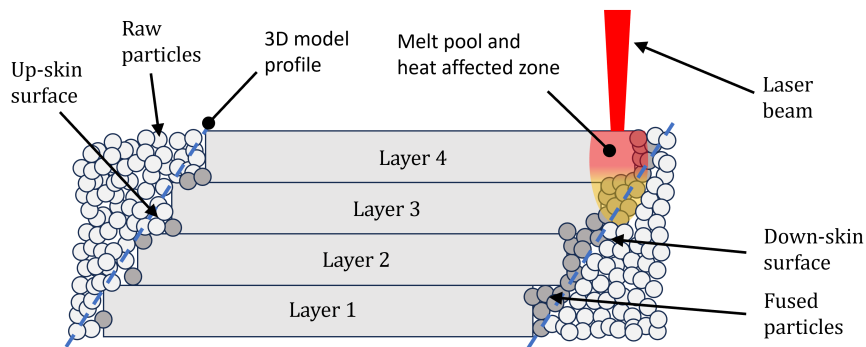


**Figure 2.3:** *Illustration of staircase effect causing an irregular down-skin surface with a high number of fused powder particles.*

Topologically simple additively manufactured components can have their surface roughness reduced through subsequent treatments. However, additive manufacturing is often used for producing topologically complex products, where subtractive post-treatments such as milling, turning, and grinding are not feasible [107]. Additionally, processing titanium

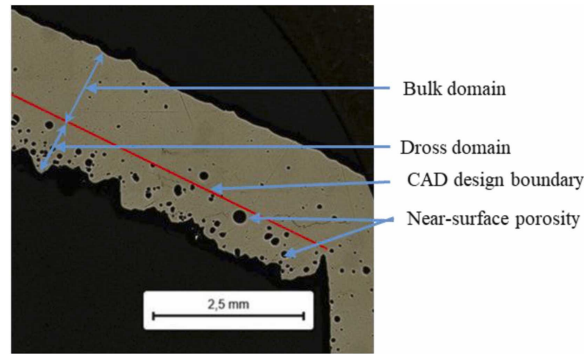


**Figure 2.4:** Cross-sectional image of the internal volume near the down-facing surface revealing significant near-surface porosity and irregular surface. Reproduced from [106].

alloys presents significant challenges [23, 108, 109]. Hence, understanding the influence of PBF-LB process parameters on surface roughness is crucial. Accurate and reliable measurements are essential for investigating these effects. However, measuring surface roughness in metallic materials manufactured using PBF-LB is challenging. Contact measurements using profilometers often encounter issues as the stylus may get jammed or hindered by loose powder particles [12, 110]. The stylus may not reach narrow surface gaps due to its tip radius, adversely affecting measurement accuracy. Non-contact measurements are preferable as they avoid contact problems but can be influenced by surface reflectivity or insufficient magnification [107, 110].

A wide range of average surface roughness values for PBF-LB Ti6Al4V specimens from various researchers is reported in the literature [3, 9, 80, 111].

Pal et al. reported  $R_a$  for vertical surfaces in the range between 4.91 and 6.79  $\mu\text{m}$  depending on scanning speed [9]. Mierzejewska et al. reported  $R_a$  for side surfaces in the range between 9.19 and 21.06  $\mu\text{m}$  depending on the scanning speed and for top surfaces in the range between 3.76 and 10.22  $\mu\text{m}$  [3]. Wilson-Heid et al. reported values of  $22.25 \pm 5.58$  and  $33.90 \pm 5.51$   $\mu\text{m}$  for top and side surfaces, respectively [80]. Typically, the surface roughness of the side surface is higher than the top surface due to the higher number of partially melted particles attached to the surface.

Despite advancements in customizing the surface roughness of PBF-LB Ti6Al4V alloy, knowledge in this field remains incomplete. Rare studies provide regression models for the effects of laser power and scanning speed on surface roughness [11]. Therefore, further research is needed to expand understanding of how altering the component position at the build platform or adjusting laser power and scanning speed combinations can influence surface

roughness.

## 2.4. Lattice Structures

Additive manufacturing has enabled the creation of lattice structures from metallic materials, noted for their complex topologies as highlighted in [112, 113, 114]. These structures comprise unit cells that can be strut-based, skeletal, and sheet-triply periodic minimal surfaces as shown in Figure 2.5 [115].

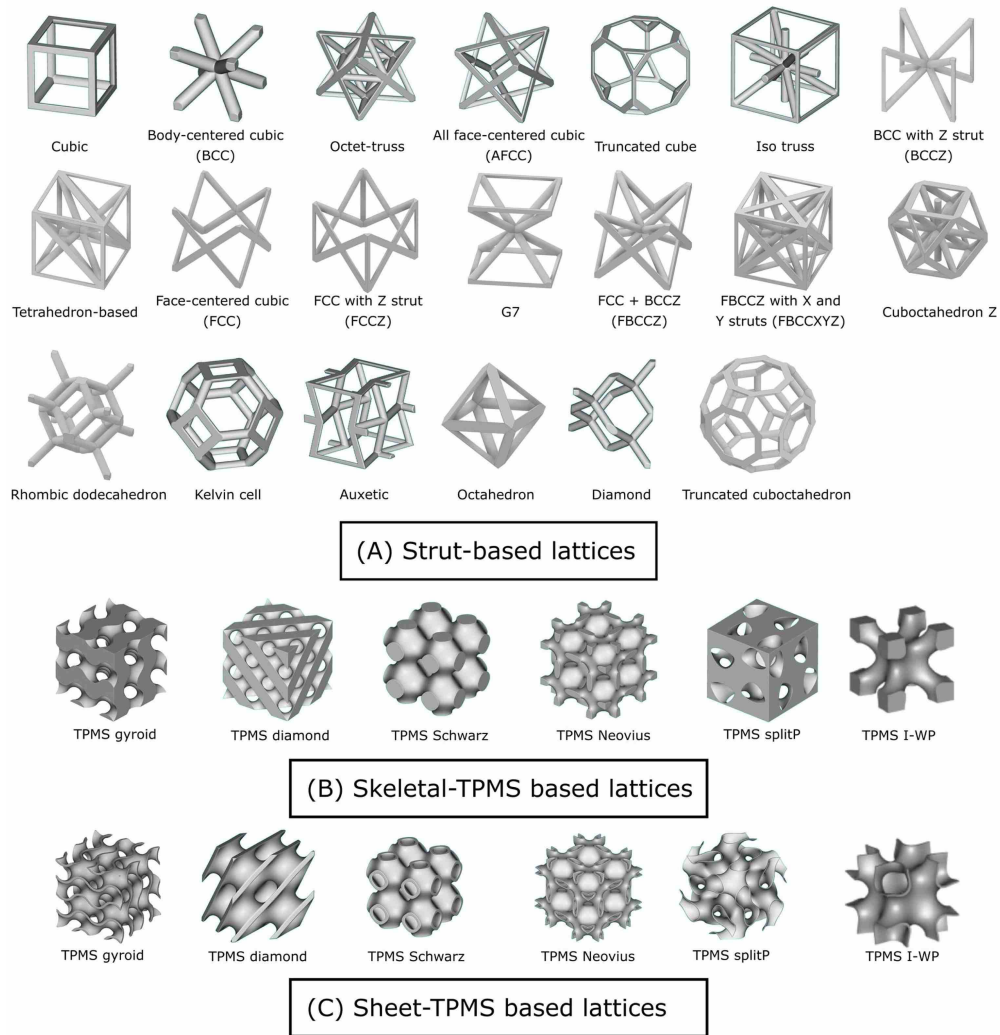


**Figure 2.5:** The first three rows showcase various strut-based lattice cell architectures, followed by skeletal and sheet-triply periodic minimal surfaces. Reproduced from [115].

Their potential applications span across various industries, including automotive, aerospace, and biomedicine [116]. Lattice structures are advantageous due to their high strength-to-mass ratio, low mass from high porosity, and customizable mechanical responses [116].

Additive manufacturing technologies in medicine offer the possibility to manufacture implants tailored to match every individual. To closely match the elastic modulus of implants with that of bone, topological solutions are being implemented, achieving more consistent elastic modulus values between the implant and the bone. For this purpose, Surmeneva et al. [117] developed and produced a lattice structure with a variable elastic modulus to mimic the trabecular part of human bone. Depending on the achieved porosity (65-21%), the elastic modulus ranged from 0.9 to 3.6 GPa, while the compressive strength ranged from 31 to 212 MPa [117]. Kolken et al. [118] investigated the concept of hybrid meta-materials to improve the contact between bone and implant. Their approach is based on combining unit cells with different Poisson's ratio values, which results in additional stabilization of the meta-implant (Figure 2.6) within the bone [118]. This ensures improved contact between the implant and the bone, reducing the risk of bone-implant interface failure and wear.

Lvov et al. [119] described a method for modifying commercially available spinal implants. They found that the elastic modulus of spinal implants with implemented auxetic unit cells is  $6.68 \pm 0.28$ , comparable to the elastic modulus of the cortical part of human bone [119]. They also implemented a honeycomb structure and, in that case, reported an elastic modulus of the implant to be  $1.19 \pm 0.03$  GPa, similar to the elastic modulus of the trabecular part of human bone and the vertebra [119].

Modifying the microstructure or the topological features of components, such as incorporating unit cells, can strongly influence the mechanical behavior of metallic parts produced using AM processes. Furthermore, adjusting the geometry of these unit cells enables control over the elastoplastic behavior and damage mechanisms under various applied loads. Due to the wide variety of unit cell types, their topological features, and different materials, efforts have been made to develop simple analytical models capable of estimating the mechanical properties of lattice structures. The most widely used model is the Ashby-Gibson model [120], which enables the estimation of Young's modulus and yield strength:

$$\frac{E_{\text{lattice}}}{E_{\text{solid}}} = C_1 \left( \frac{\rho_{\text{lattice}}}{\rho_{\text{solid}}} \right)^{n_1}, \quad (2-3)$$

$$\frac{\sigma_{y,\text{lattice}}}{\sigma_{y,\text{solid}}} = C_2 \left( \frac{\rho_{\text{lattice}}}{\rho_{\text{solid}}} \right)^{n_2}. \quad (2-4)$$

In this context,  $E_{\text{lattice}}$  and  $\sigma_{y,\text{lattice}}$  represent the Young's modulus and yield strength of the

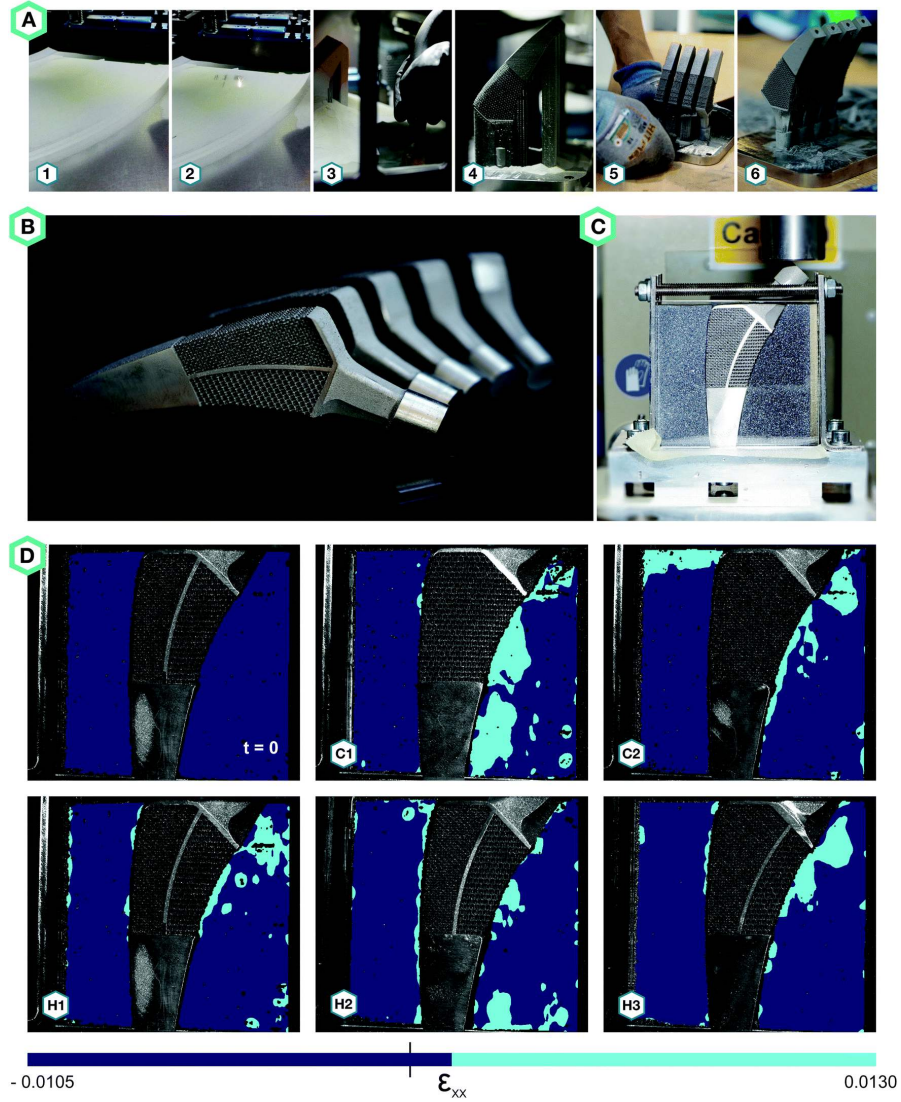


**Figure 2.6:** (A) The production of meta-implants was carried out using selective laser melting (SLM): (1) A wiper deposits a fresh layer of Ti-6Al-4V powder. (2) Powder particles are melted selectively using a high-power laser. (3) Post-manufacturing, excess powder is removed with a suction tube. (4) The build plate holds the parts along with supports. (5) The supports are then carefully detached. (6) The build plate now contains the parts without supports. (B) The additively manufactured meta-implants. (C) The test setup used for loading the meta-implants, including bone-mimicking materials. (D) Horizontal strains in the bone-mimicking materials surrounding the meta-implants at  $t = 0$  and  $t = 180$  seconds with a displacement of 1.5 mm for C1, C2, H1, H2, and H3. Reproduced from [118].

lattice structure, respectively.  $E_{\text{solid}}$  and  $\sigma_{y,\text{solid}}$  are Young's modulus and yield strength of the solid structure, respectively.  $C_1$  and  $C_2$  are dimensionless constants that are usually experimentally determined and are influenced by the size and shape of the pores [121].  $n_1$  and  $n_2$  are density factors that should be as well determined experimentally. Lastly,  $\rho_{\text{lattice}}$  and  $\rho_{y,\text{lattice}}$  represent the density of lattice and solid material, respectively.

In some cases, such as for estimating the Young's modulus and yield strength of the

curving PBF-LB Ti6Al4V lattice structures, Ashby-Gibson model proved to be precise [116]. However, this model does not consider the cell type, size, and edge-face connectivity [122]. Consequently, Ataee et al. reported significantly higher values of yield strength than those predicted using Ashby-Gibson model for the lattice structures with gyroid unit cells made from commercially pure titanium using PBF-LB technology [4].

#### 2.4.1. BCC Unit Cells

In general, strut-based unit cells can be classified into bending- or stretching-dominated [123, 124]. The dominant deformation mechanism for the three-dimensional unit cell can be identified by calculating the Maxwell number using the following equation [122, 123]:

$$M = s - 3n + 6, \quad (2-5)$$

where  $s$  represents the number of struts, and  $n$  is the number of nodes in the unit cell. If unit cells with  $M < 0$  are subjected to load, their deformation is bending-dominated. If  $M = 0$ , the unit cell will have a stretching-dominated deformation behavior. Lastly, if  $M > 0$ , the deformation behavior of the unit cell is statically indeterminate. Given that the BCC unit cell has 8 struts and a total of 9 nodes (see Figure 2.5), according to equation (2-5), their Maxwell number is -13, which classifies them as structures with bending-dominated deformation. However, it is found that the deformation behavior of the BCC lattice structures can be changed from bending- to stretching-dominated by changing the load direction from uniaxial to tangential (shear) loading [124, 125].

The mechanical properties of lattice structures with BCC unit cells were primarily investigated in previous studies by varying the size of the unit cells, strut angle, strut length, strut diameter, and the material used [122, 126, 127]. In addition, Ren et al. have studied the impact of added spheres on the nodes of the BCC unit cell [128]. They have found that by adding spheres at the nodes, stress concentration can be reduced, and the stiffness of the lattice structure can be increased without significantly increasing the relative density and surface area [128]. Bai et al. reported that by employing curved struts of the BCC unit cells, the stress concentrations at the nodes are reduced, while the elastic modulus, specific compressive strength, and energy absorption are increased compared to regular BCC configuration [116]. Zhao et al. created BCC lattice structures using triply periodic minimal surfaces and reported that the struts were, in this case, more affected by the axial force

and showed brittle failure, while struts of regular BCC lattice structures had bending as a dominant deformation mechanism and showed ductile failure on the nodes [129]. In their following study, Zhao et al. investigated the influence of the degree of strut tapering on mechanical behavior [124]. They have reported that by strut tapering, the anisotropy of BCC lattice structures can be reduced, and elastic modulus can be increased [124]. However, it should be noted that strut tapering was restricted to the reduction of the size of the hexagon base at the strut midpoint with respect to the size at the node region. Tancogone-Dejan and Mohr reported that BCC lattice structure made of PBF-LB 316L alloy is advantageous for energy absorption applications due to the absence of instability failures such as elastic buckling or plastic collapse at the mesoscale, resulting in a smooth, monotonically increasing stress-strain curve with a long plateau region [125]. This low hardening regime which occurs in the plateau region, is ideal for impact absorption systems requiring constant force and deceleration [125]. Platek et al. [130] investigated the impact of lattice structure density on the damage mechanisms in BCC lattice structures made from 316L material. They observed that higher-density structures primarily experienced tension-compression damage under quasi-static and dynamic loads, whereas lower-density structures were more prone to bending damage. Jin et al. [131] studied the effects of heat treatment on BCC and FCC lattice structures, discovering that BCC structures are more sensitive to heat treatment, suggesting that their mechanical properties can be tuned by adjusting heat treatment parameters and unit cell geometry.

After an extensive review of advanced additive manufacturing technologies, PBF-LB technology was chosen for processing Ti6Al4V alloy powder. This technology requires proper adjustment of the PBF-LB process parameters to achieve the desired product quality. Since laser power and scanning speed have essential roles in customizing mechanical properties and surface roughness, given their broad adjustability, they have been selected for research in this thesis. To ensure consistent processing of Ti6Al4V alloy powder using PBF-LB, laser power and scanning speed combinations should be carefully set to ensure a stable PBF-LB process to produce solid and lattice parts. Therefore, it is necessary to define the adequate ranges for those two parameters and their levels by employing an adequate design of experiments, such as a central composite design, to investigate how they influence the mechanical and surface properties.

## 3. MATERIALS AND METHODS

This chapter comprehensively details the experimental design, specimen manufacturing procedures, modeling techniques, and statistical analysis. To investigate the influence of process parameters, experimental designs like the central composite design specify the necessary levels and repetitions for mathematical modeling and statistical analysis. The central composite design of experiments proves particularly effective in assessing how process parameters influence product quality [132, 133, 134]. Furthermore, to investigate the influence of annealing heat treatment on hardness and Young's modulus on micro and nano-scale, the as-built and annealed subset of specimens is required. These specimens enable micro- and nano-scale indentation procedures to be conducted to determine hardness and Young's modulus across groups manufactured under varying process parameters. Tensile tests on flat specimens are necessary to explore the influence of process parameters on macro-scale mechanical properties. Furthermore, the larger size of these specimens ensures enough space for representative measurements of average surface roughness. Optical microscopy and porosity measurements are also critical to enhance the interpretation of tensile test results. Additionally, the specimen's location on the build plate will be considered as an additional variable to explain observed mechanical properties and surface roughness behaviors. Furthermore, lattice structures are included in this study to investigate the potential for customizing mechanical properties through geometric modifications. Hence, a detailed description of the lattice specimens and the experimental tensile test procedure applied will be provided.

### 3.1. Central Composite Design

The face-centered central composite design (FC-CCD) of experiments has been utilized to determine the levels of laser power and scanning speed in the PBF-LB process. This design includes star points at the center of each face of the factorial space [135], requiring three levels for each predictor variable. The central composite design has been proven effective



in modeling the influence of process parameters in various manufacturing technologies [132, 133, 134, 136]. This experimental design offers a balance between the number of experiments required and the information obtained.

There are three types of central composite designs [135]: circumscribed (C-CCD), inscribed (I-CCD), and face-centered (FC-CCD). The FC-CCD has the star points at the center of each face of the factorial space (see Figure 3.1), meaning the distance of the star points from the center is  $\alpha_{\text{ccd}} = \pm 1$ . While, the  $\alpha_{\text{ccd}}$  for a C-CCD design can be calculated as  $\alpha_{\text{ccd}} = (2^k)^{1/4}$ , where  $k$  is the number of factors. For the case of 2 factors, as in this study, the  $\alpha_{\text{ccd}} = \pm\sqrt{2}$  for C-CCD. In the case of I-CCD, the distance from corner points to the center point would be  $\pm 1/\sqrt{2}$ . Both C-CCD and I-CCD for two factors require conducting experiments at five different levels. On the other hand, the FC-CCD requires only three levels of each factor, which minimizes the risk of selecting extreme levels that could result in inadequate values of laser power or scanning speed when producing specimens using the PBF-LB process. However, this design has lower precision in estimating pure quadratic coefficients, as the star points are closer to the center. The laser power and scanning speed are two of the most important factors in the PBF-LB process [51, 137]. Therefore, this design was selected to investigate whether it is possible to tailor mechanical properties and surface roughness by combining three different levels of these two factors.

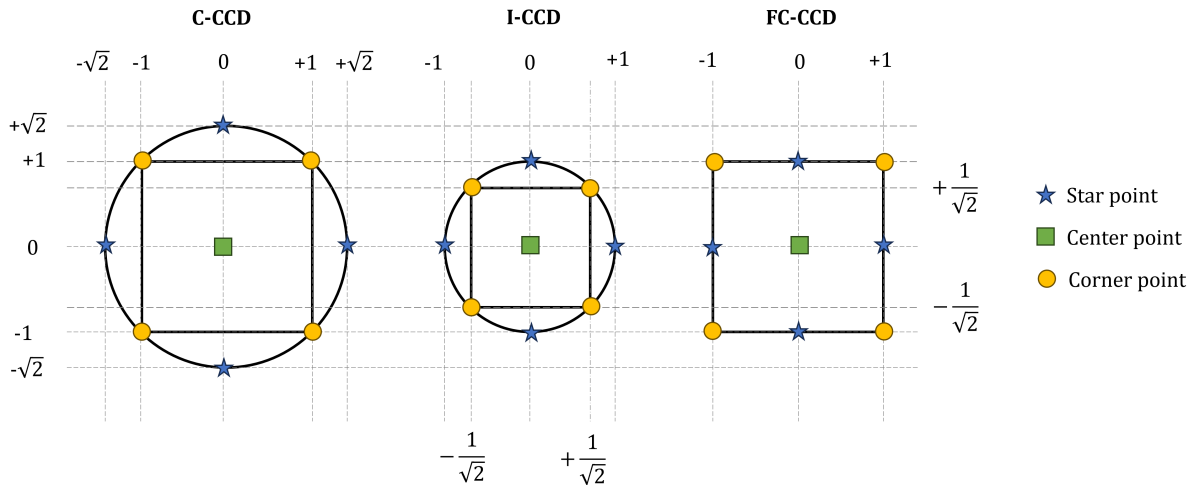


**Figure 3.1:** Graphical comparison of the three CCD types with two factors.

The  $P$  and  $v$  levels were chosen based on previous research on the appropriate range of linear energy density ( $E_L = P/v$ ) for successful manufacturing of Ti6Al4V alloy [50]. According to [50], linear energy densities in the range of 0.1 – 0.2 J/mm are optimal for

producing bulk parts. Therefore, the laser power and scanning speed levels were carefully determined to ensure that the center point of the utilized FC-CCD remained within the specified range. While most points were selected within the recommended interval, two of them were selected outside but still close to the optimal range. These process parameters provide a stable PBF-LB process, allowing for the development of reliable regression models.

It should be noted that a wider range of parameters could lead to completely different melting modes [46, 50] at different levels, which would affect surface roughness values differently [18]. In such cases, a single regression model may not be suitable, as different melting modes would have varying effects on surface roughness. Therefore, the reported  $P$  and  $v$  levels in Table 3.1 were carefully selected to ensure consistent melting modes for each combination, enabling the manufacturability of bulk parts.

**Table 3.1:** *Selected parameters and levels according to FC-CCD.*

Parameters		Laser power ( $P$ )	Scanning speed ( $v$ )
Levels	-1	200 W	1000 mm/s
	0	225 W	1250 mm/s
	1	250 W	1500 mm/s

## 3.2. Mathematical Modeling and Statistical Analysis

Response surface methodology will be used to model the influence of  $P$  and  $v$  on mechanical properties and average surface roughness. The homoscedasticity of proposed models will be tested using non-constant variance score tests, while the normality of the distribution of studentized residuals will be tested using the Shapiro-Wilk test. For this reason, the significance level ( $\alpha$ ) for each test and analysis has been set to the commonly used value of 0.05. Furthermore, multiple comparison tests will be performed to identify differences in nano-mechanical properties between different specimen groups.

### 3.2.1. Response Surface Modeling

The response surface for each variable was created using the Ordinary Least Squares (OLS) procedure, which is a standard method implemented in the linear model function in R statistical programming environment [138]. For each prediction variable, the initial step involved fitting the full quadratic model. Before fitting the full quadratic model, the predictors were

normalized from -1 to 1 to ensure an equal chance for each predictor to survive in the model, as they have different scales. The  $P$  and  $v$  have been normalized using the following equations:

$$P_n = \frac{P - P_{\text{mean}}}{P_{\text{max}} - P_{\text{mean}}}, \quad (3-1)$$

$$v_n = \frac{v - v_{\text{mean}}}{v_{\text{max}} - v_{\text{mean}}}. \quad (3-2)$$

Where  $P_n$  and  $v_n$  are normalized values,  $P$  and  $v$  are observed values,  $P_{\text{mean}}$  and  $v_{\text{mean}}$  are mean values,  $P_{\text{max}}$  and  $v_{\text{max}}$  are maximum values.

Since there are two factors ( $P$  and  $v$ ) for each prediction variable, the full quadratic model takes the following form [139]:

$$y = \beta_0 + \beta_1 x_1 + \beta_2 x_2 + \beta_{11} x_1^2 + \beta_{22} x_2^2 + \beta_{12} x_1 x_2 + \varepsilon \quad (3-3)$$

where  $y$  is the response variable,  $x_1$  and  $x_2$  are predictor variables,  $\beta_0$  is the intercept,  $\beta_1$  and  $\beta_2$  are the coefficients for the linear term,  $\beta_{11}$  and  $\beta_{22}$  are the coefficients for the quadratic term,  $\beta_{12}$  is the coefficient for the interaction term, and  $\varepsilon$  is the error term.

The 95% confidence intervals have been determined for each prediction variable using the following equation [139]:

$$\mu_{y|x_0} = \hat{y}(x_0) \pm t_{\alpha/2, df(\text{error})} \sqrt{\hat{\sigma}^2 \cdot \mathbf{x}'_0 (\mathbf{X}'\mathbf{X})^{-1} \mathbf{x}_0}. \quad (3-4)$$

In this context,  $\hat{y}(x_0)$  denotes the estimated mean response at the specified grid point, while  $\mathbf{x}_0$  represents a vector containing these grid points. The matrix  $\mathbf{X}$  is constructed by transforming the levels of the independent variables into their respective modeling form. The term  $\hat{\sigma}^2$  refers to the estimated variance of errors, and  $t_{\alpha/2, df(\text{error})}$  signifies the  $t$ -value linked to the desired confidence level and the degrees of freedom associated with the residuals.

Once the coefficients of the full quadratic model are determined, the assumption of normally distributed studentized residuals is checked using the Shapiro-Wilk (S-W) test [135, 140]. In addition, the assumption of normally distributed studentized residuals has been checked by plotting residuals versus prediction variables and by using Q-Q plots. It is also necessary to test whether the model has homoscedastic variance in the error term. For

this purpose, the non-constant variance (NCV) score test has been used [135, 140].

Given the complexity of the physical phenomena being approximated using regression models, it is often the case that multiple models can fit the data with adequate accuracy [141]. Typically, more complex models tend to have better fitting performance, although they also have increased interdependence among their terms compared to simpler models [141]. Hence, increasing the number of model terms is justified only when the more complex model significantly improves fit over the simpler one. Consequently, two models are proposed for each prediction variable, subjected to multiple statistical tests, and thoroughly compared in terms of fitting performance and complexity. The first model for each variable shows better fitting performance but also comes with increased complexity. Conversely, the secondary model presents lower complexity, which is desirable, but at the cost of some fitting performance. This systematic approach facilitates the examination of model terms' influence and the identification of significant ones for each prediction variable. Notably, the second proposed models (i.e., those with lower complexity) are formed by eliminating non-significant terms from the full quadratic model and by testing whether there is a statistically significant difference in fitting performance between the two by using the analysis of variance (ANOVA).

The ANOVA procedure allows for testing different models' performance in fitting for the given prediction variable. Specifically, this procedure has been used to determine whether there is a statistically significant difference between the residual sum of squares for each developed model.

#### 3.2.2. Multiple Comparison Tests

To investigate potential statistically significant differences in nano-mechanical properties among various specimen groups and indentation locations, multiple comparison tests have been used. The statistical tests described in this subsection were conducted using the R statistical programming environment [138]. The Shapiro-Wilk test was used to test the presence of non-normality in data distribution. If non-normality is detected, non-parametric tests, specifically the Kruskal-Wallis test, will be utilized to check the presence of statistically significant differences among independent samples. Conversely, in the absence of evidence of non-normality, a parametric method, specifically the one-way ANOVA procedure, will be employed to test differences between the samples.

In instances where non-normality is not evident, the parametric one-way ANOVA procedure will be utilized to test for statistically significant differences in mean values of independent samples. Alternatively, in the presence of evidence of non-normality, the non-parametric Kruskal-Wallis test will be employed to examine differences in median values of the samples. If statistically significant differences are observed, Dunn’s multiple comparison test will be employed in post hoc analysis to precisely identify the independent samples that exhibit statistically significant differences in their median values. It is important to note that a higher number of multiple comparisons increases the risk of false discoveries. Therefore, the Benjamini-Hochberg method will be used to decrease the false discovery rate when conducting multiple comparison tests.

### 3.3. Specimen Design and Manufacturing

To conduct experimental tests, three types of specimens need to be designed and manufactured: cubic, tensile, and lattice test specimens.

For this purpose, extra low interstitial Ti6Al4V (ELI) Grade 23 powder, with spherical particles, is employed in the fabrication of the specimens as shown in Figure 3.2a. The particle size distribution is determined through 530 measurements conducted using a Keyence VHX 7000 microscope. The diameters of the powder sample particles ranged from approximately 4  $\mu\text{m}$  to 48  $\mu\text{m}$  (see Figure 3.2b), with a median diameter of 27.06  $\mu\text{m}$ . The 10th and 90th percentiles were 12.98  $\mu\text{m}$  and 38.92  $\mu\text{m}$ , respectively.

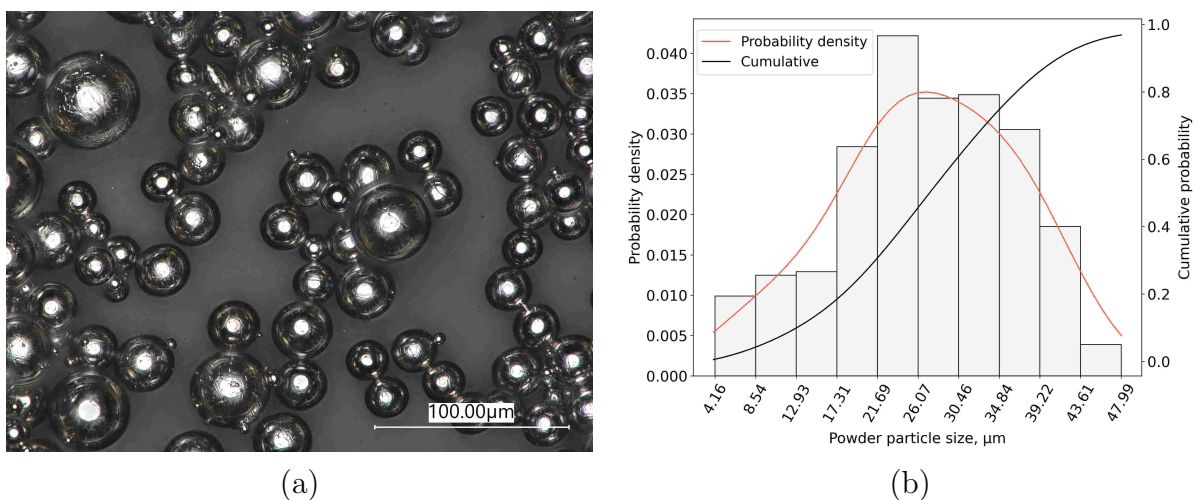


**Figure 3.2:** (a) *Ti6Al4V (ELI) Grade 23 powder particles*, and (b) *their size distribution, including cumulative and probability density functions*.

### 3.3.1. Cubic Specimens

Cubic specimens (Figure 3.3b),  $10 \times 10 \times 10 \text{ mm}^3$  in size, were produced to investigate microstructural characteristics and defects resulting from the PBF-LB method. These specimens were also utilized for nanoindentation and low-force Vickers hardness tests. In total, ten cubic specimens were fabricated, each using one of nine distinct sets of process parameters (Table 3.2), matching those used in the manufacturing of tensile test specimens. Manufacturing an additional specimen ( $D^{\text{an}}$ ) using the same process parameters as an as-built specimen ( $D^{\text{ab}}$ ) enabled the investigation of the effects of annealing heat treatment on microstructure. Therefore, after the manufacturing,  $D^{\text{an}}$  specimen was subjected to annealing heat treatment. PBF-LB process time of cubic specimens was 3h and 3 minutes using the scanning strategy depicted in Figure 3.3a.

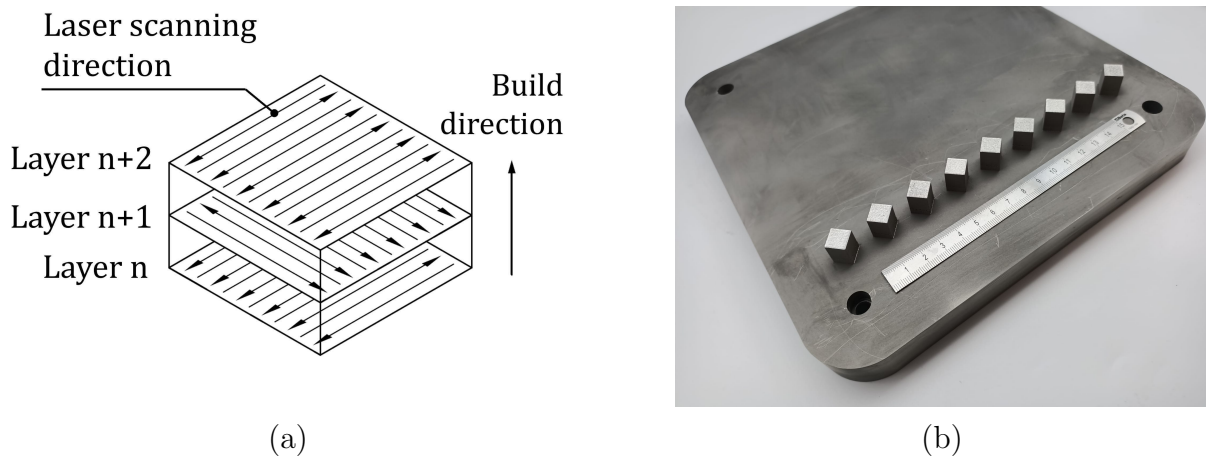


**Figure 3.3:** (a) Scanning strategy used to manufacture (b) Cubic specimens using PBF-LB process.

The laser spot diameter was set to 0.1 mm, a common choice in commercial PBF-LB machines as it balances productivity and dimensional accuracy. Although smaller laser spot diameters can improve the dimensional accuracy of smaller components, they were not considered here due to their significant impact on manufacturing productivity. Given the relatively large size of the cuboid specimens ( $10 \times 10 \times 10 \text{ mm}^3$ ), a 0.1 mm spot diameter was considered appropriate.

In the absence of specific recommendations or guidelines for determining the hatch distance ( $h_D$ ), it was determined empirically. The melt pool width ( $w$ ) was assumed to be 1.5 times the spot diameter ( $d$ ). An overlap of 60% between adjacent laser beam passages

**Table 3.2:** Process parameters used to manufacture cubic specimens.

Constant process parameters									
$t$	0.025 mm								
$h_D$	0.09 mm								
$d$	0.1 mm								
Scanning strategy	Bi-directional, single pass, 90° rotation of scan vector between layers								
Levels									
$P, W$	200			225			250		
$v, \text{mm/s}$	1000	1250	1500	1000	1250	1500	1000	1250	1500
$E_V, \text{J/mm}^3$	88.9	71.1	59.3	100	80	66.7	111.1	88.9	74.1
$E_L, \text{J/mm}$	0.2	0.16	0.13	0.23	0.18	0.15	0.25	0.2	0.17
ID	A	B	C	D <sup>ab</sup> , D <sup>an</sup>	E	F	G	H	I

Notes: The term layer thickness ( $t$ ) is derived from existing literature and refers to the leveling height of the build platform. It is important to note that during PBF-LB processes, the actual thickness of the powder layer can be 4 to 5.5 times greater than the specified layer thickness values in PBF-LB machines [142]. <sup>ab</sup> specimen in as-built state. <sup>an</sup> specimen in annealed state.

( $O_{LB}$ ) was chosen, resulting in a hatch distance value of 0.09 mm ( $h_D = w \times O_{LB}$ ). This ensures adequate overlapping of individual laser passes and maximizes the density of the test specimens. The build platform's leveling height ( $t$ ) was set to 25  $\mu\text{m}$  to minimize the occurrence of porosities within the material microstructure [87].

It is important to note that the actual powder layer height during the PBF-LB process is not the same as the leveling height of the build platform, contrary to common belief. The actual powder layer height is 4 to 5.5 times higher than the leveling height set in the PBF-LB machine prior to manufacturing [142]. Therefore, the recoater in the PBF-LB machine was able to spread the powder across the entire build platform evenly, even though the powder median diameter (27.06  $\mu\text{m}$ ) was larger than the build platform leveling height (25  $\mu\text{m}$ ).

### 3.3.2. Flat Specimens

Flat specimens of PBF-LB Ti6Al4V alloy were designed similarly to the recommended dimensions of flat test specimens defined within the ASTM E8/E8M - 16a standard [143], while maintaining the ratio of length to width of the measuring area of 5:1. Consequently, the gauge's length measured 20 mm, and its width was 4 mm. Meanwhile, the reduced parallel section had a length of 22 mm, clearly illustrated in Figure 3.4a.

The flat specimens were positioned vertically on the build platform, with their respective

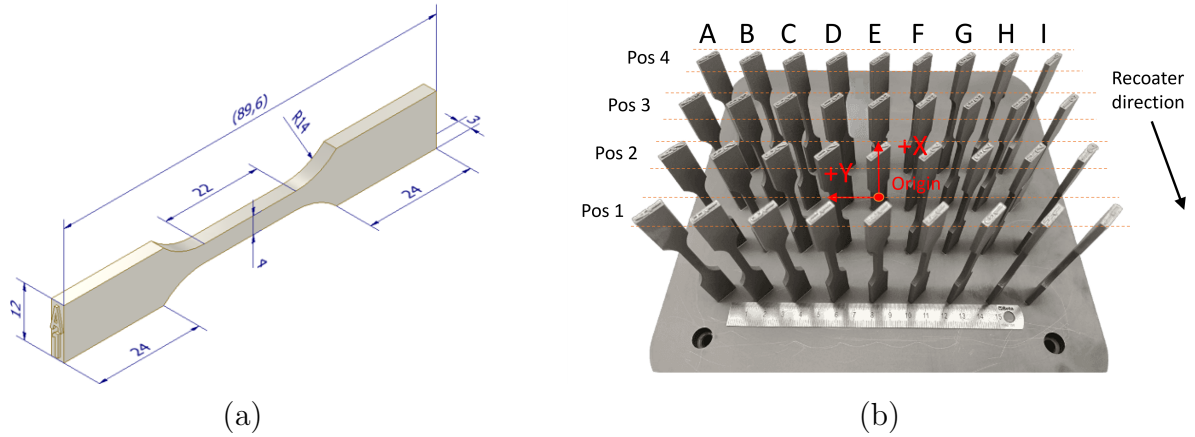


**Figure 3.4:** (a) Dimensions of tensile tests specimens, (b) Tensile test specimens after manufacturing with marked positions on the build platform.

positions indicated in Figure 3.4b. The coordinates for each specimen on the build platform, relative to the origin located at its center, are listed in Table 3.3. All reported coordinates indicate the position of the specimens relative to the origin (mid-point) of the build platform. In this way, the potential influence of specimen position on the mechanical properties and surface roughness has been considered. The specimens were rotated  $45^\circ$  around the Z-axis to ensure that the recoater does not encounter a straight wall while moving across all specimens, as illustrated in Figure 3.4b.

**Table 3.3:** Tensile test specimen coordinates respect to the origin of the build platform.

Pos 1	ID	A1	B1	C1	D1	E1	F1	G1	H1	I1
	X	-70	-70	-70	-70	-70	-70	-70	-70	-70
	Y	88	66	44	22	0	-22	-44	-66	-88
Pos 2	ID	A2	B2	C2	D2	E2	F2	G2	H2	I2
	X	-40	-40	-40	-40	-40	-40	-40	-40	-40
	Y	88	66	44	22	0	-22	-44	-66	-88
Pos 3	ID	A3	B3	C3	D3	E3	F3	G3	H3	I3
	X	-10	-10	-10	-10	-10	-10	-10	-10	-10
	Y	88	66	44	22	0	-22	-44	-66	-88
Pos 4	ID	A4	B4	C4	D4	E4	F4	G4	H4	I4
	X	20	20	20	20	20	20	20	20	20
	Y	88	66	44	22	0	-22	-44	-66	-88

A total of 36 tensile test specimens were created and divided into nine distinct groups (A-I), each consisting of four repetitions. The process parameters used in each group matched those used in producing cubic specimens (see Table 3.2). PBF-LB process time of tensile test specimens was 1 day, 3 hours and 5 minutes. After the PBF-LB process, all specimens underwent annealing to reduce residual stress and transform the brittle and hard  $\alpha'$  phase



into the more desirable  $\alpha + \beta$ . Since all tensile specimens were annealed,  $D^{\text{ab}}$  and  $D^{\text{an}}$  IDs were renamed to D. This procedure allowed for the investigation of the potential effect of PBF-LB process parameters on mechanical properties after heat treatment.

### 3.3.3. Lattice Specimens

The study also examines lattice specimens comprising  $\sim 4.6 \times 5 \times 5$  body-centered cubic unit cells, as depicted in Fig. 3.5. Dimensions of each unit cell are fixed at a size  $4 \times 4 \times 4$  mm. Consequently, the overall height of the lattice portion of the specimen is 18.5 mm, with dimensions of 20 mm in length and width. Additionally, a total of 4.6 unit cells in height was selected to enable the positioning of the extensometer at the solid region of the specimen and to mitigate failure at contact regions between the solid and lattice regions. This led to shorter struts of boundary unit cells near solid parts, increasing their stiffness and preventing failure at contact regions. A total of  $5 \times 5$  repeating unit cells in a row (width  $\times$  length) was selected to reduce the edge effects and enable reliable representation of the whole lattice structure.

BCC unit cells considered within this study are characterized by the following: the diameter at the ends of the struts ( $d_{\text{end}}$ ) varies between 0.6, 0.8, or 1 mm, while the diameter at the midpoint of the struts ( $d_{\text{mid}}$ ) is either 0.6, 0.8, or 1 mm. Moreover, the height of the joint nodes ( $h$ ) is set to 2 mm. Thus, the identification of each specimen used in this study follows the format:  $d_{\text{end}} - d_{\text{mid}} - h$ .

**Table 3.4:** *Unit cell configurations.*

Specimen ID	$d_{\text{end}}$ , mm	$d_{\text{mid}}$ , mm	$h$ , mm	No. of specimens
06-06-2	0.6	0.6	2	3
06-08-2	0.6	0.8	2	1
06-1-2	0.6	1	2	1
08-06-2	0.8	0.6	2	1
08-08-2	0.8	0.8	2	3
08-1-2	0.8	1	2	1
1-06-2	1	0.6	2	1
1-08-2	1	0.8	2	1
1-1-2	1	1	2	3

The tapering diameter range from 0.6 mm to 1 mm was selected considering the limitations of the PBF-LB technology and BCC unit cell geometry. Manufacturing of lattice specimens with BCC unit cells having struts smaller than 0.6 mm is challenging, as manufacturing defects are more likely to occur, and due to the thin struts, their effect on the

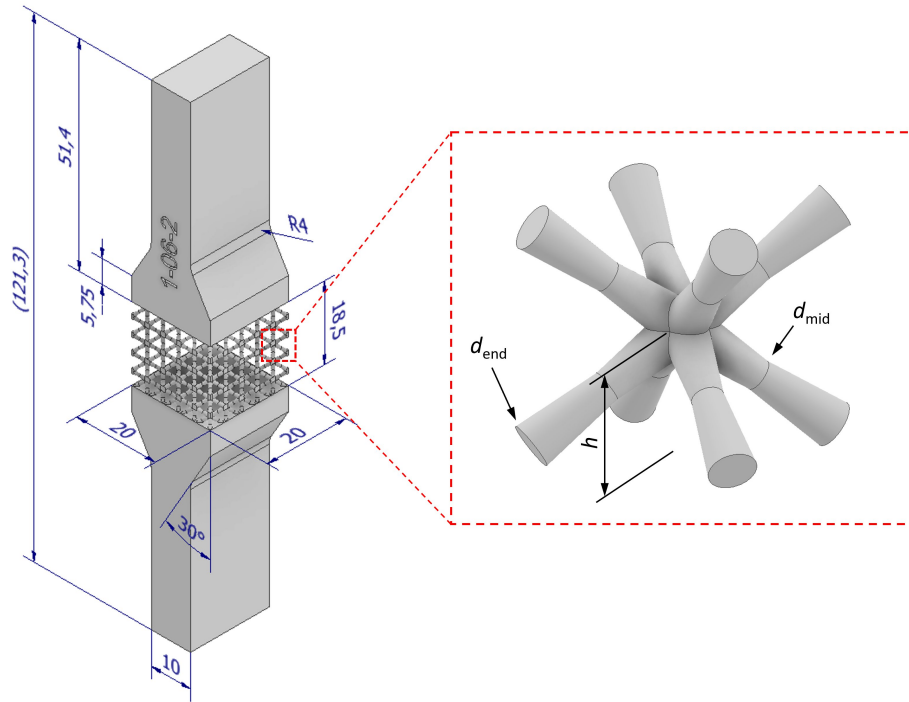


**Figure 3.5:** Model of specimen with lattice structure.

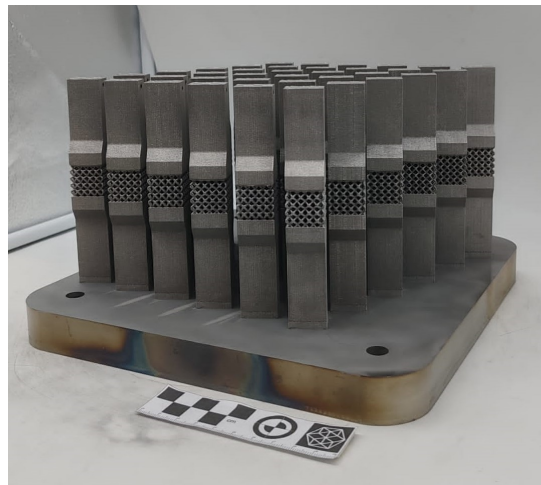


**Figure 3.6:** Manufactured test specimens with BCC unit cells arranged in a lattice structure.

mechanical response is more pronounced. This, in turn, affects the representability of the experimental results. On the other hand, the upper limit of 1 mm was set in order to reduce the cross formation when using tapering combinations having  $d_{\text{end}}$  diameter set to 0.6 mm, and  $d_{\text{mid}}$  to 1 mm. Given that struts in BCC unit cells are inclined, larger tapering ratios increase cross formations. This, in turn, compromises the representativeness of results as such formations often feature high concentrations of defects, surface irregularities, and significant surface roughness. In addition, accurate measurement of actual strut diameters after

manufacturing is challenging.

A total of 36 specimens with various configurations of BCC unit cells were manufactured using the process parameters detailed in Table 3.5 and shown in Figure 3.6. However, only the specimens listed in Table 3.4 underwent tensile tests, while the rest were reserved for future research on high and low-cycle fatigue.

**Table 3.5:** *PBF-LB process parameters used to manufacture lattice structure specimens.*

ID	$P, W$	$v, \text{mm/s}$	$t, \text{mm}$	$h_D, \text{mm}$	$d, \text{mm}$	$E_V, \text{J/mm}^3$	$E_L, \text{J/mm}$	Scan. strat.
D	225	1000	0.025	0.09	0.1	100	0.23	Island

### 3.4. Heat Treatment

All nine cubic specimens, as well as the flat and lattice specimens, underwent annealing heat treatment. Only one of the cubic specimens was kept in its original as-built state. This approach enabled the investigation of the impact of annealing heat treatment on nanomechanical properties, hardness, and microstructure. Both the tensile test and lattice specimens were annealed to investigate the influence of PBF-LB parameters on mechanical properties after annealing.

The annealing heat treatment was carried out in a protective inert gas (argon) atmosphere to prevent oxidation. The heating rate was set at  $3.5^\circ\text{C}/\text{min}$  up to a temperature of  $840^\circ\text{C}$ , which was kept constant for 2 hours, after which cooling in the furnace started as illustrated in Figure 3.7. The cooling time in the furnace from  $800^\circ\text{C}$  to  $500^\circ\text{C}$  is 290 min ( $\Delta t_{8/5} = 290$  min). After reaching a temperature of  $150^\circ\text{C}$  during cooling, the argon flow was closed, and the cooling to room temperature was carried out in air.

### 3.5. Metallographic Preparation

Adequate metallographic preparation of cubic specimens is crucial to ensure precise and reliable nanoindentation and optical microscopy measurements. Consequently, the cubic specimens were embedded in resin and subsequently ground in water using SiC papers of various grit sizes (320, 600, 800, 1200, and 2400). Following this, a polishing sequence was employed, starting with polycrystalline diamond paste ( $3 \mu\text{m}$  grain size, succeeded by  $1 \mu\text{m}$ ) applied to a polishing cloth with a lubricant. The final polishing phase involved colloidal

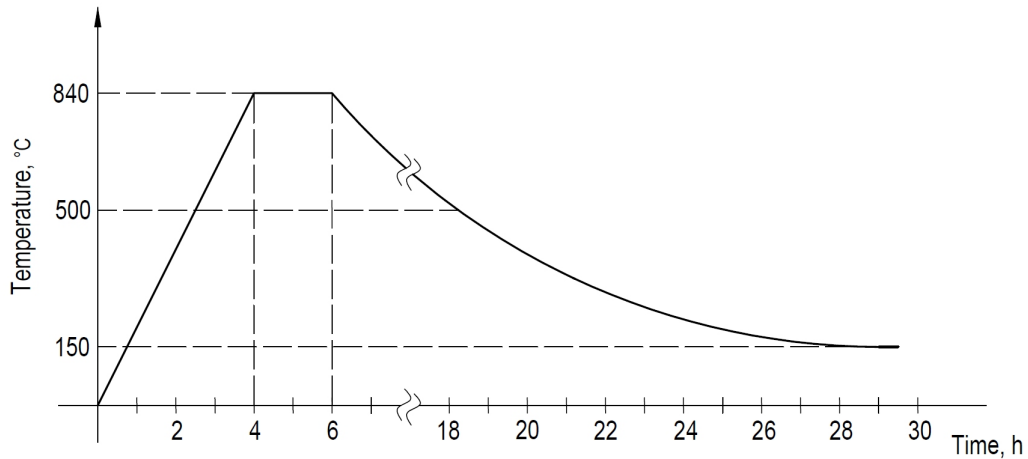


**Figure 3.7:** Schematic diagram of the annealing heat treatment.

silica suspension with a grain size of 0.03  $\mu\text{m}$ . To further enhance the specimens, they were etched with Kroll's reagent (composed of 92% distilled water, 6%  $\text{HNO}_3$ , and 2%  $\text{HF}$ ) for 20 seconds, followed by thorough rinsing with warm water. The selection of Kroll's reagent for etching aimed to eliminate surface damage while imparting minimal contrast, a beneficial feature for both nanoindentation experiments and optical microscopy.

### 3.6. Indentation Experiments

Low-force Vickers hardness measurements (HV1) were performed with seven repetitions on all cubic specimens using a STRUERS DURAMIN hardness tester. These measurements employed a holding time of 12 seconds and an indentation force of 9.807 N in accordance with the ISO 6507-1:2018 standard [144]. In addition to HV1 measurements, specimens underwent nanoindentation procedures to determine their nano-mechanical properties.

All nanoindentation experiments were conducted at room temperature using a Keysight G200 Nanoindenter, employing a three-sided Berkovich diamond indenter. Throughout the tests, strict control was maintained to limit drift to below 0.05 nm/s. This was done to mitigate the adverse effects of temperature variations on results, ensuring more precise measurements. A Poisson's ratio ( $\nu$ ) of 0.33, characteristic of Ti6Al4V alloy as referenced in [20], was utilized.

Due to potential Berkovich tip blunting and the considerable time involved in high indentation load tests (up to 500 mN), strain rate sensitivity analysis and creep tests were specifically conducted on  $D^{\text{ab}}$  and  $D^{\text{an}}$  specimens. This investigation aimed to assess the

impact of heat treatment on nano-mechanical properties, given the potential alterations in material behavior under such conditions.

In order to test location influence on nanoindentation results, the experiments involved conducting 7 indents using the continuous stiffness measurement (CSM) method within each of 5 distinct prior- $\beta$  columnar grains. The aim was to explore potential variations in Young's modulus and nano-hardness among these grains. All measurements were conducted on the specimen plane aligned parallel to the build direction, ensuring sufficient space within the prior- $\beta$  columnar grains for the nanoindentation experiments. Notably, at these planes, the area encompassed by each prior- $\beta$  columnar grain was notably larger compared to areas on planes perpendicular to the build direction. Recent research by Chen et al. supports the finding that Young's modulus remains consistent across testing planes, while nano-hardness values may be up to 20% lower when measured on planes perpendicular to the build direction [97].

Additionally, employing the same method, an indentation depth interval was identified wherein nano-mechanical properties converge to a stable value. This interval was retained as a benchmark for further data analysis across all CSM tests. Following recommendations from [37–39], specific parameters such as a frequency target of 45 Hz and a harmonic amplitude of 2 nm were set to ensure direct comparability of data. The maximum indentation depth was fixed at 2500 nm to thoroughly assess the impact of indentation depth on both Young's modulus and hardness data. Moreover, the CSM method was applied for evaluating Young's modulus and hardness across specimens produced using different L-PBF process parameters.

Young's modulus ( $E$ ) was determined for both the CSM and the load-unload method using equation (3-5) specified in [145, 146]:

$$E = \frac{(1 - \nu^2)E_r E_i}{E_i - E_r(1 - \nu_i^2)}, \quad (3-5)$$

where  $E_r$  is reduced modulus,  $\nu$  is Poisson's ratio of the specimen,  $E_i$  and  $\nu_i$  are Young's modulus and Poisson's ratio of the Berkovich tip, respectively. The reduced modulus can be determined using equation (3-6), where  $\beta = 1$  for Berkovich tip, as described in [145].

$$E_r = \frac{\sqrt{\pi} \cdot S}{\beta \cdot 2 \cdot \sqrt{A_p}}, \quad (3-6)$$

where  $\beta = 1$  for the Berkovich tip,  $S$  represents the contact stiffness, while  $A_p$  is the projected

area of the Berkovich tip. When employing the CSM method, the contact stiffness can be calculated using equation (3-7) as reported in [145, 147]:

$$S = \left( \frac{1}{\frac{F_{\text{amp}}}{h_{\text{amp}}} \cos(\phi) - (K_s - m \cdot \omega^2)} - \frac{1}{K_f} \right)^{-1}, \quad (3-7)$$

where  $F_{\text{amp}}$  is the excitation amplitude,  $h_{\text{amp}}$  is the displacement amplitude,  $\phi$  is the phase angle,  $K_f$  represents the load-frame stiffness,  $K_s$  is the stiffness of the support springs,  $m$  is the mass of the loading column, and  $\omega$  is the excitation frequency. In the other hand, when the load-unload method is used, contact stiffness can be calculated using equation (3-8) as stated in [145].

$$S = \left. \frac{dP_{\text{unload}}}{dh} \right|_{h=h_{\text{max}}} \quad (3-8)$$

where  $P_{\text{unload}}$  is the unloading force, while  $h$  and  $h_{\text{max}}$  represent indentation depth and maximum indentation depth, respectively. The nano-hardness can be determined using equation (3-9) as shown in [145].

$$H = \frac{P_{\text{max}}}{A_p}, \quad (3-9)$$

where  $P_{\text{max}}$  refers to the maximum indentation load, while  $A_p$  represents the projected area of the Berkovich tip, determined through the nanoindentation procedure.

Creep tests were also conducted, with nine repetitions on specimens D<sup>ab</sup> and D<sup>an</sup>, employing six different holding loads (10, 20, 50, 100, 200, and 500 mN) to explore the creep behavior across a broader load range. For these creep tests, the loading and unloading rates were set at 0.5 mN/s, and the maximum load was sustained for 500 s to align with the test parameters detailed in [30].

Equation (3-10) was used on the creep stage data to determine the creep displacement ( $h_{\text{cr}}$ ), as described in [99]:

$$h_{\text{cr}} = h_0 + a(t - t_0)^b + kt, \quad (3-10)$$

where  $h_0$  is the time at the beginning of the creep stage,  $t_0$  is the time at the beginning of the creep stage, and  $t$  is the holding time. Using the material response data obtained through the load-unload method, the region of the creep stage was assessed to determine

fitting parameters  $a$ ,  $b$ , and  $k$  needed for modeling creep behavior. Hence, these parameters were determined by fitting equation (3-10) to the experimental data of displacement versus holding time during the creep stage. The determination of the creep strain rate ( $\dot{\epsilon}$ ) was achieved by employing the equation (3-11) on the data obtained from the creep stage, as indicated in reference [99].

$$\dot{\epsilon} = \frac{1}{h_{\text{cr}}} \frac{dh_{\text{cr}}}{dt}, \quad (3-11)$$

where  $dh_{\text{cr}}/dt$  represents the rate of change of indentation depth over time during creep stage. After deriving the function of displacement of the indenter tip over time, it follows that the deformation rate is equal to:

$$\dot{\epsilon} = \frac{1}{h_{\text{cr}}} abt^{b-1} + k \quad (3-12)$$

The unloading part of the  $P - h$  curve is modeled using the following equation [145]:

$$P_{\text{unload}} = B(h - h_f)^m, \quad (3-13)$$

where  $P_{\text{unload}}$  is the unloading force as a function of depth  $h$  during sample unloading,  $h_f$  is the residual displacement at the end of unloading, while  $B$  and  $m$  are parameters of the model that need to be identified. The contact stiffness of the material  $S$  is determined from the previously defined unloading curve (3-13). The contact stiffness of the material is defined as a slope of the tangent to the unloading curve at the maximum indentation depth  $h_{\text{max}}$  [145]. It is determined based on the elastic response of the material at the upper part of the unloading curve. For this purpose, the upper half of the unloading curve is used, as stated in [148]. After substituting (3-13) in (3-8), contact stiffness can be determined as:

$$S = Bmh_{\text{max}}^{(m-1)} \quad (3-14)$$

After the material's contact stiffness is known, it is possible to determine the  $h_c$  using the following expression, as stated in [145]:

$$h_c = h_{\text{cr}} - \varepsilon^* \frac{P_{\text{cr}}}{S} \quad (3-15)$$

Since the Berkovich tip has been used,  $\varepsilon^*$  was set to 0.75 [145].  $P_{\text{cr}}$  denotes the constant

force exerted on the sample during the creep stage, implying a consistent load applied throughout this phase of the experiment. After the contact depth  $h_c$  is known, it is possible to determine the projected area of the Berkovich tip  $A_p$  using the following expression [145]:

$$A_p = C_1 h_c^2 + C_2 h_c \quad (3-16)$$

Where  $C_1$  and  $C_2$  is the area coefficient corresponding to the used Berkovich tip. These two coefficients takes into account the blunting of the indenter tip over time and are determined through the calibration process of the nanoindenter tip. In this research,  $C_1$  and  $C_2$  are determined to be 24.56 and 3919.039, respectively. After calculating the projected area of the Berkovich tip, which depends on the depth of indentation and the geometry of the tip itself, it is possible to determine the nanohardness  $H_{cr}$  during the creep stage. The  $H_{cr}$  is a function representing the ratio of the constant force and the projected area of the Berkovich indenter [145].

$$H_{cr} = \frac{P_{cr}}{A_p} \quad (3-17)$$

After the creep strain rate (3-12) and the nanohardness during the creep stage (3-9) are known, it is possible to determine the creep exponent ( $n$ ) [99].

$$n = \frac{\partial \ln(\dot{\epsilon})}{\partial \ln(H_{cr})} \quad (3-18)$$

The  $n$  represents the slope of the tangent to the curve defined by the second half of the data points characteristic of the stabilized creep stage.

### 3.7. Tensile Tests

Tensile tests on flat specimens were performed using the INSTRON 1255 – 8500 plus universal servohydraulic machine (Figure 3.8a), simultaneously using two load sensors with a capacity of 20 kN and 250 kN. The displacement speed was kept constant at 0.01 mm/s in the elastic and plastic regions. The specimen's gauge length, width, and thickness were 20 mm, 4 mm, and 3 mm, respectively. All tensile tests were performed at room temperature with an average of 23°C. Deformation fields during the tensile test were recorded using the DIC system GOM ARAMIS adjustable 2D/3D 12M with a sampling frequency of 2 Hz, which



recorded around 700 images during the experiment. The facet size was set to 19 px, the point distance to 16 px, and the calculation method to standard.

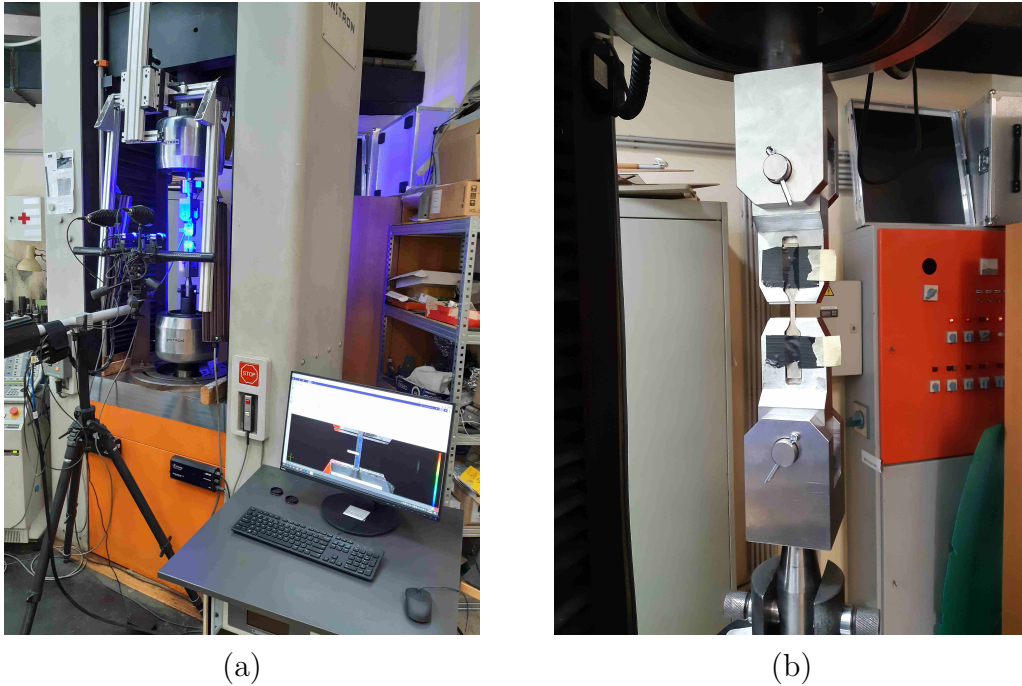


**Figure 3.8:** Tensile test setup consisting of: (a) INSTRON 1255 – 8500 plus universal servohydraulic machine and GOM ARAMIS adjustable 2D/3D 12M system, (b) Self-aligning grips.

Specialized self-aligning grips were designed and manufactured to conduct tensile tests on flat specimens. These grips, equipped with three joints, ensured proper alignment and prevented specimen slippage during testing. Figure 3.8b shows the self-aligning grips securely holding the specimen by its shape along the radius section. This design effectively eliminated any slippage of the specimen.

The engineering stress ( $\sigma$ ) is calculated after the tensile test using recorded tensile load ( $F$ ) and area of the specimen's cross-section ( $A$ ) as follows:

$$\sigma = \frac{F}{A}. \quad (3-19)$$

The maximum value of  $\sigma$  represents the ultimate tensile strength ( $R_m$ ). In order to determine  $E$  and  $R_{p0.2}$  the engineering strain ( $\varepsilon$ ) measurements are needed. The  $E$  is defined as the slope of the linear part of the engineering stress-strain curve and can be determined using the following equation:

$$E = \frac{\sigma}{\varepsilon}. \quad (3-20)$$

Once the  $E$  is known, the  $R_{p0.2}$  can be determined by offsetting the line having the slope defined by  $E$  from the origin to the value corresponding to 0.2% (0.002 mm/mm) of engineering strain. The point where the offset line crosses the engineering stress-strain curve represents the  $R_{p0.2}$ .

The engineering strain, typically measured using contact and non-contact methods, is defined as:

$$\varepsilon = \frac{l - l_0}{l_0}, \quad (3-21)$$

where,  $l_0$  represents initial length, and  $l$  the current length. When strains in more than one direction are known in the elastic region, the Poisson's ratio can be calculated as:

$$\nu = -\frac{d\varepsilon_{\text{trans}}}{d\varepsilon_{\text{axial}}}, \quad (3-22)$$

where,  $d\varepsilon_{\text{trans}}$  represents transverse strain and  $d\varepsilon_{\text{axial}}$  represents the axial strain. Assuming the material has isotropic elastic constants, the shear modulus can be determined using the following equation:

$$G = \frac{E}{2(1 + \nu)}. \quad (3-23)$$

In order to simulate material behavior observed in flat and lattice specimens using FEM, it is required to use true strain and true stress form. The true strain is calculated from the engineering strain using the following equation:

$$\varepsilon_{\text{true}} = \ln(1 + \varepsilon). \quad (3-24)$$

Furthermore, the true stress is defined as:

$$\sigma_{\text{true}} = \sigma(1 + \varepsilon). \quad (3-25)$$

In order to perform tensile tests on lattice specimens, a StepLAB electromechanical actuator equipped with a 25 kN load cell (Figure 3.9a) was used. The crosshead speed was set to 0.01 mm/s to ensure consistent conditions with the tensile tests on flat specimens.

Strain values were recorded using an Epsilontech 3442-010M-050M-ST extensometer with a gauge length of 20 mm (Figure 3.9b).

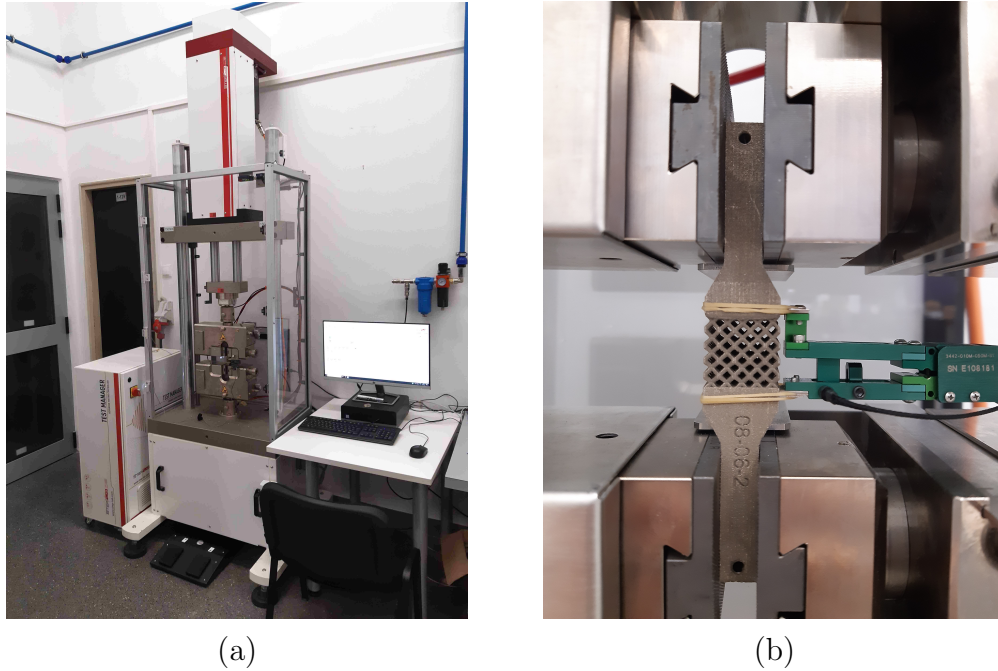


**Figure 3.9:** Tensile test setup: (a) StepLAB electro-mechanical actuator, (b) Epsilontech extensometer with 20 mm gauge length attached to specimen with lattice structure.

When determining the macroscopic stress in tensile testing of lattice specimens, the force was divided by the cross-sectional area of the specimen ( $20 \text{ mm} \times 20 \text{ mm}$ ), neglecting the presence of the hollow regions. This approach enables lattice structure to be treated as a homogeneous equivalent material, ensuring the independence of mechanical properties on unit cell geometry [72]. As a result, the mechanical properties, such as  $E$ ,  $R_m$ , and  $R_{p0.2}$  can be determined from the macroscopic engineering stress-strain curves.

## 3.8. Surface Roughness Measurements

Preceding the measurements, all specimens underwent a thorough cleaning process in a distilled water ultrasonic bath for 10 minutes to eliminate any loose particles potentially interfering with measurement accuracy.

### 3.8.1. Contact Measurements

Surface roughness measurements, specifically the average surface roughness ( $R_a$ ), were conducted on tensile test specimens employing the TESA Rugosurf 10-G profilometer (Figure

3.10a). To enhance reliability, measurements were iterated 6 times along the gauge length of the specimen surface (Figure 3.11a). Parameters for measurement adhered to ISO 4288:1996 and ISO 3274:1996 standards [149, 150], thus setting traverse length ( $l_t$ ) to 15 mm, evaluation length ( $l_n$ ) to 12.5 mm, cut-off ( $\lambda_c$ ), and sampling length ( $l_r$ ) to 2.5 mm, with the short-wave profile filter ( $l_s$ ) set to 8  $\mu\text{m}$ .

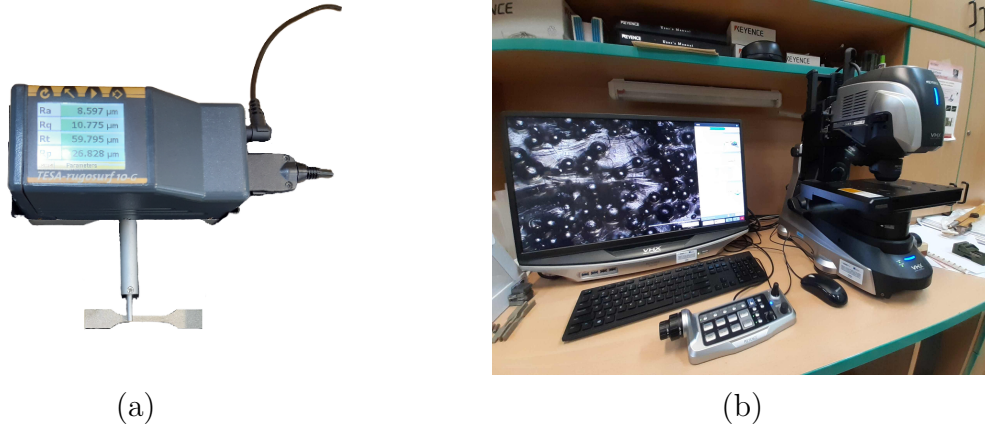


**Figure 3.10:** Surface roughness measurements using: (a) TESA Rugosurf 10-G profilometer, (b) Keyence VHX 7000 microscope.

### 3.8.2. Non-contact Measurements

For area average surface roughness ( $S_a$ ) measurements, Keyence VHX 7000 microscope was utilized (Figure 3.10b). Setting parameters involved configuring the  $S$ -filter value to 25  $\mu\text{m}$  (approximately 3 times the pixel size) at 1000 $\times$  magnification. The  $L$ -filter value was determined as 2.5 mm based on the insights from [110, 151]. Prior to conducting  $S_a$  measurements, a sensitivity analysis was performed by scanning the same area using various vertical pitch and magnification levels, as illustrated in Figure 3.11b.

Generally, higher magnifications provide more robust and reliable results due to enhanced detail quality of the scanned surface. However, this comes at the cost of increased microscope scanning time and data processing, making it crucial to find a balance between measurement accuracy and time efficiency. As depicted in Figure 3.11b, magnifications of 500 $\times$  or higher produce similar  $S_a$  values, aligning with previous findings [107]. The lowest variation in results among different vertical pitch values was observed at a magnification of 1000 $\times$ . Consequently, based on sensitivity analysis outcomes, a magnification of 1000 $\times$  and a vertical pitch of 1  $\mu\text{m}$  were chosen for further measurements. Area surface roughness measurements, utilized in response surface analysis, were conducted three times on each specimen's gauge

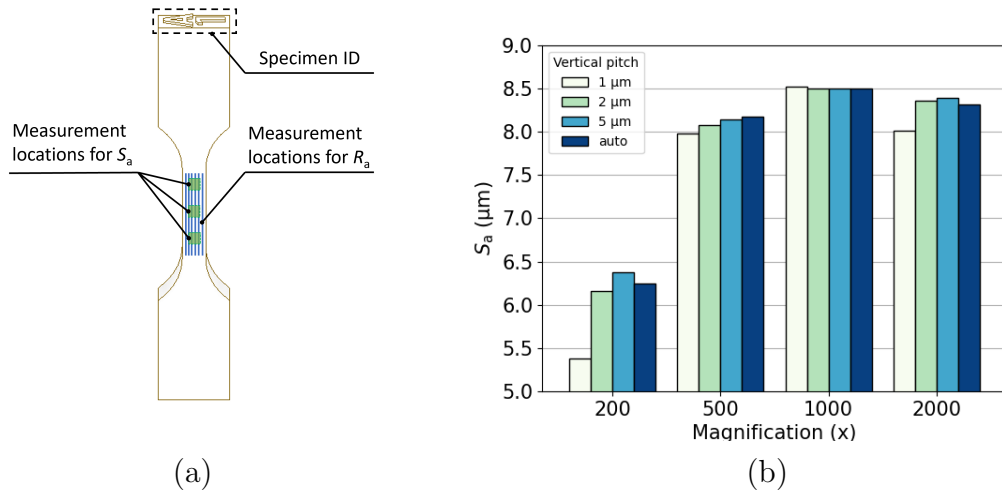


**Figure 3.11:** (a) Positions for surface roughness measurements, (b) Influence of vertical pitch and magnification on  $S_a$ .

length, scanning and evaluating a  $2 \times 2 \text{ mm}^2$  area at three distinct locations as illustrated in Figure 3.11a.

### 3.9. Optical Microscopy

In order to record the microstructural features present in both the as-built and annealed states, we have utilized the Keyence VHX 7000 microscope (Figure 3.10b). With its magnification range of up to  $6000\times$ , this microscope facilitates the observation and recording of various microstructural features. This enables the identification of columnar prior- $\beta$  grains, as well as the distinctive  $\alpha'$  and  $\alpha+\beta$  phases inherent to PBF-LB Ti6Al4V alloy. Utilizing this cutting-edge technology, microstructural features and defects specific to the PBF-LB process were investigated across a range of magnification levels. Equipped with stereo-optical capabilities, as well as depth compensation and stitching options, the microscope ensures sharp and precise imaging, even capturing features at varying heights. This functionality proves particularly crucial for accurately documenting fracture surfaces.

### 3.10. Relative Density Measurements

Archimedes' principle was applied to calculate the relative density of tensile test specimens. The material volume of  $20 \times 12 \times 3 \text{ mm}^3$  was subtracted from the grip section of one specimen from each specimen group. Archimedes method is a fast and inexpensive method

for measuring relative density [152]. It is also accepted as a standard method for measuring the relative density of parts manufactured using powder metallurgy [153, 154]. The analytical balance (Figure 3.12a) with a readability of 0.1 mg and accuracy of 1 mg was used to weigh specimens in air and ethanol with a density setup shown in Figure 3.12b. Measurements were repeated five times, and between each measurement, specimens were dried. During the measurements, special precautions were taken to ensure there were not visible air bubbles on the specimen's surfaces. After weighing, the relative density for each specimen was determined using the following equation:

$$\rho = \frac{m_a}{m_a - m_e} \times \rho_e \quad (3-26)$$

where,  $\rho$  is specimen density,  $m_a$  mass of the specimen in air,  $m_e$  mass of the specimen in ethanol, and  $\rho_e$  is density of ethanol. Furthermore, if theoretical density  $\rho_t$  of the material is known, porosity  $p$  can be determined using following equation:

$$p = 100 - \left( \frac{\rho}{\rho_t} \times 100 \right) \quad (3-27)$$

The theoretical density of the Ti6Al4V alloy  $\rho_t = 4.432 \text{ g/cm}^3$ , used for porosity calculation, was adopted from [15].

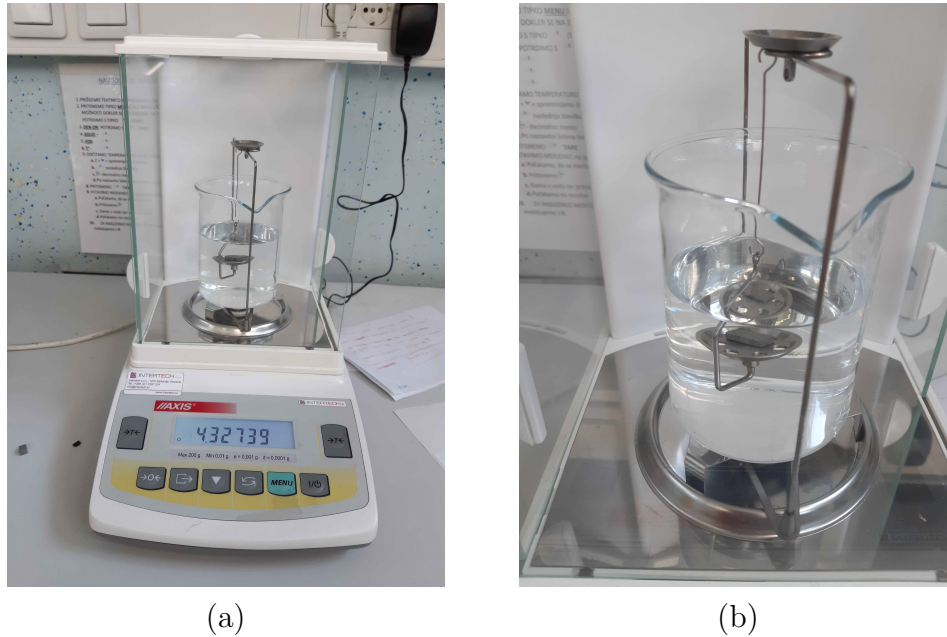


**Figure 3.12:** (a) Analytical balance, (b) Setup for relative density measurements.

## 4. CHARACTERIZATION OF PBF-LB Ti6Al4V ALLOY

In order to widen the potential field of application for produced PBF-LB Ti6Al4V parts, it is crucial to thoroughly investigate their mechanical and surface properties. For this purpose, multiple aspects will be considered, including microstructure, porosity, mechanical properties at different scales, and hardness. By including these aspects, mechanical behavior or properties identified through one experimental procedure can be explained and supported through another experimental procedure. For example, relatively low ductility determined at one group of specimens using tensile tests can be explained and supported by estimating porosity type and fraction on those specimen groups. Furthermore, observed hardness results can be explained by investigating the resultant microstructure. Therefore, the characteristic microstructure of the PBF-LB alloy in its as-built state and the effects of annealing heat treatment will be described. The porosity fraction and their type will be reported for different combinations of PBF-LB process parameters. The influence of PBF-LB process parameters on mechanical properties at different scales will be reported, along with corresponding models and statistical analysis. Fracture surfaces will be analyzed to provide an insight into the nature and cause of failure. Lastly, the mechanical behavior of lattice specimens will be investigated through tensile tests. Their mechanical properties and the global failure mode of the considered BCC lattice structure will be provided.

### 4.1. Microstructure

When considering microstructure, titanium alloys are often classified into  $\alpha$ , near- $\alpha$ ,  $\alpha + \beta$ ,  $\beta$ , or metastable  $\beta$  categories [155]. The Ti6Al4V alloy, which is particularly significant in this thesis, is an  $\alpha + \beta$  alloy. It contains Al and V as alloying elements, and each is added to stabilize different phases: Al stabilizes the  $\alpha$  phase, while V stabilizes the  $\beta$  phase [155]. In titanium alloys, the  $\alpha$  and  $\alpha'$  phases have a hexagonal close-packed (HCP) structure,

whereas the  $\beta$  phase has a body-centered cubic (BCC) structure [58].

In the as-built state, the PBF-LB Ti6Al4V alloy predominantly exhibits an  $\alpha'$  phase within columnar prior- $\beta$  grains, which grow along the build direction (see Figure 4.1a). These columnar prior- $\beta$  grains typically extend over several millimeters and span multiple layers. Their growth is driven by the repeated heat input from the laser beam as it passes through the powder layers above. The rapid cooling inherent to the PBF-LB process induces the formation of the  $\alpha'$  phase within the columnar prior- $\beta$  grains. This  $\alpha'$  phase contributes to the alloy's high yield and ultimate tensile strength (exceeding 1000 MPa), high hardness, and relatively low ductility (less than 10%) [6, 29].

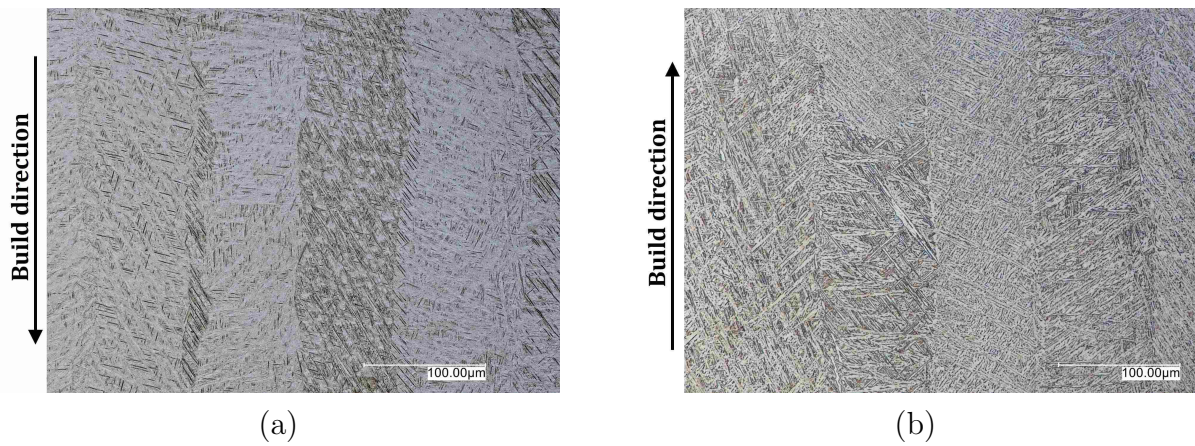


**Figure 4.1:** Microstructure of PBF-LB Ti6Al4V alloy in: (a) as-built and, (b) annealed condition.

Annealing heat treatment at 840°C for 2 hours, followed by furnace cooling, transforms the microstructure from a dominant  $\alpha'$  phase to fine  $\alpha + \beta$  laths (see Figure 4.1b). Although the columnar prior- $\beta$  grains remain present, the microstructure inside them consists mainly of fine  $\alpha + \beta$  laths. This new microstructure slightly reduces yield strength, ultimate tensile strength, and hardness while increasing ductility.

## 4.2. Porosity Estimation

The porosities, voids, and other microstructural defects inherent to the PBF-LB process represent important factors influencing the mechanical performance of components. Therefore, it is important to reduce them as much as possible by optimizing the PBF-LB process. The results of the PBF-LB Ti6Al4V alloy density and porosity are summarised in Table 4.1, and correspond to different specimen groups produced using different laser power - scan-



ning speed combinations. Porosity values measured using Archimedes' method indicate that slightly higher values with the utilized laser power of 250 W are present when compared to other laser power levels. Maximum porosity values were found on specimens manufactured with a 250 W laser power level. Since porosity measurements were performed only at the subtracted material volume from the grip section of the specimen, values listed in Table 4.1 do not represent the porosity of the whole specimen. In addition, Archimedes' method overestimates the porosity values of the PBF-LB metallic when compared to X-ray Computed Tomography or 2D optical analysis [73, 152], making the reported values in Table 4.1 relatively high. Therefore, the measured porosity values using Archimedes' method were only used for the relative comparison of porosity proportions and interpretation of results between distinct groups of specimens. It is worth noting that the specimens were not subjected to tensile nor compressive stress at the grip sections during the tensile test due to the specific design of utilized self-aligning grips. Hence, the potential change in density caused by plastic deformation that occurs during gripping and tensile testing of specimens was eliminated.

**Table 4.1:** *The average relative density and calculated porosity values with corresponding standard deviations.*

$P$ , W	$v$ , mm/s	Sample ID	Average density, g/cm <sup>3</sup>	COV, %	Porosity, %	COV, %
200	1000	A	4.325 (0.005)	0.116	2.40 (0.12)	5
	1250	B	4.327 (0.004)	0.092	2.38 (0.09)	3.78
	1500	C	4.325 (0.003)	0.069	2.42 (0.06)	2.48
225	1000	D	4.323 (0.005)	0.116	2.46 (0.11)	4.47
	1250	E	4.325 (0.002)	0.046	2.42 (0.04)	1.65
	1500	F	4.326 (0.003)	0.069	2.40 (0.07)	2.92
250	1000	G	4.316 (0.003)	0.07	2.62 (0.06)	2.29
	1250	H	4.318 (0.003)	0.069	2.58 (0.06)	2.33
	1500	I	4.316 (0.002)	0.046	2.62 (0.04)	1.53

Notes: The theoretical density of Ti6Al4V alloy:  $\rho_t = 4.432$  g/cm<sup>3</sup> [15]. Reported results are expressed in the following form: mean value (standard deviation). COV represents the coefficient of variation.

Accumulation of voids occurred close to the specimen's side surfaces. This is related to the unfavorable fusion conditions at the starting and ending positions of the laser scan vectors used in the PBF-LB process. Figure 4.2a shows a cluster of spherical voids near the side surface of the specimen produced using the highest energy density within this work (111.1 J/mm<sup>3</sup>) by applying laser power of 250 W and 1000 mm/s scanning speed. Interconnected voids that form one cavity longer than 0.5 mm can be seen in Figure 4.2b and belong

to the specimen manufactured using the energy density of  $66.7 \text{ J/mm}^3$  by applying laser power of 225 W and 1500 mm/s scanning speed. Inside the long cavity, unmelted Ti6Al4V powder particles can be seen, the appearance of which is attributed to the unfavorable fusion conditions that occur at the laser fusion starting and ending positions during the PBF-LB process. Kasperovich et al. related energy density to different types of void defects and found that the application of excessive energy density leads to spherical voids with a diameter of  $>50 \mu\text{m}$ , while insufficient energy densities cause the formation of narrow and elongated crack-like voids oriented perpendicular to the build direction indicating the lack-of-fusion [51]. However, these findings cannot be applied to interpret mechanisms responsible for the formation of voids located close to the specimen surfaces due to unfavorable fusion conditions specific for those regions. In this work, spherical voids and narrow elongated voids were found close to the side surfaces of specimens manufactured using similar energy densities (i.e.,  $71.1$  and  $74.1 \text{ J/mm}^3$ ) achieved by different  $P$  and  $v$  combinations. Narrow and elongated voids (Figure 4.2c) were found close to the surface of specimen produced using energy density of  $71.1 \text{ J/mm}^3$  ( $P = 200 \text{ W}$  and  $v = 1250 \text{ mm/s}$ ), while spherical voids (Figure 4.2d) were found close to the surface of the specimen produced using the energy density of  $74.1 \text{ J/mm}^3$  ( $P = 250 \text{ W}$  and  $v = 1500 \text{ mm/s}$ ).

These voids formed close to the side surfaces, together with surface defects, are stress concentrators that act as potential crack initiation sites [156]. The specimens in this study exhibited different void types within their microstructure caused by unfavorable fusion conditions at locations close to the side surfaces.

### 4.3. Mechanical Properties of PBF-LB Ti6Al4V Alloy

In order to ensure the reliable, safe, and efficient application of PBF-LB components, the mechanical properties of the material they are made should be determined, mainly as these properties can be influenced by process parameters. Mechanical properties of PBF-LB Ti6Al4V alloy determined using tensile tests are reported in Table 4.2 along with PBF-LB process parameters used to produce test specimens. It is important to note that  $G$  was calculated using equation (3-23), assuming isotropic behavior of the PBF-LB Ti6Al4V alloy. The Poisson's ratio and Young's modulus used in this calculation were determined using the GOM ARAMIS adjustable 2D/3D 12M system. The ductile behavior in the plastic region has been observed on all specimens, as can be seen in Figure 4.3a. Moreover, the high strain

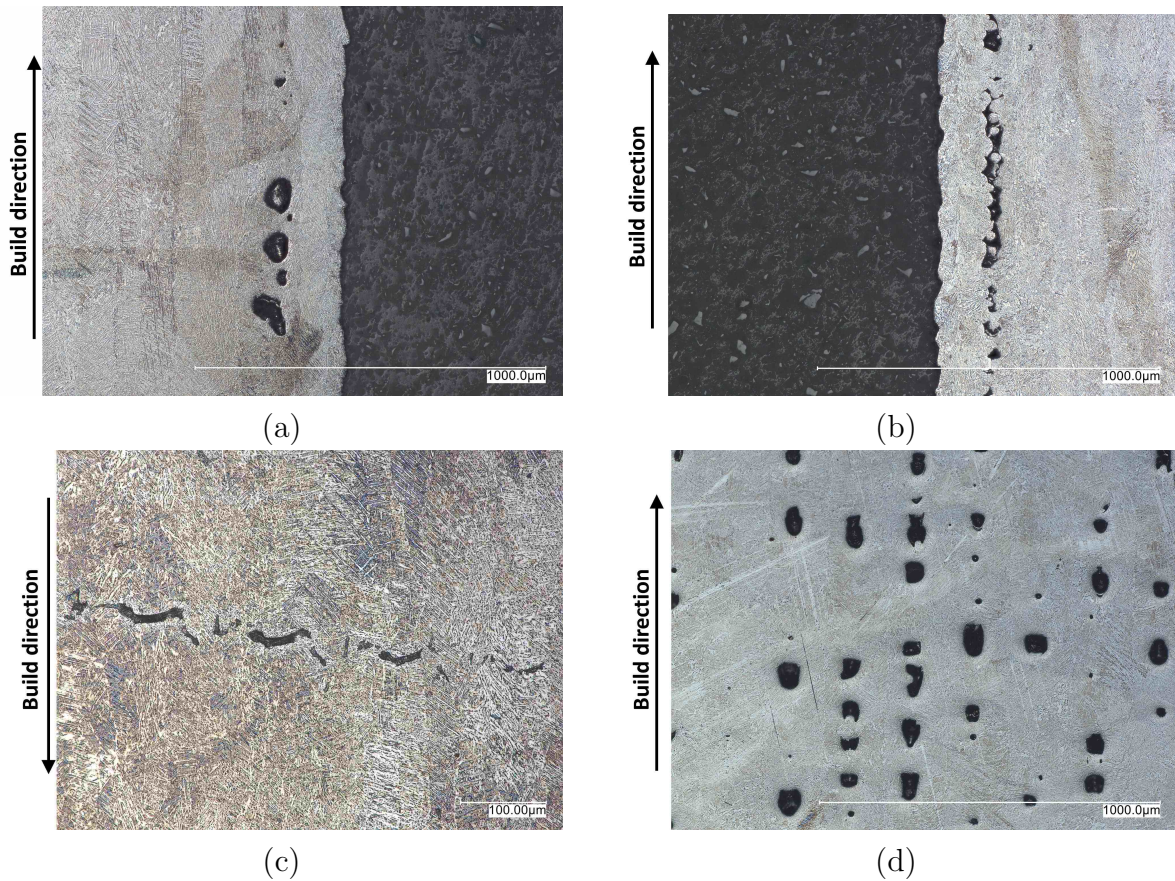


**Figure 4.2:** Different void defects found close to the side surface of specimens manufactured using the: (a)  $E_V$  of  $111.1 \text{ J/mm}^3$  ( $P = 250 \text{ W}$  and  $v = 1000 \text{ mm/s}$ ) caused formation of spherical voids, (b)  $E_V$  of  $66.7 \text{ J/mm}^3$  ( $P = 225 \text{ W}$  and  $v = 1500 \text{ mm/s}$ ) caused interconnected voids with entrapped powder particles, (c)  $E_V$  of  $71.1 \text{ J/mm}^3$  ( $P = 200 \text{ W}$  and  $v = 1250 \text{ mm/s}$ ) caused formation of elongated and narrow voids, (d)  $E_V$  of  $74.1 \text{ J/mm}^3$  ( $P = 250 \text{ W}$  and  $v = 1500 \text{ mm/s}$ ) caused formation of spherical voids.

field was located inside the gauge length on each specimen prior to the failure, in a similar manner as shown in Figure 4.3b. The highest elongation at break values of 12.7% (std. 0.4 %) were found on specimens manufactured using the laser power of 200 W and 1250 mm/s scanning speed, while the lowest values of 10% (std. 1%) were found on specimens manufactured using laser power of 250 W and 1000 mm/s scanning speed. In this case, the differences in elongation at break values are quite small to be relevant for distinguishing different specimen groups from each other based on those results.

Although the measured porosity values using Archimedes' method were higher than 2%, the measured elongation at break values are typical for PBF-LB Ti6Al4V alloy in the annealed condition and comparable with previously published results [157]. The ability to withstand high plastic deformations during loading (i.e., elongation at break) is one of the most important properties of the PBF-LB materials. However, that material property is

**Table 4.2:** Mechanical properties of PBF-LB Ti6Al4V alloy determined using tensile tests.

PBF-LB process parameters				Mechanical properties					
$P, W$	$v, \text{mm/s}$	$E_V, \text{J/mm}^3$	ID	$R_{p0.2}, \text{MPa}$	$R_m, \text{MPa}$	$E, \text{GPa}$	$G, \text{GPa}$	$\nu, -$	El. at break, %
200	1000	88.9	A	943 (13)	983 (11)	109 (2)	41.8 (0.9)	0.308 (0.006)	10.5 (0.7)
	1250	71.1	B	944 (14)	975 (21)	108.9 (0.9)	41.5 (0.4)	0.313 (0.008)	12.7 (0.4)
	1500	59.3	C	943 (1)	977 (2)	109 (3)	42 (1)	0.30 (0.02)	12 (1)
225	1000	100	D	953 (17)	994 (11)	111.3 (0.6)	42.5 (0.2)	0.310 (0.004)	11 (1)
	1250	80	E	972 (14)	1003 (11)	111 (1)	42.7 (0.4)	0.305 (0.004)	11 (2)
	1500	66.7	F	962 (8)	997 (14)	115 (1)	44.1 (0.3)	0.302 (0.007)	11 (1)
250	1000	111.1	G	950 (8)	1001 (5)	109 (2)	42 (1)	0.29 (0.01)	10 (1)
	1250	88.9	H	952 (8)	1001 (3)	113 (1)	43 (1)	0.30 (0.02)	11.3 (0.9)
	1500	74.1	I	924 (9)	981 (7)	110.3 (0.9)	42.7 (0.4)	0.293 (0.009)	10.8 (0.9)

Notes: Results are expressed in the following form: mean value (standard deviation). Total of three specimens ( $n = 3$ ) were tested from each group of specimens.

quite limited in the case of PBF-LB Ti6Al4V alloy, which exhibits dominant  $\alpha'$  phase in as-built state and  $\alpha + \beta$  laths after the annealing heat treatment [29, 157].

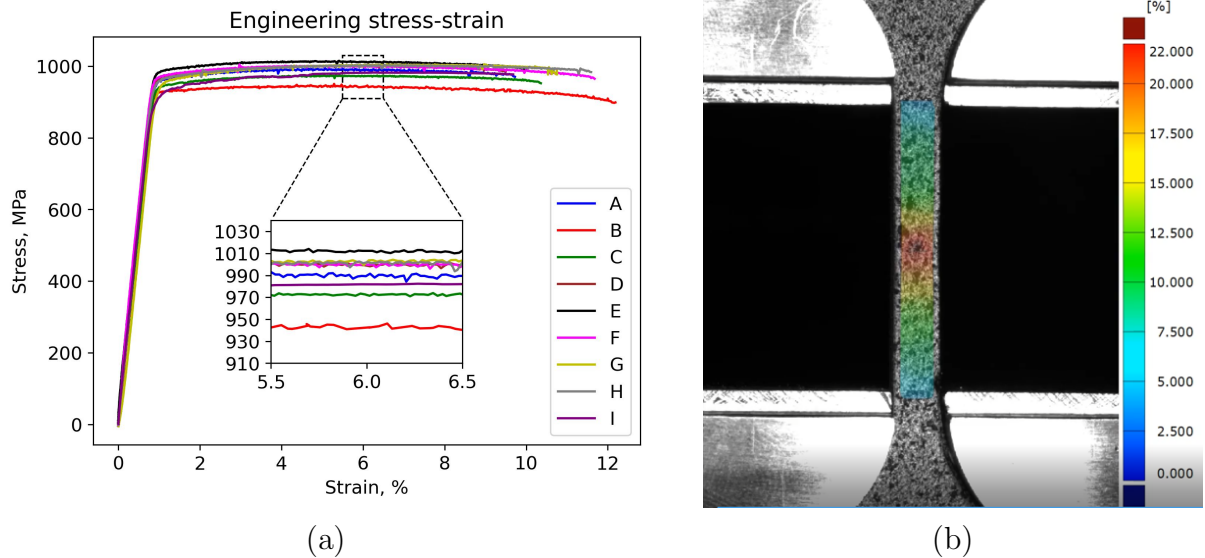


**Figure 4.3:** Typical mechanical response: (a) Engineering stress – strain curves with pronounced plastic deformation characteristic to each group of specimens, (b) Local high strain field formed at the midpoint of gauge section - specimen from B group.

The obtained values of mechanical properties were first individually evaluated with respect to specimen position using the Kruskal-Wallis rank sum test, as most of the groups had a non-normal distribution of data. The effect of position on mechanical properties can be seen in Figure 4.4 as well. Levene’s test has shown that all specimen groups have equal variances of mechanical properties, as in each case, the calculated  $p$ -values were higher than 0.05 (see Table A11). The calculated  $p$ -values using the Kruskal-Wallis test were significantly higher than 0.05 for all observations except for the elongation at break values measured

at position 1 (see Table A11). However, the difference between the observed positions is relatively small to be of practical relevance for engineering applications. Nevertheless, this occurrence should be further investigated in more detail using a higher number of specimens. Further regression models for mechanical properties will be developed using only  $P$  and  $v$  as predictor variables since position showed no effect on  $R_{p0.2}$ ,  $R_m$ ,  $\nu$ ,  $E$ , and  $G$ .

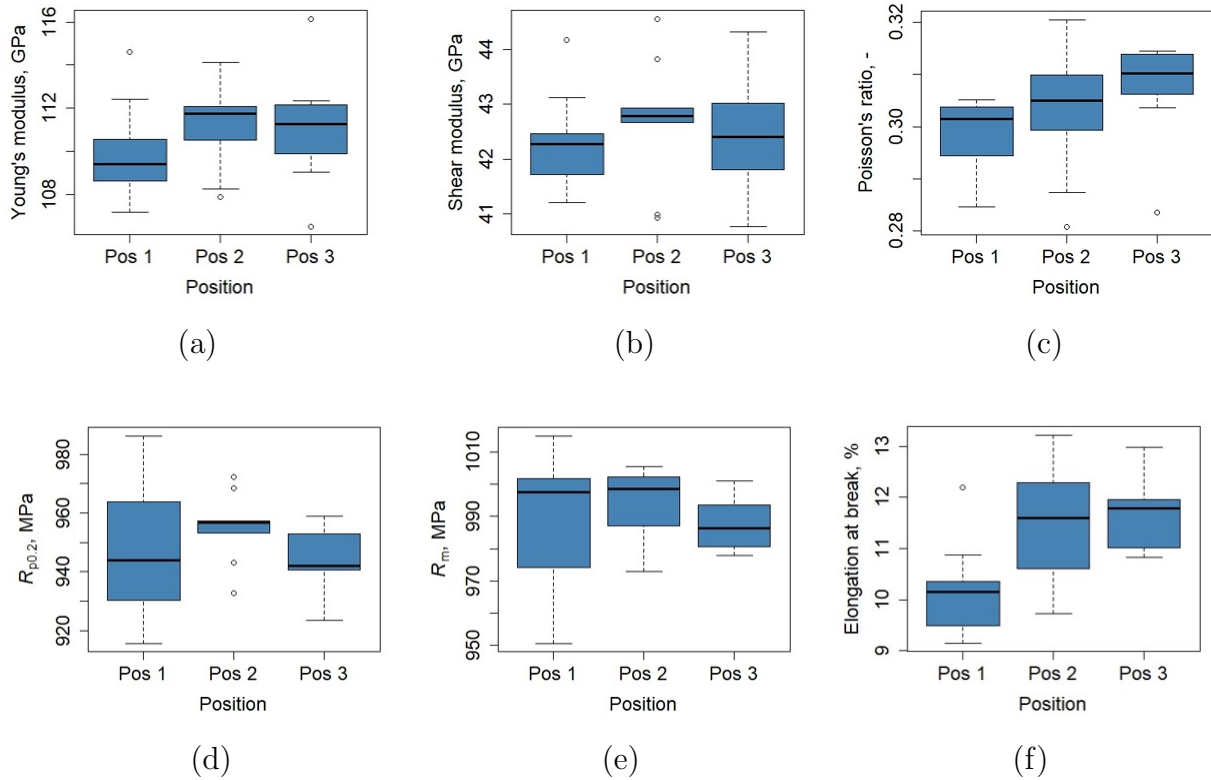


**Figure 4.4:** Distributions across different positions for: (a) Young's modulus, (b) shear modulus, (c) Poisson's ratio, (d)  $R_{p0.2}$ , (e)  $R_m$ , (f) elongation at break (the corresponding specimen positions are detailed in Table 3.3 and illustrated in Figure 3.4a).

The influence of  $P$  and  $v$  on prediction variables has been identified and described using empirical models since the exact relationship between prediction variables (i.e., mechanical properties) and predictor variables (laser power  $P$  and scanning speed  $v$ ) is unknown due to the complex nature of the Ti6Al4V (ELI) alloy manufactured using PBF-LB technology. Due to low  $R^2$  and adjusted  $R^2$  values, developed regression models cannot be efficiently used for the prediction of mechanical properties. However, they can be used to better understand the influence of  $P$  and  $v$  on the mechanical properties of PBF-LB Ti6Al4V alloy. Using these models, it has been investigated which predictor has a more dominant effect on the mechanical properties reported in Table 4.2.

Furthermore, these models give insight into to what extent and with what confidence ta-

iloring of mechanical properties is possible by changing only the  $P$  and  $v$  values in previously stated ranges (i.e., 200 – 250 W and 1000 – 1500 mm/s), ensuring the manufacturability of parts.

### 4.3.1. Young’s modulus and shear modulus

Young’s modulus values of the Ti6Al4V alloy manufactured using different AM technologies and heat treatments are widely reported in the literature [6, 78, 158]. However, the regression models that describe the influence of  $P$  and  $v$  on Young’s modulus of PBF-LB Ti6Al4V alloy are thus far rarely reported. By testing models reported in Table 4.3 using ANOVA procedure, it was found that model M1 does not have a significantly better fit than model M2 ( $p$ -value = 0.223). More specifically,  $P$  is a more dominant predictor than  $v$  when modeling of  $E$  is required as can be seen in Table A1. Both models have a homoscedastic variance of the error term and normally distributed studentized residuals ( $p$ -value > 0.05 in all cases), see Table 4.3.<sup>1</sup>

**Table 4.3:** Regression models for Young’s modulus and their statistical properties [159].

Model	Young’s modulus ( $E$ )	$R^2$	Adj. $R^2$	$p$ -value (NCV)	$p$ -value (S-W)
M1	$E = -4.2604P^2 - 0.0055v^2 + 1856.7874P + 1.0876v + 0.071Pv - 1.02 \times 10^5$	0.453	0.322	0.793	0.212
M2	$E = 0.0585P^2 + 1.078 \times 10^5$	0.291	0.262	0.817	0.690

As can be seen in Figure 4.5a, the  $P$  has more dominant influence on the Young’s modulus, as the curvature of the response surface is more pronounced along  $P$  axis. The highest mean value of Young’s modulus, i.e., 115 GPa (std. 1 GPa), was found on specimen group manufactured using 225 W laser power and 1500 mm/s scanning speed. The lowest mean value of Young’s modulus, i.e., 108.9 GPa (std. 0.9 GPa), was found on the group of specimens manufactured using the laser power of 250 W and the scanning speed of 1250 mm/s.

For different applied heat treatments, Vrancken et al. reported Young’s modulus values in ranges from  $112 \pm 3.4$  GPa to  $115.5 \pm 2.4$  GPa [6]. Hence, the applied heat treatments also do not affect the Young’s modulus values. If specific Young’s modulus or stiffness values

<sup>1</sup>The results in this section are derived from the work published by the author and collaborators in conference proceedings [159]. This publication was created to fulfill the requirements of a doctoral study at the Faculty of Engineering, University of Rijeka, Croatia. The publication contains relevant content that has been cited and incorporated into this section.

for the PBF-LB components are required, then an integration of the unit cells with targeted sizes and types should be considered in the early product design phase.

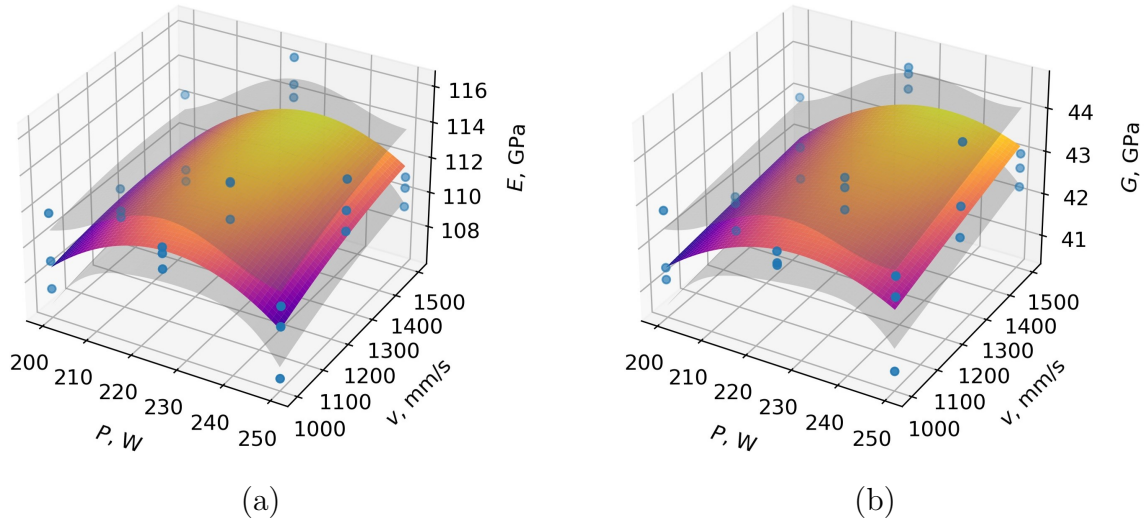


**Figure 4.5:** Response surfaces with added 95% confidence intervals visible as grey surfaces representing the influence of  $P$  and  $v$  on the: (a) Young's modulus prediction variable, (b) Shear modulus prediction variable.

The confrontation of the two considered models used to model the effect of  $P$  and  $v$  on shear modulus (M3 and M4), did not reveal a statistically significant difference in their fitting performances ( $p$ -value = 0.283). In this case, too,  $P$  has stronger influence on the shear modulus than the scanning speed (see Table A2). This can be visualized in Figure 4.5b by comparing the curvature of the response surface along  $P$  and  $v$  axis. Both models have homoscedastic variance of error term ( $p$ -value > 0.05 in both cases) and normally distributed studentized residuals Table 4.4. The highest mean value of the shear modulus was calculated for the same group of specimens (F group), as was the case with Young's modulus. The lowest reported mean value of the shear modulus was found in the same group of specimens (B group), as was the case with Young's modulus. However, the differences between measured Young's modulus values, as well as the differences between shear modulus values, are too small to be considered relevant for engineering applications. This implies that the side surface roughness can be customized within the  $P$  and  $v$  range without negatively affecting Young's modulus and shear modulus values.

For the Ti6Al4V alloy manufactured using a blended elemental powder metallurgy process, subjected to different heat treatment procedures, shear modules were in the range between 40.4 GPa and 44.8 GPa [160]. Tevet et al. in their work reported shear modulus

**Table 4.4:** Regression models for shear modulus and their statistical properties.

Model	Shear modulus ( $G$ )	$R^2$	Adj. $R^2$	$p$ -value (NCV)	$p$ -value (S-W)
M3	$G = -1.4172P^2 - 0.0002v^2 + 628.0671P - 3.2483v + 0.0231Pv - 2.863 \times 10^4$	0.447	0.316	0.731	0.495
M4	$G = -1.4172P^2 + 656.9763P - 3.299 \times 10^4$	0.340	0.285	0.628	0.221

values for PBF-LB Ti6Al4V alloy, measured using dynamic ultrasonic technique for three different propagating directions, to be 43.65, 43.63, and 43.73 GPa [78]. These values are consistent with the results shown in Figure 4.5b.

### 4.3.2. Offset Yield Strength and Ultimate Tensile Strength

The influence of  $P$  and  $v$  on the offset yield strength ( $R_{p0.2}$ ) has been described and evaluated using two regression models, M5 and M6, as stated in Table 4.5 Model M5 has higher  $R^2$  and adjusted  $R^2$  values, which implies that this model has better fitting performance than model M6. However, model M5 has a higher complexity than model M6.

The confrontation of the two proposed models against each other using the ANOVA procedure did not reveal a statistically significant difference in their fitting performances ( $p$ -value = 0.053), though it is close to the specified significance level of 0.05. If higher modeling precision is desired, it can be achieved using model M5, where  $R^2$  is 0.549. Both models have a homoscedastic variance of the error term ( $p$ -value > 0.05 in both cases), which is confirmed using the NCV test, see Table 4.5. Furthermore, both models have normally distributed studentized residuals since  $p$ -values determined using the S-W test are, in both cases, larger than 0.05. Therefore, the use of the OLS regression method for modeling  $R_{p0.2}$  is valid as well.

**Table 4.5:** Regression models for  $R_{p0.2}$  and their statistical properties.

Model	$R_{p0.2}$	$R^2$	Adj. $R^2$	$p$ -value (NCV)	$p$ -value (S-W)
M5	$R_{p0.2} = -0.0315P^2 - 0.00016v^2 + 15.4379P + 0.6329v - 0.001Pv - 1153.2247$	0.549	0.442	0.337	0.202
M6	$R_{p0.2} = -0.0315P^2 + 14.1408P - 625.588$	0.354	0.301	0.725	0.459

When the same ANOVA procedure is applied to model M7 and M8, the result ( $p$ -value = 0.288) implies that model M7 does not have a better fit than model M8. In this case too, predictor variable  $P$  has a stronger effect on the ultimate tensile strength ( $R_m$ ) than predictor variable  $v$  (see Table A4). Both models have a homoscedastic variance of the error



term ( $p$ -value  $> 0.05$  in both cases), as can be seen in Table 4.6. However, only the M8 model has normally distributed studentized residuals, as the  $p$ -value determined by S-W test is larger than 0.05 for this model. Therefore, model M8 has more advantage over model M7 when the interpretation of  $R_m$  is needed inside  $P$  and  $v$  intervals considered within DoE.

**Table 4.6:** Regression models for  $R_m$  and their statistical properties.

Model	$R_m$	$R^2$	Adj. $R^2$	$p$ -value (NCV)	$p$ -value (S-W)
M7	$R_m = -0.019P^2 - 6.926 \times 10^{-5}v^2 + 9.5618P + 0.2865v - 0.0006Pv - 280.0222$	0.478	0.354	0.407	0.008
M8	$R_m = -0.0190P^2 + 8.8539P - 33.6410$	0.378	0.327	0.683	0.076

Both  $R_{p0.2}$  and  $R_m$  variables reaches their maximum values when  $P = 225$  W and  $v = 1250$  mm/s were used in PBF-LB process (Figure 4.6). In general,  $R_{p0.2}$  values for PBF-LB Ti6Al4V alloy are in range between 924 MPa (std. 9 MPa) and 972 MPa (std. 14 MPa) when different combinations of  $P$  and  $v$  are used in ranges between 200 – 250 W and 1000 – 1500 mm/s, respectively.  $R_m$  values are in range between 975 MPa (std. 21 MPa) and 1003 MPa (std. 11 MPa). Interestingly,  $P$  and  $v$  have shown a higher influence on  $R_{p0.2}$  (Figure 4.6a) than on  $R_m$  (Figure 4.6b) prediction variable. This can be visualized by comparing the response surface curvatures shown in Figure 4.6a and 4.6b. The curvature of  $R_{p0.2}$  response surface is more pronounced than the curvature of  $R_m$  response surface. Therefore, by changing  $P$  and  $v$  in ranges considered within this DoE, it is possible to influence  $R_{p0.2}$  slightly more than  $R_m$ . However, the differences in measured  $R_{p0.2}$  and  $R_m$  values are too small to be relevant for engineering applications. It implies that considered  $P$  and  $v$  range can be used for achieving desired side surface roughness without adversely affect  $R_{p0.2}$  and  $R_m$ .

By applying different heat treatments, Vrancken et al. managed to achieve  $R_{p0.2}$  and  $R_m$  values in ranges from  $760 \pm 19$  MPa to  $1118 \pm 39$  MPa, and  $874 \pm 23$  MPa to  $1223 \pm 52$  MPa respectively [6]. When those values are compared with values of  $R_{p0.2}$  and  $R_m$  reported in Figure 4.6a and 4.6b, it is evident that  $R_{p0.2}$  and  $R_m$  can be influenced to a larger extent by applying adequate heat treatment than controlling  $P$  and  $v$  in the ranges specified within this research. By changing  $P$  and  $v$  in ranges specified within DoE, the differences between  $R_m$  values are within statistical uncertainty. Surely, if specific combinations of PBF-LB process parameters are used which cause incomplete melting or unstable PBF-LB process, mechanical properties, and consequently  $R_{p0.2}$  and  $R_m$ , can be substantially

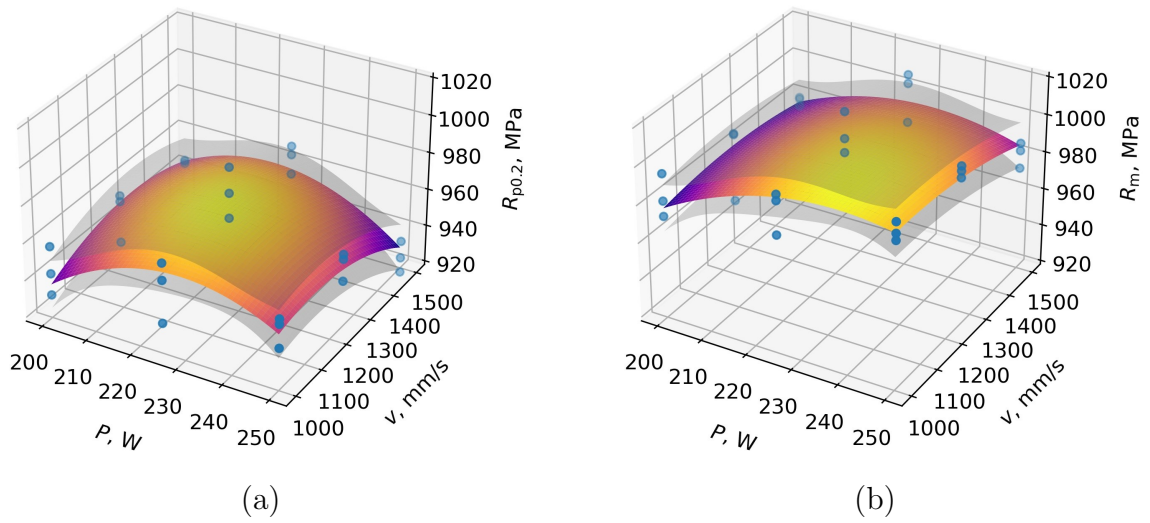


**Figure 4.6:** Response surfaces with added 95% confidence intervals visible as grey surfaces representing the influence of  $P$  and  $v$  on the: (a)  $R_{p0.2}$  prediction variable, (b)  $R_m$  prediction variable.

reduced. However, this could adversely affect the structural integrity of components. In that case, advantage should be given to architected materials (metamaterials, scaffolds or lattice structures) which opens the possibility for tailoring of mechanical properties as shown in [19]. In this way, the adequate combination of PBF-LB process parameters should be used, which ensures the manufacturability of architected materials and reduces undesired defects inside material microstructure, which usually cause premature and unexpected failure of components.

### 4.3.3. Poisson's ratio

Experimental results regarding the Poisson's ratio of the PBF-LB Ti6Al4V alloy are limited in scope even for a single utilized combination of PBF-LB process parameters and even more incomprehensible and scarcely reported when the influence of different PBF-LB process parameter combinations is the subject of research.

The confrontation of models reported in Table 4.7 showed that model M9 does not have a better fit ( $p$ -value = 0.579). Therefore, the influence of  $P$  and  $v$  on Poisson's ratio can be described with equal proficiency using only  $P$  as a predictor variable (see Table A5). The  $R^2$  and adj.  $R^2$  values are low in this case due to the relatively high data scatter of measured Poisson's ratios at observed groups of specimens. However, both models have a homoscedastic variance of the error term and normally distributed studentized residuals

( $p$ -value  $> 0.05$  in every case), which justifies their validity from the statistical point of view.

**Table 4.7:** Regression models for Poisson's ratio and their statistical properties.

Model	Poissons' ratio ( $\nu$ )	$R^2$	Adj. $R^2$	$p$ -value (NCV)	$p$ -value (S-W)
M9	$\nu = -6.419 \times 10^{-6}P^2 - 6.206 \times 10^{-8}v^2 + 0.0026P + 0.0001v + 1.266 \times 10^{-7}Pv - 0.0457$	0.342	0.186	0.312	0.472
M10	$\nu = -2.563 \times 10^{-4}P + 0.361$	0.250	0.220	0.940	0.144

The effect of  $P$  and  $v$  on the Poisson's ratio is shown in Figure 4.7a using model M9. It is evident that  $P$  influences the Poisson's ratio slightly more than  $v$ , as the curvature of the response surface is more pronounced along  $P$  axis. Therefore, the change in the utilized laser power levels in the range from 200 to 250 W resulted in the mean values of Poisson's ratios between 0.313 (std. 0.008) and 0.293 (std. 0.009), respectively. The low values of Poisson's ratios measured on specimens manufactured using the high laser power values occur presumably due to a higher fraction of entrapped porosities inside the material's microstructure (see section **Porosity Estimation**). Consequently, a higher proportion of porosities entrapped inside the material's microstructure cause a reduction in Poisson's ratio as demonstrated in [161].

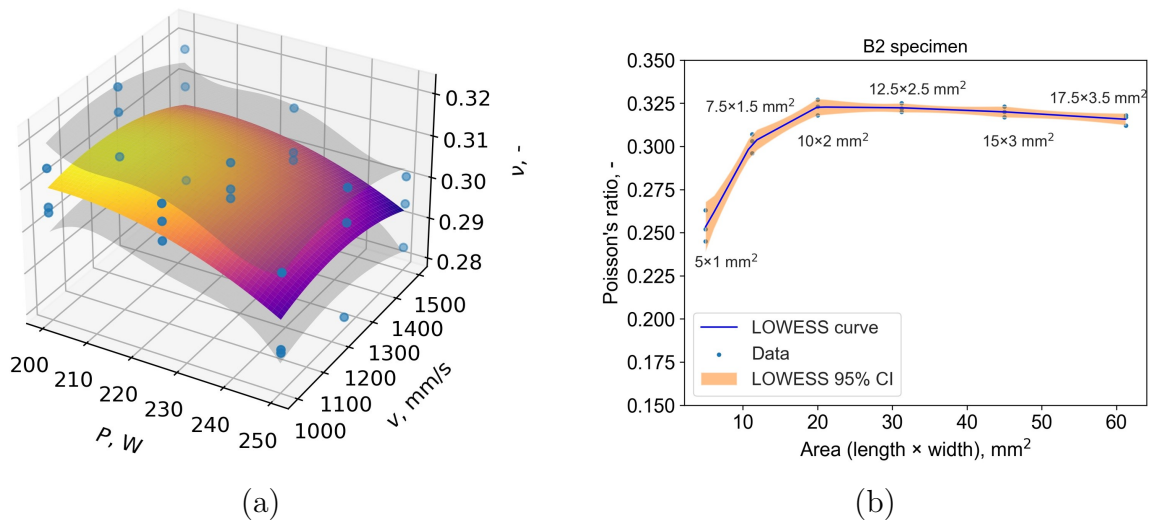


**Figure 4.7:** Poisson's ratio in function of the: (a) Utilized PBF-LB  $P$  and  $v$  levels with superimposed 95% confidence intervals visible as grey surfaces, (b) Length and width of the measurement area in ratio 5:1.

Pantawane et al., in their work, measured dynamic Poisson's ratio of a wrought and PBF-LB Ti6Al4V alloy using ultrasound technique to be  $0.28 \pm 0.0005$  and  $0.3 \pm 0.003$ , respectively [162]. In general,  $\alpha + \beta$  microstructures present in wrought Ti6Al4V alloy are

characteristic by lower Poisson's ratios when compared to the  $\alpha'$  microstructure present after the heat treatment followed by quenching [160], or in this case after the PBF-LB process. Since PBF-LB is often used to produce thin-walled components or components with complex topology, experimental testing should be as well carried out on specimens with relevant size. However, it is challenging to perform uniaxial tensile tests with high confidence on such small specimens, and reliably determine Poisson's ratio. Therefore, an additional sensitivity analysis was performed on one specimen, analysing different gauge lengths and widths by maintaining the same length to width ratio (5:1) and results are shown in the Figure 4.7b. When the measurement areas larger than  $10 \times 2 \text{ mm}^2$  were used, a slight negative trend of Poisson's ratio is present. At measurement areas smaller than  $10 \times 2 \text{ mm}^2$  a substantial decrease in Poisson's ratio with a decrease in measurement area is present, which is expected. Furthermore, at measurement areas smaller than  $10 \times 2 \text{ mm}^2$ , the resolution of the DIC equipment used has a significant role as higher data scatter is pronounced due to the small measurement area.

#### 4.3.4. Fracture surfaces

Characteristic fracture surfaces obtained from different specimen groups are shown in Figure 4.8. In each case, the plateau was formed in the inner part of the specimen, and shear surfaces were found in the outer part of the specimen. This occurrence represents a ductile-brittle (mix mode) failure [163], achieved by annealing heat treatment. In the case of pure brittle failure, the tensile fracture surfaces should be flat, which is characteristic of PBF-LB Ti6Al4V alloy in the as-built state, with a dominant  $\alpha'$  phase [74]. On the other hand, when a pure ductile failure occurs, fracture surfaces are characterized by shear surfaces in the outer part of the specimen and homogeneous spongy structures in the inner part of the specimen [73]. In the case of PBF-LB Ti6Al4V alloy homogeneous spongy structure can be achieved by applying proper heat treatments with high holding temperatures (900 °C or higher) or by applying hot isostatic pressing (HIP) treatments [73].

Spherical voids formed due to unfavorable fusion conditions that occur close to the specimen's side surfaces are present and visible in the highest fraction at specimen G1, shown in Figure 4.8. These voids, located in the dashed red square, act as crack initiation sites. This resulted in a symmetrical fracture surface concerning the longer axis of the specimen's cross-section. In all cases, the plateau regions spread from locations close to the side sur-

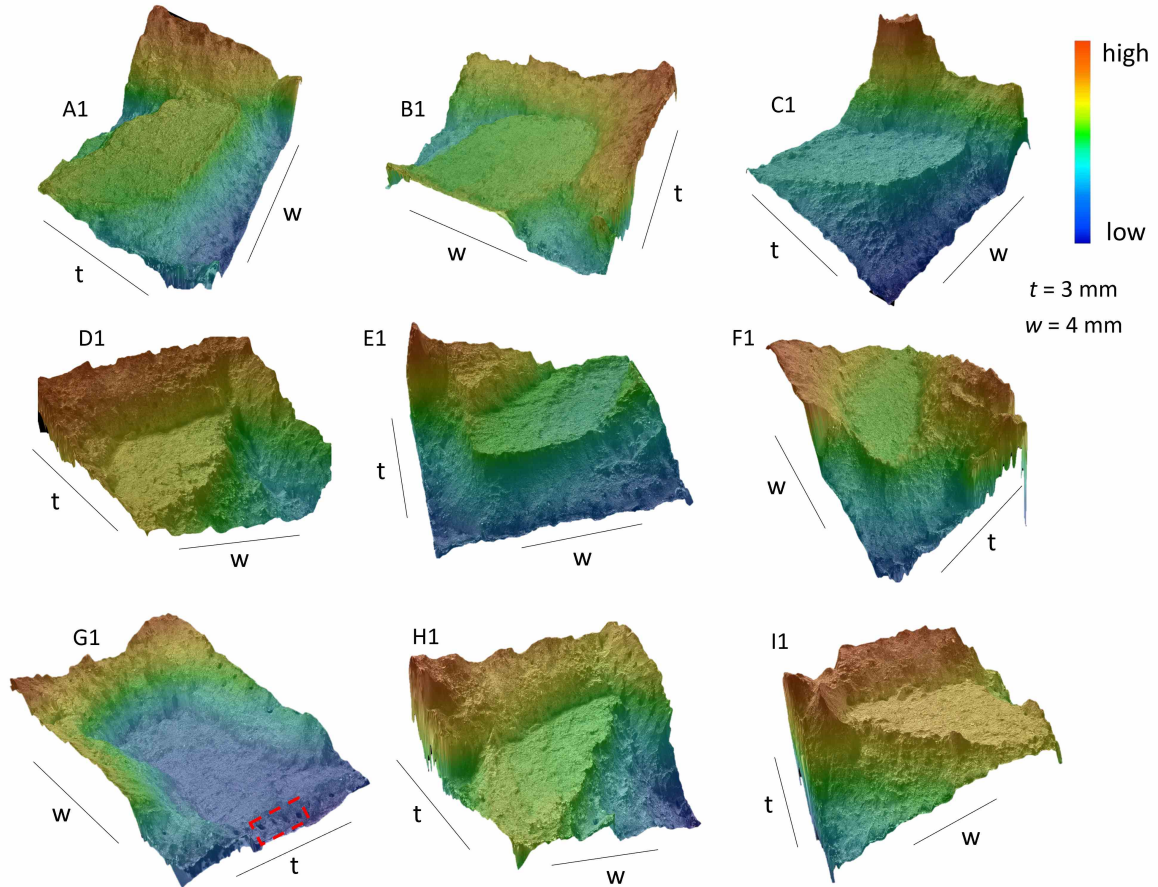


**Figure 4.8:** Fracture surfaces with pronounced plateau region in the inner section and shear surfaces in the outer section, consistently observed across all specimen groups .

faces, where crack nuclei sites occur presumably due to defects located near the specimen's surface or due to surface imperfections characteristic of the PBF-LB process.

#### 4.4. Low-force Vickers Hardness

In order to provide additional insights from a different perspective, particularly when interpreting mechanical properties at the macro-scale and nano-scale, hardness was measured at the micro-scale using the low-force Vickers method. In this way, observations made at the two different scales can be confirmed, and potential anomalies can be identified. In addition, low-force Vickers testing (HV1), in literature often referred to as micro-hardness testing [16], is used to examine the effects of laser power, scanning speed, and annealing on the hardness of the resultant microstructure. Figure 4.9 shows the distribution of HV1 hardness values based on seven measurements within each category. Sample D<sup>ab</sup> was manufactured using

identical process parameters as sample D<sup>an</sup>, with the exception of performing the subsequent annealing heat treatment. Upon comparing the HV1 hardness values of these samples, it becomes evident that the annealing heat treatment process has reduced the HV1 hardness. The Shapiro-Wilk test applied to the HV1 data did not indicate evidence of non-normality. The calculated  $p$ -values for the D<sup>ab</sup> and D<sup>an</sup> specimens were 0.43 and 0.12, respectively. Moreover, there is a notable difference in the mean HV1 values between the as-built (385 HV1, std. 6) and annealed (364 HV1, std. 8) specimens, as indicated by the calculated  $p$ -value using the  $t$ -test being less than 0.001. The reported mean HV1 hardness values of the as-built specimen are in agreement with findings reported in [15, 16]. The reduction in hardness by 21 HV1 after annealing is comparable to the results of Vilaro et al. [60], who reported a decrease of 24-29 HV2 after annealing heat treatments conducted at 800-850°C.

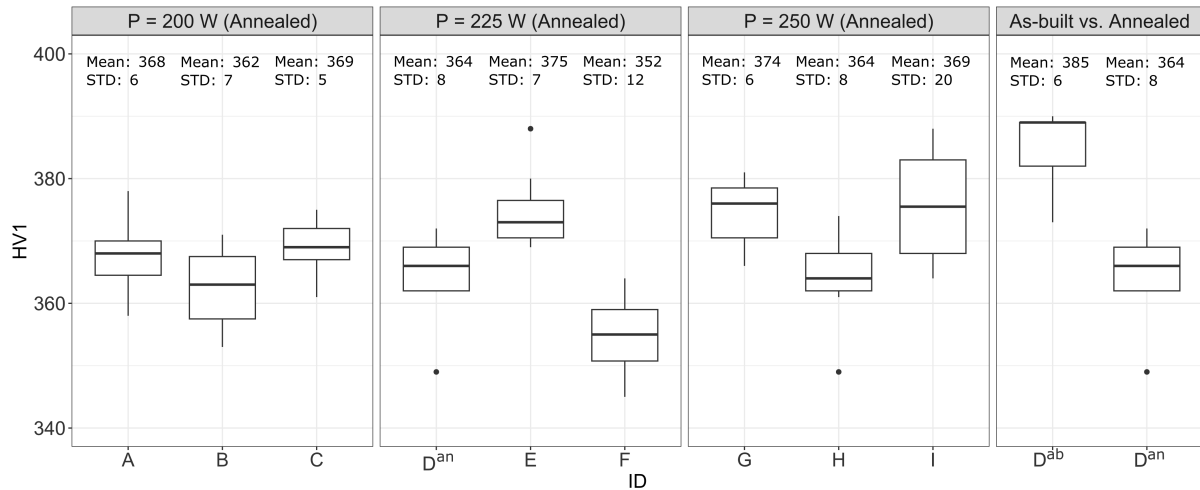


**Figure 4.9:** Distribution of HV1 hardness across specimen groups.

The reduction in hardness is attributed to the annealing heat treatment’s ability to dissolve martensite needles ( $\alpha'$ ) within the microstructure, leading to the dominance of  $\alpha + \beta$  laths. The  $\alpha'$  phase exhibits a higher dislocation density than the  $\alpha$  phase, leading to a higher hardness in comparison to the  $\alpha$  phase. Consequently, the annealed specimen with  $\alpha + \beta$  microstructure exhibits a decrease in hardness compared to the as-built specimen with the dominant  $\alpha'$  phase within its microstructure.

The influence of  $P$  and  $v$  on HV1 hardness values of annealed specimens is unclear, as specimens produced using  $P = 225$  W exhibit a different trend than those produced using  $P$  levels of 200 W and 250 W. The potential influence of  $P$  and  $v$  on HV1 hardness should be further investigated both in as-built and annealed conditions using higher numbers of  $P$  and  $v$  levels.

## 4.5. Nano-mechanical Properties

With the advancement of AM technologies, especially in creating complex, thin-walled, and low-volume structures, reliable determination of their mechanical properties is crucial. However, reliable determination, in that case, is challenging, considering that it should be performed on representative tensile and compressive test specimens with sizes matching the walls of those complex, thin-walled, and low-volume structures. For this purpose, the determination of mechanical properties at the nano-scale using the nanoindentation procedure is beneficial, particularly for titanium and its alloys. Those materials in an as-built state after PBF-LB consist dominantly of a single  $\alpha'$  phase whose features are smaller than the size of the indenter itself. This opens the possibility of determining mechanical properties at the nano-scale, such as, Young's modulus and hardness, and potentially transferring them to the macro-scale in order to describe the material's behavior. However, the nanoindentation method has high sensitivity of to surface imperfections [164], voids [165], tip contamination, and other alterations [166]. As a result, some measurements are expected to differ from the rest significantly. Therefore, it is crucial to use an objective method to detect and eliminate potential outliers from each dataset. Grubbs' test was employed for this purpose on all datasets [135]. Prior to applying Grubbs' test, the normality of the data distribution was verified using the S-W test [135]. Additionally, the potential impact of etching on nano-hardness results was considered, as etching increases the surface roughness of polished samples and could affect measurement accuracy [167]. However, no significant effect of the etchant on the nano-hardness results of as-built specimens was observed (see Table 4.8, likely due to the higher nano-indentation loads and depths used in the experiments. Experimental investigation of the etchant's influence on nano-hardness, combined with the use of statistical tests in data analysis, ensures reliable and meaningful results. To eliminate the potential influence of voids, nanoindentation measurements were taken away from visible surface defects. Each nanoindentation experiment included a high number of repetitions, and Grubbs' test was applied to identify outliers resulting from subsurface defects or other microstructural anomalies. All values reported in this research are presented as mean values with (STD)<sup>2</sup>.

---

<sup>2</sup>The results in this subsection are derived from the work published by the author and collaborators in a peer-reviewed scientific paper [168]. This publication was created to fulfill the requirements of a doctoral study at the Faculty of Engineering, University of Rijeka, Croatia. The publication contains relevant content that has been cited and incorporated into this section.

**Table 4.8:** *The impact of Kroll’s etchant on nano-hardness.*

Surface state	Nano-hardness ( $H$ ), GPa	STD, GPa	COV, %
Not-etched	4.64	0.08	1.7
Etched	4.65	0.13	2.8

#### 4.5.1. Dependence of Nano-mechanical Properties on Indentation Location

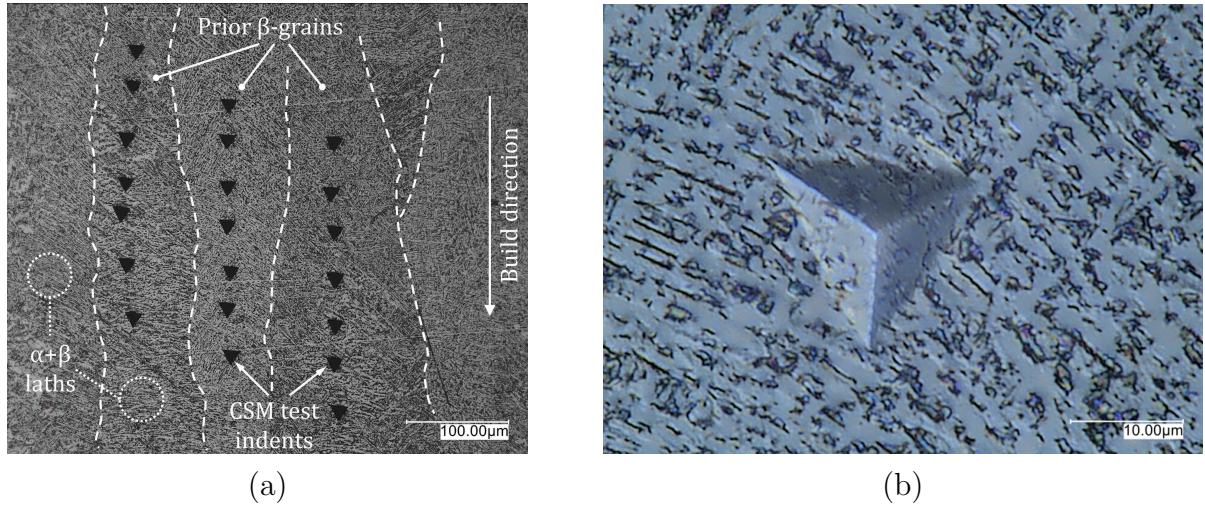
The nanoindentation procedure offers insights into material properties at a local level, which can usually be extrapolated for materials with homogeneous microstructures. However, in many cases involving PBF-LB and PBF-EB technologies, homogeneous microstructures are not achieved due to rapid cooling rates during manufacturing [29]. Moreover, the element partitioning occurs within PBF-LB Ti6Al4V alloy during heat treatment [169], leading to typical local compositional variations. However, it remains uncertain whether these local compositional variations influence the mechanical properties of annealed PBF-LB Ti6Al4V alloy across different testing locations. To address this, nano-mechanical properties were evaluated at five distinct locations (corresponding to five prior- $\beta$  grains), each tested seven times to ensure robustness and reliability. Grubbs’ test was employed to detect and mitigate potential outliers that could negatively affect the results’ representativeness. If microstructural heterogeneity or local compositional variations significantly affect nano-mechanical properties, variations would be expected among the results obtained from different prior- $\beta$  grains. Surprisingly, both nano-hardness and Young’s modulus remained consistent across all tested prior- $\beta$  grains (Table 4.9), as confirmed by nanoindentation experiments conducted on specimen A (Figure 4.10a). Statistical analysis, including one-way ANOVA with  $p$ -values of 0.95 for Young’s modulus and 0.99 for nano-hardness, indicated no significant differences between the groups. The high  $p$ -values suggest no substantial distinctions exist among the compared groups. Notably, the Shapiro–Wilk normality test (S-W) yielded  $p$ -values exceeding  $\alpha = 0.05$  for all prior- $\beta$  grains (Table 4.9). Additionally, Levene’s test confirmed equal variances for both Young’s modulus and nano-hardness data, with  $p$ -values of 0.24 and 0.22, respectively. Thus, the application of ANOVA procedure was justified, given the absence of evidence for non-normality and the presence of equal variances.

Hence, nanoindentation on the PBF-LB Ti6Al4V (ELI) alloy can be conducted across various grains without compromising the representability of results. The insensitivity of nanoindentation results to local microstructural variations in this alloy can be attributed



**Table 4.9:** Influence of indentation location on nano-mechanical properties - specimen A.

Columnar Prior- $\beta$ Grain ID	1	2	3	4	5
Young's modulus (GPa)	120 (10)	122 (5)	123 (9)	122 (6)	128 (5)
Nano-hardness (GPa)	4.2 (0.6)	4.2 (0.3)	4.2 (0.7)	4.2 (0.4)	4.1 (0.4)
$p$ -value (S-W) for Young's modulus	0.25	0.43	0.63	0.27	0.65
$p$ -value (S-W) for nano-hardness	0.25	0.32	0.76	0.48	0.26

**Figure 4.10:** (a) CSM tests conducted in different columnar prior- $\beta$  grains of the annealed specimen, (b) residual imprint of the Berkovich tip used [168].

to the significant size difference between the Berkovich tip and microstructural features (Figure 4.10b). Hence, the nanoindentation procedure remains suitable for characterizing nano-mechanical properties, particularly in the as-built condition as indicated in [167]. The edges of residual imprints from the Berkovich tip, with depths up to 3000 nm, measured approximately 20  $\mu\text{m}$  long (Figure 4.10b). According to [29], an energy density of 71.4 J/mm<sup>3</sup> yields average lath sizes of 0.68  $\mu\text{m}$  and 1.8  $\mu\text{m}$  for PBF-LB Ti6Al4V alloy in as-built and annealed conditions, respectively. Moreover, annealed PBF-LB Ti6Al4V exhibits decreasing average lath sizes with increasing energy density [29]. These lath sizes are notably smaller than the dimensions of the Berkovich tip, further justifying its applicability for characterizing nano-mechanical properties when required. Additionally, conducting numerous repetitions at diverse locations enhances result robustness and reliability. As demonstrated in [29], high energy density values ( $E_V > 37 \text{ J/mm}^3$ ) generate a distinct texture with fine  $\alpha/\alpha'$  laths within the columnar microstructure of as-built PBF-LB Ti6Al4V. Multiple laths consistently emerge beneath the Berkovich tip during nanoindentation measurements in each case. This approach addresses variations arising from different orientations and potential local hete-

rogeneities within the microstructure, particularly the fine  $\alpha/\alpha'$  laths within the columnar microstructure, by increasing the number of repetitions.

#### 4.5.2. Young's modulus and Nano-hardness

CSM tests indicated that an indentation depth interval from 1000 to 2400 nm is optimal for further data evaluation. At depths greater than 1000 nm, Young's modulus and nano-hardness stabilize to a constant value, as shown in Figure 4.11c-4.11f. Additionally, using higher indentation depths in this study produced more robust results and better illustrated the influence of indentation depth on nano-hardness and Young's modulus. Generally, the CSM method is preferred over the load-unload method for determining Young's modulus due to its use of small loading-unloading cycles, allowing measurements at multiple points rather than just one [170].

A significant concern in nano-indentation and low-force Vickers hardness methods is the indentation size effect (ISE) [171]. Typically, ISE manifests as an increase in hardness with a decrease in indentation depth, becoming significant at depths less than 1000 nm, as described in [172]. This common effect is known as the normal ISE. However, a reverse ISE, where nano-hardness decreases with decreasing indentation depth, can also occur [172]. By selecting an evaluation interval between 1000 and 2400 nm, the influence of ISE was minimized, ensuring more reliable and robust nano-mechanical results.

The Young's modulus of the D<sup>ab</sup> specimen reaches a constant value at lower indentation depths compared to the D<sup>an</sup> specimen, as shown in Figures 4.11c and 4.11d. This trend is also observed in the nano-hardness values, as seen in Figures 4.11e and 4.11f. Specifically, the D<sup>an</sup> specimen's Young's modulus and nano-hardness stabilize at around 1000 nm, while the D<sup>ab</sup> specimen's stabilizes at approximately 300 nm. The microstructure of the as-built Ti6Al4V (ELI) alloy, produced under extremely high cooling rates during PBF-LB ( $10^4$ – $10^6$  K/s) [41], comprises acicular martensite ( $\alpha'$ ) within columnar prior- $\beta$  grains (Figure 4.11a). Through annealing heat treatment, the nano-hardness can be reduced by transforming the  $\alpha'$  into  $\alpha + \beta$  laths (Figure 4.11b). Due to the mechanical property differences between  $\alpha$  and  $\beta$  laths, the nano-hardness and Young's modulus data for the D<sup>an</sup> specimen are more variable compared to the more uniform microstructure ( $\alpha'$ ) of the D<sup>ab</sup> specimen, as illustrated in Figure 4.11.

Young's modulus values for the D<sup>an</sup> and D<sup>ab</sup> specimens (Table 4.10) show that the an-

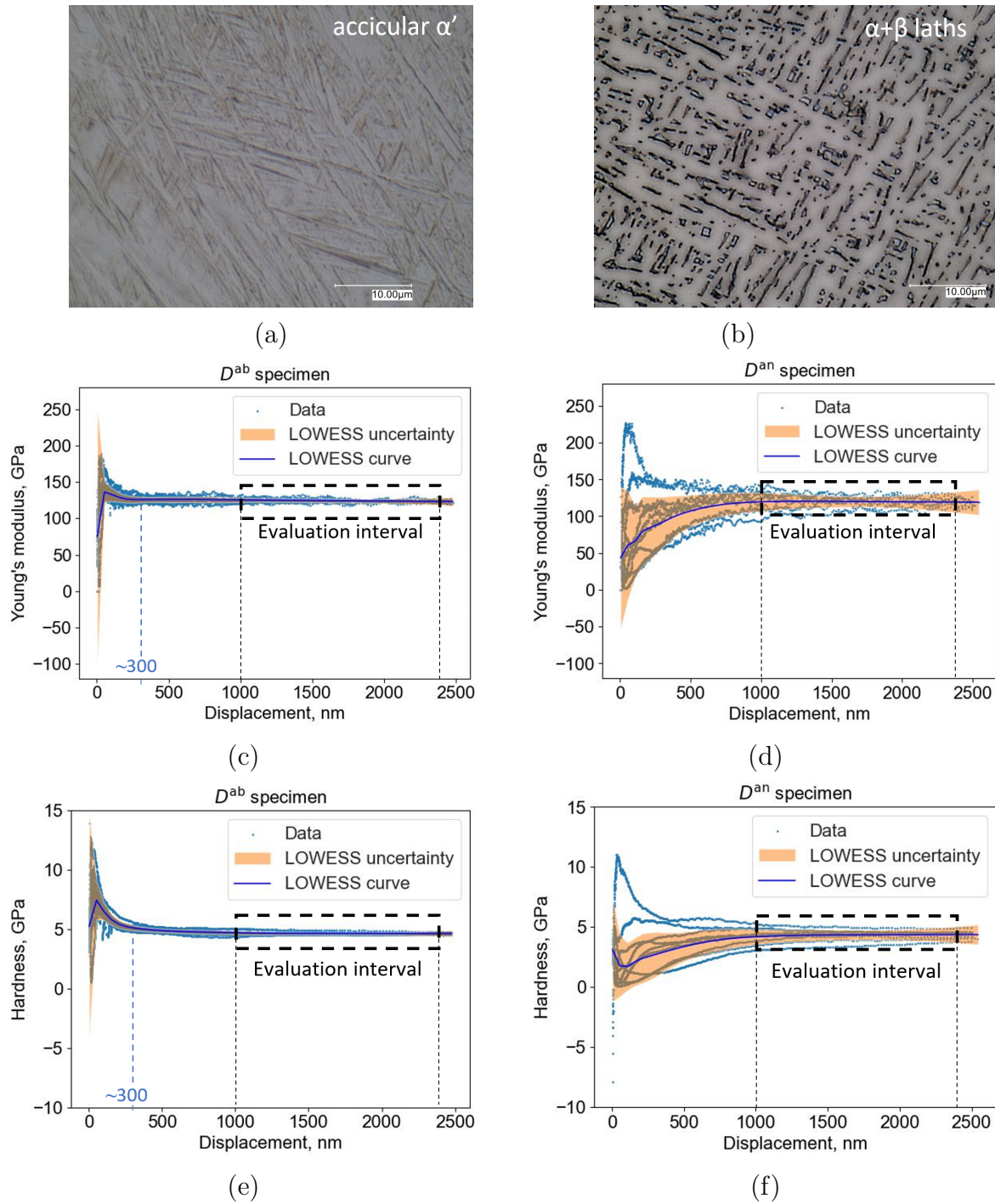


**Figure 4.11:** Typical Young's modulus and nano-hardness CSM measurements on as-built and annealed specimens, with 95% confidence intervals shown as shaded areas: (a) Microstructure of the  $D^{ab}$  specimen featuring a dominant  $\alpha'$  phase, and (b) Microstructure of the annealed  $D^{an}$  specimen with a dominant  $\alpha + \beta$  phase; (c) Young's modulus values as a function of indentation depth for the  $D^{ab}$ , and (d) for the  $D^{an}$  specimen; (e) Nano-hardness values as a function of indentation depth for the  $D^{an}$  specimen, and (f) for the  $D^{ab}$  specimen [168].

nealing heat treatment did not significantly affect the mean Young's modulus values. The  $t$ -test resulted in a  $p$ -value of 0.12, suggesting no significant difference between the mean

values of the D<sup>an</sup> and D<sup>ab</sup> specimens. Additionally, the normality of the Young’s modulus distribution for each specimen was confirmed, with  $p$ -values exceeding the significance level of  $\alpha = 0.05$  (0.92 for D<sup>ab</sup> and 0.55 for D<sup>an</sup>). These results justify the use of the  $t$ -test for comparing the mean values. Liu et al. also found that different heat treatments have minimal impact on the Young’s modulus of PBF-LB Ti6Al4V alloy [96], which aligns with these findings.

**Table 4.10:** Young’s modulus and nano-hardness for different PBF-LB process parameters combinations and heat treatment conditions.

PBF-LB parameters				$E$ , GPa			$H$ , GPa		
$P$ , W	$v$ , mm/s	$E_V$ , J/mm <sup>3</sup>	ID	Mean (STD)	%COV	$p$ -value (S-W)	Mean (STD)	%COV	$p$ -value (S-W)
200	1000	88.9	A	126 (8)	6.28	0.09	4.3 (0.5)	11.01	0.35
	1250	71.1	B	129 (4)	3.27	<b>0.025</b>	4.6 (0.3)	6.09	0.2
	1500	59.3	C	129 (9)	6.71	0.36	4.4 (0.5)	11.36	0.34
225	1000	100	D <sup>an</sup>	121 (8)	6.97	0.55	4.3 (0.5)	11.34	0.56
		100	D <sup>ab</sup>	125 (2)	1.45	0.92	4.7 (0.1)	2.8	0.09
	1250	80	E	129 (6)	4.57	0.36	4.4 (0.4)	8.41	0.36
	1500	66.7	F	134 (1)	1.04	<b>0.037</b>	4.6 (0.2)	3.67	0.54
250	1000	111.1	G	137 (3)	1.98	0.78	4.9 (0.2)	3.67	0.73
	1250	88.9	H	131 (3)	1.91	0.95	4.8 (0.2)	3.74	0.94
	1500	74.1	I	128 (2)	1.33	0.3	4.8 (0.1)	2.3	0.77

Notes: The S-W test was performed to test the normality of distribution. Bolded values highlight statistically significant differences – evidence of non-normality.

When comparing the nano-hardness values of the D<sup>an</sup> and D<sup>ab</sup> specimens (Table 4.10), it was found that the mean nano-hardness of the as-built specimen is slightly higher than that of the annealed specimen. The  $t$ -test provided a  $p$ -value of 0.036, indicating a statistically significant difference between the two mean values, although this  $p$ -value is close to the significance level of  $\alpha = 0.05$ . Both specimens’  $p$ -values calculated using the S-W test were higher than  $\alpha = 0.05$ , justifying the  $t$ -test’s applicability (0.09 for D<sup>ab</sup> and 0.56 for D<sup>an</sup>). These results suggest that annealing heat treatment slightly decreases the nano-hardness values measured by nanoindentation methods.

In contrast, when comparing hardness results obtained using low-force Vickers hardness tests (HV1), the difference in mean values between the annealed and as-built specimen is more pronounced than the results from the nanoindentation method (Table 4.11). The S-W test on HV1 data did not indicate non-normality, with  $p$ -values of 0.43 for D<sup>ab</sup> and 0.12 for

**Table 4.11:** HV1 values for different PBF-LB process parameter combinations and heat treatment conditions.

PBF-LB parameters				HV1		
$P$ , W	$v$ , mm/s	$E_V$ , J/mm <sup>3</sup>	ID	Mean (STD)	%COV	$p$ -value (S-W)
200	1000	88.9	A	368 (6)	1.7	0.81
	1250	71.1	B	362 (7)	1.8	0.93
	1500	59.3	C	369 (5)	1.2	0.6
225	1000	100	D <sup>an</sup>	364 (8)	2.1	0.12
		100	D <sup>ab</sup>	385 (6)	1.6	0.43
	1250	80	E	375 (7)	1.8	0.053
	1500	66.7	F	352 (12)	3.4	0.15
250	1000	111.1	G	374 (6)	1.5	0.52
	1250	88.9	H	364 (8)	2.1	0.5
	1500	74.1	I	369 (20)	5.4	0.07

Notes: The S-W test was performed to test the normality of distribution.

D<sup>an</sup>. Furthermore, the  $t$ -test for HV1 values produced a  $p$ -value of less than 0.001, confirming that the annealing procedure significantly reduced the HV1 values for the D<sup>an</sup> specimen. Additionally, annealing heat treatment does not affect the Young's modulus values.

The higher HV1 value of the as-built specimen compared to the annealed specimen can be attributed to the dominant  $\alpha'$  phase, which has a higher dislocation density than the annealed specimen, which features a microstructure with dominant  $\alpha + \beta$  laths [96]. Chen et al. [97] measured nano-hardness in different planes of the as-built PBF-LB Ti6Al4V alloy and reported values of  $4.2 \pm 0.5$  GPa and  $5.1 \pm 0.5$  GPa for different planes, which align with the results shown in Table 4.10, confirming their relevance.

As shown in Table 4.10, the highest mean Young's modulus value for annealed specimens was obtained for test specimen G, which was manufactured using a laser power of 250 W and a scanning speed of 1000 mm/s, resulting in the highest energy density of 111 J/mm<sup>3</sup>. The Dunn's multiple comparison test (Table 4.12) indicates statistically significant differences in Young's modulus values between specimen G and other specimens produced with lower and intermediate laser power levels, except for specimen F. This suggests that laser power might influence Young's modulus. Notably, the Young's modulus values for specimen F were not normally distributed, as indicated by the S-W test with a  $p$ -value of 0.037.

To investigate the potential effect of laser power on nano-hardness values further, it would be beneficial to include a wider range and a higher number of laser power levels in the design

**Table 4.12:** The  $p$ -values obtained from Dunn’s multiple comparison test conducted on annealed specimens\*.

$p$ -values for $E$									
ID	A	B	C	D	E	F	G	H	I
A	1								
B	0.72	1							
C	0.5	0.76	1						
D	0.36	0.16	0.083	1					
E	0.4	0.7	0.89	0.056	1				
F	<b>0.008</b>	<b>0.036</b>	0.078	< <b>0.001</b>	0.094	1			
G	< <b>0.001</b>	<b>0.003</b>	<b>0.009</b>	< <b>0.001</b>	<b>0.011</b>	0.46	1		
H	0.33	0.59	0.76	<b>0.047</b>	0.84	0.2	<b>0.034</b>	1	
I	0.77	0.93	0.75	0.21	0.7	<b>0.036</b>	<b>0.003</b>	0.57	1

$p$ -values for $H$									
ID	A	B	C	D	E	F	G	H	I
A	1								
B	0.26	1							
C	0.57	0.7	1						
D	0.91	0.4	0.68	1					
E	0.78	0.43	0.75	0.91	1				
F	0.22	0.92	0.59	0.34	0.36	1			
G	<b>0.002</b>	<b>0.033</b>	<b>0.012</b>	<b>0.006</b>	<b>0.005</b>	<b>0.047</b>	1		
H	<b>0.014</b>	0.2	0.07	<b>0.027</b>	<b>0.029</b>	0.23	0.6	1	
I	<b>0.016</b>	0.2	0.068	<b>0.028</b>	<b>0.031</b>	0.23	0.6	0.98	1

\* To find statistically significant differences among multiple specimen groups, the Kruskal–Wallis rank sum test was employed due to the non-normal distribution of Young’s modulus data for specimens B and F (Table 4.10). Subsequently, Dunn’s multiple comparison test was applied in post hoc analysis to identify significant differences in median  $E$  and  $H$  values across annealed specimens. To mitigate false discovery rates, calculated  $p$ -values were adjusted using the Benjamini–Hochberg method. Statistically significant differences are indicated by bold values.

of experiments.

When comparing the nano-hardness results in Table 4.12, it is clear that no statistically significant differences exist among specimens manufactured with the highest laser power levels (G, H, and I). Furthermore, there were no significant differences in nano-hardness values between specimens produced with 200 W and 225 W laser power levels. The mean nano-hardness value for specimen G was higher than those of specimens manufactured with 200 W and 225 W laser power levels (Table 4.10). Notably, the highest nano-hardness value obtained through nanoindentation was for specimen G, which was produced with the highest energy density. This suggests that the annealing heat treatment cannot completely negate

the effects of the PBF-LB process parameters used.

Cepeda-Jiménez et al. [29] discussed the impact of energy density on the microstructural and textural evolution of annealed PBF-LB Ti6Al4V alloy. Their findings revealed a slight increase in hardness with increasing energy density within a range of 24.2 to 44.3 J/mm<sup>3</sup>. However, this trend shifted when utilizing an energy density of 71.4 J/mm<sup>3</sup>, suggesting that hardness is not directly proportional to energy density. Additionally, they noted that similar energy densities can be achieved using different combinations of PBF-LB process parameters, highlighting the complexity of this relationship.

For example, specimens A and H, which were manufactured with identical energy densities but different laser power and scanning speed combinations, exhibited statistically significant differences in nano-hardness values (Table 4.10). Previous research [44] has indicated that specimens produced with higher energy densities experience lower thermal gradients and remain at elevated temperatures for longer durations. Consequently, these specimens exhibit greater microstructural stability, leading to reduced grain coarsening during heat treatment and the development of highly textured microstructures [29].

Despite these observations, it is unexpected that the G specimen, subjected to annealing heat treatment, demonstrates a higher mean nano-hardness value than the as-built D<sup>ab</sup> specimen (Table 4.10). This discrepancy highlights the complex relationship between processing parameters, microstructure, and mechanical properties in PBF-LB Ti6Al4V.

The low-force Vickers hardness test confirmed that the G specimen, manufactured with the highest energy density, exhibits a high HV1 value of 374 HV1 (std. 6 HV1) when compared to other annealed specimens. However, this value does not surpass the HV1 value of the D<sup>ab</sup> specimen, which measures 385 HV1 (std. 6 HV1). The discrepancy in HV1 hardness between the specimens may be attributed to differences in indentation depths and strain rates between the two test methods. Unlike the nanoindentation method, the low-force Vickers hardness test applies the indenter tip to larger indentation depths with different strain rates and utilizes a larger indenter size, which can impact the measured hardness values. Despite these methodological differences, both the nano-hardness and low-force Vickers hardness tests provided results that are consistent with findings in existing literature [173, 174].

Moreover, the Young's modulus values for specimens manufactured using a laser power of 250 W exhibit slightly higher mean values and lower standard deviations compared to

other reported results. The Young's modulus ranges from its lowest mean value of 121 GPa (std. 8 GPa) when utilizing  $P = 225$  W and  $v = 1000$  mm/s, to its highest mean value of 137 GPa (std. 3 GPa) when employing  $P = 250$  W and  $v = 1000$  mm/s. These findings are in line with previous studies. Chen et al. reported Young's modulus value of  $127 \pm 4$  GPa for an as-built specimen, which aligns with the observed trend [97].

In efforts to correlate mechanical properties at the nano and macro scales, Tuninetti et al. found a relationship that estimates macro-scale flow stress from nano-hardness results of conventionally processed Ti6Al4V alloy [175]. Additionally, the flow stress can be related to nano-hardness using the Tabor relation [172]. To estimate the Young's modulus ( $E$ ) value based on nano-hardness ( $H$ ) or vice versa, a linear regression model was applied to nano-mechanical experimental data from all annealed specimens. The analysis revealed a well-represented relationship between  $E$  and  $H$  using a simple linear model:  $E = 15.066|H| + 60.514$  with  $R^2 = 0.744$  (Figure 4.12a). Furthermore, the calculated correlation coefficient ( $r = 0.863$ ) indicates a strong correlation between Young's modulus and nano-hardness  $E$  and  $H$ .

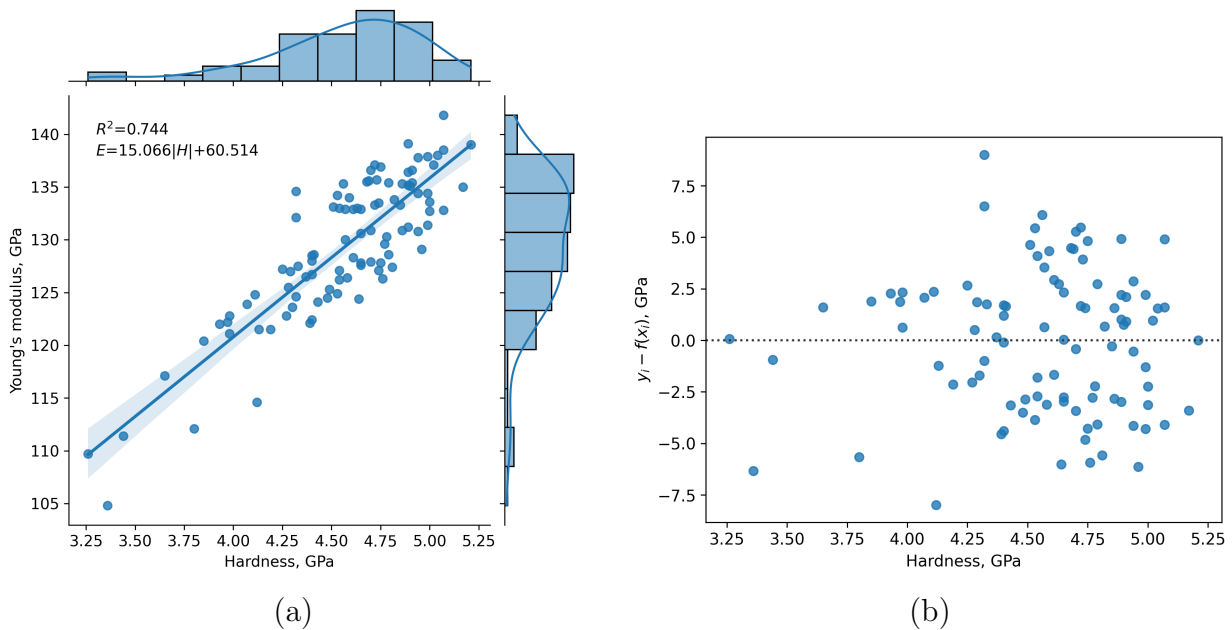


**Figure 4.12:** (a) Linear regression model depicting the relationship between Young's modulus and nano-hardness for annealed Ti6Al4V alloy, accompanied by a 95% confidence interval shown as a shaded area; (b) Residual plot showing random scatter around the zero line, indicating the validity of the linear regression model [168].

By applying this relationship, Young's modulus can be estimated from the nano-hardness data for PBF-LB Ti6Al4V alloy within laser power and scanning speed ranges of 200-250 W



and 1000–1500 mm/s, respectively. This model serves as a reference for comparing the  $E-H$  relationship across various heat treatment conditions, process parameters, manufacturing technologies, or even new materials with limited nano-mechanical data in the literature.

To validate the proposed model, a non-constant variance score test was conducted, confirming that the model exhibits homoscedastic variance of the error term ( $p = 0.715$ ). This finding supports the assumption of equal variances, which is crucial for the accurate application of the linear regression model. Additionally, the residual plot (Figure 4.12b) shows random scattering, further indicating the suitability of a linear model. The S-W normality test on studentized residuals was also performed to test the normality of the model errors. The results indicated no evidence against the normality of model errors ( $p = 0.378$ ), thereby further supporting the validity of the proposed model.

### 4.5.3. Creep properties

According to the load-unload curves from nanoindentation tests on the  $D^{\text{ab}}$  and  $D^{\text{an}}$  specimens, it is evident that the load plateaus widen with increasing indentation load (Figure 4.13a and 4.13b). The  $D^{\text{an}}$  specimen generally shows wider load plateaus ( $\sim 58$  nm at a 200 mN holding load) compared to the  $D^{\text{ab}}$  specimen ( $\sim 40$  nm at a 200 mN holding load), suggesting that annealing reduces creep resistance. This conclusion is further supported by (Figure 4.13c and 4.13d), where the  $D^{\text{an}}$  specimen curves exhibit a steeper increasing trend compared to those of the  $D^{\text{ab}}$  specimen.

All indentation depth versus time curves exhibit a pronounced increasing trend in both transient and steady-state creep regimes. Initially, the creep displacement increases rapidly with time and then significantly slows down, maintaining an almost linear trend in the later stage. To analyze the experimental data, a least squares fitting procedure was used to fit equation (3-10) and equation (3-13) to the data. The parameters  $a$ ,  $b$ , and  $k$  (Table 4.13) were obtained by fitting equation (3-10) to the experimental data from the creep stage. equation (3-10) demonstrated a high level of agreement with the experimental data for all applied holding loads, as shown in the  $D^{\text{an}}$  specimen subjected to a 200 mN indentation load (Figure 4.14a), with a mean absolute error (MAE) of 0.331 nm. Figure 4.14a also highlights the high creep strain rate dependence on time, particularly in the transient creep regime. Additionally, equation (3-13) was fitted to the unloading part of the curve with a high agreement (MAE < 0.415 mN) (Figure 4.14b). From this part of the curve, the material

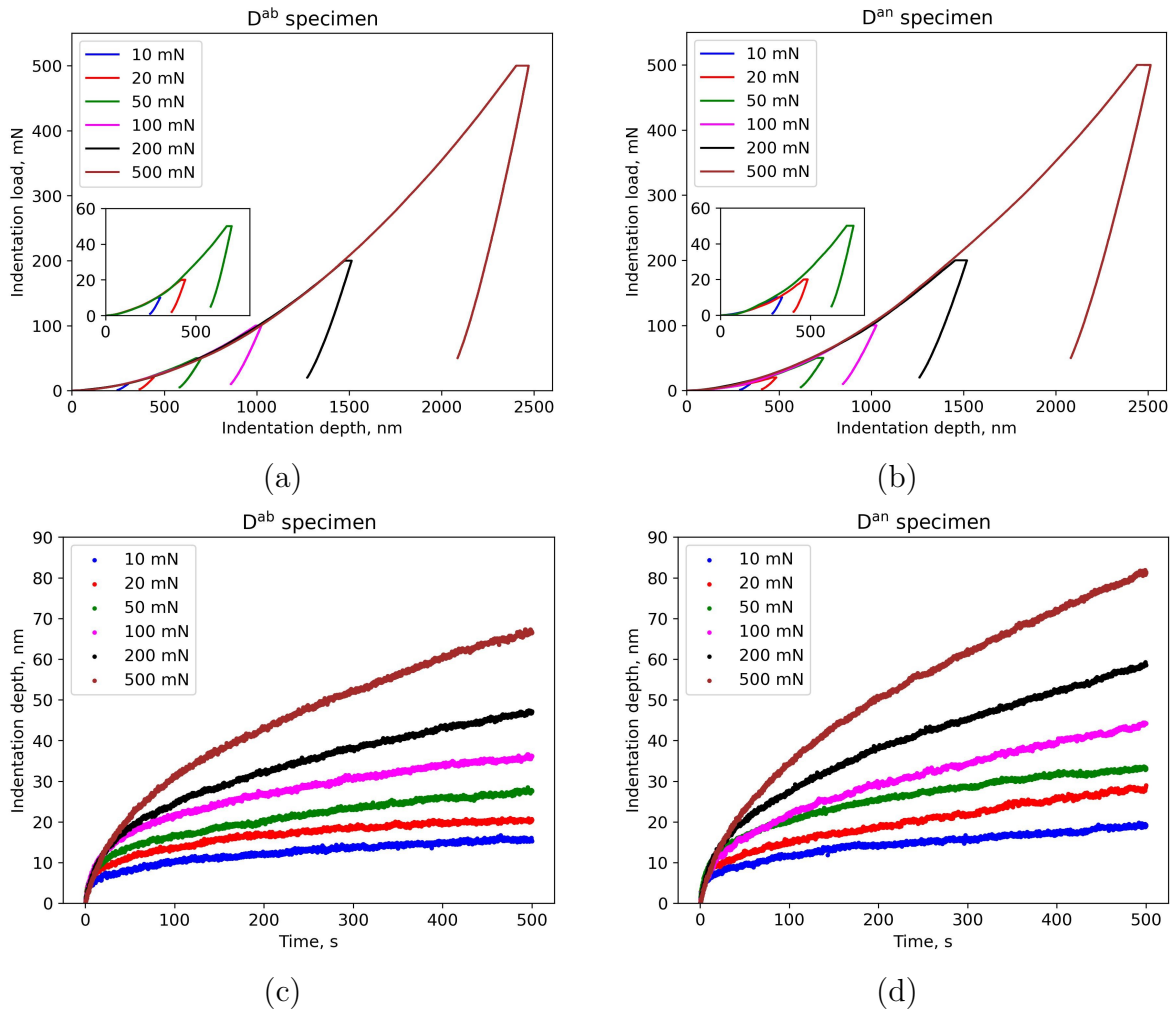


**Figure 4.13:** Nano-mechanical response of as-built and annealed specimens under nanoindentation creep tests: (a) Load–unload curves for the as-built specimen and (b) the annealed specimen under various holding loads during the creep stage; (c) indentation depth versus time curves during the creep stage for the as-built specimen and (d) the annealed specimen under different holding loads [168].

constants  $B$  and  $m$  were derived and used to determine the contact stiffness ( $S$ ) (Table 4.14) using equation (3-8).

Pharr and Bolshakov reported that the parameter  $m$  ranges between 1.2 and 1.6 for six different materials they tested experimentally [176], which aligns with results reported in Table 4.14. This study revealed that the parameters  $B$  and  $m$  vary with the maximum applied indentation load, suggesting that the curvature of the unloading curve is load-dependent (Figure 4.13a and 4.13b). As a result, the calculated contact stiffness values increased with higher applied loads (Table 4.14). Given that the parameters  $B$  and  $m$  for Ti6Al4V alloy produced via PBF-LB are either not available or rarely reported in existing literature, these findings are particularly significant.

**Table 4.13:** Fitting parameters for the creep stage.

Load, mN	$D^{an}$			$D^{ab}$		
	$a$	$b$	$k$	$a$	$b$	$k$
10	3.306 (0.510)	0.272 (0.026)	0.008 (0.009)	3.334 (0.748)	0.246 (0.039)	0.003 (0.009)
20	3.918 (0.529)	0.258 (0.030)	0.006 (0.007)	3.815 (0.608)	0.263 (0.038)	-0.001 (0.007)
50	3.666 (0.489)	0.346 (0.026)	0.002 (0.009)	4.145 (0.449)	0.296 (0.025)	0.004 (0.006)
100	3.854 (0.502)	0.383 (0.020)	0.004 (0.009)	4.038 (0.424)	0.350 (0.020)	-0.003 (0.009)
200	3.359 (0.326)	0.470 (0.019)	-0.011 (0.009)	3.527 (0.343)	0.424 (0.022)	-0.011 (0.008)
500	2.442 (0.283)	0.607 (0.029)	-0.053 (0.013)	2.172 (0.209)	0.604 (0.024)	-0.052 (0.015)

**Table 4.14:** Parameters for fitting the unloading portion of the curve and contact stiffness.

Load, mN	$D^{an}$			$D^{ab}$		
	$B$	$m$	$S, \text{mN/nm}$	$B$	$m$	$S, \text{mN/nm}$
10	0.056 (0.002)	1.265 (0.011)	0.207 (0.005)	0.054 (0.006)	1.280 (0.023)	0.211 (0.004)
20	0.077 (0.010)	1.260 (0.030)	0.297 (0.009)	0.082 (0.007)	1.249 (0.015)	0.299 (0.004)
50	0.125 (0.010)	1.224 (0.015)	0.449 (0.007)	0.117 (0.006)	1.246 (0.009)	0.470 (0.008)
100	0.165 (0.015)	1.216 (0.017)	0.614 (0.014)	0.167 (0.007)	1.229 (0.009)	0.661 (0.010)
200	0.220 (0.013)	1.207 (0.010)	0.836 (0.012)	0.221 (0.008)	1.223 (0.008)	0.915 (0.022)
500	0.332 (0.018)	1.189 (0.009)	1.236 (0.020)	0.334 (0.024)	1.210 (0.012)	1.411 (0.040)

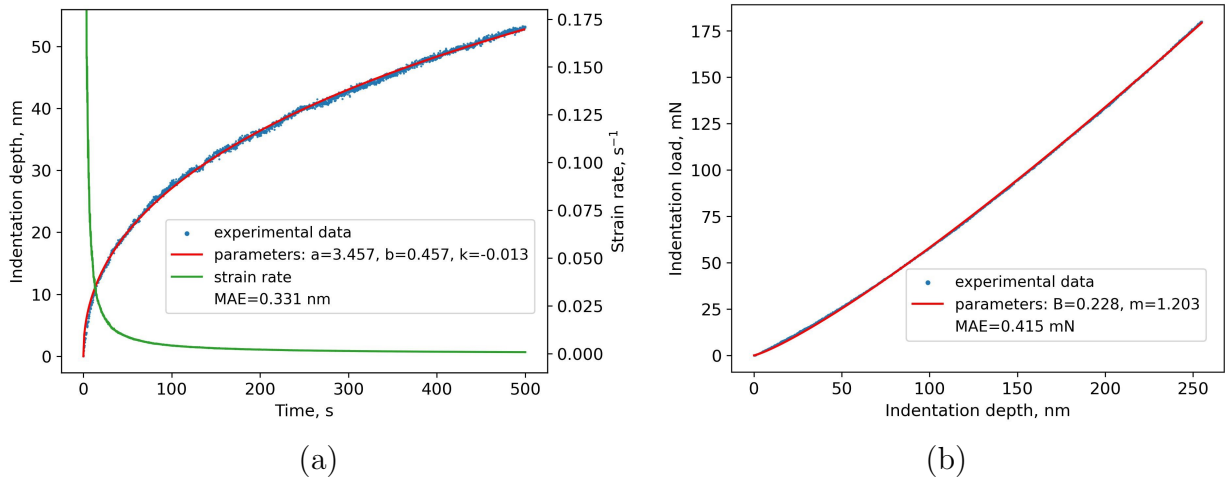


**Figure 4.14:** Fitting curves and experimental data for the annealed specimen under a 200 mN holding load during the creep stage: (a) Experimental indentation depth vs. time data along with model parameters; (b) Experimental data and model parameters for the upper portion of the unloading curve [168].

Additionally, the slope of the  $\ln \dot{\epsilon} - \ln H_{cr}$  curves decreases sharply as the creep process nears its steady state, as shown in Figure 4.15a and 4.15b. By applying equation (3-18) to the  $\ln \dot{\epsilon} - \ln H_{cr}$  data, we can determine the creep stress exponent  $n$ , which helps evaluate the dominant creep mechanism and the creep stability. An  $n$  value of 1 indicates a diffusion creep mechanism,  $n = 2$  suggests grain boundary sliding, and  $n > 3$  implies dislocation movement as the primary creep mechanism [177, 178]. As shown in Figure 4.15c and 4.15d,  $n > 3$  for both  $D^{an}$  and  $D^{ab}$  specimens, indicating that dislocation movement governs the

creep deformation.

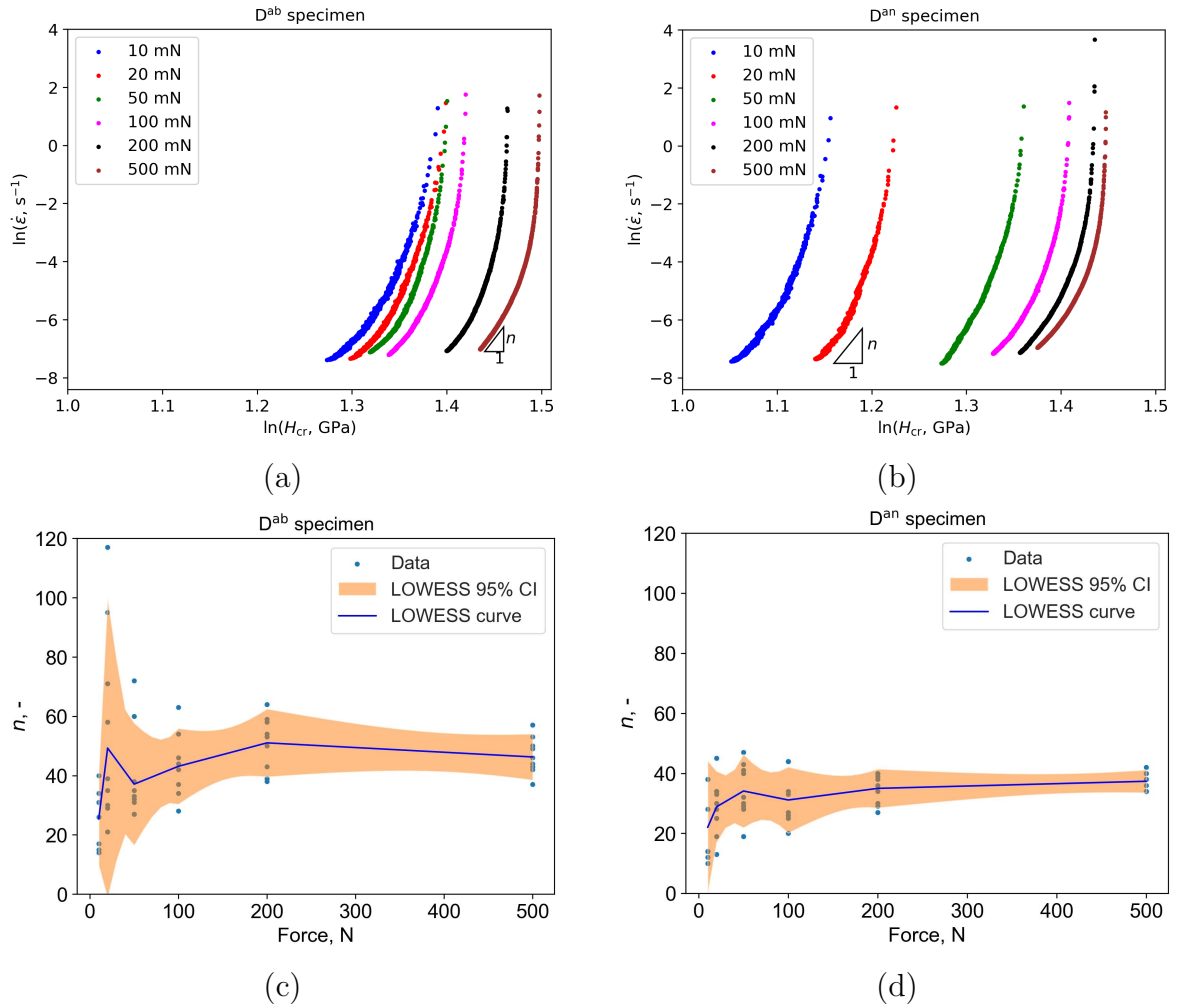


**Figure 4.15:** Creep properties and behavior under various maximum indentation loads during the creep stage: (a) Representative  $\ln \dot{\epsilon} - \ln H_{cr}$  curves for as-built specimen and (b) annealed specimen; (c) creep stress exponent for as-built specimen and (d) annealed specimen, each with 95% confidence intervals [168].

In both cases, the highest applied indentation load during the creep stage resulted in the lowest data scatter for the calculated  $n$  values (Figure 4.15c and 4.15d). Conversely, lower indentation loads led to more prominent data scatter in the calculated  $n$  values for both specimens (Figure 4.15c and 4.15d). Both specimens exhibited high mean  $n$  values, aligning with observations for a CoCrNi multi-principal element alloy, which also exhibited dislocation movement as the dominant creep mechanism [102]. However, it is worth noting the ongoing debate regarding the existence of specific creep mechanisms, such as Harper–Dorn diffusion creep [179].

When comparing mean  $n$  values for identical indentation loads (Figure 4.15c and 4.15d), it is evident that the as-built specimen consistently has higher mean  $n$  values than the

annealed specimen. Generally, the mean  $n$  values of the as-built specimen are shifted upwards compared to those of the annealed specimen. This indicates that annealing heat treatment reduces the creep resistance of PBF-LB Ti6Al4V alloy, corroborating the behavior observed in Figure 4.13c and 4.13d. Although annealing is beneficial for residual stress relaxation [85], increased ductility [66], and reduced anisotropy [180], it also decreases creep resistance, which is undesirable for Ti6Al4V alloys used in high-temperature applications where creep deformation is a concern.

## 4.6. Mechanical Properties of BCC Lattice Specimens

With the development of AM technologies, manufacturing limitations related to the machining of lattice structures in order to achieve targeted mechanical properties have been overcome. This offered flexibility in the manufacturing of lattice structures in many fields, such as automotive, aerospace, and biomedicine [116]. When such structures are used, it is crucial to know how they will behave when subjected to different loads. The behavior of different types of lattice structures is thoroughly investigated in compression, however, tensile tests are scarcely reported [181]. More specifically, for energy absorption applications, compressive behavior is usually more substantial. However, when light-weight structural design is needed, tensile performance is particularly important, and experimental investigation is needed [181]. Therefore, the mechanical response of lattice specimens under tensile load is tested and shown by the stress-strain curves in Figure 4.16. It can be seen that different configurations caused significant variations in mechanical responses. Configurations 1-1-2 and 1-08-2 withstood a force of 16 kN, the maximum capacity of the testing equipment, which was insufficient to cause failure. Consequently, these configurations were used solely to determine Young's modulus.

In Figure 4.16, the lattice specimens are grouped according to the  $d_{\text{end}}$  diameter. It is evident that increasing the  $d_{\text{mid}}$  diameter while keeping  $d_{\text{end}}$  diameter constant, in all cases, results in steeper stress-strain curves, indicating higher Young's modulus values, as detailed in Table 4.15. The same principle applies when increasing the  $d_{\text{end}}$  diameter while keeping the  $d_{\text{mid}}$  diameter constant.

It is noteworthy to address the observed differences in material properties between specimens 06-08-2 and 08-06-2 when compared with specimens 08-1-2 and 1-08-2. In the case of the first pair (06-08-2 and 08-06-2), Young's modulus is higher in the former specimen

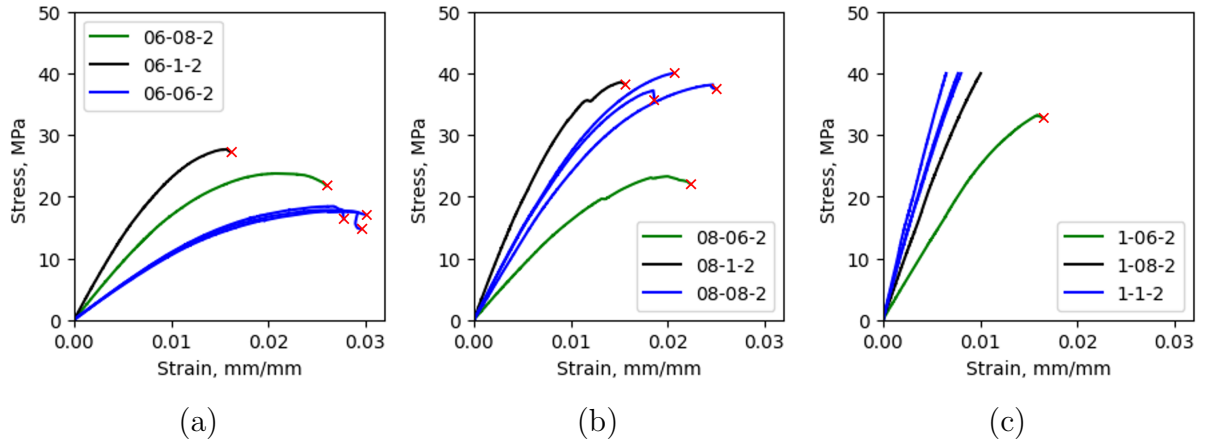


**Figure 4.16:** Stress-strain curves of lattice specimens grouped by  $d_{\text{end}}$ : (a) 0.6 mm, (b) 0.8 mm, and (c) 1 mm (red  $\times$  indicate beginning of the progressive damage of struts).

(08-06-2). However, in the case of the second pair (08-1-2 and 1-08-2), the former specimen (1-08-2) has a lower Young's modulus. These variations may result from defects or dimensional inaccuracies inherent to the PBF-LB process and can fluctuate based on the nominal diameters specified in the CAD design. Therefore, a higher number of specimens is necessary to systematically investigate the influence of these two diameters on mechanical properties. For this purpose, numerical analysis will be employed, as it allows for investigating various combinations while minimizing the risk of introducing additional factors, such as manufacturing defects and dimensional inaccuracies.

**Table 4.15:** Mechanical properties of lattice specimens.

ID	$d_{\text{end}}$ , mm	$d_{\text{mid}}$ , mm	$E$ , MPa	$R_{p0.2}$ , MPa	$R_m$ , MPa	Spec. tested
06-06-2	0.6	0.6	1048 (29)	15.8 (0.4)	18 (0.4)	3
06-08-2	0.6	0.8	1741	20.4	23.8	1
06-1-2	0.6	1	2650	24.2	27.7	1
08-06-2	0.8	0.6	1657	19.6	23.3	1
08-08-2	0.8	0.8	2631 (87)	33.3 (2.7)	38.4 (1.5)	3
08-1-2	0.8	1	3823	34.2	38.6	1
1-06-2	1	0.6	2562	31.4	33.2	1
1-08-2	1	0.8	4347	-	-	1
1-1-2	1	1	5722 (803)	-	-	3

Notes: The reason for a std. of 803 MPa for a specimen group 1-1-2 is the damage that occurred at two specimens in the manufacturing phase at the junctions between solid and lattice parts (see Figure 6.11). Spec. tested refers to the total number of specimens tested for a given configuration.

All specimens failed inside the lattice region away from junctions between the solid and lattice part, supporting the representability of reported results. As can be seen in Figure

4.17, all specimens failed along oblique planes crossing multiple rows of unit cells. At 6 lattice specimens (see Figure 4.17), there were two or more fracture planes illustrated by the white planes at yellow cubes. The damage predominately occurred at the nodes, despite the  $d_{mid}$  in configuration 1-06-2 is smaller than  $d_{end}$ . This is attributed to the configuration of the BCC unit cell, which nodes serve as plastic hinges. The struts rotate around nodes, forming a plastic hinge where the accumulation of plastic deformation occurs until failure. These nodes are critical regions due to the small angle between the neighboring struts connected at the node, which acts as a notch. Furthermore, the utilized PBF-LB process naturally creates smooth transitions at strut midpoints in cases when  $d_{end}$  is larger than  $d_{mid}$ , further reducing stress concentration at the middle of the struts. The PBF-LB process naturally creates fillets at nodes as well, which also has a beneficial influence on reducing stress concentration.

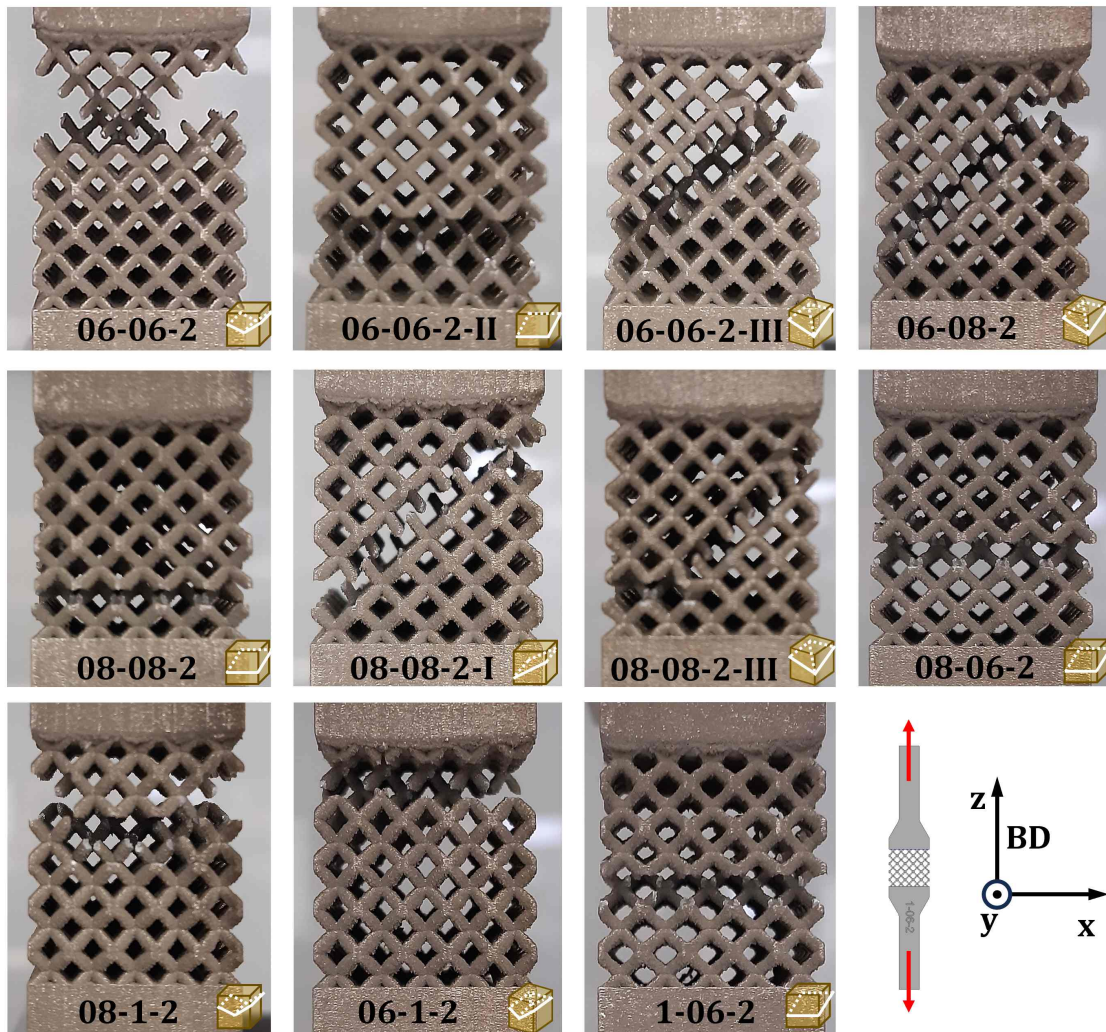


**Figure 4.17:** Failure of different lattice configurations subjected to tensile load (white planes on yellow cubes illustrate fracture planes).

Results of tensile mechanical properties of lattice structures are rarely found in the literature, whereas compressive mechanical properties are widely reported [122, 126, 127, 128]. This scarcity might be attributed to the more challenging design and manufacturing process of tensile lattice specimens. Additionally, producing these specimens is costly as they should be printed vertically (or nearly vertically) to minimize warpage from residual stresses and to avoid the need for support structures at lattice regions. If lattice specimens for tensile tests are not designed and manufactured properly, this can lead to early failure at the junctions between the lattice and solid parts due to abrupt changes in stiffness. To cope with this, gradual densification of the lattice can be performed close to the junctions between the solid and lattice part, forming a smoother stiffness transition [72]. However, in that case, the extensometer should be attached to the lattice part, which is delicate in the case of BCC structures considered in this thesis since the only available contact regions are the nodes. As the load increases, axial and rotational displacements at these nodal regions also increase, and due to inevitable imperfections in the lattice specimens, these displacements are not uniformly distributed. Consequently, attaching the extensometer to the nodes could negatively influence strain measurements. To avoid this potential issue, the extensometer was instead attached to the solid part. Additionally, the strut lengths at the junctions were shortened by incorporating  $\sim 4.6 \times 5 \times 5$  BCC unit cells. As illustrated in Figure 4.17, this approach ensured that fracture planes occurred within the lattice regions, away from the junctions between the solid and lattice parts, which is required for tensile tests to be representative.

In this chapter, PBF-LB Ti6Al4V alloy was characterized by considering multiple aspects at different scales while taking into account the influence of process parameters, specimen position, and heat treatment. It was found that PBF-LB Ti6Al4V alloy in an as-built state consists predominantly of  $\alpha'$  phase within columnar prior- $\beta$  grains. After annealing, the  $\alpha'$  phase is transformed into  $\alpha + \beta$  laths inside columnar prior- $\beta$  grains. Furthermore, an accumulation of voids occurred near the specimen's side surfaces. Those voids, along with surface defects, serve as potential stress concentrators and crack initiation sites [156], reducing the mechanical performance of the materials.

Although there are differences in mechanical properties, these variations are too minor to significantly alter the mechanical response and characteristics of the produced components. Thus, laser power and scanning speed combinations can be chosen within the specified range without compromising mechanical performance. This flexibility permits the customization



of other properties, such as surface roughness, without impacting the mechanical integrity of the components. In each case, the fracture surface had a pronounced plateau region formed in the inner part of the specimen and shear surfaces in the outer part of the specimen. This occurrence represents a ductile-brittle (mix mode) failure [163], achieved by annealing heat treatment. When modeling mechanical properties using laser power and scanning speed at three levels, the resulting  $R^2$  and adjusted  $R^2$  values were relatively low. This suggests that additional parameters should be considered and a broader range of levels for these parameters should be explored. However, expanding the range might lead to different melting modes during the PBF-LB process, each governed by distinct physical mechanisms [182]. As a result, capturing these variations with the single regression model approach used in this study may prove challenging.

Furthermore, micro-hardness measurements using the HV1 method and nano-hardness measurements revealed that annealing reduced hardness from 385 HV1 to 364 HV1 and nano-hardness from 4.7 GPa to 4.3 GPa. The highest nano-hardness, 4.9 GPa, was observed in specimens with the highest energy density, correlating with a highly textured microstructure. Variations in Young's modulus values were also noted, with the highest mean value of 137 GPa achieved using 250 W laser power and 1000 mm/s scanning speed. The nanoindentation creep procedure revealed that although beneficial, annealing heat treatment reduces creep resistance at the nano-scale. Given the widespread use of this alloy in high-temperature applications, this finding is particularly important when selecting appropriate heat treatments. Another aspect worth considering when applying the nanoindentation method is the required indentation depth, which ensures the stable measurements of Young's modulus and hardness at the nano-scale. After an extensive literature review, no research was found that reported indentation depths, which ensure stable measurements. It was found that indentation depths exceeding 1000 nm are necessary for stable measurements in annealed specimens, whereas depths exceeding 300 nm are sufficient for as-built specimens. A large number of Young's modulus and hardness measurements conducted within these stable regions facilitated the investigation of their correlation. It was found that Young's modulus and hardness at the nano-scale are highly correlated, having  $r = 0.863$ .

In order to investigate the customization of mechanical properties in a broader range at the macroscopic level, the incorporation of BCC unit cells to form a lattice structure has been considered. This approach opens the possibility of customizing mechanical response by

changing the geometry of the unit cell, which can be easily achievable by utilizing PBF-LB technology. In this way, even hard-to-machine materials such as titanium and its alloys can be efficiently processed to form complex shaped components. In such components, lattice structures can be used to customize the mechanical behavior of the entire component or just locally at the region of interest. Often, lattice structures are used for energy absorption purposes, and in such cases, experimental investigation of compressive behavior is required [181]. However, for lightweight structural design, tensile performance is crucial, necessitating experimental investigation as well [181]. For this purpose, tapering of the struts forming a BCC unit cell was performed by incorporating different combinations of  $d_{\text{end}}$  and  $d_{\text{mid}}$  diameters. Increasing the diameter  $d_{\text{mid}}$  while maintaining a constant  $d_{\text{end}}$  consistently led to steeper stress-strain curves across all cases, indicating higher Young's modulus values. Similarly, the stress-strain curves steepened when increasing  $d_{\text{end}}$  diameter while holding  $d_{\text{mid}}$  constant. An increase in both diameters leads to a potential increase in  $R_{p0.2}$  and  $R_m$ . However, further investigation is required as  $R_{p0.2}$  and  $R_m$  were not determined for the 1-1-2 and 1-08-2 configurations due to testing equipment limitations. At the remaining lattice specimen configurations, failure occurred inside lattice regions at oblique planes. This confirmed the effectiveness of incorporating shorter struts at the junctions between the solid and lattice regions in order to reduce sudden jumps in stiffness, which could cause premature failure across the horizontal planes located at the junctions between the solid and lattice regions, making experimental results incorrect.

## 5. SURFACE ROUGHNESS OF PBF-LB Ti6Al4V ALLOY COMPONENTS

Controlling the surface roughness in materials produced using PBF-LB is essential for ensuring the functional performance of components, expanding their range of applications, and influencing fatigue performance. When AM components are in their as-built state, surface roughness becomes the dominant factor influencing fatigue performance [105]. Consequently, factors like internal defect size, defect distribution, and microstructure are less relevant [105]. Numerous factors can affect the surface roughness of materials produced by PBF-LB. Consequently, the surface roughness analysis of PBF-LB Ti6Al4V alloy has been extensively studied and documented in many publications [9, 10, 11, 12, 13, 14, 15, 16, 17, 18]. However, models that establish connections between PBF-LB process parameters and surface roughness are scarcely reported, especially in the case of titanium and its alloys. Therefore, it is necessary to investigate the possibility of customizing the surface roughness of components by changing the easily adjustable PBF-LB parameters, such as laser power and scanning speed.

In general, surface roughness is defined as the variations in surface height compared to a reference plane [183]. This chapter will provide results on the line average surface roughness measured using contact methods and the area average surface roughness measured using non-contact methods.

To investigate the influence of ultrasonic cleaning, one specimen (H2) was subjected to surface roughness measurements before and after ultrasonic cleaning to assess its potential influence. The average surface roughness before cleaning was  $6.670 \mu\text{m}$  (std.  $0.406 \mu\text{m}$ ), and after cleaning, it was  $6.788 \mu\text{m}$  (std.  $0.389 \mu\text{m}$ ). The negligible differences in means and standard deviations indicate that ultrasonic cleaning had no significant influence on the surface roughness measurements.

In addition, the influence of specimen position on the build platform on surface roughness

has been investigated by calculating the average surface roughness on line ( $R_a$ ) and area ( $S_a$ ). The surface roughness refers to the variations in surface height relative to a reference plane [183]. The dependence of  $R_a$  and  $S_a$  values on specimen positions was evaluated using the Kruskal-Wallis rank sum test, as  $R_a$  and  $S_a$  were not normally distributed across all specimen groups. Levene's test was employed to check the equality of variances for  $R_a$  and  $S_a$  data between the groups. The  $p$ -values for  $R_a$  and  $S_a$  data were 0.84 and 0.79, respectively, indicating equal variances. The Kruskal-Wallis test provided  $p$ -values of 0.80 for  $R_a$  and 0.90 for  $S_a$ , suggesting that specimen positions do not have a statistically significant effect on  $R_a$  and  $S_a$  values, as shown in Figure 5.1. This result aligns with the findings in [11], which demonstrated that  $P_L$  and  $v$  are the most significant factors influencing side surface roughness. Consequently, further regression models for surface roughness can be developed using only  $P_L$  and  $v$  as predictor variables.<sup>3</sup>

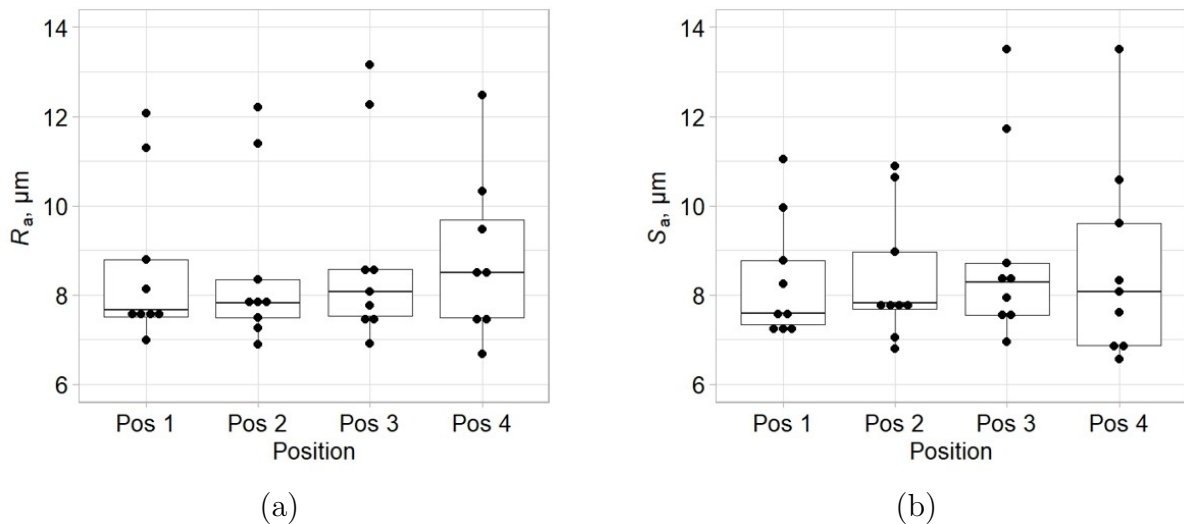


**Figure 5.1:** Variation of (a)  $R_a$  values, (b)  $S_a$  values based on different specimen positions on the build platform [184] (the corresponding specimen positions are detailed in Table 3.3 and illustrated in Figure 3.4a).

Regression models are also provided, enabling surface roughness to be modeled using  $P_L$  and  $v$  as factors. In all response surface figures, models with higher  $R^2$  values have been shown, to facilitate a visual assessment of the effects of  $P_L$  and  $v$  on the prediction variables. Two models will be presented for each prediction variable, subjected to various statistical tests, and compared, and their fitting performance and complexity will be thoroughly exami-

<sup>3</sup>The content in this chapter is based on research published by the author and collaborators in a peer-reviewed scientific paper [184]. The creation of this publication was driven by the necessity to fulfill the doctoral study requirements at the Faculty of Engineering, University of Rijeka, Croatia. It incorporates relevant findings and insights cited from the paper to contribute to the discussion in this section.

ned. The first model for each variable exhibits superior fitting performance but comes with higher complexity. Conversely, the second model boasts lower complexity, which is desirable, but also features lower fitting performance. This approach enables the investigation of model parameters' influence, identifying significant model parameters for each prediction variable. Consequently, four regression models (M11 – M14) will be provided, compared, evaluated, and extensively discussed. Notably, the second proposed models (i.e., models with lower complexity) will be crafted by removing non-significant terms of the full quadratic model.

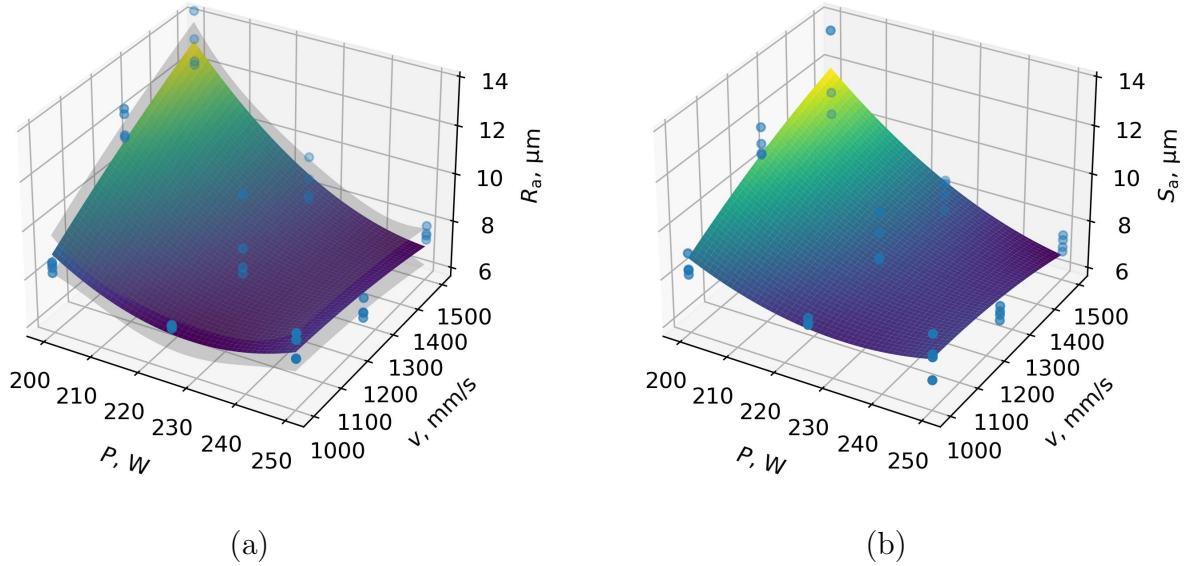
### 5.1. Line Average Surface Roughness

The comparison between models M11 and M12, assessing their fitting abilities through ANOVA, revealed that model M11 does not offer a superior fit over model M2. The calculated  $p$ -value using the ANOVA procedure was 0.581, exceeding the significance level ( $\alpha = 0.05$ ). Consequently, the influence of  $P_L$  and  $v$  on line average surface roughness ( $R_a$ ) can be effectively described without the term  $v^2$  (see Table A6). This observation is supported by the  $p$ -values reported for each parameter used in the development of model M11, as shown in Table A6.

Both models developed for  $R_a$  exhibit homoscedastic variance in the error term, as indicated by  $p$ -values exceeding 0.05 in both cases, a confirmation supported by the NCV score test results (Table 5.1). This finding suggests that the chosen levels of predictors do not significantly influence the variance of model errors, reinforcing the suitability of the OLS regression method. Moreover, the test confirms that  $R_a$  can be effectively modeled using both models across the entire range of  $P_L$  and  $v$  specified within the DoE, owing to consistent model error variance. Additionally, both models have normally distributed studentized residuals, as evidenced by  $p$ -values exceeding 0.05 in both cases according to the S-W normality test, a prerequisite for the valid application of the OLS regression method. High  $R^2$  and adjusted  $R^2$  values are evident for both models, as depicted in Table 5.1. The influence of  $P_L$  and  $v$  on  $R_a$  is illustrated in Figure 5.2a, with superimposed 95% confidence intervals calculated using equation (3-4).

**Table 5.1:** Regression models for  $R_a$  and their statistical properties (back transformed).

Model	$R_a$	$R^2$	Adj. $R^2$	$p$ -value (NCV)	$p$ -value (S-W)
M11	$R_a = 0.0021P^2 - 2.721 \times 10^{-6}v^2 - 0.7686P + 0.0563v - 0.0002Pv + 65.154$	0.852	0.827	0.417	0.074
M12	$R_a = 0.0021P^2 - 0.7686P + 0.0495v - 0.002Pv + 69.2928$	0.850	0.831	0.297	0.057


**Figure 5.2:** Response surfaces illustrating the effects of  $P_L$  and  $v$  on: (a)  $R_a$  values, with 95% confidence intervals displayed as gray surfaces, and (b)  $S_a$  values, incorporating experimental data shown as blue dots [184].

## 5.2. Area Average Surface Roughness

Using the ANOVA procedure to compare the  $S_a$  models, it was found that model M13 does not have a better fit than model M14 ( $p$ -value = 0.406). This indicates that the influence of  $P_L$  and  $v$  on  $S_a$  can be efficiently described without including the term  $v^2$  (see Table A7). The  $p$ -values for each parameter used in developing model M13 are listed in Table A7.

However, both models exhibit heteroscedastic variance of the error term, as indicated by the  $p$ -values being lower than 0.05 (see Table 5.2). As a result, the heteroskedasticity-robust HC3 method was used to evaluate the model coefficients obtained via the OLS method. This analysis confirmed the validity of previously determined model coefficients of terms stated in Table A7.

Consequently, confidence intervals are not shown in Figure 5.1b because the assumption of equal variance of residuals is violated. Instead, Figure 5.1b includes only the scatter plot

added to the response surface plot, illustrating both the experimentally measured data and the corresponding nonlinear regression model M13.

**Table 5.2:** Regression models for  $S_a$  and their statistical properties (back transformed).

Model	$S_a$	$R^2$	Adj. $R^2$	$p$ -value (NCV)	$p$ -value (S-W)
M13	$S_a = 0.0014P^2 - 4.123 \times 10^{-6}v^2 - 0.4884P + 0.0505v - 0.0002Pv + 37.256$	0.802	0.769	<0.001	-
M14	$S_a = 0.0014P^2 - 0.4884P + 0.0402v - 0.0002Pv + 43.526$	0.797	0.771	<0.001	-

A strong linear relationship ( $r = 0.948$ ) exists between  $R_a$  values measured with a contact profilometer and  $S_a$  values measured with a microscope. This correlation is evident when comparing the shapes of the response surfaces shown in Figure 5.2, where the shape and curvature are almost identical, confirming the relationship between these two measurements. Both  $R_a$  and  $S_a$  reach their maximum values in the C group of specimens, where  $P = 200$  W and  $v = 1500$  mm/s were used for the PBF-LB of Ti6Al4V alloy, resulting in  $R_a$  and  $S_a$  values of  $12.937 \mu\text{m}$  (std.  $1.039 \mu\text{m}$ ) and  $11.966 \mu\text{m}$  (std.  $1.821 \mu\text{m}$ ), respectively. This is due to the stacking and incomplete melting of powder particles near the surface, caused by the lowest utilized energy input ( $59.3 \text{ J/mm}^3$ ), consistent with findings in [11]. Comparing the surface topographies of the C group (with the highest mean  $R_a$  and  $S_a$  values) and the I group (with the lowest mean  $R_a$  and  $S_a$  values) in Figure 5.3a and 5.3b, it is clear that the C group exhibits higher peaks, reaching up to  $119.4 \mu\text{m}$ .

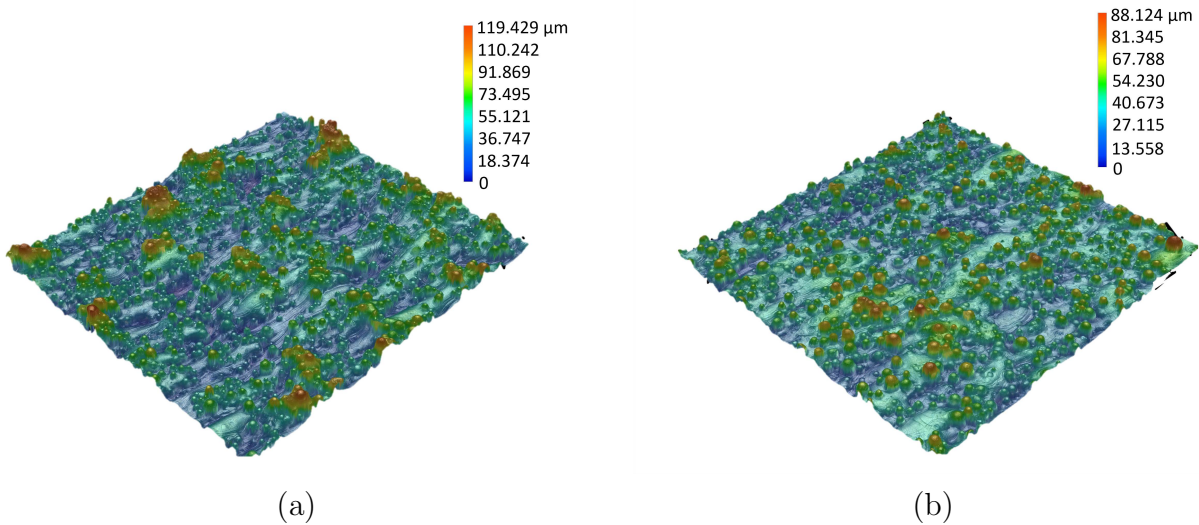


**Figure 5.3:** (a) Typical surface from the specimen group C, characterized by the highest  $R_a$  and  $S_a$  values measured, (b) Typical surface from the specimen group I, characterized by the lowest  $R_a$  and  $S_a$  values measured [184].

In the analysis, it's notable that the C group of specimens exhibits higher coefficients of variation (COV) compared to the I group, with values of 8.03% for  $R_a$  and 15.22% for  $S_a$  versus 3.26% for  $R_a$  and 4.36% for  $S_a$ , respectively. This suggests more irregular and uneven powder particle melting in the C group. Specifically, the I group displays  $R_a$  and  $S_a$  values of 7.612  $\mu\text{m}$  (std. 0.248  $\mu\text{m}$ ) and 7.195  $\mu\text{m}$  (std. 0.314  $\mu\text{m}$ ), respectively. Consequently, it can be inferred that surface roughness in the C group is comparatively lower and more consistent than in the I group.

The surface roughness of products produced via PBF-LB technology is primarily influenced by factors such as powder particle size distribution [185], inclination angle concerning the build platform [10], and heat treatment [3]. Consequently, various studies have reported a wide range of average surface roughness values for PBF-LB Ti6Al4V specimens [9, 18, 80, 111]. Regarding process parameters, Mierzejewska et al. discovered that energy densities ranging from 88 to 113 J/mm<sup>3</sup> correlate with decreased surface roughness, while energy densities between 44 and 63 J/mm<sup>3</sup> lead to increased surface roughness [3]. However, it is important to note that similar or identical energy density values can be achieved through entirely different combinations of  $P$  and  $v$ , as illustrated in Table 3.2. Thus, when values of a higher number of process parameters are changed iteratively from part to part, the energy density cannot be examined in isolation and independently used to interpret results [22].

Hence, it is necessary to separately analyze the effects of  $P$  and  $v$  on the prediction variables. Notably, the influence of  $v$  on  $R_a$  and  $S_a$  values is most pronounced at the lowest laser power level (200 W). Higher laser power levels diminish the impact of  $v$  on  $R_a$  and  $S_a$  while reducing  $v$  mitigates the influence of laser power on these values. Therefore, higher laser power values should be prioritized to achieve low surface roughness in Ti6Al4V PBF-LB parts. This conclusion aligns with previous findings indicating a decrease in  $R_a$  and  $S_a$  with increasing laser power [11, 186]. Elsayed et al. have observed a similar trend, even at lower laser power levels ranging from 35 to 50 W, where  $R_a$  decreases significantly with increasing  $P$  [49].

Research findings from [32, 187] indicate that elevating  $P$  increases energy density, thereby improving melt pool wettability. This effect diminishes differences in surface tensions, consequently mitigating the balling effect [49, 187]. Consequently, irregular bead formation or spherical drops decrease, reducing the average surface roughness. Higher  $P$  are recommended to achieve lower average surface roughness on both top and side surfaces [32, 33].



Mumtaz et al. support this [32], noting that higher  $P$  facilitate flattening of the melt pool surface and enhance wettability, thereby reducing the likelihood of the balling effect.

In this chapter, the average surface roughness of the PBF-LB Ti6Al4V alloy has been systematically studied through experimental tests, followed by comprehensive regression analysis and model verification. Nonlinear regression models were developed to correlate laser power and scanning speed with average surface roughness. The influence of position, laser power, and scanning speed on average surface roughness were also interpreted. These findings are particularly relevant for the PBF-LB manufacturing of Ti6Al4V alloy using laser powers between 200 and 250 W and scanning speeds between 1000 and 1500 mm/s. Nonlinear regression models, incorporating laser power and scanning speed as predictor variables, accurately describe the influence on the average surface roughness of the PBF-LB Ti6Al4V alloy. Specifically, laser power and scanning speed significantly affect average surface roughness values. Higher laser powers can reduce average surface roughness and diminish the effect of scanning speed. It is worth mentioning that  $R^2$  and adj.  $R^2$  values for the models developed for surface roughness have significantly higher values than those developed to model mechanical properties. This indicates that surface roughness can be modeled more reliably using the two proposed predictors ( $P$  and  $v$ ) compared to mechanical properties. Furthermore, the position of the specimen on the build platform showed a non-significant impact on average surface roughness. This systematically conducted experimental research, supported by comprehensive statistical analysis, enhances the understanding of how PBF-LB process parameters affect the surface roughness of the widely used Ti6Al4V alloy.

## 6. NUMERICAL MODELING

In the early design phase of a product with a lattice structure, it is crucial to connect its geometric features to its mechanical properties, particularly when specific load-bearing requirements are defined. Application of such products spans across many industries, including automotive, aerospace, and biomedicine [116]. When incorporated, lattice structures offer significant advantages due to their high strength-to-mass ratio, low weight due to high porosity, and customizable mechanical properties [116]. Numerical analysis can be utilized in this context to estimate mechanical properties, thereby saving time and financial resources typically spent on manufacturing specimens and conducting experimental tests. For this purpose, the geometric parameters of the BCC unit cell can be modified, thereby influencing the mechanical properties of the lattice structure. By customizing only the relative density, a wide range of values for  $E$ ,  $R_{p0.2}$ , and  $R_m$  can be achieved. However, in that way, the important information on how exactly specific unit cell features affect the mechanical response and properties is not included. The influence of the relative density, unit cell type, size, and geometric features on compressive mechanical properties is widely reported [122, 126, 127, 128]. However, their influence on the tensile mechanical properties of BCC lattice produced using PBF-LB Ti6Al4V alloy is rarely available. Therefore, the influence of the tapered struts by changing two diameters,  $d_{\text{end}}$  and  $d_{\text{mid}}$ , on tensile mechanical properties ( $E$ ,  $R_{p0.2}$ , and  $R_m$ ) will be investigated. A numerical analysis will be performed, and the results will be validated by comparing them with the experimental results.

For this purpose, the Abaqus 2022 software package will be used, which allows using either the Abaqus/Standard or Abaqus/Explicit solver. The Abaqus/Standard solver is designed for general-purpose simulations and employs implicit time integration. It is notably robust for simulations involving large deformations and efficient for small deformation simulations. This solver is primarily intended for linear and nonlinear static analysis, providing a smooth response without sudden jumps caused by complex contacts or damage evolution.

On the other hand, the Abaqus/Explicit solver is primarily intended to simulate material

behavior under high deformation rates, contacts, and impacts. The explicit time integration used by Abaqus/Explicit allows for solving problems with pronounced nonlinearities, sudden changes in material response, high speeds, deformations, and damage. Given that this thesis focuses on lattice structures subjected to quasi-static loading, involving complex contacts and material damage, the Abaqus/Explicit solver is chosen.

## 6.1. Material Modeling

In order to model material behavior observed on flat and lattice specimens, the elastoplastic model with continuum damage is used. This enabled the capture of the progressive damage on both flat and lattice specimens. The plastic behavior is modeled using the von Mises plasticity model where the yield function ( $f$ ) is defined as:

$$f = \sigma_e - \sigma_y, \quad (6-1)$$

where  $\sigma_e$  represents von Mises equivalent stress and  $\sigma_y$  is the yield stress. When  $f(\boldsymbol{\sigma}) < 0$  the material deforms elastically. If  $f(\boldsymbol{\sigma}) = 0$  the yielding begins, and when  $f(\boldsymbol{\sigma}, \boldsymbol{\varepsilon}^{\text{pl}}) \geq 0$  the plastic flow occurs, which is defined by the associated flow rule. For isotropic material, which was the case in this thesis, it holds that  $f(\boldsymbol{\sigma}) = 0$ . The associated flow rule defines the direction of flow of plasticity by the increment of the plastic strain tensor  $\boldsymbol{\varepsilon}^{\text{pl}}$ , once the yield has started, and it is defined as:

$$d\boldsymbol{\varepsilon}^{\text{pl}} = d\lambda \frac{\partial f}{\partial \boldsymbol{\sigma}} \quad (6-2)$$

In this context, the direction flow according to the normality hypothesis is defined with  $\partial f / \partial \boldsymbol{\sigma}$ , and its magnitude with  $\lambda$  which is the plastic multiplier. Furthermore, the  $d\lambda$  is the hardening parameter, and in the case of material hardening it is  $d\lambda > 0$ .

This flow rule is based on the assumption that the increase in plastic strain within a metallic material occurs in the same direction as the principal deviatoric stresses and is normal to the tangent of the yield surface. It also assumes that during plastic strain, the current stress state always remains on the current yield surface. Therefore, it is required that  $f(\boldsymbol{\sigma}) = 0$ . It is important to emphasize that the yield surface (or yield function) changes during plastic strain, but the current stress state always lies on the current surface during this evolutionary behavior.

The von Mises equivalent stress is defined as:

$$\sigma_e = \sqrt{\frac{3}{2}(\text{dev}(\boldsymbol{\sigma}) : \text{dev}(\boldsymbol{\sigma}))}, \quad (6-3)$$

with  $\text{dev}(\boldsymbol{\sigma})$  being the deviator of the Cauchy stress tensor. The Cauchy or true stress tensor is defined as:

$$\text{dev}(\boldsymbol{\sigma}) = \boldsymbol{\sigma} - p\mathbf{I}, \quad (6-4)$$

where  $p$  is the hydrostatic pressure and  $\mathbf{I}$  is the identity tensor.

Hence, the mechanical response of the PBF-LB Ti6Al4V alloy is characterized as follows: in the linear elastic region, the response is described using Young's modulus and Poisson's ratio; in the plastic region, the von Mises yield criterion and associated flow rule are applied, with hardening parameters identified through experimental tests; and the ductile damage criterion is employed to determine the onset of damage. Damage initiation occurs when the accumulated plastic strain reaches a critical value, which usually corresponds to the value of plastic strain when ultimate tensile strength is reached. Therefore, the damage is initiated when the state variable  $\omega_D$  reaches value of 1:

$$\omega_D = \sum \left( \frac{d\bar{\varepsilon}^{\text{pl}}}{\bar{\varepsilon}_D^{\text{pl}}} \right) = 1. \quad (6-5)$$

Here,  $d\bar{\varepsilon}^{\text{pl}}$  is the increment of equivalent plastic strain,  $\bar{\varepsilon}_D^{\text{pl}}$  represents the value of plastic strain at the onset of damage initiation, with summation across all increments. Once the damage has been initiated, the damage evolution stage starts, and the overall damage variable  $D$  is introduced. In this stage, the elastoplastic material's stress-carrying capability and elasticity are reduced as damage evolves. Therefore, the stress tensor is determined using the scalar damage equation:

$$\boldsymbol{\sigma} = (1 - D)\bar{\boldsymbol{\sigma}}, \quad (6-6)$$

where  $\bar{\boldsymbol{\sigma}}$  is the effective (undamaged) stress tensor and  $D \in [0, 1]$ . When the damage has been initiated, usually when the ultimate tensile strength is reached, the  $D = 0$ . As the damage evolves, the  $D$  increases until it reaches the value of 1, indicating material failure.

The value of the accumulated equivalent plastic strain at failure ( $\bar{\varepsilon}_f^{\text{pl}}$ ) depends on the

characteristic length of the finite element ( $L$ ), and therefore cannot be used as a material parameter to define the nature of progressive damage in reality. For this purpose, it is necessary to define the value of equivalent plastic displacement at failure  $\bar{u}^{\text{pl}}$  or fracture energy dissipation  $G_f$ . The fracture energy is defined as:

$$G_f = \int_{\bar{\varepsilon}_D^{\text{pl}}}^{\bar{\varepsilon}_f^{\text{pl}}} L \sigma_y d\bar{\varepsilon}^{\text{pl}} = \int_0^{\bar{u}_f^{\text{pl}}} \sigma_y d\bar{u}^{\text{pl}}, \quad (6-7)$$

where  $\bar{u}^{\text{pl}}$  represents the equivalent plastic deformation. The  $L$  depends on the type and order of the finite element, and for the first-order tetrahedral elements (C3D4), it can be calculated using the following equation:

$$L = \sqrt[3]{V_e}, \quad (6-8)$$

where  $V_e$  is the element volume. If it is assumed that the damage evolution is linear, the equivalent plastic displacement at failure  $\bar{u}_f^{\text{pl}}$  is defined as:

$$\bar{u}_f^{\text{pl}} = \frac{2G_f}{\sigma_{y0}}, \quad (6-9)$$

where  $\sigma_{y0}$  represents the yield stress at the time when the failure criterion is reached. In addition, the  $\bar{u}_f^{\text{pl}}$  can be defined as [188]:

$$\bar{u}_f^{\text{pl}} = L(\bar{\varepsilon}_f^{\text{pl}} - \bar{\varepsilon}_D^{\text{pl}}). \quad (6-10)$$

By substituting (6-10) into (6-9) the  $G_f$  can be defined as:

$$G_f = \frac{\sigma_{y0} L (\bar{\varepsilon}_f^{\text{pl}} - \bar{\varepsilon}_D^{\text{pl}})}{2}. \quad (6-11)$$

In order to fully characterize material elastoplastic behavior and its behavior with the evolution of damage, it is necessary to identify material parameters using the experimental data.

### 6.1.1. Identification and Validation of Material Parameters

Since there was no significant difference in the mechanical properties determined by tensile tests on flat specimens, specimen group D was selected for further consideration. The lattice specimens were also produced using this  $P - v$  combination:  $P = 225 \text{ W}$  and  $v = 1000$

mm/s. The mechanical properties for the D specimen group are reported in Table 6.1.

**Table 6.1:** Mechanical properties of PBF-LB Ti6Al4V alloy corresponding to specimen group D.

PBF-LB process parameters			Mechanical properties					
$P, W$	$v, \text{mm/s}$	ID	$R_{p0.2}, \text{MPa}$	$R_m, \text{MPa}$	Young's mod., GPa	Shear mod., GPa	Poisson's ratio, -	El. at break, %
225	1000	D	953 (17)	994 (11)	111.3 (0.6)	42.5 (0.2)	0.310 (0.004)	11 (1)

Notes: Results are expressed in the following form: mean value (standard deviation). Total of three specimens ( $n = 3$ ) were tested.

Therefore, Young's modulus is set to 111300 MPa, and the Poisson's ratio to 0.31. The relative density is set to  $4.432 \times 10^{-9} \text{ kg/m}^3$  [15], which is an important parameter when using an explicit solver to simulate mechanical response.

In order to describe plastic behavior, the engineering stress-strain curve has to be converted into the true stress-strain curve. This is achieved by using equations (3-24) and (3-25). As can be seen in Figure 6.1a there is a high agreement in the linear elastic region, while a minor difference occurs in the plastic region of the engineering stress-strain curve. To define plastic behavior, the D2 specimen has been selected as it represents a median plastic response. Therefore, its engineering stress-strain curve is converted into the true stress-strain curve and shown in the Figure 6.1b along with required  $\sigma_{y0}$ ,  $\bar{\epsilon}_D^{\text{pl}}$  and  $\bar{\epsilon}_f^{\text{pl}}$  values.

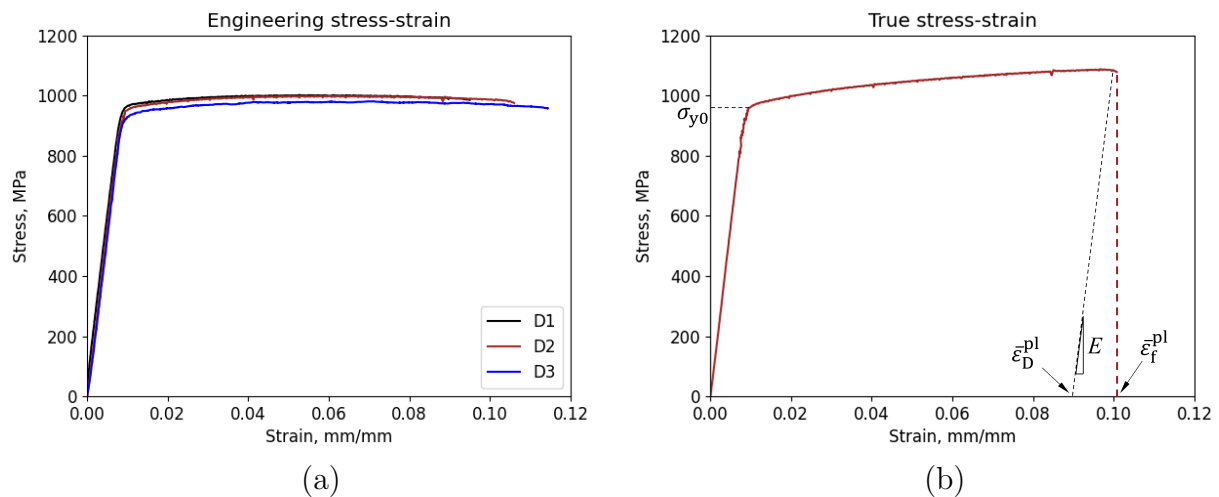


**Figure 6.1:** (a) Engineering stress-strain curve of D group specimens and (b) true stress-strain curve with marked  $\sigma_{y0}$ ,  $\bar{\epsilon}_D^{\text{pl}}$  and  $\bar{\epsilon}_f^{\text{pl}}$  values

It is worth noting that only the plastic part of the true stress-strain curve after the  $\sigma_{y0}$ , has to be used to describe the plastic behavior of the material. Hence, only the portion of the true stress-strain curve after the  $\sigma_{y0}$  has been selected, and the elastic strain component has been

removed from the total strain to obtain only the plastic strain component. Consequently,  $\sigma_{y0}$  and  $\bar{\varepsilon}_D^{\text{pl}}$  are set to 958 MPa and 0.09 mm/mm, respectively. Another important parameter required to define damage evolution is the  $G_f$ , which is calculated using equation (6-11). For tetrahedral finite elements with sizes of 0.3, 0.2, and 0.1 mm, the  $G_f$  is calculated to be 0.861, 0.574, and 0.287 N/mm, respectively.

The nonlinear analyses performed in this thesis also consider geometric nonlinearities by including the NLgeom option. In this way, the effects of large deformations are included, increasing the accuracy and representativeness of the model. The time and mass scaling methods are used to speed up the simulation process using Abaqus/Explicit, which reduces the required computation time. For this purpose, the time is set to 250 s, and the mass scaling factor to  $10^7$ . By using time and mass scaling, the inertial forces in the system are being increased. Therefore, their influence should be monitored to ensure the reliability of the results. Therefore, the influence of inertial forces is limited by keeping the system's kinetic energy within 5% of the system's internal energy. As stated in [189], the kinetic energy of the deforming material should not exceed 5% to 10% of its internal energy across the major part of the analysis.

The validation of the identified material and damage parameters was carried out by comparing the results of the tensile test simulation and the experimental results. For this purpose, the model of the flat specimen is meshed with linear (C3D4) and then quadratic (C3D10) tetrahedral elements, as this shape is suitable for meshing topologically complex lattice structures. Quadratic finite elements are defined by more nodes connected by nonlinear shape functions. Therefore, quadratic elements enable a more accurate representation of the model's geometry and a more precise mechanical response in cases of nonlinear behavior and large deformations. Compared to C3D4 elements, C3D10 elements have a higher degree of accuracy. However, they require longer computation times.

Figure 6.2 shows the boundary conditions used in the tensile test simulation. The translational and rotational displacements of the left end of the test sample are fully constrained. A reference point (RP) with a defined displacement of 2.5 mm in the direction indicated by the red arrow is placed on the right end of the test sample. The displacement defined at the reference point is mapped using additional constraints to the right gripping section of the test sample, symbolically represented by red circles. In this way, similar conditions prevailing during the tensile experiment are achieved.

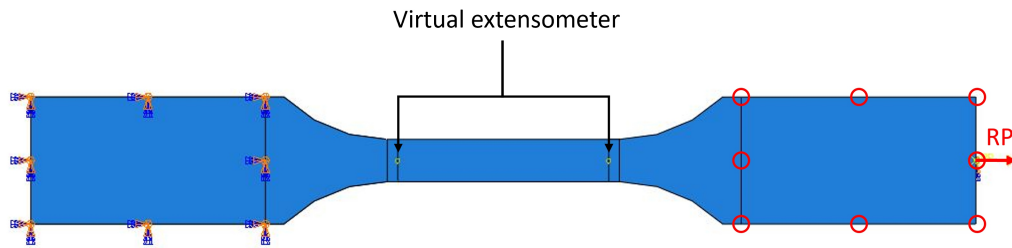


**Figure 6.2:** The boundary conditions set on the flat specimen for simulating tensile tests with added points used as a virtual extensometer to calculate engineering strain.

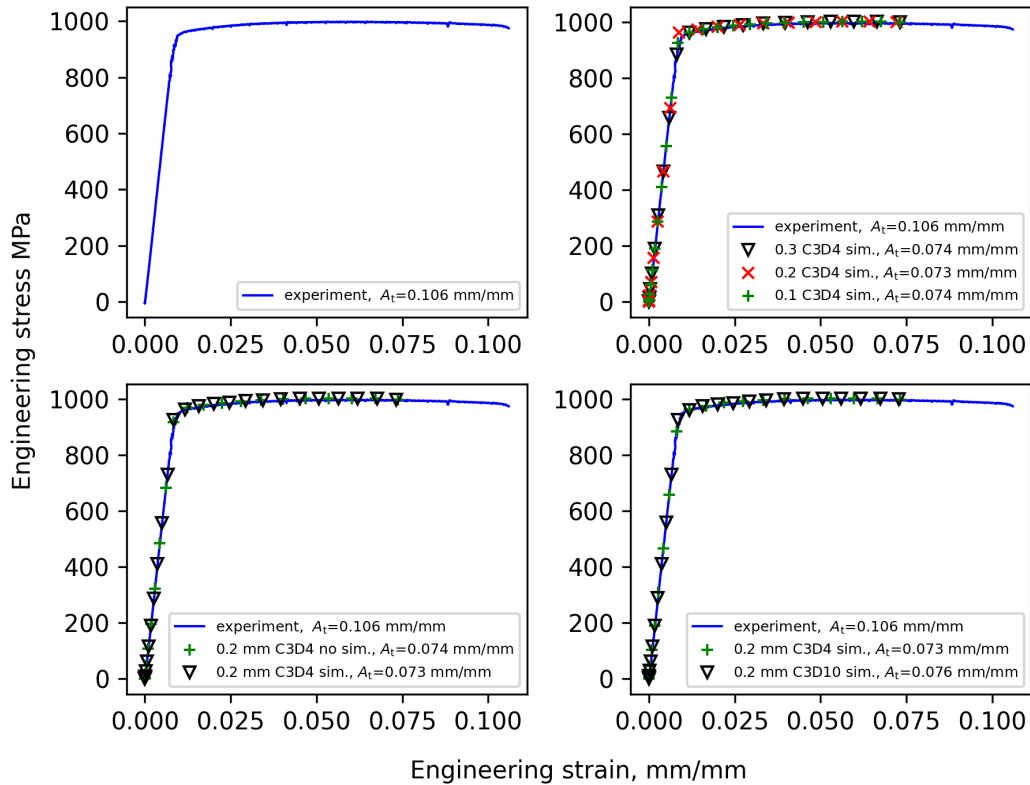
Within the measurement area of the test specimen, two points named *virtual extensometer* were added where axial displacements were measured. During the data post-processing phase of the simulation, these data were used to determine engineering strain, while the engineering stress data were calculated based on the initial cross-sectional area of the test specimen ( $4 \times 3 \text{ mm}^2$ ) and the force data collected from point RP.

Figure 6.3 shows the numerically estimated engineering stress-strain curves of flat specimens compared to the experimentally determined one on flat specimen D2, based on which the material parameters are identified. It can be observed that the size and type of the finite elements, as well as the symmetry boundary condition, do not significantly affect the elastoplastic behavior of the material, as the curves overlap.

The elongation at break ( $A_t$ ) did not show a high sensitivity to the element size, as the elongation at break is estimated to be 0.073 or 0.074 mm/mm, depending on the element size. If these values are compared with experimentally determined elongation at break value of 0.106 mm/mm, a difference higher than 0.03 mm/mm can be observed. This difference occurred due to the relatively low  $\bar{\varepsilon}_D^{\text{pl}}$  and  $G_f$  values identified from the experimental data. By increasing the  $\bar{\varepsilon}_D^{\text{pl}}$  value to higher values, such as 0.18 mm/mm, higher numerically estimated elongation at break values can be achieved without sacrificing the high agreement in elastoplastic response. However, that value is not selected since it is not in agreement with the experimentally observed behavior of the material. Furthermore, experimentally observed  $\bar{\varepsilon}_D^{\text{pl}}$ ,  $\bar{\varepsilon}_f^{\text{pl}}$  and  $G_f$  values provide a more conservative solution, pushing the numerical simulation more towards the safe side.

By further analyzing the results presented in Figure 6.3, it is evident that the symmetry boundary condition applied to the longitudinally sectioned specimen along its axis does not influence the elastoplastic response. In this case as well, the numerically estimated elongation at break values are lower than the experimentally determined one. Therefore,





**Figure 6.3:** Comparison of numerically estimated engineering stress-strain curves using different element type, size and symmetry condition with experimentally determined engineering stress-strain curve.

the applicability of the symmetry boundary condition is justified, as it provides accurate results while reducing computational time. The maximum true principal stress reached in the simulation is shown in Figure 6.4a, closely matching experimental results (see Figure 6.1b). The averaging threshold used at the stress contour plots for visualizing nodal results in Figures 6.4 and 6.10 was set to a default value of 75% to reduce numerical noise while preserving prominent variations and discontinuities in stress contour plots. In this way, smooth contour plots are achieved, ensuring a more coherent visualization of results at different sections of the model. No prominent necking occurred near the failure location, as depicted in Figure 6.4b, aligning with experimental observations.

Lastly, the influence of the element order is analyzed since quadratic tetrahedral (C3D10) elements could potentially result in higher accuracy when compared with linear tetrahedral (C3D4) elements. To verify the validity of using linear tetrahedral C3D4 elements, an additional comparison of these two types of finite elements was conducted (Figure 6.3). In this case, the simulation results also match the experimental test results. There is still a difference higher than 0.03 mm/mm in the elongation at break values, with the elongation at

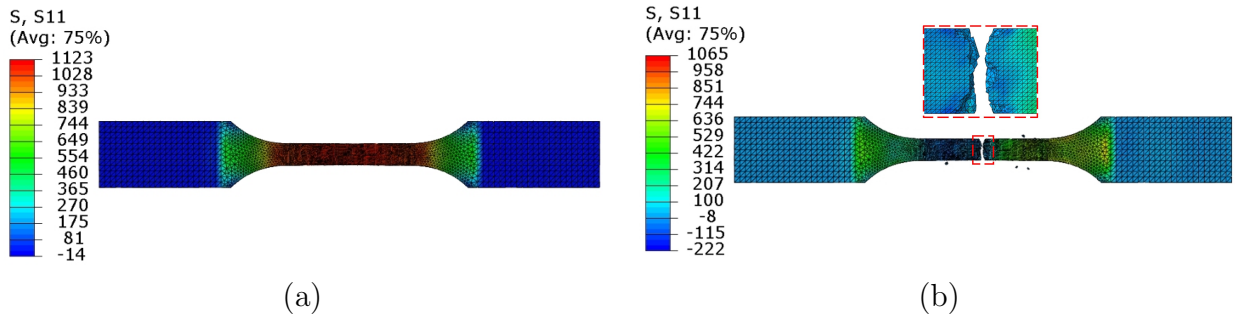


**Figure 6.4:** (a) True principal stress shown at the time step at which the ultimate tensile strength is reached and (b) failure of flat specimen.

break value obtained from the simulation being smaller than that determined experimentally in both cases.

Since no significant difference is observed between elastoplastic behavior and elongation at break values estimated using linear and quadratic elements, the linear elements with the size of 0.2 mm are selected for further analysis on lattice specimens as they are less computationally intensive. In addition, the applicability of selected element type and size will be investigated on lattice structures as well.

## 6.2. Lattice Specimen Modeling

The PBF-LB manufacturing process causes a staircase effect, resulting in strut diameters that surpass those outlined in the CAD models. Consequently, the average strut diameters measured were greater than the pre-manufacturing specifications. To address this discrepancy, the finite element analysis models include the actual average strut diameters as listed in Table 6.2. These actual diameters were measured twelve times prior to the tensile tests using a caliper with a resolution of 0.01 mm, repeatability of 0.01 mm, and a maximum error of 0.02 mm.

**Table 6.2:** Designed and actual strut diameters after PBF-LB.

$d_{\text{designed}}$ , mm	$d_{\text{major}}$ (std.), mm	$d_{\text{minor}}$ (std.), mm	$d_{\text{effective}}$ (std.)
0.6	0.58 (0.02)	0.98 (0.05)	0.78 (0.21)
0.8	0.78 (0.03)	1.18 (0.04)	0.98 (0.21)
1	0.98 (0.02)	1.41 (0.03)	1.20 (0.22)

The number of unit cells in lattice structures has a limited effect on elastic behavior, but its effect on plastic behavior is prominent [122]. It has also been reported that using just one

or a small number of lattice cells is sufficient to estimate the mechanical properties of lattice structures using the finite element method [190]. When using only one unit cell, making certain assumptions when applying boundary conditions is necessary, as the real interaction between neighboring unit cells is not present in that case. However, by using only one unit cell and periodic boundary condition, a higher discrepancy between experimental and numerical results is present while modeling lattice structures with a smaller number of unit cells in a row ( $4 \times 4$ ) [191].

### 6.2.1. Material Parameters

Determination of material parameters inherent to the solid material of the lattice structure is a challenging task. In general, mechanical properties such as  $E$ ,  $R_{p0.2}$ , and  $R_m$  can be determined using standardized tensile test specimens. However, those specimens often differ significantly from the actual unit cell strut in both thickness and shape, raising concerns about their representativeness. In the case of PBF-LB 316L alloy, Roach et al. considered six different specimen width and thickness combinations in the range between 6.25 mm and 0.4 mm and reported strong dependency on the effective yield strength, ultimate tensile strength and Young's modulus on the specimen size [192]. They have reported an increase in Young's modulus with an increase in specimen size. For designed strut diameters of 250, 300 and 350  $\mu\text{m}$ , Hossain et al. reported that  $E$  of the solid material does not change significantly with the build angle or strut diameter when determined using the average diameter method [70]. This is true for the narrow range of the considered diameters in that study. Razavi et al. showed that specimen thickness influences the mechanical properties under both quasistatic and fatigue loading [193]. Additionally, Moura et al. reported that a specimen's width and thickness influence fracture modes and associated micromechanisms [93]. Razavi et al. also stated that the geometry and material characteristics of additively manufactured parts are interrelated, implying that changes to part geometry will affect the manufacturing process [193]. Furthermore, using subsize or thin specimens to match the actual strut thickness makes tensile testing difficult, complicating the reliable determination of mechanical properties. By using nanoindentation, the determination of mechanical properties of small-volume specimens is possible. This opens up the possibility of performing tests on low-volume and topologically complex structures without producing subsize specimens for tensile tests. Using this method, it may become possible to avoid the difficulties

associated with conducting reliable tensile tests on subsize specimens. On the other hand, nanoindentation allows for determining mechanical properties in small-volume specimens. This technique enables testing on low-volume and topologically complex structures without creating subsize specimens for tensile testing.

As reported in Table 4.2, tensile tests performed on flat specimens of the D group resulted in a mean  $E$  of 113.3 GPa (std. 0.6 GPa). The mean  $E$  determined using nanoindentation on the same specimen group was 121 GPa (std. 8 GPa), as reported in Table 4.10. These values are both significantly higher than the value of 80.3 GPa reported by Murchio et al. [194], for the 45° oriented strut with a nominal diameter of 0.6 mm.

In the preliminary FEM analysis, the mechanical behavior of lattice specimens under tensile load was simulated using material parameters determined via tensile test performed on flat specimens. In that case, a large deviation between the numerical and experimental results of the lattice specimen was found. Given that the nanoindentation procedure provided even larger  $E$  when compared to tensile tests performed on flat specimens, numerical analysis performed using  $E$  determined via nanoindentation showed an even larger discrepancy between numerical and experimental results.

Therefore, in this thesis, material parameters used to model the behavior of lattice specimens are adopted from Murchio et al. [194]. They have determined the mechanical properties of a 45° oriented strut with a nominal diameter of 0.6 mm using DIC equipment. Therefore, the elastoplastic behavior of the lattice specimens will be described using the bilinear model. The  $E$  has been set in this thesis to 80300 MPa for the solid material of all considered lattice specimen configurations, corresponding to the 45° oriented strut with a nominal diameter of 0.6 mm [194]. The Poisson's ratio is set to 0.31 and mass density to 4.432 g/cm<sup>3</sup>, as was the case for the flat specimens. After the conversion of results into true stress and true strain form, the yield strength is set to 582.2 MPa, and the ultimate tensile strength to 768.3 MPa reached at the plastic strain of 0.031 mm/mm. Fracture strain is set to 0.031 mm/mm as well, stress triaxiality is set to 0.33, and strain rate is set to 0. Damage evolution is defined through fracture energy considering characteristic element length. Therefore, for the element size of 0.2 mm the  $G_f$  is calculated using equation (6-11) to be 0.36 N/mm.

### 6.2.2. Boundary Conditions

To model the behavior of the lattice specimen under tensile loading, the analytical rigid surface is used to apply the load to the nodes of the observed lattice specimen, as shown in Figure 6.5. For this setup, the analytical rigid surface is displaced by 0.6 mm, with the remaining five degrees of freedom restricted at one point. The displacement of the analytical rigid surface is defined using a smooth step function to minimize inertial forces at the start and end of the simulation. To reduce computational time, the simulation time period is set to 1 s with a mass scale factor of 1000. This approach results in a simulation period time approximately 90 times shorter than the actual duration required for experimental tests on lattice specimens, while the mass of the specimen in the simulation is 1000 times greater than its actual mass. The one-eighth symmetry boundary condition is applied to reduce the computational time further. A reference point is positioned on the analytical rigid surface where the reaction force, displacement, and system's energies are recorded. During post-processing, engineering stress and strain are calculated based on the reaction force and displacement data. The nominal area of the lattice specimen ( $400 \text{ mm}^2$ ) is used to compute the engineering stress. Additionally, a tied (bonded) contact is established between the lattice structure and the analytical rigid surface.

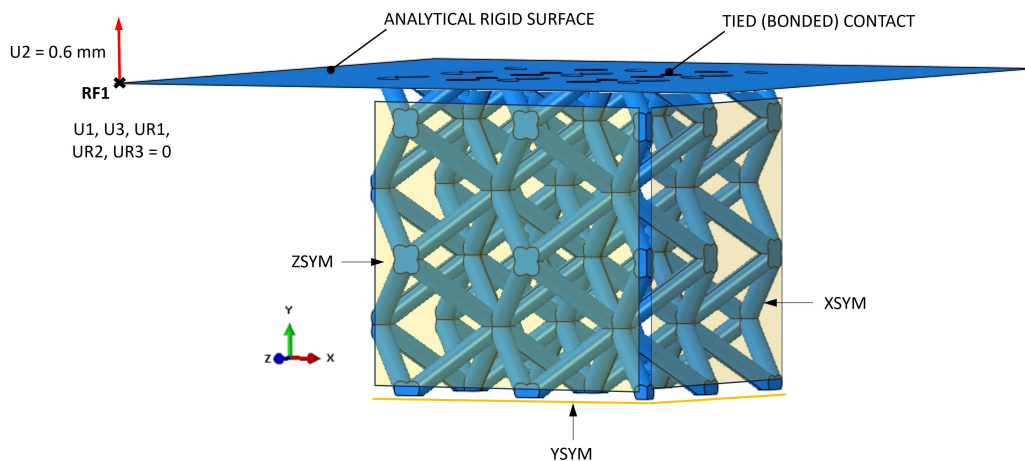


**Figure 6.5:** *FE model with analytical rigid surface, reference point, boundary conditions and constraints.*

### 6.2.3. Mesh Sensitivity Analysis

The convergence analysis is performed to identify the appropriate number of linear tetrahedral elements per one-unit cell. For this purpose, six different options have been considered, as shown in Figure 6.6. It can be seen that by increasing the number of elements, both  $E$  and  $R_m$  tend to converge while computational time increases. The balance between the accuracy and computational time is achieved by setting approximately 6378 elements per unit cell, corresponding to an element size of 0.2 mm. Therefore, this element size has been selected for further analysis.

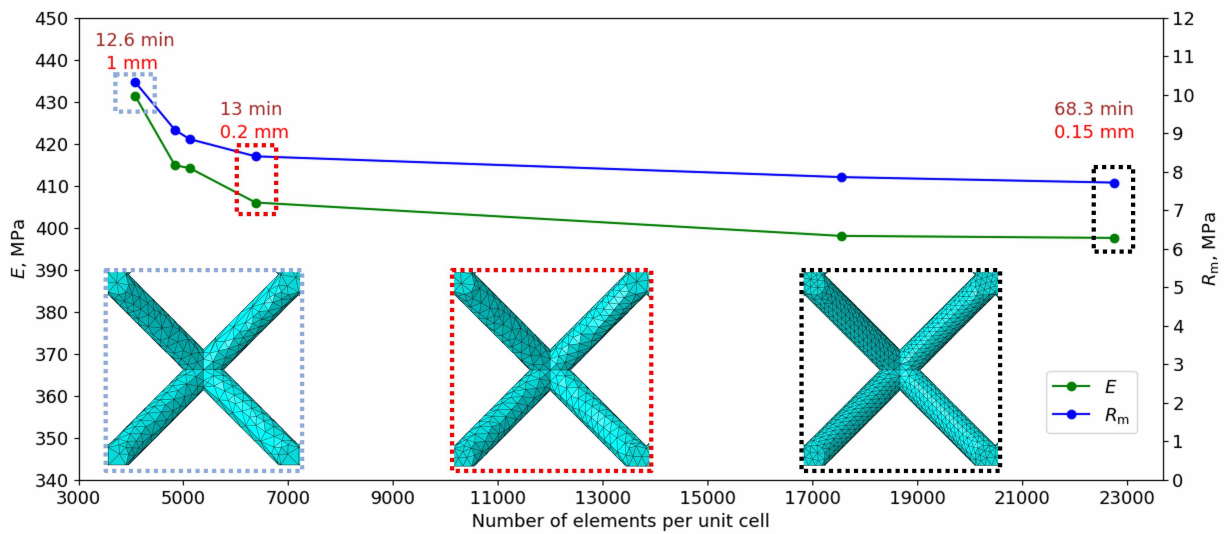


**Figure 6.6:** Convergence of  $E$  and  $R_m$  respect to the number of finite elements per unit cell (brown text indicates the computational time required to complete simulation, red text indicates the element size).

The applicability of symmetry boundary conditions to model the behavior of lattice specimens subjected to tensile load is also tested. The symmetry boundary condition offers a reduction in time by reducing the domain, which needs to be discretized using finite elements. In this way, the computational time is significantly reduced. The BCC unit cells considered within this thesis have 3 planes of symmetry, making lattice specimens consisting of those unit cells appropriate for applying 3 planes of symmetry boundary conditions. In this way, only one-eighth of the entire model is used in the analysis, as shown in Figure 6.7. By comparing the engineering stress-strain response of the lattice specimen, it can be seen that the curves overlap, with a difference present only in the upper part. This is attributed to the higher number of potential damage initiation sites when using a specimen model without symmetry, as the domain has more unit cells and critical locations prone to

damage initiation. As a result, the damage initiates and evolves earlier, leading to earlier failure of the lattice specimen. Consequently, there is a 2.88% increase in  $R_m$  when using 3-plane symmetry boundary conditions compared to the result obtained without symmetry boundary conditions.

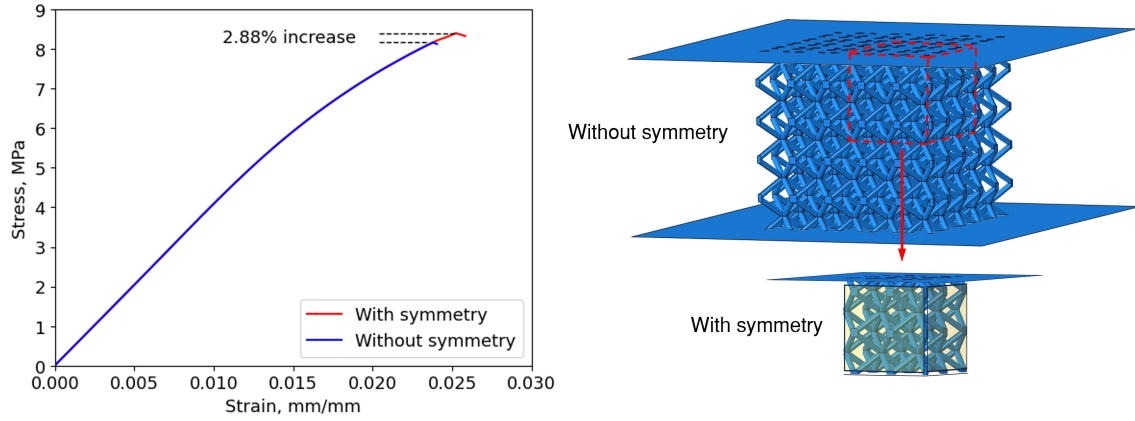


**Figure 6.7:** Influence of symmetry boundary condition on engineering stress-strain curve on the example of 06-06-2 lattice specimen configuration.

The ratio of kinetic energy ( $E_{KE}$ ) to internal energy ( $E_I$ ) within the system is tracked throughout each simulation since time and mass scaling methods are used to decrease computational time. In Figure 6.8a, it is shown that  $E_{KE}$  for the major part of the simulation remains under 5% of  $E_I$ , thereby minimizing the effects of inertial forces.

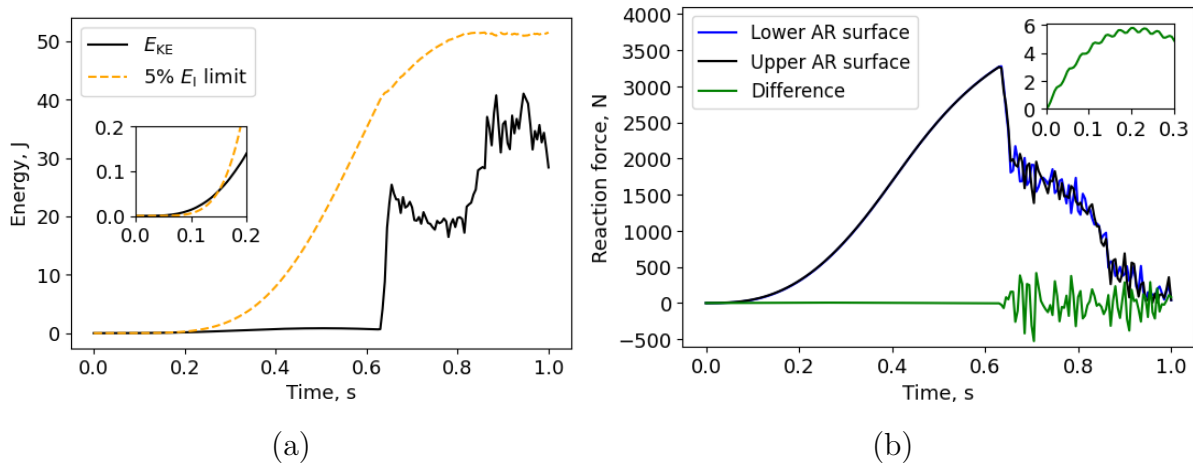


**Figure 6.8:** (a) Internal and kinetic energies of the 06-06-2 lattice specimen while simulating tensile test, (b) reaction forces recorded at the upper and lower analytical rigid surface and their difference.

It can also be observed that at the initial part of the simulation, when time is no higher than 0.15 s, the  $E_{KE}$  is slightly higher than the 5% of  $E_I$  limit. In that case,  $E_{KE}$  is lower

than 0.1 J. Such low  $E_{KE}$  is achieved by applying the smooth step displacement to the lattice specimen. As a result,  $E_{KE}$  does not influence the mechanical response significantly, as with such low energy values, the inertial forces at the beginning of the simulation are low, as shown in Figure 6.8b. The influence of the inertial forces induced by the time and mass scaling approach is illustrated in the example of the 06-06-2 lattice without applied symmetry boundary condition, as this approach enables recording of the reaction forces at both analytically rigid surfaces attached to the upper and lower part of the lattice specimen. If the system has high  $E_{KE}$ , substantial inertial forces will occur, causing a difference in the reaction forces monitored on the two analytically rigid surfaces. As can be seen in Figure 6.8b, the difference in reaction forces of the undamaged lattice reaches the value of 6 N at 0.2 s and starts to drop until the damage initiates after 0.6 s, where fluctuations and higher differences in reaction forces can be observed.

When damage progresses across multiple struts, a disturbance in  $E_{KE}$  also becomes apparent, indicating the presence of elevated inertial forces. However, these disturbances do not influence estimated values of Young's modulus, yield strength, and ultimate tensile strength, as these mechanical properties of the lattice specimen were derived from the initial part of the stress-strain curve, where damage has not yet occurred.

### 6.2.4. Validation of Results

By comparing numerical and experimental results shown in Figure 6.9, a high agreement can be observed in the elastoplastic region of the material's behavior. The proposed approach provides as well reasonable estimate of the lattice specimen behavior under progressive damage. In this region, a higher difference between experimentally determined and numerically estimated mechanical responses is expected due to the many factors involved, such as the complex geometry of lattice structures with many potential damage initiation sites, inevitable manufacturing defects, dimensional inaccuracies, inaccuracies in parameter estimation, mesh dependency, and others.

After manufacturing, actual strut diameters are larger than the designed ones in the CAD model (see Table 6.2). Therefore, the numerical analysis of lattice specimens with corrected  $d_{end}$  and  $d_{mid}$  diameters is compared with the corresponding experimental pair. In this way, corresponding models in the numerical analysis have effective mean  $d_{end}$  and  $d_{mid}$  diameters in size matching closer to the actual size measured on actual lattice specimens,



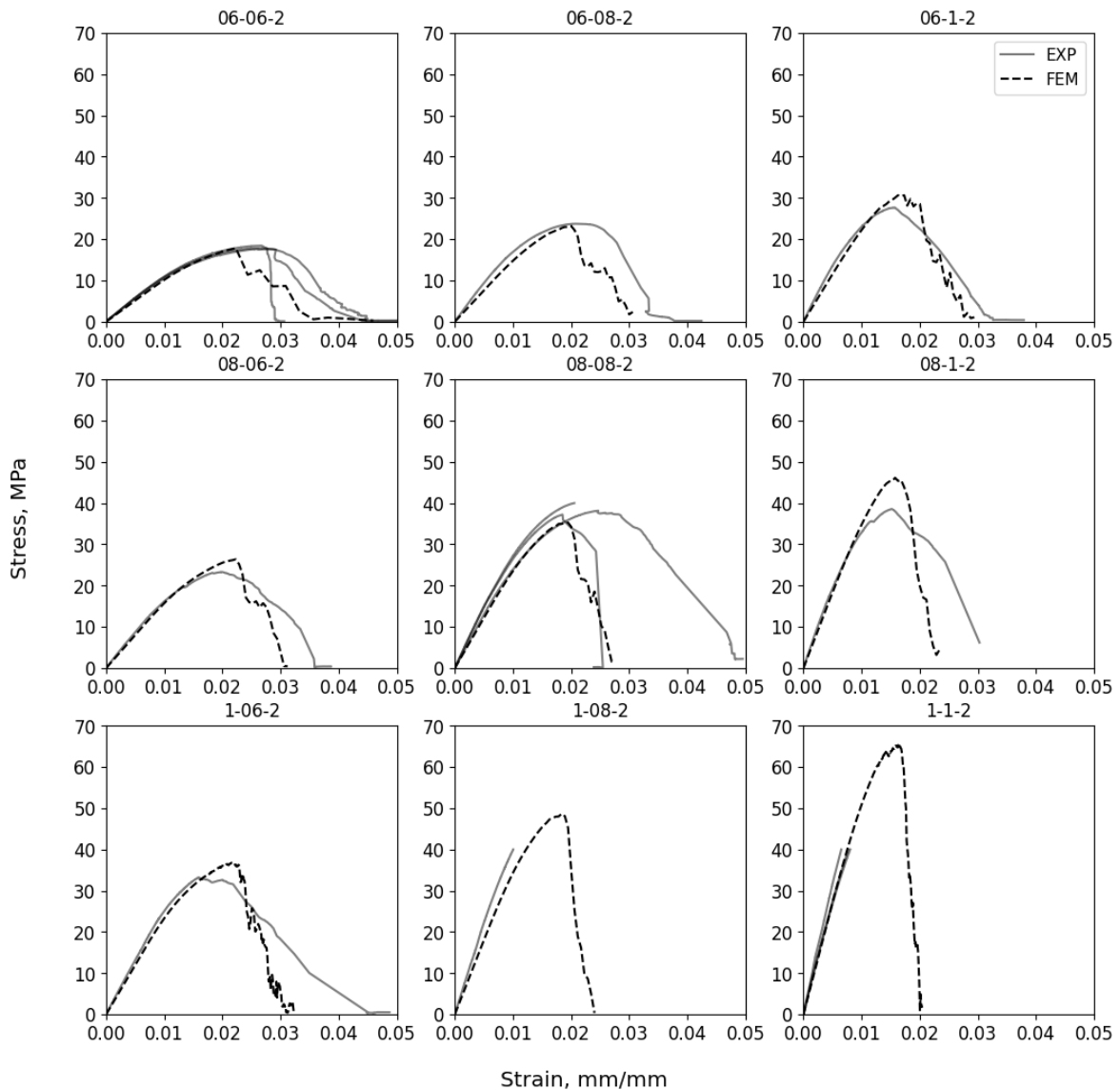


**Figure 6.9:** Comparison between experimental and numerical results of lattice specimens with corrected strut diameters.

ensuring a representative comparison. In numerical analysis, all lattice specimens with corrected diameters failed at the nodal regions as shown in Figure 6.10, matching experimental observations. However, in numerical analysis, planar failure occurred at all lattice specimen configurations, while in experiments, struts failed along oblique planes (see Figure 4.17).

These discrepancies in failure planes observed experimentally and numerically are attributed to differences between these two approaches. The proposed numerical approach simplifies actual geometry by using effective mean  $d_{\text{end}}$  and  $d_{\text{mid}}$  diameters. Furthermore, it neglects inevitable surface and internal defects inherent to the PBF-LB process and potential specimen warping induced due to inevitable residual stresses. If the specimen is even slightly warped or misaligned when performing tensile tests, the high clamping loads might induce

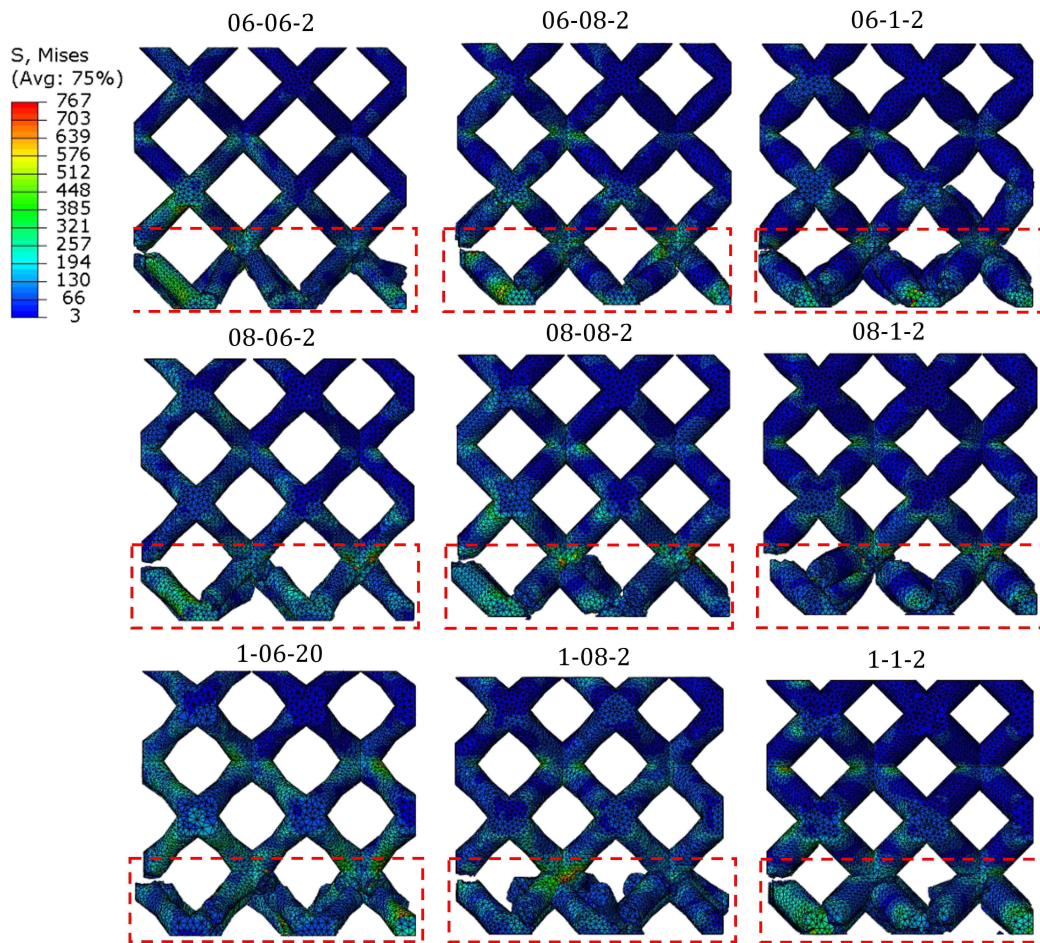


**Figure 6.10:** Failure of different lattice configurations with corrected effective mean  $d_{\text{end}}$  and  $d_{\text{mid}}$  diameters and 1/8th symmetry (damaged struts are marked with red rectangle, and averaging threshold was set to the default value of 75%).

additional bending stress to the lattice region and induce differences between experimental and numerical results. Despite differences in failure planes, a high agreement exists between numerically estimated and experimentally determined mechanical engineering stress-strain curves in elastic regions. As a result, numerical analysis can be used to estimate the mechanical properties of lattice specimens, which is helpful in the early engineering design phase. In this way, the effects of many factors involved in specimens' manufacturing and experimental testing can be isolated and eliminated, enabling only the investigation of desired parameters. This, in turn, provides flexibility in investigating various lattice configurations, reducing the necessity of performing costly and time-consuming manufacturing and experimental testing. For this reason, it is beneficial to establish simple regression models that enable quick estimation of mechanical properties such as  $E$ ,  $R_{p0.2}$ , and  $R_m$ .

### 6.2.5. Regression Models

During the initial design phase of a product with a lattice structure, it is beneficial to connect its geometric characteristics to its mechanical properties, particularly when specific load-bearing requirements are defined. For BCC unit cells, altering various geometric parameters can significantly impact the mechanical properties of the lattice. Adjusting the relative density alone can achieve a broad range of  $E$ ,  $R_{p0.2}$ , and  $R_m$  values. However, this approach does not provide detailed insights into how specific unit cell features affect mechanical performance. Therefore, this investigation will focus on how changing the diameters of tapered struts, specifically  $d_{\text{end}}$  and  $d_{\text{mid}}$  in the range between 0.6 and 1.2 mm, influences the tensile mechanical properties ( $E$ ,  $R_{p0.2}$ , and  $R_m$ ).

By changing the  $d_{\text{end}}$  and  $d_{\text{mid}}$  diameters in the proposed range, the numerically estimated  $E$  ranges from 406 MPa to 5200 MPa. For this purpose, the regression model reported in Table 6.3 can be used. With its high  $R^2$  value, it allows for an accurate description of the influence of the  $d_{\text{end}}$  and  $d_{\text{mid}}$  diameters on  $E$  with a residual standard error of 48 MPa. In ANOVA analysis, all terms of full quadratic models are identified as significant (see Table A8), suggesting that the included variables and their relationships are very important in modeling  $E$ . The model exhibits homoscedastic variance in the error term, as indicated by the NCV test's  $p$ -value of 0.084. It has normally distributed studentized residuals as well since the S-W test's  $p$ -value is 0.225.

**Table 6.3:** Regression model for  $E$  of lattice specimens and its statistical properties.

Model	$E$	$R^2$	Adj. $R^2$	$p$ -value (NCV)	$p$ -value (S-W)
M15	$E = 1828.6d_{\text{end}}^2 + 2778.2d_{\text{mid}}^2 - 6122.8d_{\text{end}} - 8221.3d_{\text{mid}} + 7580.2d_{\text{end}}d_{\text{mid}} + 4738.3$	0.9984	0.9982	0.084	0.225

The numerical estimation of  $E$  is in high agreement with experimental results, especially when combining lower values of the  $d_{\text{end}}$  and  $d_{\text{mid}}$  diameters. As both diameters increase, higher errors between numerical and experimental results can be observed, as shown in Figure 6.11. This discrepancy between experimental and numerical results is attributed to higher actual values of  $E$  specific to larger strut diameters. This opens the possibility to further increase the accuracy of numerical analysis in the estimation of  $E$  of the lattice specimen by assigning higher  $E$  values to the solid material of lattice specimens with larger strut diameters. This can be easily achieved when non-tapered struts are being modeled, while

tapered struts with variable diameters along their length require higher effort when assigning size-dependent mechanical properties specific to each location. The significant variation in the experimentally determined  $E$  for group 1-1-2 is attributed to damage sustained by two specimens during manufacturing. Specifically, the junctions between the solid and lattice parts were compromised, leading to decreased stiffness in these specimens and a subsequent reduction in  $E$ .

In Figure 6.11 and 6.12, the horizontal shift of red dots with respect to the green dots can be observed. This is due to the fact that the actual mean  $d_{\text{end}}$  and  $d_{\text{mid}}$  diameters measured on the specimen are different than those defined using CAD model. The regression models and response surfaces are created based on the numerical analysis performed using  $d_{\text{end}}$  and  $d_{\text{mid}}$  diameters in the range between 0.6 mm and 1.2 mm with increments of 0.1 mm.

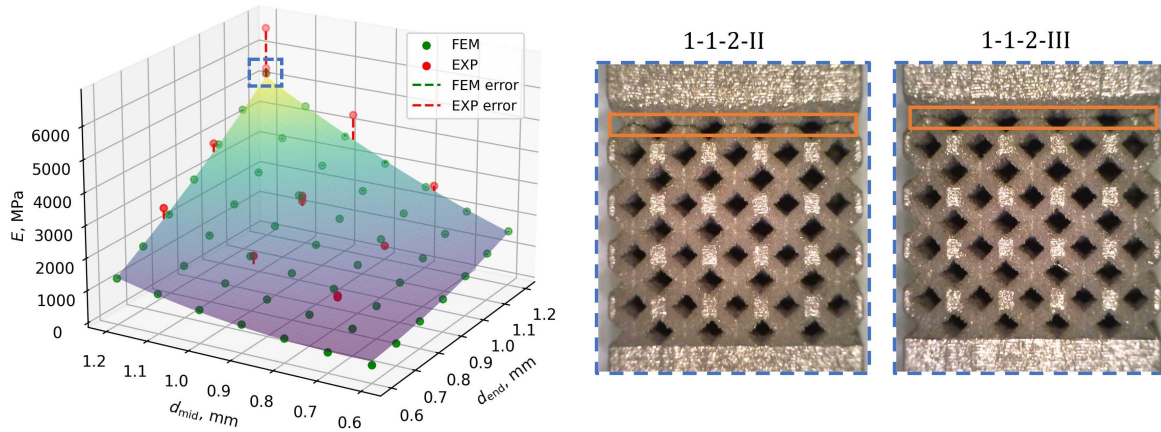


**Figure 6.11:** Response surface plot showing the influence of  $d_{\text{end}}$  and  $d_{\text{mid}}$  on Young's modulus highlighting the damage at the struts occurred while manufacturing lattice specimens 1-1-2-II and 1-1-2-III (the red dashed line indicates the difference between the experimental results and the model at a given point).

Furthermore, by changing the  $d_{\text{end}}$  and  $d_{\text{mid}}$  diameters the  $R_{p0.2}$  and  $R_m$  can be changed as well. By changing the  $d_{\text{end}}$  and  $d_{\text{mid}}$  diameters in the range between 0.6 mm and 1.2 mm the  $R_{p0.2}$  is numerically estimated to be in the range between 7.6 and 62.9 MPa. The influence of two diameters on the  $R_{p0.2}$  is described with high accuracy using the model reported in Table 6.4. This model has a high  $R^2$  value of 0.9996 and a residual standard error of 0.3 MPa. All terms of full quadratic models are identified as significant in ANOVA analysis (see Table A9), suggesting the high importance of the included variables and their relationships in modeling  $R_{p0.2}$ . The model has homoscedastic variance in the error term, as confirmed by the NCV test's  $p$ -value of 0.268. It also has normally distributed studentized

residuals since the S-W test's  $p$ -value is 0.262.

**Table 6.4:** Regression model for  $R_{p0.2}$  of lattice specimens and its statistical properties.

Model	$R_{p0.2}$	$R^2$	Adj. $R^2$	$p$ -value (NCV)	$p$ -value (S-W)
M16	$R_{p0.2} = 6.662d_{\text{end}}^2 + 17.158d_{\text{mid}}^2 - 41.373d_{\text{end}} - 66.982d_{\text{mid}} + 87.040d_{\text{end}}d_{\text{mid}} + 32.799$	0.9996	0.9995	0.268	0.262

The influence of the two considered tapering diameters on the  $R_{p0.2}$  is shown in Figure 6.12a. In this case, higher agreement between numerical and experimental results can also be found when lower combinations of the  $d_{\text{end}}$  and  $d_{\text{mid}}$  diameters are being used. This is reasonable since the behavior of the solid material in the plastic region is described according to the results provided for the struts having a nominal diameter of 0.6 mm [194]. Therefore, a higher agreement between experimental and numerical results is expected for the diameters closer to the value of 0.6 mm. A higher difference between numerical and experimental results can be observed with the increase in diameters.

By adjusting the diameters  $d_{\text{end}}$  and  $d_{\text{mid}}$  within the range of 0.6 mm to 1.2 mm, the  $R_m$  value is numerically estimated to be in the range between 8.4 and 65.3 MPa. The effect of these diameters can be accurately described using models outlined in Table 6.5. The full quadratic model M17 has identical  $R^2$  value, as the model M18 with removed  $d_{\text{end}}^2$  term. The  $d_{\text{end}}^2$  term is removed as the  $p$ -value determined using ANOVA for the given term is 0.295 (see Table A10).

By comparing models M17 and M18 using the ANOVA procedure to evaluate their fitting performance (i.e., testing if the difference in their residual sum of squares is statistically significant), it is found that model M17 does not outperform model M18. The ANOVA test resulted in a  $p$ -value of 0.295, which is above the level of significance. Consequently, the effect of the tapering diameters on the  $R_m$  can be effectively described without including the  $d_{\text{end}}^2$  term. The model M18 has a high  $R^2$  value and a residual standard error of 0.65 MPa. The model exhibits homoscedastic error variance, confirmed by the NCV test's  $p$ -value of 0.394, and its studentized residuals are normally distributed, as indicated by the S-W test's  $p$ -value of 0.293.

Similarly, higher agreement between numerical and experimental results is observed when smaller  $d_{\text{end}}$  and  $d_{\text{mid}}$  diameters are used. The response surfaces of  $R_{p0.2}$  and  $R_m$  have similar shapes, as illustrated in Figure 6.12 and their estimations for the given combination of

**Table 6.5:** Regression models for  $R_m$  of lattice specimens and their statistical properties.

Model	$R_m$	$R^2$	Adj. $R^2$	$p$ -value (NCV)	$p$ -value (S-W)
M17	$R_m = 2.859d_{\text{end}}^2 + 11.578d_{\text{mid}}^2 - 29.532d_{\text{end}} - 57.024d_{\text{mid}} + 85.878d_{\text{end}}d_{\text{mid}} + 23.855$	0.998	0.9978	0.358	0.316
M18	$R_m = 11.578d_{\text{mid}}^2 - 24.386d_{\text{end}} - 57.024d_{\text{mid}} + 85.878d_{\text{end}}d_{\text{mid}} + 21.654$	0.998	0.9978	0.394	0.293

diameters are similar as there is no prominent strain hardening. Once the  $R_{p0.2}$  of the lattice specimen is reached, a relatively small increase in plastic strain triggers damage initiation, leading to a sudden drop in load-bearing capacity after reaching  $R_m$ .

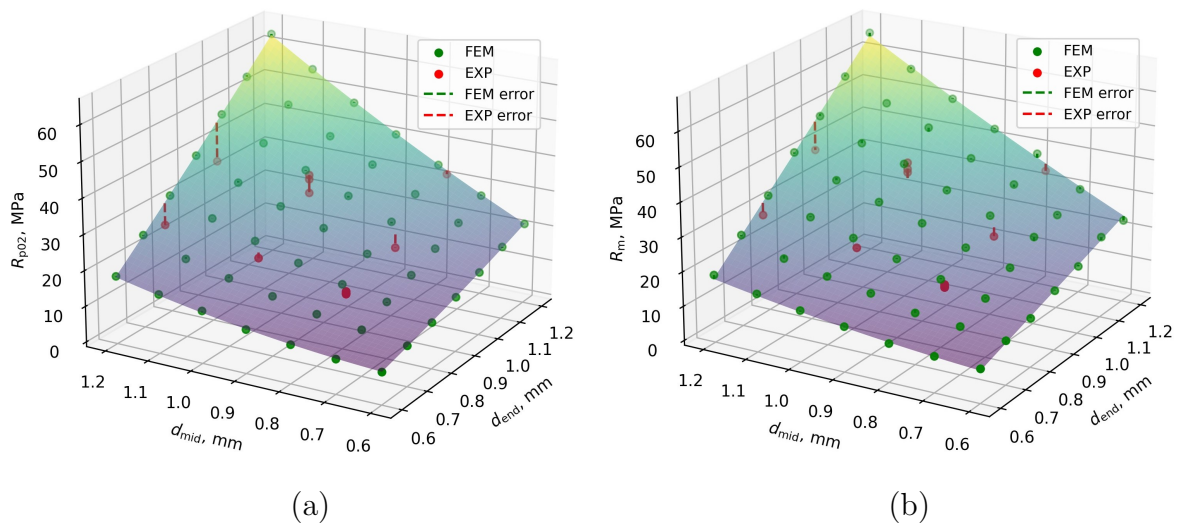


**Figure 6.12:** Response surface plot showing the influence of  $d_{\text{end}}$  and  $d_{\text{mid}}$  on (a)  $R_{p0.2}$  and (b)  $R_m$  (the red dashed line indicates the difference between the experimental results and the model at a given point).

Analyzing the numerical results reveals that within the tapering diameter range of 0.6 mm to 1.2 mm for  $d_{\text{end}}$  and  $d_{\text{mid}}$ , the values of  $E$ ,  $R_{p0.2}$ , and  $R_m$  can be increased by 12.8, 8.2, and 7.7 times, respectively. This demonstrates a broad spectrum of achievable  $E$ ,  $R_{p0.2}$ , and  $R_m$  values by simply tapering the struts using the two proposed diameters.

In this chapter, the tensile behavior of 49 lattice specimen configurations with different tapering diameters was simulated. In order to simulate the elastoplastic and damage behavior of lattice specimens, material parameters were adopted from [194], since material parameters determined on flat specimens resulted in a high discrepancy between numerically and experimentally observed lattice specimen behavior. Given that elastoplastic and damage behavior is being modeled, high computational time is typical, particularly for lattice specimens

employing large strut diameters. After performing mesh sensitivity analysis, it was found that linear tetrahedral elements with a size of 0.2 mm provide a balance between accuracy and computational time. Furthermore, the applied one-eight symmetry boundary condition provides additional reduction in computational time without compromising the accuracy. When compared with experimental results, a high agreement in elastoplastic behavior was found, especially when lattice specimens with smaller struts were compared. When numerical results of lattice specimens with larger strut diameters are compared with experimental results, a lower agreement is evident. This outcome is reasonable since material parameters experimentally determined on struts with a nominal diameter of 0.6 mm were used in all simulations. Due to the inevitable size effect, actual mechanical properties increase as strut diameter increases. Therefore, a higher discrepancy between numerical and experimental results is expected when comparing lattice configurations with larger diameters.

Furthermore, it was demonstrated that the influence of tapering, by altering  $d_{\text{end}}$  and  $d_{\text{mid}}$ , on mechanical properties, can be described with high accuracy using quadratic regression models. According to the NCV and S-W tests, there is no need to doubt the normality of the distribution of studentized residuals and the models' homoscedasticity. Therefore, developed models can be reliably used to estimate  $E$ ,  $R_{p0.2}$ , and  $R_m$  in the considered strut diameter range between 0.6 and 1.2 mm.

Concerning the lattice specimen behavior, once the progressive damage started, a decent agreement between numerically estimated and experimentally observed behavior was found. It should be noted that material behavior under progressive damage is highly mesh-dependent, and reliable experimental determination of material parameters is challenging. Therefore, somewhat higher deviations of numerical results in this region are typical in contrast to the elastoplastic region. All lattice specimens with corrected diameters failed at the nodal regions, aligning with experimental observations. Nevertheless, while numerical analysis indicated planar failure across all lattice specimen configurations, experimental results showed that struts failed along oblique planes. Presumably, this occurred due to the differences between the proposed numerical and experimental approaches, given that the proposed numerical approach neglects aspects, such as defects, imperfections, and dimensional inaccuracies inherent to actual lattice specimens used in experimental tests. Nevertheless, the numerical approach proposed in this thesis enables reliable estimation of  $E$ ,  $R_{p0.2}$ , and  $R_m$  of lattice specimens subjected to tensile load.

## 7. DISCUSSION

Additive manufacturing technologies facilitate the efficient fabrication of components with complex geometries using different process parameters. Consequently, the mechanical properties and surface roughness of these components might differ when compared to each other and to those components produced using conventional methods such as casting, forging, or machining. Altering various combinations of process parameters in additive manufacturing technology can potentially customize the mechanical performance and surface roughness to align with the specific design requirements of the component. Additionally, modifying unit cells to form lattice structures in specific component locations may further widen the range to customize mechanical performance. Therefore, this study aimed to investigate if changing laser power and scanning speed in the PBF-LB process used to manufacture Ti6Al4V components could allow for customization of mechanical performance and surface roughness to meet specific design criteria. Furthermore, it examined whether modifying the unit cells in lattice structures could broaden the spectrum of achievable mechanical properties.

For this purpose, state-of-the-art additive manufacturing technologies were thoroughly reviewed, and the PBF-LB technology was selected to process Ti6Al4V alloy powder. To achieve the desired product quality, the parameters of the PBF-LB process should be appropriately set. Among those process parameters, laser power and scanning speed are of practical industrial relevance for customizing the product quality regarding their mechanical properties and surface roughness, as those process parameters can be easily tuned in a wide range. To ensure stable processing of Ti6Al4V alloy powder using the PBF-LB process, the laser power levels are set to 200, 225, and 250 W, while scanning speed levels to 1000, 1250, and 1500 mm/s.

The influence of the two process parameters on mechanical properties at the macro-scale was investigated on flat specimens vertically oriented during processing to reduce residual stresses, achieve the highest dimensional accuracy, and ensure equal thermal history across the whole gauge length. After annealing heat treatment, the high  $R_{p0.2}$  and  $R_m$  were achieved



for all combinations of process parameters. The achieved  $R_m$  values were in the range between 975 MPa (std. 21 MPa) and 1003 MPa (std. 11 MPa), which is comparable to the typical  $R_m$  of  $1006 \pm 10$  MPa for the conventionally processed alloy using hot forging and mill annealing reported in [6]. The achieved elongation at break values were in the range between 10% (std. 1%) and 12.7% (std. 0.4%), which is significantly lower compared with conventionally processed alloy typically having elongation at break of  $18.37 \pm 0.88\%$  [6]. The Young's modulus values were in the range between 108.9 GPa (std. 0.9 GPa) and 115 GPa (std. 1 GPa), which is slightly lower than the typical value of  $120.2 \text{ GPa} \pm 1.9 \text{ GPa}$  for the conventionally processed alloy [6]. The Poisson's ratio was determined to be in the range between 0.29 (std. 0.01) and 0.313 (std. 0.008), which is lower than the value of 0.33 reported for high-purity polycrystalline  $\alpha$  titanium [155]. The  $G$  was not directly measured on flat specimens. Instead, it was calculated using equation (3-23), assuming the material has isotropic elastic constants [58, 80]. It was in the range between 41.5 GPa (std. 0.4 GPa) and 44.1 (std. 0.3 GPa), which is comparable to the  $G$  of 44 GPa reported for high-purity polycrystalline  $\alpha$  titanium [155]. While modeling mechanical properties using laser power and scanning speed at three levels, relatively low  $R^2$  and adj.  $R^2$  occurred. This indicates that there are other parameters worth considering, along with incorporating a higher number of levels distributed in wider range of those parameters. However, this may induce varying melting modes during the PBF-LB process, each governed by different physical processes [182]. Consequently, these variations might be challenging to capture with a single regression model approach used in this study. Despite existing differences in mechanical properties, these variations are considered too minor to customize the mechanical properties of the produced components significantly. Therefore, laser power and scanning speed combinations can be selected within the specified range without compromising mechanical performance. This flexibility allows for the customization of other properties, such as surface roughness, without affecting the mechanical performance of the components.

The influence of laser power and scanning speed on the average surface roughness of PBF-LB Ti6Al4V alloy components was investigated by taking measurements across the gauge lengths of flat specimens. The influence of laser power and scanning speed on the average surface roughness of PBF-LB Ti6Al4V alloy components can be described with high precision using nonlinear regression models incorporating these two parameters, which is supported by the high  $R^2$  and adj  $R^2$  values. Laser power and scanning speed substantially

influence the average surface roughness. Higher laser powers can effectively reduce average surface roughness and mitigate the effects of scanning speed. The maximum values of both  $R_a$  and  $S_a$  were observed when laser power was set to 200 W and scanning speed to 1500 mm/s. Specifically, in this case, mean  $R_a$  reached 12.937  $\mu\text{m}$  (std. 1.039  $\mu\text{m}$ ), while mean  $S_a$  reached 11.966  $\mu\text{m}$  (std. 1.821  $\mu\text{m}$ ). When using the highest laser power level set to 250 W and the lowest scanning speed level set to 1000 mm/s, the mean  $R_a$  reached 7.612  $\mu\text{m}$  (std. 0.248  $\mu\text{m}$ ), while mean  $S_a$  reached 7.195  $\mu\text{m}$  (std. 0.314  $\mu\text{m}$ ). This, in turn, provides a wide range of average surface roughness achievable by changing the laser power and scanning speed in the considered range. Since mechanical properties are not influenced significantly by the laser power and scanning speed, this opens up the possibility of customizing the average surface roughness of components without affecting the mechanical properties. Additionally, the positions of the specimens on the build platform were also considered, revealing no significant influence on the average surface roughness while investigating the influence of the laser power and scanning speed.

In addition to investigating mechanical properties at the macro-scale, the influence of laser power, scanning speed, and annealing heat treatment was analyzed at the micro-scale using the HV1 method and at the nano-scale using nanoindentation. It was found that the annealing heat treatment caused hardness reduction from 385 HV1 (std. 6 HV1) to 364 HV1 (std. 8 HV1) in the case of the specimen produced using laser power 225 W and scanning speed 1000 mm/s. Concerning annealed specimens, the highest HV1 hardness of 375 HV1 (std. 7 HV1) was found on the specimen produced using the laser power of 225 W and scanning speed of 1250 mm/s, while the lowest of 352 HV1 (std. 12 HV1) was found on the specimen produced using laser power 200 W and scanning speed 1250 mm/s. Using this method, the high HV1 value of 374 HV1 (std. 6 HV1) was found on the specimen produced using the highest energy density by combining the laser power of 250 W and scanning speed of 1000 mm/s. The highest nano-hardness was found when the same specimen was subjected to the nanoindentation procedure, reaching 4.9 GPa (std. 0.2 GPa). This can be attributed to the highly textured microstructure found when such high energy densities are used. According to Cepeda-Jiménez et al., an increase in energy density leads to a transition from a weakly textured prior- $\beta$  microstructure to a highly textured one [29]. However, it is unclear why this specimen belonging to group G has higher hardness than the as-built specimen marked as D<sup>ab</sup>. To find an answer, further nano-indentation investigation paired

with electron backscatter diffraction is required. Furthermore, the specimens produced with a laser power of 250 W exhibit slightly higher mean Young's modulus values and lower standard deviations than other specimen groups. The lowest mean Young's modulus value, 121 GPa (std. 8 GPa), was observed with a laser power of 225 W and a speed of 1000 mm/s, while the highest mean value, 137 GPa (std. 3 GPa), was achieved with a laser power of 250 W and the same scanning speed. These results are in accordance with results stated in [97], where Young's modulus of  $127 \pm 4$  GPa was reported. There was a statistically significant difference between the highest mean Young's modulus value corresponding to specimen G when compared with the remaining specimens except for specimen F. Therefore, the laser power and scanning speed influence Young's modulus at the nano-scale. When measuring hardness and Young's modulus at the nano-scale, the indentation depth is particularly important. It was found that both nano-hardness and Young's modulus stabilize at indentation depths exceeding 300 nm when as-built specimens are being tested. When performing nano-indentation on annealed specimens, indentation depths exceeding 1000 nm were required to achieve stable nano-hardness and Young's modulus results. The annealing heat treatment benefits the PBF-LB Ti6Al4V alloy, as it reduces residual stresses and improves ductility. However, it also reduces the creep resistance, as observed by nanoindentation creep tests. Since this alloy is widely used for high-temperature applications, performing annealing heat treatments on additively manufactured components is not beneficial in achieving the highest possible creep resistance for such components.

Given that the laser power and scanning speed do not prominently influence mechanical properties at the macro scale, the potential of customizing mechanical properties by incorporating lattice structure at the macro scale was investigated. For this purpose, a BCC unit cell with tapered struts was considered. This is particularly important given that the mechanical behavior of such lattice structures under tensile loading is scarcely reported. This scarcity might be due to the more complex design and production processes involved in creating tensile lattice specimens. Additionally, producing these specimens incurs higher costs as they need to be manufactured vertically or nearly vertically to reduce warpage from residual stresses and eliminate the need for support structures in lattice regions. Improper design and manufacturing of lattice specimens for tensile tests can cause early failures at the junctions between the lattice and solid parts due to sudden changes in stiffness. To address this, gradual densification of the lattice near the junctions can create a smoother

stiffness transition [72]. However, this requires the extensometer to be attached to the lattice part, which is delicate in BCC structures, as the only contact points are the nodes. As the load increases, axial and rotational displacements at these nodes also increase, and due to unavoidable imperfections in the lattice specimens, these displacements are not evenly distributed. Consequently, attaching the extensometer to the nodes could adversely affect strain measurements. To mitigate this issue, the extensometer was attached to the solid part instead. Furthermore, the strut lengths at the junctions were reduced by incorporating approximately  $4.6 \times 5 \times 5$  BCC unit cells to slightly increase the stiffness at the junctions between the lattice and solid parts.

When modeling the influence of tapering using FEM by changing  $d_{\text{end}}$  and  $d_{\text{mid}}$  in the range between 0.6 mm and 1.2 mm, it is crucial to have representative material parameters for considered strut diameters. For this purpose, the material parameters determined on flat specimens were used in the first attempt. However, this resulted in a high discrepancy between numerical and experimental results. This discrepancy occurred due to high differences in mechanical properties specific to flat tensile specimens compared to the actual mechanical properties of struts. When the size of components manufactured using PBF-LB is reduced, their mechanical properties are reduced due to the higher influence of surface imperfections, voids, and a lower thickness-to-grain-size ratio. Therefore, to obtain representative material parameters, tensile tests should be performed using micro-DIC equipment on strut specimens having identical shape, size, and orientation as those struts used in lattice structures. In this study, struts of actual lattice specimens were designed to be cylindrical or tapered with diameters of 0.6, 0.8, or 1 mm. After manufacturing, struts were often larger, irregular, and had a high surface roughness. All those factors make micro-DIC analysis challenging to perform. Moreover, strain measurements performed by tracking crosshead positions are not precise. Therefore, in this study, along with investigating the influence of laser power and scanning speed on mechanical properties and surface roughness, the flat specimens were initially used to model the behavior of lattice specimens. Due to the significant discrepancies observed, an additional literature review was conducted to find material parameters based on reported tensile test data of actual struts. For this purpose, mechanical properties reported by Murchio et al. for inclined struts by an angle of  $45^\circ$  with a nominal diameter of 0.6 mm were further used in FE analysis [194], since they have used DIC equipment for strain measurements. Those parameters enabled a more accurate esti-

mation of the mechanical properties of lattice specimens using FEM. The higher agreement between numerical and experimental results was found when investigating lattice specimens with strut diameters similar to 0.6 mm. With the increased strut size, there was a higher difference between numerical and experimental results. FEM has a great advantage in investigating the influence of particular geometrical features of unit cells since it enables the isolation of all unwanted parameters and eliminates the influence of all other effects present when performing experimental tests. In this way, the influence of selected parameters, such as  $d_{\text{end}}$  and  $d_{\text{mid}}$ , on mechanical properties can be systematically investigated, having all manufacturing defects, voids, and irregularities eliminated. This is the main reason why all developed models for relating  $d_{\text{end}}$  and  $d_{\text{mid}}$  with  $E$ ,  $R_{p0.2}$ , and  $R_m$  have high values of  $R^2$  and adj.  $R^2$ . Those high values of  $R^2$  and adj.  $R^2$  confirm that all unwanted effects are eliminated from the FEA and that the effects of  $d_{\text{end}}$  and  $d_{\text{mid}}$  on mechanical properties can be described with high accuracy using quadratic models. Both experimental and numerical analyses have shown that by increasing  $d_{\text{end}}$  and  $d_{\text{mid}}$  there is an increase in  $E$ ,  $R_{p0.2}$ , and  $R_m$  of lattice specimens. Numerical results indicate that for a tapering diameter range from 0.6 mm to 1.2 mm for  $d_{\text{end}}$  and  $d_{\text{mid}}$ , the values of  $E$ ,  $R_{p0.2}$ , and  $R_m$  can be amplified by factors of 12.8, 8.2, and 7.7, respectively. This highlights the wide range of possible  $E$ ,  $R_{p0.2}$ , and  $R_m$  values achievable by tapering the struts with the specified diameters. In the case of experimental results,  $E$  can be customized from 1048 MPa (std. 29 MPa) to 5722 MPa (std. 803 MPa), for unit cells having effective strut diameters in the range from 0.78 mm to 1.2 mm. The reason for such a high standard deviation of 803 MPa in the case when lattice specimens with effective  $d_{\text{end}}$  and  $d_{\text{mid}}$  of 1.2 mm are considered, is the damage that occurred at two specimens in the manufacturing phase at the junctions between solid and lattice parts. This resulted in lower stiffness of the two specimens and a reduction of  $E$ . Due to the limitations of the load capacity of utilized equipment and the high strength of the specimen groups 1-1-2 and 08-08-2, their  $R_{p0.2}$  and  $R_m$  values are not experimentally determined since they exceeded the maximum tensile load of 16 kN available at the utilized StepLAB electromechanical actuator. The second attempt was performed on an additional universal tensile test machine with a load capacity of 50 kN and mechanical wedge grips. However, specimen slippage occurred due to the high hardness of the specimens. Therefore, additional experimental tests are required in future work on those specimen groups by employing pneumatically, hydraulically operating, or custom-made grips.

## 8. CONCLUSION

This study was motivated by the potential of AM technologies to produce geometrically complex and customized components, particularly those made from challenging-to-machine metals, which are often used for modern-day applications. After a thorough review of AM technologies, PBF-LB was selected for its exceptional flexibility and broad applicability to process a wide range of metallic materials. This technology facilitates the processing of the widely used Ti6Al4V alloy, enabling the fabrication of complex-shaped components that present substantial challenges when produced using traditional subtractive machining methods, particularly from this challenging-to-machine material. There is potential for the mechanical performance of such components to be achieved by selecting appropriate process parameters and introducing porosity by incorporating unit cells forming a lattice structure.

Therefore, this research aimed to investigate whether varying combinations of laser power and scanning speed in the PBF-LB process applied to fabricate Ti6Al4V components could provide the possibility to customize the mechanical performance and surface roughness to meet design requirements. Additionally, it explored whether altering the unit cells of lattice structures could expand the range of achievable mechanical properties. The comprehensive investigation and analysis during this research have led to several significant conclusions, each providing valuable insights into the specific areas of interest. These findings are outlined as follows:

- There is no prominent difference in mechanical properties ( $R_{p0.2}$ ,  $R_m$ ,  $E$ ,  $G$ ,  $\nu$ ) at the macro scale when changing the laser power between 200 and 250 W and scanning speed between 1000 and 1500 mm/s. Controlling the laser power and scanning speed at three levels resulted in surprisingly low  $R^2$  and adjusted  $R^2$  values of the regression models developed for mechanical properties. A more comprehensive range of parameters should be considered to achieve higher representability.
- Annealing heat treatment at the micro-scale reduces HV1 hardness, as well as nano-

hardness and creep resistance at the nano-scale. Annealing heat treatment does not affect Young's modulus at the nano-scale. Furthermore, the statistically significant difference in Young's modulus values at the nano-scale of annealed specimens was found on the specimen manufactured using the highest energy density utilizing the highest laser power and lowest scanning speed. The nano-hardness and Young's modulus at the nano-scale stabilize at indentation depths exceeding 300 nm for the as-built specimen and at depths exceeding 1000 nm for the annealed specimen. A linear relation between nano-hardness and Young's modulus at the nano-scale is found on annealed specimens produced using different combinations of laser powers and scanning speeds.

- The effect of laser power and scanning speed on the average surface roughness of the PBF-LB Ti6Al4V alloy can be precisely analyzed and described using quadratic regression models that incorporate these two factors. Both laser power and scanning speed play significant roles in determining surface roughness. Increasing laser power tends to lower the average surface roughness and diminishes the influence of scanning speed. This allows for the customization of the surface roughness without sacrificing the mechanical properties at the macro scale, as the two considered factors do not prominently influence mechanical properties.
- Tapering the diameters at the midpoint and endpoints of the struts in the body-centered cubic cell used for lattice formation can significantly influence the values of  $E$ ,  $R_{p0.2}$ , and  $R_m$ . The proposed FE approach enables efficient estimation of the  $E$ ,  $R_{p0.2}$ , and  $R_m$  values of the body-centered cubic lattice structure by considering geometrical features of the unit cells.

Nevertheless, future work is necessary to develop a model relating the mechanical properties of struts with their diameter and orientations. This will provide more accurate estimations of the mechanical properties of the lattice structures with different diameters and strut orientations. Additional parameters, such as the height of the central node and unit cell size for the BCC unit cells, will be included, and their influence on mechanical response will be analyzed. This will provide higher flexibility in achieving desired mechanical properties by customizing selected parameters. Given that lattice structures are increasingly used in applications with cyclic loads, their high and low cyclic fatigue behavior will be investigated.

## BIBLIOGRAPHY

- [1] P. Tao, J. Zhong, H. Li, Q. Hu, S. Gong, and Q. Xu, “Microstructure, Mechanical Properties, and Constitutive Models for Ti–6Al–4V Alloy Fabricated by Selective Laser Melting (SLM),” *Metals*, vol. 9, p. 447, 4 2019.
- [2] S. I. Shakil, A. Hadadzadeh, H. Pirgazi, M. Mohammadi, and M. Haghshenas, “Indentation-derived creep response of cast and laser powder bed fused AlSi10Mg alloy: Air temperature,” *Micron*, vol. 150, p. 103145, 11 2021.
- [3] Z. A. Mierzejewska, R. Hudák, and J. Sidun, “Mechanical properties and microstructure of DMLS Ti6Al4V alloy dedicated to biomedical applications,” *Materials*, vol. 12, no. 1, 2019.
- [4] A. Ataei, Y. Li, M. Brandt, and C. Wen, “Ultrahigh-strength titanium gyroid scaffolds manufactured by selective laser melting (SLM) for bone implant applications,” *Acta Materialia*, vol. 158, pp. 354–368, 2018.
- [5] D. Wang, Y. Yang, X. Su, and Y. Chen, “Study on energy input and its influences on single-track, multi-track, and multi-layer in SLM,” *International Journal of Advanced Manufacturing Technology*, vol. 58, no. 9-12, pp. 1189–1199, 2012.
- [6] B. Vrancken, L. Thijs, J. P. Kruth, and J. Van Humbeeck, “Heat treatment of Ti6Al4V produced by Selective Laser Melting: Microstructure and mechanical properties,” *Journal of Alloys and Compounds*, vol. 541, pp. 177–185, 2012.
- [7] C. L. Yang, Z. J. Zhang, S. J. Li, Y. J. Liu, T. B. Sercombe, W. T. Hou, P. Zhang, Y. K. Zhu, Y. L. Hao, Z. F. Zhang, and R. Yang, “Simultaneous improvement in strength and plasticity of Ti-24Nb-4Zr-8Sn manufactured by selective laser melting,” *Materials and Design*, vol. 157, pp. 52–59, 2018.
- [8] M. Leary, M. Mazur, H. Williams, E. Yang, A. Alghamdi, B. Lozanovski, X. Zhang, D. Shidid, L. Farahbod-Sternahl, G. Witt, I. Kelbassa, P. Choong, M. Qian, and M. Brandt, “Inconel 625 lattice structures manufactured by selective laser melting (SLM): Mechanical properties, deformation and failure modes,” *Materials and Design*, vol. 157, no. 2017, pp. 179–199, 2018.
- [9] S. Pal, N. Gubelj, R. Hudak, G. Lojen, V. Rajtukova, J. Predan, V. Kokol, and I. Drstvensek, “Tensile properties of selective laser melting products affected by building orientation and energy density,” *Materials Science and Engineering A*, vol. 743, pp. 637–647, 2019.
- [10] Z. Chen, X. Wu, D. Tomus, and C. H. Davies, “Surface roughness of Selective Laser Melted Ti-6Al-4V alloy components,” *Additive Manufacturing*, vol. 21, pp. 91–103, 2018.



- [11] E. Vaglio, *Research on Process Parameter Optimization in Selective Laser Melting (Doctoral Thesis)*. PhD thesis, University of Udine, 2018.
- [12] A. Molinari, S. Ancellotti, V. Fontanari, E. Iacob, V. Luchin, G. Zappini, and M. Benedetti, “Effect of Process Parameters on the Surface Microgeometry of a Ti6Al4V Alloy Manufactured by Laser Powder Bed Fusion: 3D vs. 2D Characterization,” *Metals*, vol. 12, p. 106, 1 2022.
- [13] A. Dareh Baghi, S. Nafisi, R. Hashemi, H. Ebendorff-Heidepriem, and R. Ghomashchi, “A New Approach to Empirical Optimization of Laser Powder Bed Fusion Process for Ti6Al4V Parts,” *Journal of Materials Engineering and Performance*, vol. 32, pp. 9472–9488, 10 2023.
- [14] J. Chen, K. Wang, C. Zhang, and B. Wang, “An efficient statistical approach to design 3D-printed metamaterials for mimicking mechanical properties of soft biological tissues,” *Additive Manufacturing*, vol. 24, pp. 341–352, 2018.
- [15] T. Pasang, B. Tavlovich, O. Yannay, B. Jackson, M. Fry, Y. Tao, C. Turangi, J.-c. Wang, C.-p. Jiang, Y. Sato, M. Tsukamoto, and W. Z. Misiolek, “Directionally-Dependent Mechanical Properties of Ti6Al4V Manufactured by Electron Beam Melting (EBM) and Selective Laser Melting (SLM),” *Materials*, vol. 14, p. 3603, 6 2021.
- [16] D. Wang, W. Dou, and Y. Yang, “Research on selective laser melting of Ti6Al4V: Surface morphologies, optimized processing zone, and ductility improvement mechanism,” *Metals*, vol. 8, no. 7, 2018.
- [17] Z. Chen, X. Wu, and C. H. Davies, “Process variation in Laser Powder Bed Fusion of Ti-6Al-4V,” *Additive Manufacturing*, vol. 41, no. October 2020, p. 101987, 2021.
- [18] M. A. Buhairi, F. M. Foudzi, F. I. Jamhari, A. B. Sulong, N. A. M. Radzuan, N. Muhammad, I. F. Mohamed, A. H. Azman, W. S. W. Harun, and M. S. Al-Furjan, “Review on volumetric energy density: influence on morphology and mechanical properties of Ti6Al4V manufactured via laser powder bed fusion,” *Progress in Additive Manufacturing*, vol. 8, no. 2, pp. 265–283, 2023.
- [19] S. Limmahakhun, A. Oloyede, K. Sitthiseripratip, Y. Xiao, and C. Yan, “Stiffness and strength tailoring of cobalt chromium graded cellular structures for stress-shielding reduction,” *Materials and Design*, vol. 114, pp. 633–641, 2017.
- [20] Y. Xu, D. Zhang, S. Hu, R. Chen, Y. Gu, X. Kong, J. Tao, and Y. Jiang, “Mechanical properties tailoring of topology optimized and selective laser melting fabricated Ti6Al4V lattice structure,” *Journal of the Mechanical Behavior of Biomedical Materials*, vol. 99, no. June, pp. 225–239, 2019.
- [21] A. Spadoni and M. Ruzzene, “Numerical and experimental analysis of the static compliance of chiral truss-core airfoils,” *Journal of Mechanics of Materials and Structures*, vol. 2, no. 5, pp. 965–981, 2007.
- [22] V. Viale, J. Stavridis, A. Salmi, F. Bondioli, and A. Saboori, “Optimisation of down-skin parameters to produce metallic parts via laser powder bed fusion process: an overview,” *International Journal of Advanced Manufacturing Technology*, vol. 123, no. 7-8, pp. 2159–2182, 2022.

- [23] C. Zhang, D. Zou, M. Mazur, J. P. Mo, G. Li, and S. Ding, “The State of the Art in Machining Additively Manufactured Titanium Alloy Ti-6Al-4V,” *Materials*, vol. 16, no. 7, 2023.
- [24] A. Cutolo, B. Neirinck, K. Lietaert, C. de Formanoir, and B. Van Hooreweder, “Influence of layer thickness and post-process treatments on the fatigue properties of CoCr scaffolds produced by laser powder bed fusion,” *Additive Manufacturing*, vol. 23, pp. 498–504, 2018.
- [25] Y. Zhai, H. Galarraga, and D. A. Lados, “Microstructure, static properties, and fatigue crack growth mechanisms in Ti-6Al-4V fabricated by additive manufacturing: LENS and EBM,” *Engineering Failure Analysis*, vol. 69, pp. 3–14, 2016.
- [26] D. Agius, K. I. Kourousis, C. Wallbrink, and T. Song, “Cyclic plasticity and microstructure of as-built SLM Ti-6Al-4V: The effect of build orientation,” *Materials Science and Engineering A*, vol. 701, no. May, pp. 85–100, 2017.
- [27] M. Brandt, S. Sun, M. Leary, S. Feih, J. Elambasseril, and Q. Liu, “High-value SLM aerospace components: From design to manufacture,” *Advanced Materials Research*, vol. 633, pp. 135–147, 2013.
- [28] S. Ford and M. Despeisse, “Additive manufacturing and sustainability: an exploratory study of the advantages and challenges,” *Journal of Cleaner Production*, vol. 137, pp. 1573–1587, 11 2016.
- [29] C. M. Cepeda-Jiménez, F. Potenza, E. Magalini, V. Luchin, A. Molinari, and M. T. Pérez-Prado, “Effect of energy density on the microstructure and texture evolution of Ti-6Al-4V manufactured by laser powder bed fusion,” *Materials Characterization*, vol. 163, no. September 2019, p. 110238, 2020.
- [30] H. Peng, W. Fang, C. Dong, Y. Yi, X. Wei, B. Luo, and S. Huang, “Nano-Mechanical Properties and Creep Behavior of Ti6Al4V Fabricated by Powder Bed Fusion Electron Beam Additive Manufacturing,” *Materials*, vol. 14, p. 3004, 6 2021.
- [31] H. Pan, T. Dahmen, M. Bayat, K. Lin, and X. Zhang, “Independent effects of laser power and scanning speed on IN718’s precipitation and mechanical properties produced by LBPF plus heat treatment,” *Materials Science and Engineering: A*, vol. 849, p. 143530, 8 2022.
- [32] K. Mumtaz and N. Hopkinson, “Top surface and side roughness of Inconel 625 parts processed using selective laser melting,” *Rapid Prototyping Journal*, vol. 15, no. 2, pp. 96–103, 2009.
- [33] H. Hassanin, M. A. El-Sayed, M. Ahmadein, N. A. Alsaleh, S. Ataya, M. M. Ahmed, and K. Essa, “Optimising Surface Roughness and Density in Titanium Fabrication via Laser Powder Bed Fusion,” *Micromachines*, vol. 14, no. 8, pp. 1–20, 2023.
- [34] A. Ullah, A. Ur Rehman, M. U. Salamci, F. Pıtır, and T. Liu, “The influence of laser power and scanning speed on the microstructure and surface morphology of Cu2O parts in SLM,” *Rapid Prototyping Journal*, vol. 28, pp. 1796–1807, 10 2022.
- [35] L. Hao, W. Wang, J. Zeng, M. Song, S. Chang, and C. Zhu, “Effect of scanning speed and laser power on formability, microstructure, and quality of 316L stainless steel prepared by selective laser melting,” *Journal of Materials Research and Technology*, vol. 25, pp. 3189–3199, 7 2023.

- [36] G. Hou, Z. Yu, and D. Ye, “The influence of laser power and scanning speed on the dimensional accuracy of SLS formed parts,” *IOP Conference Series: Earth and Environmental Science*, vol. 791, p. 012154, 6 2021.
- [37] N. Agarwal, M. C. Monu, K. Tamil Selvam, M. A. Obeidi, and D. Brabazon, “Study of the effects of laser power and scanning speed on the microstructural morphologies and physical properties of L-PBF produced Ni52.39Ti47.61,” *Journal of Materials Research and Technology*, 11 2023.
- [38] “ISO/ASTM 52900:2021(en) Additive manufacturing — General principles — Fundamentals and vocabulary,” 2021.
- [39] I. Gibson, D. Rosen, and B. Stucker, *Additive manufacturing technologies: 3D printing, rapid prototyping, and direct digital manufacturing, second edition*. Springer New York, second edi ed., 2015.
- [40] W. S. Harun, M. S. Kamariah, N. Muhamad, S. A. Ghani, F. Ahmad, and Z. Mohamed, “A review of powder additive manufacturing processes for metallic biomaterials,” *Powder Technology*, vol. 327, pp. 128–151, 2018.
- [41] P. K. Gokuldoss, S. Kolla, and J. Eckert, “Additive manufacturing processes: Selective laser melting, electron beam melting and binder jetting-selection guidelines,” *Materials*, vol. 10, no. 6, 2017.
- [42] M. Lutter-Günther, C. Gebbe, T. Kamps, C. Seidel, and G. Reinhart, “Powder recycling in laser beam melting: strategies, consumption modeling and influence on resource efficiency,” *Production Engineering*, vol. 12, pp. 377–389, 6 2018.
- [43] H. K. Rafi, N. V. Karthik, H. Gong, T. L. Starr, and B. E. Stucker, “Microstructures and mechanical properties of Ti6Al4V parts fabricated by selective laser melting and electron beam melting,” *Journal of Materials Engineering and Performance*, vol. 22, no. 12, pp. 3872–3883, 2013.
- [44] L. Thijs, F. Verhaeghe, T. Craeghs, J. V. Humbeeck, and J. P. Kruth, “A study of the microstructural evolution during selective laser melting of Ti-6Al-4V,” *Acta Materialia*, vol. 58, no. 9, pp. 3303–3312, 2010.
- [45] X. Li, X. Fang, D. Fang, W. Fu, X. Zhang, and K. Huang, “On the excellent strength-ductility synergy of wire-arc directed energy deposited Mg-Gd-Y-Zn-Zr alloy via manipulating precipitates,” *Additive Manufacturing*, vol. 77, p. 103794, 9 2023.
- [46] S. Bergmueller, L. Gerhold, L. Fuchs, L. Kaserer, and G. Leichtfried, “Systematic approach to process parameter optimization for laser powder bed fusion of low-alloy steel based on melting modes,” *International Journal of Advanced Manufacturing Technology*, pp. 4385–4398, 2023.
- [47] Z. Li, I. Kucukkoc, D. Z. Zhang, and F. Liu, “Optimising the process parameters of selective laser melting for the fabrication of Ti6Al4V alloy,” *Rapid Prototyping Journal*, vol. 24, no. 1, pp. 150–159, 2018.
- [48] X. Yan, C. Shi, T. Liu, Y. Ye, C. Chang, W. Ma, C. Deng, S. Yin, H. Liao, and M. Liu, “Effect of heat treatment on the corrosion resistance behavior of selective laser melted Ti6Al4V ELI,” *Surface and Coatings Technology*, vol. 396, p. 125955, 8 2020.

- [49] M. Elsayed, M. Ghazy, Y. Youssef, and K. Essa, "Optimization of SLM process parameters for Ti6Al4V medical implants," *Rapid Prototyping Journal*, vol. 25, no. 3, pp. 433–447, 2019.
- [50] E. Vaglio, T. De Monte, A. Lanzutti, G. Totis, M. Sortino, and L. Fedrizzi, "Single tracks data obtained by selective laser melting of Ti6Al4V with a small laser spot diameter," *Data in Brief*, vol. 33, p. 106443, 2020.
- [51] G. Kasperovich, J. Haubrich, J. Gussone, and G. Requena, "Correlation between porosity and processing parameters in TiAl6V4 produced by selective laser melting," *Materials and Design*, vol. 105, pp. 160–170, 2016.
- [52] T. Gustmann, A. Neves, U. Kühn, P. Gargarella, C. Kiminami, C. Bolfarini, J. Eckert, and S. Pauly, "Influence of processing parameters on the fabrication of a Cu-Al-Ni-Mn shape-memory alloy by selective laser melting," *Additive Manufacturing*, vol. 11, pp. 23–31, 7 2016.
- [53] H. Jia, H. Sun, H. Wang, Y. Wu, and H. Wang, "Scanning strategy in selective laser melting (SLM): a review," *International Journal of Advanced Manufacturing Technology*, vol. 113, no. 9-10, pp. 2413–2435, 2021.
- [54] C. Meier, R. Weissbach, J. Weinberg, W. A. Wall, and A. J. Hart, "Critical influences of particle size and adhesion on the powder layer uniformity in metal additive manufacturing," *Journal of Materials Processing Technology*, vol. 266, pp. 484–501, 4 2019.
- [55] A. Martucci, P. L. Tam, A. Aversa, M. Lombardi, and L. Nyborg, "The effect of powder reuse on the surface chemical composition of the Scalmetalloy powder in Powder Bed Fusion – Laser Beam process," *Surface and Interface Analysis*, vol. 55, pp. 388–395, 6 2023.
- [56] H. Ali, L. Ma, H. Ghadbeigi, and K. Mumtaz, "In-situ residual stress reduction, martensitic decomposition and mechanical properties enhancement through high temperature powder bed pre-heating of Selective Laser Melted Ti6Al4V," *Materials Science and Engineering: A*, vol. 695, pp. 211–220, 5 2017.
- [57] V. Manakari, G. Parande, and M. Gupta, "Selective Laser Melting of Magnesium and Magnesium Alloy Powders: A Review," *Metals*, vol. 7, p. 2, 12 2016.
- [58] B. E. Carroll, T. A. Palmer, and A. M. Beese, "Anisotropic tensile behavior of Ti-6Al-4V components fabricated with directed energy deposition additive manufacturing," *Acta Materialia*, vol. 87, pp. 309–320, 2015.
- [59] T. W. Na, W. R. Kim, S. M. Yang, O. Kwon, J. M. Park, G. H. Kim, K. H. Jung, C. W. Lee, H. K. Park, and H. G. Kim, "Effect of laser power on oxygen and nitrogen concentration of commercially pure titanium manufactured by selective laser melting," *Materials Characterization*, vol. 143, no. January, pp. 110–117, 2018.
- [60] T. Vilaro, C. Colin, and J. D. Bartout, "As-Fabricated and Heat-Treated Microstructures of the Ti-6Al-4V Alloy Processed by Selective Laser Melting," *Metallurgical and Materials Transactions A*, vol. 42, pp. 3190–3199, 10 2011.
- [61] A. Ladewig, G. Schlick, M. Fisser, V. Schulze, and U. Glatzel, "Influence of the shielding gas flow on the removal of process by-products in the selective laser melting process," *Additive Manufacturing*, vol. 10, pp. 1–9, 4 2016.

- [62] C. Pauzon, A. Leicht, U. Klement, P. Forêt, and E. Hryha, “Effect of the Process Gas and Scan Speed on the Properties and Productivity of Thin 316L Structures Produced by Laser-Powder Bed Fusion,” *Metallurgical and Materials Transactions A*, vol. 51, pp. 5339–5350, 10 2020.
- [63] F. I. Jamhari, F. M. Foudzi, M. A. Buhairi, A. B. Sulong, N. A. Mohd Radzuan, N. Muhamad, I. F. Mohamed, N. H. Jamadon, and K. S. Tan, “Influence of heat treatment parameters on microstructure and mechanical performance of titanium alloy in LPBF: A brief review,” *Journal of Materials Research and Technology*, vol. 24, pp. 4091–4110, 2023.
- [64] S. Ren, Y. Chen, T. Liu, and X. Qu, “Effect of Build Orientation on Mechanical Properties and Microstructure of Ti-6Al-4V Manufactured by Selective Laser Melting,” *Metallurgical and Materials Transactions A*, vol. 50, pp. 4388–4409, 9 2019.
- [65] S. C. Vogel, D. Bhattacharyya, G. Viswanathan, D. Williams, and H. Fraser, “Phase Transformation Textures in Ti-6Al-4V Alloy,” *Materials Science Forum*, vol. 495-497, pp. 681–686, 9 2005.
- [66] G. M. Ter Haar and T. H. Becker, “Selective laser melting produced Ti-6Al-4V: Post-process heat treatments to achieve superior tensile properties,” *Materials*, vol. 11, no. 1, 2018.
- [67] S. Cao, Y. Zou, C. V. S. Lim, and X. Wu, “Review of laser powder bed fusion (LPBF) fabricated Ti-6Al-4V: process, post-process treatment, microstructure, and property,” *Light: Advanced Manufacturing*, vol. 2, no. 2, p. 1, 2021.
- [68] S. Jian, J. Wang, D. Xu, R. Ma, C. Huang, M. Lei, D. Liu, and M. Wan, “Gradient microstructure and mechanical properties of Ti-6Al-4V titanium alloy fabricated by high-frequency induction quenching treatment,” *Materials & Design*, vol. 222, p. 111031, 10 2022.
- [69] S. Gruber, C. Grunert, M. Riede, E. López, A. Marquardt, F. Brueckner, and C. Leyens, “Comparison of dimensional accuracy and tolerances of powder bed based and nozzle based additive manufacturing processes,” *Journal of Laser Applications*, vol. 32, 8 2020.
- [70] U. Hossain, S. Ghose, K. Nai, and J. R. Jeffers, “Mechanical and morphological properties of additively manufactured SS316L and Ti6Al4V micro-struts as a function of build angle,” *Additive Manufacturing*, vol. 46, p. 102050, 10 2021.
- [71] F. Scalzo, G. Totis, E. Vaglio, and M. Sortino, “Experimental study on the high-damping properties of metallic lattice structures obtained from SLM,” *Precision Engineering*, vol. 71, pp. 63–77, 9 2021.
- [72] M. Pelegatti, F. Scalzo, F. Sordetti, E. Vaglio, M. Magnan, G. Totis, M. Sortino, D. Benasciutti, A. Lanzutti, F. De Bona, and E. Salvati, “Low cycle fatigue behaviour of cellular materials: Experimental comparative study of strut-based and gyroid structures made of additively manufactured 316L steel,” *International Journal of Fatigue*, vol. 178, p. 108024, 1 2024.
- [73] G. Kasperovich and J. Hausmann, “Improvement of fatigue resistance and ductility of TiAl6V4 processed by selective laser melting,” *Journal of Materials Processing Technology*, vol. 220, pp. 202–214, 2015.

- [74] W. Xu, M. Brandt, S. Sun, J. Elambasseril, Q. Liu, K. Latham, K. Xia, and M. Qian, "Additive manufacturing of strong and ductile Ti-6Al-4V by selective laser melting via in situ martensite decomposition," *Acta Materialia*, vol. 85, pp. 74–84, 2015.
- [75] G. Sander, A. P. Babu, X. Gao, D. Jiang, and N. Birbilis, "On the effect of build orientation and residual stress on the corrosion of 316L stainless steel prepared by selective laser melting," *Corrosion Science*, vol. 179, p. 109149, 2021.
- [76] A. Strondl, O. Lyckfeldt, H. Brodin, and U. Ackelid, "Characterization and Control of Powder Properties for Additive Manufacturing," *Jom*, vol. 67, no. 3, pp. 549–554, 2015.
- [77] P. Zhang, A. N. He, F. Liu, K. Zhang, J. Jiang, and D. Z. Zhang, "Evaluation of low cycle fatigue performance of selective laser melted titanium alloy Ti-6Al-4V," *Metals*, vol. 9, no. 10, pp. 1–16, 2019.
- [78] O. Tevet, D. Svetlizky, D. Harel, Z. Barkay, D. Geva, and N. Eliaz, "Measurement of the Anisotropic Dynamic Elastic Constants of Additive Manufactured and Wrought Ti6Al4V Alloys," *Materials*, vol. 15, p. 638, 1 2022.
- [79] X. Yang, Y. Li, M. g. Duan, W. Jiang, D. Chen, and B. Li, "An investigation of ductile fracture behavior of Ti6Al4V alloy fabricated by selective laser melting," *Journal of Alloys and Compounds*, vol. 890, p. 161926, 2022.
- [80] A. E. Wilson-Heid, Z. Wang, B. McCornac, and A. M. Beese, "Quantitative relationship between anisotropic strain to failure and grain morphology in additively manufactured Ti-6Al-4V," *Materials Science and Engineering A*, vol. 706, pp. 287–294, 2017.
- [81] Y. Zhang, Y.-G. Jung, and J. Zhang, "Multiscale and multiphysics modeling of metal AM," in *Multiscale Modeling of Additively Manufactured Metals*, pp. 1–10, Elsevier, 1st editio ed., 2020.
- [82] P. Edwards and M. Ramulu, "Fatigue performance evaluation of selective laser melted Ti-6Al-4V," *Materials Science and Engineering A*, vol. 598, pp. 327–337, 2014.
- [83] S. Pal, G. Lojen, N. Gubelj, V. Kokol, and I. Drstvensek, "Melting, fusion and solidification behaviors of Ti-6Al-4V alloy in selective laser melting at different scanning speeds," *Rapid Prototyping Journal*, vol. 26, no. 7, pp. 1209–1215, 2020.
- [84] P. Hartunian and M. Eshraghi, "Effect of Build Orientation on the Microstructure and Mechanical Properties of Selective Laser-Melted Ti-6Al-4V Alloy," *Journal of Manufacturing and Materials Processing*, vol. 2, no. 4, p. 69, 2018.
- [85] V. Cain, L. Thijs, J. Van Humbeeck, B. Van Hooreweder, and R. Knutsen, "Crack propagation and fracture toughness of Ti6Al4V alloy produced by selective laser melting," *Additive Manufacturing*, vol. 5, pp. 68–76, 2015.
- [86] Z. Kuai, Z. Li, B. Liu, Y. Chen, S. Lu, X. Tang, and T. Liu, "Selective laser melting of CuCrZr alloy: processing optimisation, microstructure and mechanical properties," *Journal of Materials Research and Technology*, vol. 19, pp. 4915–4931, 2022.
- [87] C. Qiu, C. Panwisawas, M. Ward, H. C. Basoalto, J. W. Brooks, and M. M. Attallah, "On the role of melt flow into the surface structure and porosity development during selective laser melting," *Acta Materialia*, vol. 96, no. May 2019, pp. 72–79, 2015.

- [88] Q. B. Nguyen, D. N. Luu, S. M. Nai, Z. Zhu, Z. Chen, and J. Wei, "The role of powder layer thickness on the quality of SLM printed parts," *Archives of Civil and Mechanical Engineering*, vol. 18, no. 3, pp. 948–955, 2018.
- [89] V. H. Baltazar Hernandez, S. K. Panda, Y. Okita, and N. Y. Zhou, "A study on heat affected zone softening in resistance spot welded dual phase steel by nanoindentation," *Journal of Materials Science*, vol. 45, no. 6, pp. 1638–1647, 2010.
- [90] T. S. Jun, D. E. Armstrong, and T. B. Britton, "A nanoindentation investigation of local strain rate sensitivity in dual-phase Ti alloys," *Journal of Alloys and Compounds*, vol. 672, pp. 282–291, 2016.
- [91] G. B. Viswanathan, E. Lee, D. M. Maher, S. Banerjee, and H. L. Fraser, "Direct observations and analyses of dislocation substructures in the  $\alpha$  phase of an  $\alpha/\beta$  Ti-alloy formed by nanoindentation," *Acta Materialia*, vol. 53, no. 19, pp. 5101–5115, 2005.
- [92] L. Shen, P. Septiwerdani, and Z. Chen, "Elastic modulus, hardness and creep performance of SnBi alloys using nanoindentation," *Materials Science and Engineering: A*, vol. 558, pp. 253–258, 12 2012.
- [93] L. S. Moura, G. D. Vittoria, A. H. G. Gabriel, E. B. Fonseca, L. P. Gabriel, T. J. Webster, and E. S. N. Lopes, "A highly accurate methodology for the prediction and correlation of mechanical properties based on the slinness ratio of additively manufactured tensile test specimens," *Journal of Materials Science*, vol. 55, pp. 9578–9596, 8 2020.
- [94] Z. Wang, C. Jiang, P. Liu, W. Yang, Y. Zhao, M. F. Horstemeyer, L. Q. Chen, Z. Hu, and L. Chen, "Uncertainty quantification and reduction in metal additive manufacturing," *npj Computational Materials*, vol. 6, no. 1, 2020.
- [95] S. Cherneva, V. Petrunov, V. Petkov, V. Bogdanov, and S. Simeonova, "Structure and Mechanical Properties of Milled and 3D-Printed Ti-6Al-4V Alloys for Subtractive and Additive CAD/CAM Manufacturing in Dentistry," *Applied Sciences*, vol. 13, p. 11958, 11 2023.
- [96] X. Liu, W. Cui, Y. Wang, Y. Long, F. Liu, and Y. Liu, "Effects of Heat Treatment on the Microstructure Evolution and Mechanical Properties of Selective Laser Melted TC4 Titanium Alloy," *Metals*, vol. 12, no. 5, 2022.
- [97] L. Y. Chen, J. C. Huang, C. H. Lin, C. T. Pan, S. Y. Chen, T. L. Yang, D. Y. Lin, H. K. Lin, and J. S. Jang, "Anisotropic response of Ti-6Al-4V alloy fabricated by 3D printing selective laser melting," *Materials Science and Engineering A*, vol. 682, no. October 2016, pp. 389–395, 2017.
- [98] X. Zhang, S. Sun, G. Sun, S. Han, Z. Jiang, and J. Lian, "Nanoindentation creep deformation behaviour of high nitrogen nickel-free austenitic stainless steel," *Materials Science and Technology (United Kingdom)*, vol. 35, no. 13, pp. 1592–1599, 2019.
- [99] Z. Xu, H. Zhang, W. Li, A. Mao, L. Wang, G. Song, and Y. He, "Microstructure and nanoindentation creep behavior of CoCrFeMnNi high-entropy alloy fabricated by selective laser melting," *Additive Manufacturing*, vol. 28, no. April, pp. 766–771, 2019.

- [100] I. C. Choi, B. G. Yoo, Y. J. Kim, and J. I. Jang, "Indentation creep revisited," *Journal of Materials Research*, vol. 27, no. 1, pp. 3–11, 2012.
- [101] W. D. Zhang, Y. Liu, H. Wu, X. D. Lan, J. Qiu, T. Hu, and H. P. Tang, "Room temperature creep behavior of Ti-Nb-Ta-Zr-O alloy," *Materials Characterization*, vol. 118, pp. 29–36, 2016.
- [102] M. Sadeghilaridjani and S. Mukherjee, "High-temperature nano-indentation creep behavior of multi-principal element alloys under static and dynamic loads," *Metals*, vol. 10, no. 2, 2020.
- [103] D. D. Gu, W. Meiners, K. Wissenbach, and R. Poprawe, "Laser additive manufacturing of metallic components: Materials, processes and mechanisms," *International Materials Reviews*, vol. 57, no. 3, pp. 133–164, 2012.
- [104] W. Y. Kim, E. Y. Yoon, J. H. Kim, and S. Kim, "Surface Characteristics of Ti-6Al-4V Alloy Based on the Process Parameter and Abrasive Process in the Laser Powder Bed Fusion," *Metals and Materials International*, vol. 29, pp. 2345–2357, 8 2023.
- [105] P. Foti, S. Mohammad Javad Razavi, A. Fatemi, and F. Berto, "Multiaxial fatigue of additively manufactured metallic components: A review of the failure mechanisms and fatigue life prediction methodologies," *Progress in Materials Science*, vol. 137, no. August 2022, p. 101126, 2023.
- [106] A. Charles, M. Bayat, A. Elkaseer, L. Thijs, J. H. Hattel, and S. Scholz, "Elucidation of dross formation in laser powder bed fusion at down-facing surfaces: Phenomenon-oriented multiphysics simulation and experimental validation," *Additive Manufacturing*, vol. 50, p. 102551, 2 2022.
- [107] S. Lee, B. Rasoolian, D. F. Silva, J. W. Pegues, and N. Shamsaei, "Surface roughness parameter and modeling for fatigue behavior of additive manufactured parts: A non-destructive data-driven approach," *Additive Manufacturing*, vol. 46, no. May, p. 102094, 2021.
- [108] S. Akincioglu, "Taguchi Optimization of Multiple Performance Characteristics in the Electrical Discharge Machining of the Tigr2," *Facta Universitatis, Series: Mechanical Engineering*, vol. 20, no. 2, pp. 237–253, 2022.
- [109] A. S. Sidhu, "Surface texturing of non-toxic, biocompatible titanium alloys via electro-discharge," *Reports in Mechanical Engineering*, vol. 2, no. 1, pp. 51–56, 2021.
- [110] A. Triantaphyllou, C. L. Giusca, G. D. Macaulay, F. Roerig, M. Hoebel, R. K. Leach, B. Tomita, and K. A. Milne, "Surface texture measurement for additive manufacturing," *Surface Topography: Metrology and Properties*, vol. 3, no. 2, 2015.
- [111] F. Cao, T. Zhang, M. A. Ryder, and D. A. Lados, "A Review of the Fatigue Properties of Additively Manufactured Ti-6Al-4V," *Jom*, vol. 70, no. 3, pp. 349–357, 2018.
- [112] Z. Alomar and F. Concli, "Compressive behavior assessment of a newly developed circular cell-based lattice structure," *Materials and Design*, vol. 205, p. 109716, 2021.
- [113] A. A. Zadpoor, "Mechanical performance of additively manufactured meta-biomaterials," *Acta Biomaterialia*, vol. 85, pp. 41–59, 2019.



- [114] S. Ma, Q. Tang, Q. Feng, J. Song, X. Han, and F. Guo, “Mechanical behaviours and mass transport properties of bone-mimicking scaffolds consisted of gyroid structures manufactured using selective laser melting,” *Journal of the Mechanical Behavior of Biomedical Materials*, vol. 93, no. August 2018, pp. 158–169, 2019.
- [115] M. Benedetti, A. du Plessis, R. Ritchie, M. Dallago, N. Razavi, and F. Berto, “Architected cellular materials: A review on their mechanical properties towards fatigue-tolerant design and fabrication,” *Materials Science and Engineering: R: Reports*, vol. 144, p. 100606, 4 2021.
- [116] L. Bai, Y. Xu, X. Chen, L. Xin, J. Zhang, K. Li, and Y. Sun, “Improved mechanical properties and energy absorption of Ti6Al4V laser powder bed fusion lattice structures using curving lattice struts,” *Materials and Design*, vol. 211, p. 110140, 2021.
- [117] M. A. Surmeneva, R. A. Surmenev, E. A. Chudinova, A. Koptioug, M. S. Tkachev, S. N. Gorodzha, and L. E. Rännar, “Fabrication of multiple-layered gradient cellular metal scaffold via electron beam melting for segmental bone reconstruction,” *Materials and Design*, vol. 133, pp. 195–204, 2017.
- [118] H. M. Kolken, S. Janbaz, S. M. Leeflang, K. Lietaert, H. H. Weinans, and A. A. Zadpoor, “Rationally designed meta-implants: A combination of auxetic and conventional meta-biomaterials,” *Materials Horizons*, vol. 5, no. 1, pp. 28–35, 2018.
- [119] V. A. Lvov, F. S. Senatov, A. S. Shinkaryov, S. V. Chernyshikhin, A. A. Gromov, and V. A. Sheremetyev, “Experimental 3D printed re-entrant auxetic and honeycomb spinal cages based on Ti-6Al-4 V: Computer-Aided design concept and mechanical characterization,” *Composite Structures*, vol. 310, no. September 2022, p. 116766, 2023.
- [120] M. F. Ashby and L. J. Gibson, “Cellular solids: structure and properties,” *Press Syndicate of the University of Cambridge, Cambridge, UK*, pp. 175–231, 1997.
- [121] F. Liu, D. Zhang, P. Zhang, M. Zhao, and S. Jafar, “Mechanical Properties of Optimized Diamond Lattice Structure for Bone Scaffolds Fabricated via Selective Laser Melting,” *Materials*, vol. 11, p. 374, 3 2018.
- [122] C. Peng, P. Tran, H. Nguyen-Xuan, and A. J. Ferreira, “Mechanical performance and fatigue life prediction of lattice structures: Parametric computational approach,” *Composite Structures*, vol. 235, p. 111821, 2020.
- [123] J. C. Maxwell, “L. On the calculation of the equilibrium and stiffness of frames,” *The London, Edinburgh, and Dublin Philosophical Magazine and Journal of Science*, vol. 27, pp. 294–299, 4 1864.
- [124] M. Zhao, D. Z. Zhang, Z. Li, T. Zhang, H. Zhou, and Z. Ren, “Design, mechanical properties, and optimization of BCC lattice structures with taper struts,” *Composite Structures*, vol. 295, no. April, p. 115830, 2022.
- [125] T. Tancogne-Dejean and D. Mohr, “Stiffness and specific energy absorption of additively-manufactured metallic BCC metamaterials composed of tapered beams,” *International Journal of Mechanical Sciences*, vol. 141, pp. 101–116, 2018.
- [126] L. Bai, C. Yi, X. Chen, Y. Sun, and J. Zhang, “Effective Design of the Graded Strut of BCC Lattice Structure for Improving Mechanical Properties,” *Materials*, vol. 12, p. 2192, 7 2019.

- [127] J. Kang, E. Dong, D. Li, S. Dong, C. Zhang, and L. Wang, “Anisotropy characteristics of microstructures for bone substitutes and porous implants with application of additive manufacturing in orthopaedic,” *Materials and Design*, vol. 191, p. 108608, 2020.
- [128] X. Ren, L. Xiao, and Z. Hao, “Multi-property cellular material design approach based on the mechanical behaviour analysis of the reinforced lattice structure,” *Materials & Design*, vol. 174, p. 107785, 7 2019.
- [129] M. Zhao, F. Liu, G. Fu, D. Zhang, T. Zhang, and H. Zhou, “Improved Mechanical Properties and Energy Absorption of BCC Lattice Structures with Triply Periodic Minimal Surfaces Fabricated by SLM,” *Materials*, vol. 11, p. 2411, 11 2018.
- [130] P. Platek, J. Sienkiewicz, J. Janiszewski, and F. Jiang, “Investigations on mechanical properties of lattice structures with different values of relative density made from 316L by selective laser melting (SLM),” *Materials*, vol. 13, no. 9, 2020.
- [131] N. Jin, Z. Yan, Y. Wang, H. Cheng, and H. Zhang, “Effects of heat treatment on microstructure and mechanical properties of selective laser melted Ti-6Al-4V lattice materials,” *International Journal of Mechanical Sciences*, vol. 190, p. 106042, 2021.
- [132] R. Kumar, V. Upadhyay, and C. Sharma, “Modeling and Optimization of Process Parameters for Friction Stir Welding of Dissimilar Aerospace Alloys Aa2014 and Aa7075,” *Engineering Review*, vol. 42, no. 2, pp. 59–78, 2022.
- [133] S. B. Gunjal and P. J. Pawar, “Improving the process performance of magnetic abrasive finishing of ss304 material using multiobjective artificial bee colony algorithm,” *Engineering Review*, vol. 41, no. 1, pp. 34–49, 2020.
- [134] A. Mulhi, S. Dehgahi, P. Waghmare, and A. J. Qureshi, “Process Parameter Optimization of 2507 Super Duplex Stainless Steel Additively Manufactured by the Laser Powder Bed Fusion Technique,” *Metals*, vol. 13, no. 4, 2023.
- [135] N. Heckert, J. Filliben, C. Croarkin, B. Hembree, W. Guthrie, P. Tobias, and J. Prinz, *Handbook 151: NIST/SEMATECH e-Handbook of Statistical Methods*. NIST Interagency/Internal Report (NISTIR), National Institute of Standards and Technology, Gaithersburg, MD, 2002.
- [136] K. P. Vasantha Kumar and M. Balasubramanian, “Multi-Response Optimization of FSW Parameters for Dissimilar Al-Mg Alloys,” *Tehnicki Vjesnik*, vol. 29, no. 3, pp. 926–932, 2022.
- [137] X. Cao, L. N. Carter, K. Man, V. M. Villapún, L. Giangiorgi, and S. C. Cox, “Improving predictability of additively manufactured Ti-6Al-4 V lattices for orthopaedic devices: A parametric and struts angle study,” *Materials & Design*, vol. 243, p. 113043, 7 2024.
- [138] R Core Team, “R: A Language and Environment for Statistical Computing,” 2024.
- [139] R. Myers, D. Montgomery, and C. Anderson-Cook, *Response Surface Methodology*. New York: John Wiley & Sons, 4th ed., 2016.
- [140] F. John and S. Weisberg, *An R Companion to Applied Regression*. Sage, third ed., 2019.

- [141] K. Jaqaman and G. Danuser, “Linking data to models: Data regression,” *Nature Reviews Molecular Cell Biology*, vol. 7, no. 11, pp. 813–819, 2006.
- [142] T. M. Wischeropp, C. Emmelmann, M. Brandt, and A. Pateras, “Measurement of actual powder layer height and packing density in a single layer in selective laser melting,” *Additive Manufacturing*, vol. 28, no. August 2018, pp. 176–183, 2019.
- [143] “ASTM E8/E8M -16a Standard Test Methods for Tension Testing of Metallic Materials,” 2016.
- [144] International Standard ISO, “Metallic materials - Vickers hardness test - Part 1: Test method,” *International Standard*, pp. 1–49, 2018.
- [145] W. Oliver and G. Pharr, “An improved technique for determining hardness and elastic modulus using load and displacement sensing indentation experiments,” *Journal of Materials Research*, vol. 7, pp. 1564–1583, 6 1992.
- [146] D. J. Shuman, A. L. Costa, and M. S. Andrade, “Calculating the elastic modulus from nanoindentation and microindentation reload curves,” *Materials Characterization*, vol. 58, no. 4, pp. 380–389, 2007.
- [147] X. Li and B. Bhushan, “A review of nanoindentation continuous stiffness measurement technique and its applications,” *Materials Characterization*, vol. 48, no. 1, pp. 11–36, 2002.
- [148] Y.-L. Shen, “Nanoindentation for Testing Material Properties,” in *Handbook of Mechanics of Materials*, pp. 1981–2012, Singapore: Springer Singapore, 2019.
- [149] “ISO 4288:1996 Geometrical Product Specifications (GPS) — Surface texture: Profile method — Rules and procedures for the assessment of surface texture,” 1996.
- [150] “ISO 3274:1996 Geometrical Product Specifications (GPS) — Surface texture: Profile method — Nominal characteristics of contact (stylus) instruments,” 1996.
- [151] A. Townsend, N. Senin, L. Blunt, R. K. Leach, and J. S. Taylor, “Surface texture metrology for metal additive manufacturing: a review,” *Precision Engineering*, vol. 46, pp. 34–47, 2016.
- [152] W. W. Wits, S. Carmignato, F. Zanini, and T. H. Vaneker, “Porosity testing methods for the quality assessment of selective laser melted parts,” *CIRP Annals - Manufacturing Technology*, vol. 65, no. 1, pp. 201–204, 2016.
- [153] “ASTM B311-13 Standard Test Method for Density of Powder Metallurgy (PM) Materials Containing Less Than Two Percent Porosity,” 2013.
- [154] “ASTM B962-13 Standard Test Methods for Density of Compacted or Sintered Powder Metallurgy (PM) Products Using Archimedes’ Principle,” 2013.
- [155] H. Warlimont, *Titanium and titanium alloys*. Wiley-VCH Verlag GmbH & Co. KGaA, 2018.
- [156] S. Zhang, S. Rauniyar, S. Shrestha, A. Ward, and K. Chou, “An experimental study of tensile property variability in selective laser melting,” *Journal of Manufacturing Processes*, vol. 43, no. May, pp. 26–35, 2019.

- [157] Z. Xie, Y. Dai, X. Ou, S. Ni, and M. Song, “Effects of selective laser melting build orientations on the microstructure and tensile performance of Ti-6Al-4V alloy,” *Materials Science and Engineering A*, vol. 776, no. November 2019, p. 139001, 2020.
- [158] A. Szafrńska, A. Antolak-Dudka, P. Baranowski, P. Bogusz, D. Zasada, J. Małachowski, and T. Czujko, “Identification of Mechanical Properties for Titanium Alloy Ti-6Al-4V Produced Using LENS Technology,” *Materials*, vol. 12, p. 886, 3 2019.
- [159] D. Liović, M. Franulović, N. Gubelj, E. Kamenar, D. Kozak, and E. Vaglio, “Tensile and nanoindentation tests analysis of Ti6Al4V alloy manufactured by laser powder bed fusion,” *Procedia Structural Integrity*, vol. 53, pp. 37–43, 2024.
- [160] Y. T. Lee, M. Peters, and G. Welsch, “Elastic moduli and tensile and physical properties of heat-treated and quenched powder metallurgical Ti-6Al-4V alloy,” *Metallurgical Transactions A*, vol. 22, no. 3, pp. 709–714, 1991.
- [161] J. P. Panakkal, H. Willems, and W. Arnold, “Nondestructive evaluation of elastic parameters of sintered iron powder compacts,” *Journal of Materials Science*, vol. 25, no. 2, pp. 1397–1402, 1990.
- [162] M. V. Pantawane, T. Yang, Y. Jin, S. Mazumder, M. Pole, S. Dasari, A. Krokhin, A. Neogi, S. Mukherjee, R. Banerjee, and N. B. Dahotre, “Thermomechanically influenced dynamic elastic constants of laser powder bed fusion additively manufactured Ti6Al4V,” *Materials Science and Engineering A*, vol. 811, no. February, p. 140990, 2021.
- [163] W. Sun, Y. Ma, W. Huang, W. Zhang, and X. Qian, “Effects of build direction on tensile and fatigue performance of selective laser melting Ti6Al4V titanium alloy,” *International Journal of Fatigue*, vol. 130, no. August 2019, 2020.
- [164] W.-g. Jiang, J.-j. Su, and X.-q. Feng, “Effect of surface roughness on nanoindentation test of thin films,” *Engineering Fracture Mechanics*, vol. 75, no. 17, pp. 4965–4972, 2008.
- [165] P. Zhu, Y. Hu, and H. Wang, “Atomistic simulations of the effect of a void on nanoindentation response of nickel,” *Science China Physics, Mechanics and Astronomy*, vol. 53, pp. 1716–1719, 9 2010.
- [166] M. Conte, G. Mohanty, J. J. Schwiedrzik, J. M. Wheeler, B. Bellaton, J. Michler, and N. X. Randall, “Novel high temperature vacuum nanoindentation system with active surface referencing and non-contact heating for measurements up to 800 °C,” *Review of Scientific Instruments*, vol. 90, 4 2019.
- [167] A. Dareh Baghi, R. Ghomashchi, R. H. Oskouei, and H. Ebendorff-Heidepriem, “Nanomechanical Characterization of SLM-Fabricated Ti6Al4V Alloy: Etching and Precision,” *Metallography, Microstructure, and Analysis*, vol. 8, no. 5, pp. 749–756, 2019.
- [168] D. Liović, M. Franulović, E. Kamenar, and D. Kozak, “Nano-Mechanical Behavior of Ti6Al4V Alloy Manufactured Using Laser Powder Bed Fusion,” *Materials*, vol. 16, p. 4341, 6 2023.

- [169] J. Haubrich, J. Gussone, P. Barriobero-Vila, P. Kürnsteiner, E. A. Jäggle, D. Raabe, N. Schell, and G. Requena, *The role of lattice defects, element partitioning and intrinsic heat effects on the microstructure in selective laser melted Ti-6Al-4V*, vol. 167. Acta Materialia Inc., 2019.
- [170] C. Yan, B. Bor, A. Plunkett, B. Domènech, G. A. Schneider, and D. Giuntini, “Nanoindentation of Supercrystalline Nanocomposites: Linear Relationship Between Elastic Modulus and Hardness,” *JOM*, vol. 74, pp. 2261–2276, 6 2022.
- [171] K. Miyahara, S. Matsuoka, and T. Hayashi, “Nanoindentation as a strength probe—a study on the hardness dependence of indent size for fine-grained and coarse-grained ferritic steel,” *Metallurgical and Materials Transactions A: Physical Metallurgy and Materials Science*, vol. 32, no. 3, pp. 761–768, 2001.
- [172] G. M. Pharr, E. G. Herbert, and Y. Gao, “The indentation size effect: A critical examination of experimental observations and mechanistic interpretations,” *Annual Review of Materials Research*, vol. 40, pp. 271–292, 2010.
- [173] W. H. Kao, Y. L. Su, J. H. Horng, and C. Y. Chang, “Tribological, electrochemical and biocompatibility properties of Ti6Al4V alloy produced by selective laser melting method and then processed using gas nitriding, CN or Ti-C:H coating treatments,” *Surface and Coatings Technology*, vol. 350, no. March, pp. 172–187, 2018.
- [174] R. Wang, D. Gu, L. Xi, K. Lin, M. Guo, and H. Zhang, “Selective laser melted TiB<sub>2</sub>/Ti6Al4V graded materials and first-principle calculations,” *Materials Letters*, vol. 254, pp. 33–36, 2019.
- [175] V. Tuninetti, A. F. Jaramillo, G. Riu, C. Rojas-Ulloa, A. Znaidi, C. Medina, A. M. Mateo, and J. J. Roa, “Experimental Correlation of Mechanical Properties of the Ti-6Al-4V Alloy at Different Length Scales,” *Metals*, vol. 11, p. 104, 1 2021.
- [176] G. M. Pharr and A. Bolshakov, “Understanding nanoindentation unloading curves,” *Journal of Materials Research*, vol. 17, no. 10, pp. 2660–2671, 2002.
- [177] X. Liu, Q. Zhang, X. Zhao, X. Yang, and L. Luo, “Ambient-temperature nanoindentation creep in ultrafine-grained titanium processed by ECAP,” *Materials Science and Engineering A*, vol. 676, pp. 73–79, 2016.
- [178] Z. Li, S. Zhao, R. O. Ritchie, and M. A. Meyers, “Mechanical properties of high-entropy alloys with emphasis on face-centered cubic alloys,” *Progress in Materials Science*, vol. 102, pp. 296–345, 2019.
- [179] P. Kumar, M. E. Kassner, and T. G. Langdon, “Fifty years of Harper-Dorn creep: A viable creep mechanism or a Californian artifact?,” *Journal of Materials Science*, vol. 42, no. 2, pp. 409–420, 2007.
- [180] A. Dareh Baghi, S. Nafisi, R. Hashemi, H. Ebendorff-Heidepriem, and R. Ghomashchi, “Effective post processing of SLM fabricated Ti-6Al-4 V alloy: Machining vs thermal treatment,” *Journal of Manufacturing Processes*, vol. 68, no. PA, pp. 1031–1046, 2021.
- [181] S. Drücker, M. Schulze, H. Ipsen, L. Bandegani, H. Hoch, M. Kluge, and B. Fiedler, “Experimental and numerical mechanical characterization of additively manufactured Ti6Al4V lattice structures considering progressive damage,” *International Journal of Mechanical Sciences*, vol. 189, p. 105986, 1 2021.

- [182] E. Vaglio, G. Totis, A. Lanzutti, L. Fedrizzi, and M. Sortino, “A novel thermo-geometrical model for accurate keyhole porosity prediction in Laser Powder-Bed Fusion,” *Progress in Additive Manufacturing*, vol. 9, pp. 247–261, 4 2024.
- [183] R. Haque, M. Sekh, G. Kibria, and S. Haidar, “Improvement of surface quality of Ti-6Al-4V alloy by powder mixed electrical discharge machining using copper powder,” *Facta Universitatis, Series: Mechanical Engineering*, vol. 21, p. 063, 4 2023.
- [184] D. Liović, M. Franulović, L. Ferlič, and N. Gubelj, “Surface roughness of Ti6Al4V alloy produced by laser powder bed fusion,” *Facta Universitatis, Series: Mechanical Engineering*, vol. 22, p. 063, 4 2024.
- [185] A. B. Spierings, N. Herres, and G. Levy, “Influence of the particle size distribution on surface quality and mechanical properties in AM steel parts,” *Rapid Prototyping Journal*, vol. 17, no. 3, pp. 195–202, 2011.
- [186] J. Gockel, L. Sheridan, B. Koerper, and B. Whip, “The influence of additive manufacturing processing parameters on surface roughness and fatigue life,” *International Journal of Fatigue*, vol. 124, no. October 2018, pp. 380–388, 2019.
- [187] J. P. Kruth, L. Froyen, J. Van Vaerenbergh, P. Mercelis, M. Rombouts, and B. Lauwers, “Selective laser melting of iron-based powder,” *Journal of Materials Processing Technology*, vol. 149, no. 1-3, pp. 616–622, 2004.
- [188] A. Mansouri, “Development of a novel haunched link for eccentrically braced frames,” *Engineering Structures*, vol. 245, p. 112870, 10 2021.
- [189] “Abaqus/CAE: SIMULIA User Assistance 2020.”
- [190] M. Smith, Z. Guan, and W. J. Cantwell, “Finite element modelling of the compressive response of lattice structures manufactured using the selective laser melting technique,” *International Journal of Mechanical Sciences*, vol. 67, pp. 28–41, 2013.
- [191] M. Pelegatti, D. Benasciutti, F. De Bona, and E. Salvati, “Experimental characterization and modelling of cyclic elastoplastic response of an AISI 316L steel lattice structure produced by laser-powder bed fusion,” *Procedia Structural Integrity*, vol. 47, pp. 238–246, 2023.
- [192] A. M. Roach, B. C. White, A. Garland, B. H. Jared, J. D. Carroll, and B. L. Boyce, “Size-dependent stochastic tensile properties in additively manufactured 316L stainless steel,” *Additive Manufacturing*, vol. 32, p. 101090, 3 2020.
- [193] N. Razavi, B. Van Hooreweder, and F. Berto, “Effect of build thickness and geometry on quasi-static and fatigue behavior of Ti-6Al-4V produced by Electron Beam Melting,” *Additive Manufacturing*, vol. 36, p. 101426, 12 2020.
- [194] S. Murchio, M. Dallago, F. Zanini, S. Carmignato, G. Zappini, F. Berto, D. Maniglio, and M. Benedetti, “Additively manufactured Ti-6Al-4V thin struts via laser powder bed fusion: Effect of building orientation on geometrical accuracy and mechanical properties,” *Journal of the Mechanical Behavior of Biomedical Materials*, vol. 119, no. March, p. 104495, 2021.

# NOMENCLATURE

---

Notations related to statistical analysis and mathematical modelling	
adj. $R^2$	The adjusted coefficient of determination
$k$	Number of factors
$P_{\max}$	Maximum laser power
$P_{\text{mean}}$	Mean laser power
$P_n$	Normalized laser power
$p$ -value	Probability value
$R^2$	The coefficient of determination
$r$	The coefficient of correlation
$t_{\alpha/2,df(\text{error})}$	The critical value from the $t$ -distribution
$v_{\max}$	Maximum scanning speed
$v_{\text{mean}}$	Mean scanning speed
$v_n$	Normalized scanning speed
$\mathbf{X}$	The matrix of all predictor values
$\mathbf{x}_0$	The vector of predictor values
$x_1, x_2$	Predictor variables
$y$	Response variable
$\hat{y}(x_0)$	The predicted value of the response variable at $x_0$
$\alpha_{\text{ccd}}$	Distance of the star points from the center
$\alpha$	Significance level
$\beta_0$	Intercept
$\beta_1, \beta_2$	Coefficients for the linear term
$\beta_{11}, \beta_{22}$	Coefficients for the quadratic term
$\beta_{12}$	Coefficient for the interaction term
$\varepsilon$	Error term
$\hat{\sigma}$	The estimated variance of the error term
$\mu_{y x_0}$	The true mean response at $x_0$

---

Notations related to additive manufacturing process	
$E_L$	Linear energy density
$E_V$	Volumetric energy density

## 8. NOMENCLATURE

---

$h_D$	Hatch distance
$O_{LB}$	Overlap between adjacent laser beam passages
$P$	Laser power
$t$	Layer thickness
$v$	Scanning speed
$w$	The melt pool width
$\Delta t_{8/5}$	The cooling time from 800°C to 500°C

---

### Notations related to porosity estimation

---

$m_a$	Mass in the air
$m_e$	Mass in the ethanol
$p$	Porosity
$\rho$	Density
$\rho_e$	Density of ethanol
$\rho_t$	Theoretical density of Ti6Al4V alloy

---

### Notations related to tensile mechanical properties of solid material

---

$A$	Area of the specimen's cross-section
$E$	Young's modulus
$F$	Tensile load
$G$	Shear modulus
$l$	The current length
$l_0$	Initial length
$R_m$	Ultimate tensile strength
$R_{p0.2}$	Offset yield strength
$\nu$	Poisson's ratio
$\sigma$	The engineering stress
$\sigma_{true}$	True stress
$\varepsilon$	Engineering strain
$\varepsilon_{axial}$	Axial strain
$\varepsilon_{trans}$	Transverse strain
$\varepsilon_{true}$	True strain

---

### Notations related to nanoindentation procedure

---

$A_p$	Projected area of the Berkovich tip
$a, b, k$	Fitting parameters
$B, m$	Fitting parameters
$C_1, C_2$	Area coefficients of the Berkovich tip
$E$	Young's modulus
$E_i$	Young's modulus of the Berkovich tip



$E_r$	Reduced modulus
$F_{\text{amp}}$	Excitation amplitude
$h$	Indentation depth
$H$	Hardness
$h_0$	Displacement at the beginning of the creep stage
$h_c$	Contact depth
$h_{\text{amp}}$	Displacement amplitude
$h_{\text{cr}}$	Creep displacement
$H_{\text{cr}}$	Nano-hardness during the creep stage
$h_f$	Residual displacement after a completed unloading stage
$h_{\text{max}}$	Maximum indentation depth
$K_f$	The load-frame stiffness
$K_s$	The stiffness of the support springs
$m$	The loading column mass
$n$	The creep strain exponent
$P_{\text{cr}}$	Load during creep stage
$P_{\text{max}}$	Maximum indentation load
$P_{\text{unload}}$	Unloading force
$S$	Contact stiffness
$t$	Time
$t_0$	Time at the beginning of the creep stage
$\beta$	Factor for the Berkovich tip
$\dot{\epsilon}$	The creep strain rate
$\epsilon^*$	Berkovich tip factor for calculation of contact depth
$\phi$	The phase angle
$\nu$	Poisson's ratio
$\nu_i$	Poisson's ratio of the Berkovich tip
$\omega$	Excitation frequency

---

**Notations related to surface roughness**

---

$l_{\text{evaluation}}$	Evaluation length
$l_r$	Sampling length
$l_s$	Short-wave profile filter value
$l_{\text{traverse}}$	Traverse length
$R_a$	Average surface roughness measured along the line
$S_a$	Average surface roughness measured over the plane
$\lambda_c$	Cut-off value

---

**Notations related to lattice specimens and their numerical modeling**

---

$C_1, C_2$	Dimensionless constants
$D$	Damage variable

$E_I$	Internal energy
$E_{KE}$	Kinetic energy
$E_{lattice}$	Young's modulus of the lattice structure
$E_{solid}$	Young's modulus of the solid structure
$G_f$	The fracture energy
$L$	Characteristic length of the finite element
$M$	Maxwell number
$V_e$	Element volume
$d\bar{\epsilon}^{pl}$	The increment of equivalent plastic strain
$d_{designed}$	Designed diameter
$d_{effective}$	Effective diameter
$d_{end}$	The diameter at the ends of the strut
$d_{major}$	Major diameter
$d_{mid}$	The diameter at the midpoint of the strut
$d_{minor}$	Minor diameter
$f$	The yield function
$h$	Height of the joint nodes
$\mathbf{I}$	The identity tensor
$n$	Number of nodes
$n_1, n_2$	Density factors
$p$	The hydrostatic pressure
$s$	Number of struts
$\bar{\sigma}$	The effective (undamaged) stress tensor
$\bar{\epsilon}_f^{pl}$	The accumulated equivalent plastic strain at failure
$\bar{\epsilon}_D^{pl}$	The value of plastic strain at the onset of damage initiation
$\bar{u}^{pl}$	Equivalent plastic displacement
$\bar{u}_f^{pl}$	Equivalent plastic displacement at failure
$\lambda$	Plastic multiplier
$\omega_D$	Damage state variable
$\rho_{lattice}$	Density of the lattice structure
$\rho_{solid}$	Density of the solid structure
$\sigma_e$	The von Mises equivalent stress
$\sigma_{lattice}$	Yield strength of the lattice structure
$\sigma_{solid}$	Yield strength of the solid structure
$\sigma_y$	The yield stress
$\sigma_{y0}$	Yield stress at failure
$\sigma$	Stress tensor
$\epsilon^{pl}$	Plastic strain tensor

---

**Abbreviations**

---

AC	Air cooling
ANOVA	Analysis of variance

BCC	Body-centered cubic
BD	Build direction
BJT	Binder jetting
C-CCD	Circumscribed central composite design
C3D10	Quadratic tetrahedral elements
C3D4	Linear tetrahedral elements
COV	Coefficients of variation
CSM	Continuous stiffness measurement
D	Diagonal
D <sup>ab</sup>	As-built specimen
D <sup>an</sup>	Annealed specimen
DED	Directed energy deposition
DF	Degrees of freedom
DMLS	Direct metal laser sintering
EBM	Electron beam melting
EBS	Electron beam sintering
ELI	Extra low interstitial
FC	Furnace cooling
FC-CCD	Face-centered central composite design
H	Horizontal
HCP	Hexagonal close-packed
HIP	Hot isostatic pressing
HV1	Low-force Vickers hardness measured with an indentation load of 9.807 N
I-CCD	Inscribed central composite design
ISE	Indentation size effect
MAE	Mean absolute error
MEX	Material extrusion
MJT	Material jetting
NCV	Non-constant variance
OLS	Ordinary least squares
PBF	Powder bed fusion
PBF-LB	Laser beam powder bed fusion
RP	Reference point
SHL	Sheet lamination
SLS	Selective laser sintering
STD	Standard deviation
S-W	Shapiro-Wilk test
V	Vertical
VPP	Vat photopolymerization

# LIST OF FIGURES

- 2.1. Schematic representation of the working principle of PBF-LB process. . . . . 9
- 2.2. Scanning strategy applied to each layer stacked along the build direction (BD):  
 (a) Continuous unidirectional, (b) Continuous bidirectional with alternations  
 of scan vectors on each layer, (c) Continuous bidirectional with meander, (d)  
 Island with translation and alternations on each layer. . . . . 12
- 2.3. Illustration of staircase effect causing an irregular down-skin surface with a  
 high number of fused powder particles. . . . . 21
- 2.4. Cross-sectional image of the internal volume near the down-facing surface  
 revealing significant near-surface porosity and irregular surface. Reproduced  
 from [106]. . . . . 22
- 2.5. The first three rows showcase various strut-based lattice cell architectures,  
 followed by skeletal and sheet-triply periodic minimal surfaces. Reproduced  
 from [115]. . . . . 23
- 2.6. (A) The production of meta-implants was carried out using selective laser  
 melting (SLM): (1) A wiper deposits a fresh layer of Ti-6Al-4V powder. (2)  
 Powder particles are melted selectively using a high-power laser. (3) Post-  
 manufacturing, excess powder is removed with a suction tube. (4) The build  
 plate holds the parts along with supports. (5) The supports are then carefully  
 detached. (6) The build plate now contains the parts without supports. (B)  
 The additively manufactured meta-implants. (C) The test setup used for lo-  
 ading the meta-implants, including bone-mimicking materials. (D) Horizontal  
 strains in the bone-mimicking materials surrounding the meta-implants at  $t$   
 $= 0$  and  $t = 180$  seconds with a displacement of 1.5 mm for C1, C2, H1, H2,  
 and H3. Reproduced from [118]. . . . . 25
- 3.1. Graphical comparison of the three CCD types with two factors. . . . . 29
- 3.2. (a) Ti6Al4V (ELI) Grade 23 powder particles, and (b) their size distribution,  
 including cumulative and probability density functions. . . . . 33
- 3.3. (a) Scanning strategy used to manufacture (b) Cubic specimens using PBF-LB  
 process. . . . . 34
- 3.4. (a) Dimensions of tensile tests specimens, (b) Tensile test specimens after  
 manufacturing with marked positions on the build platform. . . . . 36
- 3.5. Model of specimen with lattice structure. . . . . 38

3.6. Manufactured test specimens with BCC unit cells arranged in a lattice structure. . . . .	38
3.7. Schematic diagram of the annealing heat treatment. . . . .	40
3.8. Tensile test setup consisting of: (a) INSTRON 1255 – 8500 plus universal servohydraulic machine and GOM ARAMIS adjustable 2D/3D 12M system, (b) Self-aligning grips. . . . .	45
3.9. Tensile test setup: (a) StepLAB electro-mechanical actuator, (b) Epsilontech extensometer with 20 mm gauge length attached to specimen with lattice structure. . . . .	47
3.10. Surface roughness measurements using: (a) TESA Rugosurf 10-G profilometer, (b) Keyence VHX 7000 microscope. . . . .	48
3.11. (a) Positions for surface roughness measurements, (b) Influence of vertical pitch and magnification on $S_a$ . . . . .	49
3.12. (a) Analytical balance, (b) Setup for relative density measurements. . . . .	50
4.1. Microstructure of PBF-LB Ti6Al4V alloy in: (a) as-built and, (b) annealed condition. . . . .	52
4.2. Different void defects found close to the side surface of specimens manufactured using the: (a) $E_V$ of 111.1 J/mm <sup>3</sup> ( $P = 250$ W and $v = 1000$ mm/s) caused formation of spherical voids, (b) $E_V$ of 66.7 J/mm <sup>3</sup> ( $P = 225$ W and $v = 1500$ mm/s) caused interconnected voids with entrapped powder particles, (c) $E_V$ of 71.1 J/mm <sup>3</sup> ( $P = 200$ W and $v = 1250$ mm/s) caused formation of elongated and narrow voids, (d) $E_V$ of 74.1 J/mm <sup>3</sup> ( $P = 250$ W and $v = 1500$ mm/s) caused formation of spherical voids. . . . .	55
4.3. Typical mechanical response: (a) Engineering stress – strain curves with pronounced plastic deformation characteristic to each group of specimens, (b) Local high strain field formed at the midpoint of gauge section - specimen from B group. . . . .	56
4.4. Distributions across different positions for: (a) Young’s modulus, (b) shear modulus, (c) Poisson’s ratio, (d) $R_{p0.2}$ , (e) $R_m$ , (f) elongation at break (the corresponding specimen positions are detailed in Table 3.3 and illustrated in Figure 3.4a). . . . .	57
4.5. Response surfaces with added 95% confidence intervals visible as grey surfaces representing the influence of $P$ and $v$ on the: (a) Young’s modulus prediction variable, (b) Shear modulus prediction variable. . . . .	59
4.6. Response surfaces with added 95% confidence intervals visible as grey surfaces representing the influence of $P$ and $v$ on the: (a) $R_{p0.2}$ prediction variable, (b) $R_m$ prediction variable. . . . .	62
4.7. Poisson’s ratio in function of the: (a) Utilized PBF-LB $P$ and $v$ levels with superimposed 95% confidence intervals visible as grey surfaces, (b) Length and width of the measurement area in ratio 5:1. . . . .	63

4.8. Fracture surfaces with pronounced plateau region in the inner section and shear surfaces in the outer section, consistently observed across all specimen groups . . . . .	65
4.9. Distribution of HV1 hardness across specimen groups. . . . .	66
4.10. (a) CSM tests conducted in different columnar prior- $\beta$ grains of the annealed specimen, (b) residual imprint of the Berkovich tip used [168]. . . . .	69
4.11. Typical Young's modulus and nano-hardness CSM measurements on as-built and annealed specimens, with 95% confidence intervals shown as shaded areas: (a) Microstructure of the D <sup>ab</sup> specimen featuring a dominant $\alpha'$ phase, and (b) Microstructure of the annealed D <sup>an</sup> specimen with a dominant $\alpha + \beta$ phase; (c) Young's modulus values as a function of indentation depth for the D <sup>ab</sup> , and (d) for the D <sup>an</sup> specimen; (e) Nano-hardness values as a function of indentation depth for the D <sup>an</sup> specimen, and (f) for the D <sup>ab</sup> specimen [168]. . . . .	71
4.12. (a) Linear regression model depicting the relationship between Young's modulus and nano-hardness for annealed Ti6Al4V alloy, accompanied by a 95% confidence interval shown as a shaded area; (b) Residual plot showing random scatter around the zero line, indicating the validity of the linear regression model [168]. . . . .	76
4.13. Nano-mechanical response of as-built and annealed specimens under nanoindentation creep tests: (a) Load-unload curves for the as-built specimen and (b) the annealed specimen under various holding loads during the creep stage; (c) indentation depth versus time curves during the creep stage for the as-built specimen and (d) the annealed specimen under different holding loads [168].	78
4.14. Fitting curves and experimental data for the annealed specimen under a 200 mN holding load during the creep stage: (a) Experimental indentation depth vs. time data along with model parameters; (b) Experimental data and model parameters for the upper portion of the unloading curve [168]. . . . .	79
4.15. Creep properties and behavior under various maximum indentation loads during the creep stage: (a) Representative $\ln \dot{\epsilon} - \ln H_{cr}$ curves for as-built specimen and (b) annealed specimen; (c) creep stress exponent for as-built specimen and (d) annealed specimen, each with 95% confidence intervals [168]. . . . .	80
4.16. Stress-strain curves of lattice specimens grouped by $d_{\text{end}}$ : (a) 0.6 mm, (b) 0.8 mm, and (c) 1 mm (red $\times$ indicate beginning of the progressive damage of struts). . . . .	82
4.17. Failure of different lattice configurations subjected to tensile load (white planes on yellow cubes illustrate fracture planes). . . . .	83
5.1. Variation of (a) $R_a$ values, (b) $S_a$ values based on different specimen positions on the build platform [184] (the corresponding specimen positions are detailed in Table 3.3 and illustrated in Figure 3.4a). . . . .	88

5.2.	Response surfaces illustrating the effects of $P_L$ and $\nu$ on: (a) $R_a$ values, with 95% confidence intervals displayed as gray surfaces, and (b) $S_a$ values, incorporating experimental data shown as blue dots [184]. . . . .	90
5.3.	(a) Typical surface from the specimen group C, characterized by the highest $R_a$ and $S_a$ values measured, (b) Typical surface from the specimen group I, characterized by the lowest $R_a$ and $S_a$ values measured [184]. . . . .	91
6.1.	(a) Engineering stress-strain curve of D group specimens and (b) true stress-strain curve with marked $\sigma_{y0}$ , $\bar{\epsilon}_D^{pl}$ and $\bar{\epsilon}_f^{pl}$ values . . . . .	98
6.2.	The boundary conditions set on the flat specimen for simulating tensile tests with added points used as a virtual extensometer to calculate engineering strain. . . . .	100
6.3.	Comparison of numerically estimated engineering stress-strain curves using different element type, size and symmetry condition with experimentally determined engineering stress-strain curve. . . . .	101
6.4.	(a) True principal stress shown at the time step at which the ultimate tensile strength is reached and (b) failure of flat specimen. . . . .	102
6.5.	FE model with analytical rigid surface, reference point, boundary conditions and constraints. . . . .	105
6.6.	Convergence of $E$ and $R_m$ respect to the number of finite elements per unit cell (brown text indicates the computational time required to complete simulation, red text indicates the element size). . . . .	106
6.7.	Influence of symmetry boundary condition on engineering stress-strain curve on the example of 06-06-2 lattice specimen configuration. . . . .	107
6.8.	(a) Internal and kinetic energies of the of 06-06-2 lattice specimen while simulating tensile test, (b) reaction forces recorded at the upper and lower analytical rigid surface and their difference. . . . .	107
6.9.	Comparison between experimental and numerical results of lattice specimens with corrected strut diameters. . . . .	109
6.10.	Failure of different lattice configurations with corrected effective mean $d_{end}$ and $d_{mid}$ diameters and 1/8th symmetry (damaged struts are marked with red rectangle, and averaging threshold was set to the default value of 75%). . . . .	110
6.11.	Response surface plot showing the influence of $d_{end}$ and $d_{mid}$ on Young's modulus highlighting the damage at the struts occurred while manufacturing lattice specimens 1-1-2-II and 1-1-2-III (the red dashed line indicates the difference between the experimental results and the model at a given point). . . . .	112
6.12.	Response surface plot showing the influence of $d_{end}$ and $d_{mid}$ on (a) $R_{p0.2}$ and (b) $R_m$ (the red dashed line indicates the difference between the experimental results and the model at a given point). . . . .	114

# LIST OF TABLES

2.1. Comparison of mechanical properties of PBF-LB Ti6Al4V alloy. . . . .	18
3.1. Selected parameters and levels according to FC-CCD. . . . .	30
3.2. Process parameters used to manufacture cubic specimens. . . . .	35
3.3. Tensile test specimen coordinates respect to the origin of the build platform.	36
3.4. Unit cell configurations. . . . .	37
3.5. PBF-LB process parameters used to manufacture lattice structure specimens.	39
4.1. The average relative density and calculated porosity values with corresponding standard deviations. . . . .	53
4.2. Mechanical properties of PBF-LB Ti6Al4V alloy determined using tensile tests.	56
4.3. Regression models for Young's modulus and their statistical properties [159].	58
4.4. Regression models for shear modulus and their statistical properties. . . . .	60
4.5. Regression models for $R_{p0.2}$ and their statistical properties. . . . .	60
4.6. Regression models for $R_m$ and their statistical properties. . . . .	61
4.7. Regression models for Poisson's ratio and their statistical properties. . . . .	63
4.8. The impact of Kroll's etchant on nano-hardness. . . . .	68
4.9. Influence of indentation location on nano-mechanical properties - specimen A.	69
4.10. Young's modulus and nano-hardness for different PBF-LB process parameters combinations and heat treatment conditions. . . . .	72
4.11. HV1 values for different PBF-LB process parameter combinations and heat treatment conditions. . . . .	73
4.12. The $p$ -values obtained from Dunn's multiple comparison test conducted on annealed specimens. . . . .	74
4.13. Fitting parameters for the creep stage. . . . .	79
4.14. Parameters for fitting the unloading portion of the curve and contact stiffness.	79
4.15. Mechanical properties of lattice specimens. . . . .	82
5.1. Regression models for $R_a$ and their statistical properties (back transformed).	90
5.2. Regression models for $S_a$ and their statistical properties (back transformed).	91
6.1. Mechanical properties of PBF-LB Ti6Al4V alloy corresponding to specimen group D. . . . .	98
6.2. Designed and actual strut diameters after PBF-LB. . . . .	102
6.3. Regression model for $E$ of lattice specimens and its statistical properties. . .	111
6.4. Regression model for $R_{p0.2}$ of lattice specimens and its statistical properties.	113
6.5. Regression models for $R_m$ of lattice specimens and their statistical properties.	114



A1.	Summary of the full quadratic model for $E$ (M1) formulated using normalized predictors. . . . .	150
A2.	Summary of the full quadratic model for $G$ (M3) formulated using normalized predictors. . . . .	150
A3.	Summary of the full quadratic model for $R_{p0.2}$ (M5) formulated using normalized predictors. . . . .	151
A4.	Summary of the full quadratic model for $R_m$ (M7) formulated using normalized predictors. . . . .	151
A5.	Summary of the full quadratic model for $\nu$ (M9) formulated using normalized predictors. . . . .	151
A6.	Summary of the full quadratic model for $R_a$ (M11) formulated using normalized predictors. . . . .	152
A7.	Summary of the full quadratic model for $S_a$ (M13) formulated using normalized predictors. . . . .	152
A8.	Summary of the full quadratic model for $E$ (M15) of lattice specimens . . . .	152
A9.	Summary of the full quadratic model for $R_{p0.2}$ (M16) of lattice specimens . .	153
A10.	Summary of the full quadratic model for $R_m$ (M17) of lattice specimens . . .	153
A11.	$p$ -values for evaluating the dependence of mechanical properties on position .	153

## APPENDICES

**Table A1:** Summary of the full quadratic model for  $E$  (M1) formulated using normalized predictors.

Term	Estimate	Std. Error	$p$ -value	Remark
Intercept	112747.5	840.8	<0.001	significant
$P$	708.0	460.5	0.13914	not significant
$v$	803.6	460.5	0.09561	not significant
$P^2$	-2662.7	797.7	0.00312	significant
$v^2$	-346.0	797.7	0.66886	not significant
$Pv$	443.5	564.0	0.44043	not significant

Residual standard error: 1954 on 21 degrees of freedom, Multiple  $R^2$ : 0.4525, Adjusted  $R^2$ : 0.3222,  $F$ -statistic: 3.472 on 5 and 21 DF,  $p$ -value: 0.01922.

**Table A2:** Summary of the full quadratic model for  $G$  (M3) formulated using normalized predictors.

Term	Estimate	Std. Error	$p$ -value	Remark
Intercept	43097.56	356.47	<0.001	significant
$P$	481.24	195.25	0.0224	significant
$v$	375.66	195.25	0.0680	not significant
$P^2$	-885.73	338.18	0.0160	significant
$v^2$	-11.32	338.18	0.9736	not significant
$Pv$	144.55	239.13	0.5520	not significant

Residual standard error: 828.4 on 21 degrees of freedom, Multiple  $R^2$ : 0.4474, Adjusted  $R^2$ : 0.3158,  $F$ -statistic: 3.401 on 5 and 21 DF,  $p$ -value: 0.0209.

**Table A3:** Summary of the full quadratic model for  $R_{p0.2}$  (M5) formulated using normalized predictors.

Term	Estimate	Std. Error	$p$ -value	Remark
Intercept	969.0956	5.1159	<0.001	significant
$P$	-0.6672	2.8021	0.814097	not significant
$v$	-2.8131	2.8021	0.326837	not significant
$P^2$	-19.6771	4.8534	<0.001	significant
$v^2$	-10.2681	4.8534	0.046492	significant
$Pv$	-6.4854	3.4318	0.072672	not significant

Residual standard error: 11.89 on 21 degrees of freedom, Multiple  $R^2$ : 0.5489, Adjusted  $R^2$ : 0.4415,  $F$ -statistic: 5.11 on 5 and 21 DF,  $p$ -value: 0.003207.

**Table A4:** Summary of the full quadratic model for  $R_m$  (M7) formulated using normalized predictors.

Term	Estimate	Std. Error	$p$ -value	Remark
Intercept	1000.804	4.885	<0.001	significant
$P$	7.885	2.676	0.00769	significant
$v$	-3.758	2.676	0.17479	not significant
$P^2$	-11.859	4.634	0.01828	significant
$v^2$	-4.351	4.634	0.35841	not significant
$Pv$	-3.540	3.277	0.29230	not significant

Residual standard error: 11.35 on 21 degrees of freedom, Multiple  $R^2$ : 0.4783, Adjusted  $R^2$ : 0.3541,  $F$ -statistic: 3.851 on 5 and 21 DF,  $p$ -value: 0.0124.

**Table A5:** Summary of the full quadratic model for  $\nu$  (M9) formulated using normalized predictors.

Term	Estimate	Std. Error	$p$ -value	Remark
Intercept	0.3082200	0.0041401	<0.001	significant
$P$	-0.0064080	0.0022676	0.0101	significant
$v$	-0.0020738	0.0022676	0.3708	not significant
$P^2$	-0.0040120	0.0039276	0.3187	not significant
$v^2$	-0.0038788	0.0039276	0.3346	not significant
$Pv$	0.0007915	0.0027773	0.7784	not significant

Residual standard error: 0.009621 on 21 degrees of freedom, Multiple  $R^2$ : 0.3421, Adjusted  $R^2$ : 0.1855,  $F$ -statistic: 2.184 on 5 and 21 DF,  $p$ -value: 0.09469.

**Table A6:** Summary of the full quadratic model for  $R_a$  (M11) formulated using normalized predictors.

Term	Estimate	Std. Error	$p$ -value	Remark
Intercept	8.1179	0.3209	<0.001	significant
$P$	-1.7282	0.1758	<0.001	significant
$v$	0.8063	0.1758	<0.001	significant
$P^2$	1.3287	0.3045	<0.001	significant
$v^2$	-0.1701	0.3045	0.58	not significant
$Pv$	-1.2857	0.2153	<0.001	significant

Residual standard error: 0.8611 on 30 degrees of freedom, multiple  $R^2$ : 0.852, Adjusted  $R^2$ : 0.8274,  $F$ -statistic: 34.54 on 5 and 30 DF,  $p$ -value: 1.408e-1.

**Table A7:** Summary of the full quadratic model for  $S_a$  (M13) formulated using normalized predictors.

Term	Estimate	Std. Error	$p$ -value	Remark
Intercept	8.1648	0.3223	<0.001	significant
$P$	-1.5717	0.1765	<0.001	significant
$v$	0.5394	0.1765	0.004	significant
$P^2$	0.8847	0.3058	0.007	significant
$v^2$	-0.2577	0.3058	0.41	not significant
$Pv$	-1.0572	0.2162	<0.001	significant

Residual standard error: 0.8648 on 30 degrees of freedom, multiple  $R^2$ : 0.8021, Adjusted  $R^2$ : 0.7691,  $F$ -statistic: 24.32 on 5 and 30 DF,  $p$ -value: 1.012e-09.

**Table A8:** Summary of the full quadratic model for  $E$  (M15) of lattice specimens

Term	Estimate	Std. Error	$p$ -value	Remark
Intercept	4738.3	260.9	<0.001	significant
$d_{\text{mid}}$	-8221.3	390.8	<0.001	significant
$d_{\text{end}}$	-6122.8	390.8	<0.001	significant
$d_{\text{mid}}^2$	2778.2	198.5	<0.001	significant
$d_{\text{end}}^2$	1828.6	198.5	<0.001	significant
$d_{\text{mid}}d_{\text{end}}$	7580.2	171.9	<0.001	significant

Residual standard error: 48.13 on 43 degrees of freedom, Multiple  $R^2$ : 0.9984, Adjusted  $R^2$ : 0.9982,  $F$ -statistic: 5335 on 5 and 43 DF,  $p$ -value: <2.2e-16.

**Table A9:** Summary of the full quadratic model for  $R_{p0.2}$  (M16) of lattice specimens

Term	Estimate	Std. Error	$p$ -value	Remark
Intercept	32.799	1.630	<0.001	significant
$d_{\text{mid}}$	-66.982	2.442	<0.001	significant
$d_{\text{end}}$	-41.373	2.442	<0.001	significant
$d_{\text{mid}}^2$	17.158	1.240	<0.001	significant
$d_{\text{end}}^2$	6.662	1.240	<0.001	significant
$d_{\text{mid}}d_{\text{end}}$	87.040	1.074	<0.001	significant

Residual standard error: 0.3007 on 43 degrees of freedom, Multiple  $R^2$ : 0.9996, Adjusted  $R^2$ : 0.9995,  $F$ -statistic: 1.948e+04 on 5 and 43 DF,  $p$ -value: <2.2e-16.

**Table A10:** Summary of the full quadratic model for  $R_m$  (M17) of lattice specimens

Term	Estimate	Std. Error	$p$ -value	Remark
Intercept	23.855	3.544	<0.001	significant
$d_{\text{mid}}$	-57.024	5.309	<0.001	significant
$d_{\text{end}}$	-29.532	5.309	<0.001	significant
$d_{\text{mid}}^2$	11.578	2.696	<0.001	significant
$d_{\text{end}}^2$	2.859	2.696	0.295	not significant
$d_{\text{mid}}d_{\text{end}}$	85.878	2.335	<0.001	significant

Residual standard error: 0.6538 on 43 degrees of freedom, Multiple  $R^2$ : 0.998, Adjusted  $R^2$ : 0.9978,  $F$ -statistic: 4391 on 5 and 43 DF,  $p$ -value: <2.2e-16.

**Table A11:**  $p$ -values for evaluating the dependence of mechanical properties on position

Mechanical properties	Levene's test	Kruskal - Wallis
$R_{p0.2}$	0.10	0.20
$R_m$	0.13	0.42
$\nu$	0.40	0.06
$E$	0.95	0.45
$G$	0.84	0.63
$A$	0.31	0.009

## CURRICULUM VITAE

David Liović was born on January 24th, 1995 in Đakovo. He finished elementary school in Trnava and high school in Đakovo. He completed his undergraduate studies in mechanical engineering in 2016 at the Mechanical Engineering Faculty in Slavonski Brod, J.J. Strossmayer University of Osijek. Subsequently, he enrolled in the graduate study program in Product Design and Development at the same faculty and earned his master's degree in 2018.

In 2018, he joined the Faculty of Engineering, University of Rijeka as a research and teaching assistant at the Department of Engineering Design. He teaches courses in Engineering Graphics and Machine Elements Design I in the undergraduate, and Mechanical Design of Machine Components in the graduate university study of mechanical engineering.

In 2019, he enrolled in the postgraduate doctoral study in the field of mechanical engineering at the Faculty of Engineering, University of Rijeka. His scientific research focuses on engineering design for additive manufacturing of metallic materials. During his PhD, he established strong collaboration with the Polytechnic Department of Engineering and Architecture, University of Udine. He also established a strong collaboration with the Faculty of Mechanical Engineering, University of Maribor, where he spent over three months through the ERASMUS+ program. Since 2019, he has been a researcher on a project *Modelling and simulation in development of advanced materials* - SIMMAT, founded by the Croatian Science Foundation, as well as on three projects founded by the University of Rijeka. He attended two summer schools in the field of fatigue and fracture modeling and analysis. Furthermore, he has been layout editor of the Engineering Review journal from 2020 to 2023. In 2020 and 2021, he has been a member of the organizing committee at My First Conference.

He is the first author of two scientific papers published in international peer-reviewed scientific journals and the author of four scientific papers published in conference proceedings.